

---

A STUDY OF SUBMILLIMETRE GALAXIES WITH THE  
HERSCHEL SPACE OBSERVATORY

---

Matthew Allen

A THESIS SUBMITTED TO  
CARDIFF UNIVERSITY  
FOR THE DEGREE OF  
DOCTOR OF PHILOSOPHY

AUGUST 2017

*Why do we fall? So that we can learn to pick ourselves up.*

# Acknowledgements

To Mum, Dad and Lili. I could not ask for more in life than the three of you to support me. You have nurtured my passion for knowledge, every single day, without hesitation. Consider this work a reflection of the support and kindness you have always shown me. From the towering seat of your shoulders, I have seen further than I could ever dream of. Thank you.

# Abstract

This work uses data from the Herschel Space Observatory and complementary surveys to study how the properties of star forming galaxies have changed over a large redshift range.

Using the likelihood ratio technique, infrared counterparts from the VIKING survey are found for a large sample of Herschel ATLAS galaxies over the three GAMA fields. I find that approximately half of all Herschel ATLAS galaxies have a reliable VIKING counterpart. I find that the fraction of Herschel sources with a reliable VIKING counterparts remains above 30% for Herschel sources at redshifts above  $z = 3$ , beyond the VIKING detection limit. We propose that this is the result of observing a large number of gravitationally lensed sources in the Herschel ATLAS survey.

I match a sample of Herschel ATLAS sources to the optical Subaru Deep Field (SDF) catalogue, using radio data as an intermediary step to attain accurate positions. I compare this technique with matching Herschel ATLAS sources directly to the SDF catalogue and find that of the common matched sources, 6% of Herschel ATLAS sources are matched to two different SDF sources.

I study the star forming properties of Herschel ATLAS and Herschel-GOODS galaxies. I study the two galaxy samples in terms of the galaxy main sequence, Kennicutt-Schmidt relation and the K magnitude-redshift relation. I find that the Herschel galaxies are relatively homogeneous. There is little evidence that the starburst phase of galaxies plays a large role in the star formation history of Herschel galaxies. I find that the star formation efficiency of our starburst galaxies is on average the same as main sequence galaxies, implying that starburst galaxies form more stars due an increased gas mass.

The optical images of the Herschel-GOODS sample of galaxies are decomposed in to their bulge and disc components. I find that 67% feature a bulge which is best

fit with a low Sersic index profile, suggesting the majority of the population feature a disc-like or pseudo-bulge. I see little evidence of a correlation between the properties of the bulge and the overall star forming properties of the galaxy.

# Contents

<b>List of Tables</b>	<b>5</b>
<b>List of Figures</b>	<b>7</b>
<b>1 Introduction</b>	<b>17</b>
1.1 The Great Debate . . . . .	17
1.2 Galaxy evolution . . . . .	18
1.3 Star formation evolution . . . . .	19
1.4 Galaxy morphology . . . . .	22
1.5 Dust . . . . .	25
1.6 Far Infrared and Sub-millimetre Astronomy . . . . .	27
1.7 Herschel . . . . .	30
1.8 Herschel surveys and complementary surveys . . . . .	31
1.8.1 Herschel-ATLAS survey Data . . . . .	31
1.8.2 Herschel-GOODS . . . . .	33
1.8.3 VIKING survey data . . . . .	34
1.8.4 Subaru Deep Field (SDF) . . . . .	35
1.9 Thesis outline . . . . .	35
<b>2 Near infrared surveying with VIKING</b>	<b>37</b>
2.1 Introduction . . . . .	37
2.2 Data . . . . .	39
2.3 Source Matching . . . . .	41
2.3.1 Estimating $f(r)$ . . . . .	42
2.3.2 Estimating $n(m)$ and $q(m)$ . . . . .	43
2.4 Source Matching Results . . . . .	45
2.4.1 Source matching statistics . . . . .	45

2.4.2	Likelihood method false ID estimation . . . . .	48
2.4.3	Advantages and drawbacks of the likelihood ratio method . . .	48
2.4.4	Uses of the Herschel-VIKING matched catalogues . . . . .	50
2.5	Do VIKING and SDSS find the same identifications? . . . . .	52
2.5.1	Sources detected with VIKING and SDSS . . . . .	53
2.5.2	Sources only detected with SDSS . . . . .	55
2.5.3	Sources only detected with VIKING . . . . .	57
2.6	Conclusions . . . . .	58
<b>3</b>	<b>Gravitational lensing identification with VIKING</b>	<b>60</b>
3.1	Introduction . . . . .	60
3.2	Redshift distributions . . . . .	65
3.2.1	Estimating Herschel photometric redshifts . . . . .	65
3.2.2	Redshift Distributions of the Herschel and VIKING samples .	67
3.3	Density of VIKING sources around Herschel sources . . . . .	69
3.3.1	Results . . . . .	70
3.4	Estimating how many Herschel sources have an associated VIKING counterpart . . . . .	74
3.4.1	Lens-Lensed galaxy separation . . . . .	77
3.4.2	High S/N sources . . . . .	78
3.4.3	Analysis . . . . .	79
3.5	Comparison to lens candidates in other work . . . . .	81
3.5.1	Results . . . . .	82
3.6	Studying the spectral energy distributions of possible lenses . . . . .	84
3.7	The spectral energy distributions of possible lenses . . . . .	89
3.8	Possible sources of error . . . . .	90
3.9	Conclusions . . . . .	91
<b>4</b>	<b>Accurate optical identifications for Herschel ATLAS sources</b>	<b>93</b>
4.1	Introduction . . . . .	93
4.2	Data . . . . .	95
4.2.1	Subaru Deep Field (SDF) data . . . . .	95
4.2.2	Very Large Array (VLA) data . . . . .	95
4.3	Matching Herschel and Subaru catalogues . . . . .	96

4.3.1	Matching Herschel ATLAS to VLA . . . . .	97
4.3.2	Matching Herschel ATLAS to Subaru Deep Field . . . . .	99
4.4	Source matching analysis . . . . .	100
4.4.1	Herschel ATLAS to VLA matching statistics . . . . .	100
4.4.2	Herschel ATLAS to SDF matching statistics . . . . .	101
4.5	Using radio data against directly matching . . . . .	103
4.6	Testing our photometric redshifts with HYPERZ . . . . .	109
4.6.1	HYPERZ . . . . .	110
4.6.2	Testing the accuracy of HyperZ . . . . .	112
4.6.3	Redshift fitting results . . . . .	113
4.7	Possible lenses in the Subaru Deep Field . . . . .	115
4.8	K-magnitude redshift relation . . . . .	117
4.9	Conclusions . . . . .	119
<b>5</b>	<b>The properties of Herschel ATLAS galaxies</b>	<b>122</b>
5.1	Introduction . . . . .	122
5.2	Data . . . . .	126
5.2.1	Herschel-SDF . . . . .	126
5.2.2	Herschel-GOODS . . . . .	127
5.3	Magphys . . . . .	128
5.4	Estimating the gas mass . . . . .	129
5.4.1	Fundamental Metallicity Relationship . . . . .	131
5.4.2	Accuracy of the FMR . . . . .	134
5.5	The Galaxy Main Sequence . . . . .	135
5.5.1	Starburst galaxies . . . . .	137
5.6	The Kennicutt-Schmidt relation . . . . .	140
5.6.1	The star formation efficiency of starburst galaxies . . . . .	142
5.7	Conclusions . . . . .	145
<b>6</b>	<b>Analysing the profiles of Herschel galaxies</b>	<b>147</b>
6.1	Introduction . . . . .	147
6.2	GALFIT . . . . .	151
6.3	Simulating Herschel GOODS galaxies . . . . .	152
6.3.1	Simulating technique . . . . .	153

---

6.4	Running GALFIT on simulated sources . . . . .	156
6.4.1	Potential problems when running GALFIT . . . . .	157
6.4.2	Double profile fit - Variable Sersic indices . . . . .	159
6.4.3	Double profile fit - Fixed Sersic indexes . . . . .	163
6.4.4	High reduced chi values . . . . .	165
6.4.5	Discussion of the simulations . . . . .	167
6.5	Running GALFIT on Herschel GOODS galaxies . . . . .	168
6.5.1	Fitting method . . . . .	168
6.5.2	Single profile fitting . . . . .	169
6.5.3	Selecting the best double profile model . . . . .	170
6.5.4	Double profile fitting . . . . .	175
6.6	The properties of galaxies and their intensity profiles . . . . .	182
6.7	Conclusions . . . . .	185
<b>7</b>	<b>Conclusions</b>	<b>188</b>
7.1	Thesis overview . . . . .	188
7.2	Key Results . . . . .	189
7.3	Future Work . . . . .	192
<b>A</b>	<b>Herschel-VLA-SDF matched sources table</b>	<b>194</b>

# List of Tables

2.1	The number of sources in both the Herschel ATLAS and VIKING surveys over the three GAMA fields. These are the final counts after removing sources that are likely stars and sources not in areas covered by both surveys. . . . .	40
2.2	The results of our source matching between the Herschel ATLAS and VIKING catalogues over all three GAMA fields. . . . .	47
2.3	Results of matching both the SDSS and VIKING sources to the Herschel ATLAS catalogue, split over the three GAMA fields. We define reliable matches as those with a reliability of 0.8 or greater. The SDSS and VIKING sources are determined as being the same if they are within 1 arcsecond of each other. . . . .	52
2.4	Table of the different categories of SDSS cutout images at the positions of those Herschel sources with different SDSS and VIKING sources in the GAMA 9-h field. . . . .	55
3.1	Table of $Q_0$ and $\sigma_{pos}$ for Herschel sources over the three individual GAMA fields. . . . .	77
3.2	Table of $Q_0$ and $\sigma_{pos}$ for Herschel sources over the three individual GAMA fields. Only sources with a 350 micron s/n above 10 are plotted.	80
3.3	Table of lens candidates identified in Negrello et al. (2017), which we have attempted to find counterparts for in our gravitational lensing work. The Herschel redshifts from Negrello et al. (2017) are spectroscopic where available, with the remainder having photometric redshifts (identified in italics). The Herschel redshifts estimated in our work are estimated from the Herschel fluxes alone. . . . .	83

---

4.1	Table of the source matching statistics when matching the Herschel and VLA catalogues together and then by matching this sample to the SDF catalogue. . . . .	102
4.2	Those Herschel sources with two possible SDF counterparts and their properties. . . . .	102
4.3	The statistics of matching a sample of Herschel sources to the Subaru Deep Field catalogue. We compare the results of two methods: directly matching the two catalogues and using an intermediate step of first matching to a radio catalogue to get improved positions for our Herschel sources. . . . .	106
4.4	Table of our possible lenses, identified from Figure 4.9. . . . .	115
5.1	The properties of the two sources, studied by Magdis et al. (2011), that we use to test the FMR. . . . .	134
5.2	A table of the number of main sequence and starburst galaxies in each redshift bin in the Herschel-GOODS and Herschel-SDF samples. . . .	138
6.1	The range of the parameters we use to simulate our galaxies. . . . .	154
6.2	The statistics of the different types of galaxies that make up our Herschel GOODS sample. . . . .	180
6.3	The mean values of the offsets of our classic and pseudobulges from the main sequence lines, shown in Figure 6.23 . . . . .	185

# List of Figures

1.1	Evolution of the star formation density in the Universe with redshift. This figure is from Madau & Dickinson (2014) . . . . .	20
1.2	The original diagram of the Hubble sequence of galaxies, also known as Hubble’s tuning fork. This figure is from Hubble (1936). . . . .	23
1.3	Example spectral energy distribution due to the emission from dust. The spectra was created from average data of the North ecliptic pole and the Lockman hole (Arendt et al., 1998). This figure is from Popescu et al. (2011). . . . .	25
1.4	Observations of the Andromeda galaxy, as observed by IRAS (top left), Herschel (top right) and Spitzer (bottom). Credit ESA and NASA. . . . .	28
2.1	An example plot used to estimate the value of redshift dependant $Q_0$ for the GAMA 9-h field. The black dots located at integer radius values in arcseconds, from 1 to 15, are calculated as the number of Herschel blanks (red crosses) divided by the number of random blanks (black stars). The green line is the best fit line to the points of $1 - Q_0$ . . . . .	46
2.2	Cutout images from the Sloan Digital Sky Survey, representing the six categories that we split our sources with different VIKING and SDSS counterparts in to. <i>From top left, moving clockwise:</i> Multiple possible galaxies, single small galaxy, single large galaxy, possible merger or interaction, star or artifact and difficult to identify. . . . .	54
2.3	Two cutouts from the VIKING survey at the positions of Herschel sources, with reliable SDSS counterparts, but no nearby VIKING source. The image on the left shows a bright nearby galaxy imaged with VIKING, whilst the image on the right shows a bright star or artifact which has incorrectly not been removed. . . . .	56

2.4	K-band distributions of all our VIKING sources which have been reliably matched to a Herschel source (blue) and of those VIKING sources who have been reliably matched to a Herschel source, but where there is no nearby SDSS source (green) . . . . .	57
3.1	The $500\mu\text{m}$ source counts of three galaxy populations: high redshift submillimetre galaxies, low redshift late type galaxies and radio galaxies powered by AGN. Strongly lensed SMG's are dominant over unlensed SMG's above $100\text{mJy}$ , providing an easy method of selecting lensed SMG's from Herschel data. This figure is from Negrello et al. (2010). . . . .	62
3.2	The counts of predicted lensed (green line) and unlensed (orange line) sources as a function of redshift, above the flux limits given in the upper right of each plot. The black line is the sum of the two distributions. This plot is from private communications with Gianfranco De Zotti. .	63
3.3	<i>Top:</i> Cross correlation between the Herschel ATLAS sample and two samples of photometric SDSS (blue circles) and spectroscopic GAMA (cyan circles) foreground galaxies. <i>Bottom:</i> Comparison of the measured cross correlations and the auto correlation function of the foreground lens samples. This plot is from González-Nuevo et al. (2014). .	64
3.4	Photometric redshift distributions of the sources in the three GAMA fields. The three plots are the distributions for the three GAMA fields, the 9-h, 12-h and 15-h, from bottom to top. The redshifts are estimated using the 3 fluxes from the SPIRE instrument on board Herschel, at wavelengths centred at $250\mu\text{m}$ , $350\mu\text{m}$ and $500\mu\text{m}$ . . . . .	66
3.5	Normalised distributions of the VIKING and Herschel sources. The VIKING sample, whose redshifts are the photometric redshifts of the best matched SDSS source, is shown in blue. The red distribution shows the Herschel sources over the GAMA fields, whose redshifts have been estimated photometrically from the Herschel fluxes alone. The green distribution is redshift distribution of Herschel sources in the NGP field. These photometric redshifts were estimated from the optical and near infrared using the public code HyperZ, which is discussed in Section 4.6. . . . .	68

- 3.6 *Left:* The distribution of all VIKING sources around the positions of the Herschel ATLAS sources, on the GAMA 9h field. *Right:* The distribution of VIKING sources around **random** positions on the GAMA 9h field. . . . . 70
- 3.7 The background subtracted distribution of VIKING sources around the positions of the Herschel ATLAS sources on the GAMA 9-h field. Each plot denotes a minimum redshift requirement for Herschel sources. The minimum redshift of Herschel sources is  $z>0$ ,  $z>1$ ,  $z>2$  and  $z>3$ , from left to right, top to bottom. . . . . 71
- 3.8 The background subtracted distribution of VIKING sources around the positions of the Herschel ATLAS sources on the GAMA 12-h field. Each plot denotes a minimum redshift requirement for Herschel sources. The minimum redshift of Herschel sources is  $z>0$ ,  $z>1$ ,  $z>2$  and  $z>3$ , from left to right, top to bottom. . . . . 72
- 3.9 The background subtracted distribution of VIKING sources around the positions of the Herschel ATLAS sources on the GAMA 15-h field. Each plot denotes a minimum redshift requirement for Herschel sources. The minimum redshift of Herschel sources is  $z>0$ ,  $z>1$ ,  $z>2$  and  $z>3$ , from left to right, top to bottom. . . . . 73
- 3.10 Plots used to estimate the value of redshift dependant  $Q_0$  for the three GAMA fields, GAMA 9-h, 12-h and 15-h from right to left, top to bottom. The black dots located at integer radius values in arcseconds, from 1 to 15, are calculated as the number of Herschel blanks divided by the number of random blanks. The blue line is for Herschel sources with redshifts  $z>0$ , green for  $z>1$ , red for  $z>2$  and light blue for  $z>3$ . 76
- 3.11 The  $Q_0$  plots for the GAMA 9-h, 12-h and 15-h fields. Only sources with a 350 micron S/N above 10 are plotted, in order to only include sources in the analysis with the most reliable photometric redshifts. . 79
- 3.12 Distribution of Reduced Chi squared value from fitting model spectra to Herschel galaxies with optical SDSS photometry. Galaxies which are deemed non-lenses are shown in red and those which are possible lenses are in blue. . . . . 86

3.13	Example SED fits, using the public code MAGPHYS , to our samples of non-lensed and possible-lensed galaxies. The top four plots show our low redshift, non-lensed galaxies, and the bottom four plots show our possible lensed galaxies. The red line is the best fitting SED and the blue dots are the SDSS and Herschel SPIRE photometry. . . . .	88
3.14	The mean spectra of local galaxies, as created by Coleman et al. (1980), which are used by HyperZ to estimate the photometric redshifts of galaxies. This figure is from Bolzonella et al. (2011) . . . . .	89
4.1	VLA map of the area covered by both the Herschel ATLAS and Subaru Deep Field surveys. Sources detected at 5 sigma are highlighted by green circles. Fewer sources are detected as a function of radius from the centre of the map, due to the decreasing sensitivity. . . . .	96
4.2	<i>Top row:</i> The $q(\text{Flux},c)$ distributions for all Herschel sources (left) and those in the more sensitive central area (right). <i>Middle row:</i> The $n(\text{Flux},c)$ distributions for all Herschel sources (left) and those in the more sensitive central area (right). <i>Bottom row:</i> The distribution of reliabilities for all Herschel sources (left) and those in the more sensitive central area (right). . . . .	98
4.3	The distribution of separations of Herschel sources and SDF sources. The separation values are between the optical SDF positions and the radio VLA positions. . . . .	99
4.4	The two Herschel sources which have two nearby Subaru counterparts. We identify the two SDF counterparts with circles and the VLA position with a cross. . . . .	103
4.5	<i>Left:</i> Subaru Deep Field images showing those Herschel galaxies where the most likely SDF source is different in our two source matching methods. <i>Right:</i> VLA images of the same sources. Diamonds indicate the positions of the Herschel ATLAS sources, squares are the reliable VLA positions, crosses show the SDF source when first matched to a radio source and circles indicate the SDF source when we match Herschel ATLAS directly to Subaru. . . . .	107

- 
- 4.6 The mean spectra of local galaxies, as created by Coleman et al., 1980, which are used by HyperZ to estimate the photometric redshifts of galaxies. This figure is from Bolzonella et al., 2011 . . . . . 111
- 4.7 Comparison of the photometric HyperZ redshifts and spectroscopic redshifts for a sample of CANDELS galaxies. The blue line indicates a line of gradient unity. . . . . 112
- 4.8 Redshift histograms of our SDF matched Herschel sources. The plot on the left is the redshifts estimated using the Subaru photometry and the plot on the right is from using the Herschel photometry. . . . . 113
- 4.9 A plot of the SDF photometric redshifts against the Herschel photometric redshifts, of our SDF matched Herschel matched sources. The blue line indicates a gradient of unity. The red points are those sources who have  $F_{350}/E_{350} > 10$ . Green points indicate our sample of possible lenses, as studied in Section 4.7. . . . . 114
- 4.10 A plot of the K-magnitude against the redshift of our SDF matched Herschel ATLAS galaxies, shown in yellow. The red points are every other galaxy in the Subaru Deep field. The blue line indicates the completeness limit of the VISTA VIKING survey at a K-magnitude of 20.4. All magnitudes are AB magnitudes. . . . . 118
- 5.1 The galaxy main sequence at  $1.5 < z < 2.5$ . The four samples plotted are a shallow (red filled circles) and deeper (cyan squares) PACS-COSMOS sources, a BzK-GOODS sample (black filled circles) and a sample of BzK-COSMOS sources (black dots). The main sequence (MS) for star-forming galaxies at  $z \approx 2$  defined by Daddi et al. (2007) is plotted as a solid black line, while the dotted and dashed lines represent 10 and 4 times the main sequence (along the Star Formation Rate axis), respectively. This figure is from Rodighiero et al. (2011). . . . . 123
- 5.2 The redshift distribution of our two galaxy samples. The Herschel-SDF galaxies, whose redshifts are estimated photometrically from the SDF and Herschel photometry, are shown in green. The Herschel-GOODS galaxies, whose redshifts have been estimated photometrically or spectroscopically, are shown in blue. . . . . 127

- 
- 5.3 The Fundamental Metallicity Relationship, which shows the 3D surface relationship between the metallicity, star formation rate and stellar mass of SDSS galaxies. Circles without error bars are the median values of metallicity of local SDSS galaxies in bins of  $M^*$  and SFR. The colour coding also indicates SFR. The square dots are the median values of high redshift galaxies, whose labels give their redshifts. The black dots show a second-order fit to these SDSS data, extrapolated toward higher SFR. This figure is from Mannucci et al. (2010) . . . . . 132
- 5.4 A histogram of the metallicities of our galaxies, calculated using Equation 5.3. Our Herschel-GOODS sample is shown in blue and our Herschel-SDF sample in green. . . . . 133
- 5.5 Galaxy main sequence plots for our two galaxy samples which have been binned by redshift. The black line is the redshift dependant main sequence from Speagle et al. (2014) and the red and blue lines are 4 times and 10 times the main sequence respectively. The red circles and blue squares are the Herschel-GOODS and Herschel-SDF galaxies respectively, which lie below the  $10 \times MS$  line. The yellow circles and squares are the Herschel-GOODS and Herschel-SDF galaxies respectively, which lie above the  $10 \times MS$  line and hence are designated starbursts following the definition in Rodighiero et al. (2011). . . . . 136
- 5.6 The galaxy main sequence of our galaxy samples, showing the specific star formation rate. The red circles and blue squares are the Herschel-GOODS and Herschel-SDF galaxies respectively, which lie below the  $10^*MS$  line. The yellow circles and squares are the Herschel-GOODS and Herschel-SDF galaxies respectively, which lie above the  $10 \times MS$  line and hence are designated starbursts following the definition in Rodighiero et al. (2011). . . . . 139

- 5.7 The Kennicutt-Schmidt plot for our two galaxy samples, where the galaxies have been binned by redshift, which is given in the upper right of each sub-plot. The red circles and blue squares are the Herschel-GOODS and Herschel-SDF galaxies respectively, which lie below the  $10^*MS$  line. The yellow circles and squares are the Herschel-GOODS and Herschel-SDF galaxies respectively, which lie above the  $10^*MS$  line and hence are designated starbursts following the definition in Rodighiero et al. (2011). The lines of best fit to the galaxies are plotted are the black lines, whilst the line of best fit for the  $0 < z < 0.5$  bin is shown in red in each sub-plot. The gradient of each line of best fit is given in the upper left of each sub-plot. . . . . 141
- 5.8 Plot of the star forming efficiency ( $SFR/M_{GAS}$ ) for our two galaxy samples. The star formation rate was estimated using MAGPHYS whilst the gas mass was estimated from the dust mass using the fundamental metallicity relation. Herschel-SDF galaxies are plotted as blue squares and Herschel-GOODS and blue circles. Those galaxies identified as starbursts in Figure 5.5 are plotted as yellow squares (Herschel-SDF) and yellow circles (Herschel-GOODS). . . . . 143
- 6.1 The cutout region that we inject our simulated sources into. The field contains three background sources which are detected in the GOODS survey and are highlighted by green ellipses. . . . . 155
- 6.2 *Top Left:* An example of a simulated galaxy, which was built from both a bulge and a disc component. *Top Right:* The model galaxy, created by GALFIT, which best fits the profile of our simulated galaxy. The fit has a reduced chi squared value of 1.70. *Bottom:* The residual image after subtracting the model image from the simulated image. . . . . 156
- 6.3 The measured Sersic indices of our sources against the simulated Sersic indices. Here we have fit two profiles to each of our galaxies, one disc-like and one bulge-like. The most disc-like components are plotted in blue and the most bulge-like are plotted in red. The left hand plot shows the results when using variable positions to fit profiles and the right plot uses fixed positions. . . . . 161

6.4	Left: The simulated against measured magnitudes of our sources when using variable positions to fit our components. Right: The simulated against measured AB ratios of our sources when using variable positions	162
6.5	The simulated against measured effective radii of our sources, when allowing the Sersic indices to vary and using variables positions. We split our components up into the smallest effective radii (left) and largest (right) of each source. . . . .	162
6.6	The histograms of the measured Sersic indices using variable positions. The plots from top to bottom are of Single profiles, two profiles with fixed Sersic indices and fitting two profiles using variable Sersic indices.	164
6.7	Left: Comparison of the measured and simulated magnitudes of our galaxies when using fixed Sersic indices. Right: Comparison of the measured and simulated AB ratios of our galaxies. . . . .	165
6.8	The simulated against measured effective radii of our sources, when fixing the Sersic indices, using variables positions for our components. We split our components up into the smallest effective radii (left) and largest (right) of each source. . . . .	165
6.9	Histograms of the reduced chi squared values from our fits. The top plot is the values from fitting single Sersic profiles, the middle plot from fitting two profiles with fixed Sersic indices at $n=1$ and $n=4$ and at the bottom is from fitting two profiles with variable Sersic indices.	166
6.10	The artifact left over in the residual GALFIT image of each of our simulated galaxies. . . . .	167
6.11	The measured Sersic indices of our Herschel GOODS galaxies against the Sersic indices found by vdW12 . . . . .	170
6.12	Left: The measured magnitude of our galaxies against the values found by vdW12. Right: The measured effective radii of our galaxies against the values found by vdW12. . . . .	171
6.13	Histogram of the reduced chi squared values of our Herschel GOODS galaxies when fitting double Sersic profiles with variable Sersic indices.	172

6.14	Example sources whose best fit GALFIT profiles have reduced chi squared values of $> 20.0$ . The left image shows the actual galaxy, the middle image shows the GALFIT model and the right image shows the residual left after subtracting the model from the actual galaxy. . . .	173
6.15	The reduced chi squared values when using fixed positions against using variable positions of our single profile fit. . . . .	174
6.16	Histograms of the Sersic indices of the most disc-like (top) and most bulge-like (bottom) profiles. Here we have allowed the Sersic indices to vary. . . . .	175
6.17	The Sersic indices of the most disc-like profiles against the most bulge-like. . . . .	176
6.18	Histogram of the bulge to total flux ratio's of our Herschel GOODS galaxies, using variable Sersic indices. . . . .	177
6.19	The plot of measured bulge to total flux ratio against the Sersic index of the best fit single profile, using fixed Sersic indices. Those galaxies which exhibit a bulge with $n < 2.5$ , labelled as pseudo bulges, are shown in blue. Classic bulges, determined by having a Sersic index of $n > 2.5$ , are plotted in pink. Left: Our simulated galaxies are plotted as grey points. Right: We plot the CANDELS galaxies studied in Bruce et al. (2012) as grey points. . . . .	178
6.20	Histograms of the Sersic indices of our Herschel GOODS galaxies. The distributions are from fitting single Sersic profiles (top), double profiles with fixed Sersic indices (middle) and fitting double profiles with variable Sersic indices (bottom) . . . . .	179
6.21	Histograms of the effective radii of our Herschel GOODS galaxies. The top plot shows the components of each galaxy with the largest effective radius and the bottom shows those with the smallest values. . . . .	181
6.22	The galaxy main sequence, built from our Herschel GOODS sample. Galaxies shown in blue have a pseudobulge and those in red have a classical bulge. The bottom row are galaxies binned between $0 < z < 1$ , the middle row between $1 < z < 2$ and the top row between $2 < z < 3$ . The black lines are the redshift dependant main sequence lines, given in Speagle et al. (2014) . . . . .	183

6.23	Histograms showing the displacement in star formation rate of our classic (red) and pseudo bulge (blue) galaxies. . . . .	184
6.24	The redshift evolution of the fraction of our sample with pseudobulges (blue) and classical bulges (red). . . . .	186

# 1

## Introduction

*"In the beginning the Universe was created. This has made a lot of people very angry and been widely regarded as a bad move."*

– Douglas Adams, *Hitchhikers Guide to the Galaxy*

### 1.1 THE GREAT DEBATE

The first recorded observation of a galaxy was in the 10th century by the Persian astronomer Abd al-Rahman al-Sufi, who upon observing the Andromeda galaxy, described its appearance as a 'small cloud'. For centuries, astronomers contemplated what these small clouds, or *nebulae* as they became known, in the sky were and how they were distinct from stars.

The two dominant features of the sky in the southern hemisphere, the Large and Small Magellanic Clouds, were first observed by a European in the 16th century by the explorer Ferdinand Magellan. Yet it was over 200 years later that the astronomer Thomas Wright was the first person to speculate that these nebulae may not be part of our own Milky Way (Wright, 1750). It was from this work that Immanuel Kant termed these nebulae *Island Universes* and so began the idea that there existed many galaxies in the Universe, each as unique as our own Milky Way.

Evidence as to whether these Island Universes lay outside our own Milky Way, however, was difficult to come by. In 1920, the two competing theories came face to face in the now famous *Great Debate*, between the astronomers Harlow Shapley and Heber Curtis. Shapley argued that 'spiral nebulae', such as the Andromeda galaxy,

lay inside our own galaxy, based on the unbelievably large distance that they would have to be at if they lay outside the Milky Way. Curtis argued that these nebulae were, as Kant suggested, Island Universes, lying beyond the limits of the Milky Way. He showed that Andromeda had visible dust lanes and supernova rates that were similar to that of the Milky Way as a whole, implying that Andromeda must be a separate galaxy.

But with neither Shapley or Curtis able to provide concrete proof to back their arguments, the job of solving the mystery fell to another pioneering scientist. Edwin Hubble presented his paper *Cepheids in Spiral Nebulae* just three years later, in which he estimated the distance to a number of Cepheid variable stars in other galaxies (Hubble, 1925). This work proved conclusively that the observed nebulae in the night sky were indeed individual galaxies, beyond the boundary of the Milky Way, and so the field of extragalactic astronomy (as well as modern cosmology) began.

## 1.2 GALAXY EVOLUTION

The study of how galaxies and the Universe have evolved with time is only possible due to the finite speed of light. The further away an object, the further back in time the light we are seeing left it and hence the younger it appears. The light from the most distant observed galaxies was emitted over 13 billion years ago, with current observations pointing to the existence of galaxies in the Universe as early as 500 million years after the Big Bang (Oesch et al., 2016). By observing galaxies at different distances from us, we are observing galaxies at different points of time in the past. Studying how these galaxies have changed with time is the fundamental concept of the field of galaxy evolution.

Our current model of the build-up and evolution of structure in the Universe is based on the cosmological model of  $\Lambda$ -CDM. In this model, around three quarters of the energy density of the Universe is composed of dark energy, represented by  $\Lambda$ , with the remainder consisting of cold dark matter and a small fraction of baryonic matter (Planck Collaboration et al., 2015). Inflation in the early Universe created minute perturbations in the matter density; dark matter began to fall towards these overdensities, causing them to grow in mass. These dark matter distributions evolved in to the earliest dark matter halos, whilst the current day larger halos probably formed through the mergers of multiple smaller halos.

Baryons in the early Universe are expected to have been evenly distributed, before gravitationally infalling to the dark matter halos, becoming the formation sites of the first galaxies. The amount of baryons accreted on to the dark matter halos depends on the halo mass. It is this gas which eventually condenses inside the dark matter halos to form stellar birth clouds and eventually stars and planets (Baugh, 2006).

As these small dark matter halos merge, so do the galaxies contained within them. This causes galaxies to become larger with time, a model known as the hierarchical model of galaxy formation (see Baugh, 2006 for a review). If correct, we would expect to see galaxies increasing in size towards the present day; however, several observations in recent years have brought this model in to question. Local high mass galaxies have been observed with old stellar populations and high metallicities (all elements other than Hydrogen and Helium). This suggests that many galaxies may have formed their stars early in the Universe and quiescently evolved to the current day, though it could also be due to the merging of smaller galaxies with old stellar populations. Star formation in the local Universe is also observed to be dominant in smaller galaxies. Single starbursts episodes are therefore too short to account for the space density of submillimetre bright galaxies and their current day stellar masses (Lapi et al., 2011).

These observations are evidence towards the downsizing model, in which large galaxies form early in the Universe and evolve passively to the current day, whilst small galaxies continue forming stars at later time. This is one of the key challenges to the  $\Lambda$ -CDM model and one that is not yet understood. For a review of galaxy formation and evolution, see Benson (2010).

### 1.3 STAR FORMATION EVOLUTION

The study of the star formation history of galaxies provides information on the baryonic matter in the Universe. Through nuclear fusion in the centre of stars, hydrogen is transformed into larger atoms, before being expelled back into the interstellar medium through stellar winds and novae.

The star formation density of the Universe is decreasing and has been since its peak around redshift  $z \approx 2$  (Madau & Dickinson, 2014). The cause for this downturn is unclear; could it be a dwindling supply of gas, stellar feedback or a smaller role

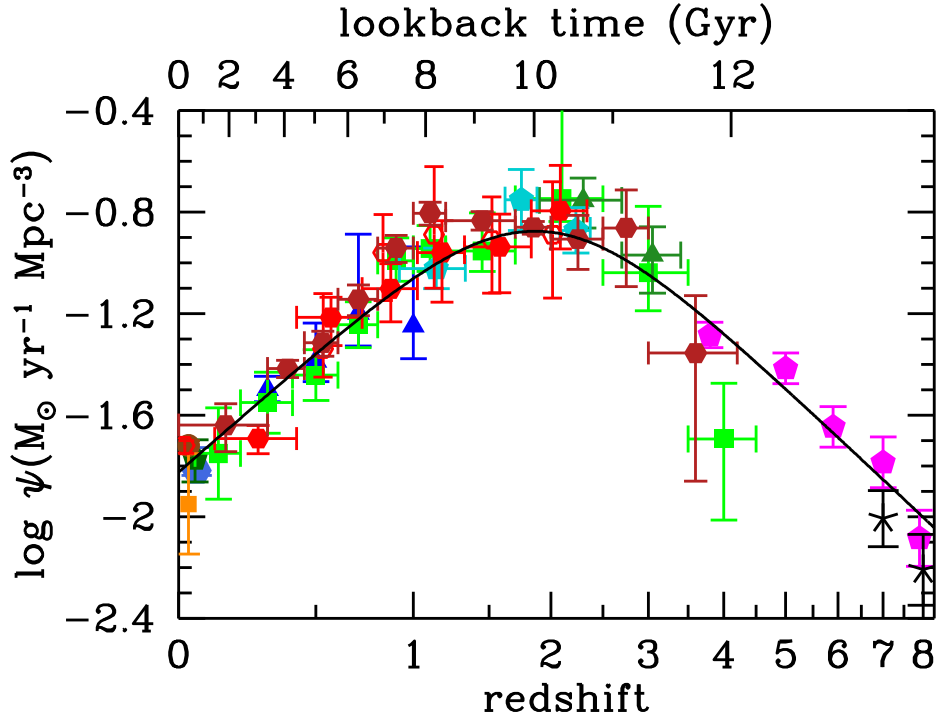


**Figure 1.1.** Evolution of the star formation density in the Universe with redshift. This figure is from Madau & Dickinson (2014)

played by mergers that is the cause of the decline in star formation. As we have shown in Eales et al. (2015), there is evidence that whatever is affecting the change in star formation rates in galaxies is also responsible for changes to their morphology. We fit Sersic profiles to Hubble Space Telescope (HST) images, with Herschel counterparts, to split our galaxy sample in to sub-samples of early-type (ETG's) and late-type(LTG's) galaxies. We showed that 51% of the stellar-mass density is in ETG's today, whilst 89% of the production of stellar mass density is in LTG's. By using deep observations, we showed that 83% of the stellar mass-density formed over the history of the Universe in LTG's. There must have therefore been some major morphological transformation of LTG's in to ETG's after the formation of the majority of stars. If these two quantities are linked, then fully understanding one of them may help us understand the other.

There are several key quantities associated with the star formation properties of galaxies: star formation rate, stellar mass, dust mass and gas mass. The evolution of each of these quantities with redshift, and their relation to each other, have been studied in great detail. The relationship between the stellar mass and star formation rate of galaxies is known as the galaxy main sequence, a term first coined by Noeske et al. (2007). The galaxy main sequence gives an indication of how many stars a galaxy is forming per stellar mass. It has been shown to have a redshift dependence, with galaxies having higher star formation rate per stellar mass with increasing redshift. The scatter of the main sequence has been used to suggest homogeneity among star forming galaxies as the relatively small scatter suggests most galaxies follow the same evolutionary paths. One key question is whether submillimetre galaxies, such as those observed by Herschel, follow the galaxy main sequence as optically selected sources. Submillimetre galaxies are typically large, dusty galaxies with large star formation rates; the question is whether these different properties place submillimetre galaxies at a different place on the galaxy main sequence than optical galaxies. This work will study the position and scatter of submillimetre galaxies on the galaxy main sequence, in relation to samples of optical galaxies.

The galaxy main sequence plot can be used to identify the most extreme star forming galaxies in the Universe. Rodighiero et al. (2011) designate galaxies that lie more than 10 times above the main sequence as starbursts, due to their unusually high star formation rates. The cause of these bursts are likely to be galaxy mergers or interactions (Di Matteo et al., 2008, Luo et al., 2014), which increase the star formation rate in the galaxies. The role of starbursts in the rise and decline of the star formation density of the Universe is contentious. It is plausible that if starbursts exist frequently enough, that they could have had a significant impact on star formation in the Universe. However, recent studies estimate that they only contribute  $\sim 10\%$  of star formation at redshift  $z \approx 2$  (Rodighiero et al., 2011), suggesting that they only play a small role in the star formation history of the Universe. In this thesis we will study whether the starburst Herschel galaxies also follow this trend of contributing little to the overall star formation of the Universe, or if these extreme galaxies play a significant role.

The Kennicutt-Schmidt relation (Schmidt, 1959, Kennicutt, 1998) is a correlation between the star formation rate and gas mass of galaxies. It is an indicator of

how efficiently a galaxy can convert its gas mass into stellar mass. It has been shown to evolve with redshift (Santini et al., 2014), with galaxies becoming more efficient at forming stars with increasing redshift. The Kennicutt-Schmidt relationship therefore gives an indication of how important the supply of gas is, and how galaxies convert this gas in to stars, across the history of the Universe. One point of interest is why those galaxies designated as starbursts from the galaxy main sequence are forming more stars than those on the main sequence. One possibility is that they have higher star formation efficiencies, possibly due to an increase in dense molecular clouds as a result of mergers. However, it may simply be that they have higher gas masses and so can form more stars. By studying both the main sequence and Kennicutt-Schmidt plot for a sample of submillimetre galaxies it may be possible to see which of these scenarios is true.

One of the key questions in galaxy evolution is what causes galaxies follow the galaxy main sequence and Kennicutt-Schmidt relation and what causes galaxies to divert from them. Do all galaxies with the same gas mass, at any given redshift, have similar star formation rates, or are there external factors which either increase or decrease it? We have already discussed that mergers and interactions can greatly increase the star formation rate in galaxies, but what events decrease or stop star formation? In low mass galaxies, the energy released from supernovae is expected to be able to drive gas out of the galaxy, quenching star formation. Accretion of matter on to the black holes believed to be at the centre of galaxies, a component of galaxies known as Active Galactic Nuclei (AGN), release a significant amount of energy. This energy can stop gas cooling to form stars and strip gas from a galaxy via winds or jets and is the key suspect in star formation quenching in large galaxies.

## 1.4 GALAXY MORPHOLOGY

Hubble's tuning fork diagram, seen in Figure 1.2, gives some indication as to how diverse the morphology of galaxies can be. Galaxies have historically been classed as one of four types, based on their shapes or light profiles: spiral, elliptical, lenticular and irregular. The origin of, and link between, spiral and elliptical galaxies is still a mystery. Many theories on galaxy evolution put disc galaxies before ellipticals in evolutionary models, but a lack of conclusive evidence leaves this a mystery yet to solve.

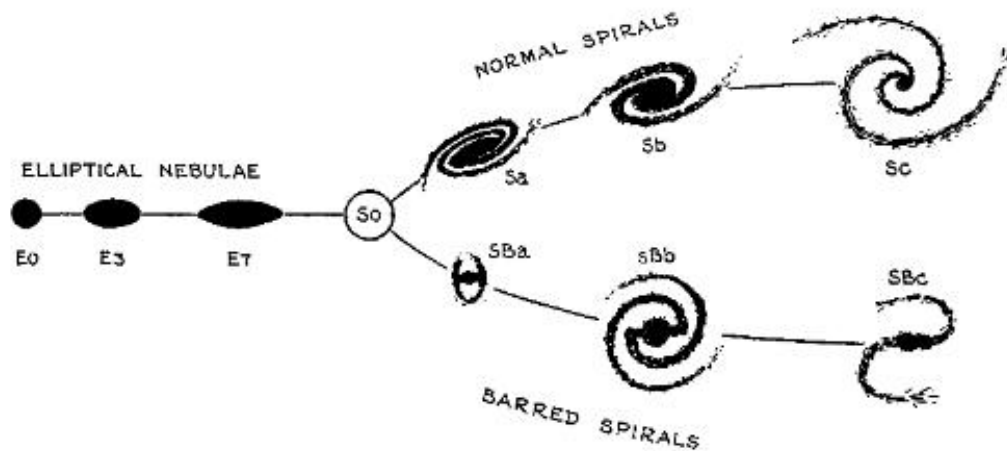


**Figure 1.2.** The original diagram of the Hubble sequence of galaxies, also known as Hubble's tuning fork. This figure is from Hubble (1936).

Disc galaxies and elliptical galaxies are very different, beyond just their shape. They are thought to have formed from gas collapsing to the centre of a dark matter halo; as the gas cloud collapses, it flattens, forming a disc shape. They are visually dominated by structures such as spiral arms and bars and are typically rich in gas and dust, fuelling star formation and hence giving them a typically blue colour. Many discs feature a bulge at the centre consisting of an older stellar population; some bulges are spheroidal shaped, like smaller early type galaxies, and are named classical bulges; some are disc shaped, like smaller late type galaxies and are named pseudo or disc-like bulges. Elliptical galaxies on the other hand tend to have smaller star formation rates as star formation has been quenched. They appear redder in general due to the lack of star formation and older stellar population.

However, the paradigm of galaxy morphology and Hubble's tuning fork is beginning to go out of favour, with newer models of galaxy structure being favoured. Two pieces of evidence are at the forefront of changing views: that the sub-structure of galaxies is itself incredibly diverse and that elliptical galaxies aren't 'red and dead'.

The idea of classical bulges has been challenged by observations of disc-like bulges at the centres of a significant fraction of galaxies. Often termed pseudo-bulges (Kormendy & Kennicutt, 2004), they have the appearance of a small disc galaxy, rather than the classical view of bulges resembling a small elliptical galaxy. They appear much flatter than classical bulges, can feature spiral structures and are

often forming a relatively high number of stars. The shape of galaxies and their components are often analysed using a variable known as the Sersic index (Sérsic, 1963), whose value depends on the shape of the light profile of galaxies. Disc profiles have a Sersic index of around  $n=1$ , whilst bulges have values of around  $n=4$ . Pseudo-bulges are better fit with a Sersic profile with index  $n=1$ , typical of discs, rather than  $n=4$ . Classical bulges and elliptical galaxies are believed to form through the mergers of galaxies, disturbing the normal order of discs and resulting in a spherical distribution of stars. This agrees with the model of hierarchical galaxy formation, in which galaxies are built up in the early Universe through mergers. However, to retain the clear disc structure of pseudo-bulges, another process must be taking place. The model of secular evolution of galaxies is one in which galaxies evolve slowly over time, as suggested by the observed galaxy main sequence, through either long term interactions or through internal processes, such as the transportation of gas to the centre of galaxies by spiral arms or bars. The relative importance of mergers and secular evolution in evolving galaxies is unclear, but the answer might lie in the properties of the bulges of galaxies.

For many years, the view of elliptical galaxies was 'red and dead'. Their cold gas supply was thought to have dwindled, halting star formation. However recent studies are beginning to question this paradigm, with many galaxies classified as ellipticals and S0's having ongoing star formation and a supply of cold gas (Smith et al., 2012). Instead of classifying galaxies by their morphology alone, other properties such as their colour are beginning to be used to separate galaxies along their evolutionary track. Bell et al. (2004) showed that galaxies can be separated into three distinct areas on an absolute magnitude-colour diagram: the red sequence, the blue cloud and the green valley. Typically, galaxies in the red sequence are spheroidal in shape, whilst those in the blue cloud are disc like, but that has been shown not to hold for all galaxies. Most galaxies are thought to migrate from the blue cloud to red sequence with time as star formation decreases. The green cloud in the middle is thought to be an intermediate step, where galaxies star formation is dwindling, but who are forming more stars than the red galaxies.

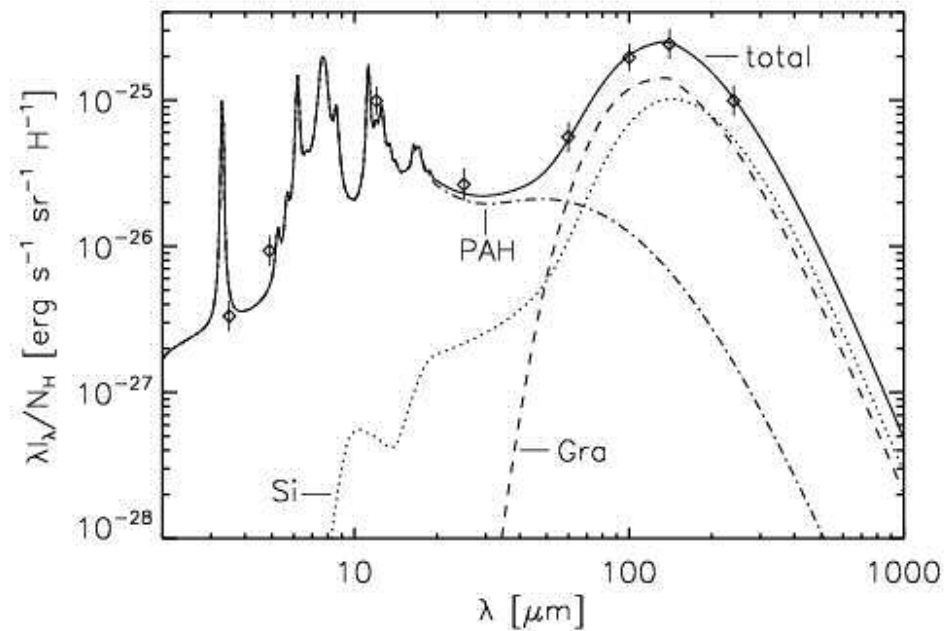


**Figure 1.3.** Example spectral energy distribution due to the emission from dust. The spectra was created from average data of the North ecliptic pole and the Lockman hole (Arendt et al., 1998). This figure is from Popescu et al. (2011).

## 1.5 DUST

Dust was long considered a nuisance by astronomers. It is opaque to optical and ultraviolet light, blocking valuable star light from astronomers. It also acts to make objects appear redder than they are, due to the favoured absorption of shorter wavelength light. But as astronomers became able to observe and study dust, through the emergence of infrared astronomy, it became clear that dust plays a pivotal role in the Universe.

The formation of dust grains is a topic of much interest. Whilst still poorly understood, the two main sources of dust production are believed to be through stellar ejecta and supernovae. The outer shells of low to intermediate mass, post main sequence stars, such as asymptotic giant branch (AGB) stars, have been suggested as a prime location for dust grains to form. Here, the high density of particles and low temperature are favourable for forming dust grains. Gas molecules join together to form seeds, on which other molecules can attach, creating dust particles. The composition of dust particles is believed to depend on the ratio of carbon to oxygen

in the host star; an excess of carbon creates carbon rich dust whilst an excess of oxygen tends to create silicates.

When summed up over an entire galaxy, it becomes clear that these low mass, post main sequence stars are not enough to recreate the dust mass seen in galaxies at high redshift, especially those which are dust rich, such as sub-millimetre galaxies. This conundrum has been named the dust budget crisis (Morgan & Edmunds, 2003), who estimate that the production of dust from these stars is an order of magnitude lower than is needed to agree with observations. One possible solution to this is the production of dust in high mass star supernovae. The supernova expels material outwards from the star in an expanding and cooling shell. When this dense shell of material reaches a certain distance from the star, it will reach the same optimum temperature and density as found around post main sequence stars and hence dust particles will begin to form. Significant dust formation has been observed around core collapse supernovae and from type Ia supernovae (Gomez et al., 2012a, Gomez et al., 2012b). Current observations suggest that even with this additional source of dust production, there may still be some deficit, though newer models such as dust grain growth in the ISM may begin to solve the mystery.

Dust destruction is another obstacle to overcome when solving the dust budget crisis. The most common source of dust grain destruction is thought to be through a process called sputtering. Here atoms or ions bombard dust grains, removing particles on the surface of the grain and slowly breaking the particle apart. Grain-grain collisions, caused by shock waves from supernovae accelerating particles to high speed, also break apart dust particles, but is believed to be a much smaller effect.

Whilst the creation of dust involves the life and death of stars, it is thought to play a key role in the birth of stars. Stars form from clouds of molecular hydrogen. However, it is unlikely that two colliding hydrogen atoms will bond together in the ISM, to create the required molecular hydrogen. Instead, they tend to bond on the surfaces of dust grains which they stick to. The dust grain acts to absorb excess energy from the collision, providing a more suitable place to form molecular hydrogen. Dust grains also help absorb much of the ionising radiation that hits the cloud, which would otherwise break apart the hydrogen molecules.

The energy absorbed by dust over the entire electromagnetic spectrum is re-emitted in the infrared, according to the balance of energy. The energy of the photons

emitted by dust depend on the temperature of the dust grain. The total emission forms the dust emission spectral energy distribution, as seen in Figure 1.3, which consists of two distinct features: the far infrared peak and the mid infrared excess. The far infrared peak is caused by the emission of dust grains at a temperature around 30-40 Kelvin (Casey et al., 2014). Typically this peak has been fit by models consisting of a single temperature, modified black body curve; however recent work has shown that most dust peaks require both a warm and cold dust component to get a good fit (Dunne & Eales, 2001). To accurately measure the dust mass and temperature, one must sample both sides of the peak, known as the Wien's tail at shorter wavelengths of the peak and the Rayleigh-Jeans tail at longer wavelengths. The Herschel Space Observatory, discussed in detail later, is unrivalled in being able to perform photometry across the dust emission peak, allowing astronomers to fit modified black body curves to dust emission using the Herschel data alone. The mid infrared excess is emission from warmer dust, typically 50-500 Kelvin. It also features the distinct emission lines from polycyclic aromatic hydrocarbons (PAH), linked hexagonal rings of Hydrogen and Carbon atoms.

## 1.6 FAR INFRARED AND SUB-MILLIMETRE ASTRONOMY

Infrared astronomy can track its roots back to the year 1800, with the discovery of infrared light by William Herschel. In the 1830's, the field of infrared astronomy began, with infrared radiation from the moon being first detected in 1873. Yet observations of galactic and extragalactic dust, one of the key uses of modern infrared telescopes, didn't come until much later.

Infrared astronomy can be separated into three broad areas: near infrared, mid infrared and far infrared. The wavelengths or frequency boundaries between these three bands are blurry, but typical values are that near infrared covers 0.7-5 micrometres, mid infrared between 5 and 25 micrometres and far infrared between 25 and 350 micrometres. The near infrared is mainly used to peer through dust, which appears the most transparent in this infrared band. It is also used for studying old stellar populations and cool stars in the Universe, such as red dwarves and red giants, which emit brightest in the near infrared. The mid infrared is where dust becomes observable, with relatively hot dust emitting at these wavelengths. The mid-infrared is one of the key methods of observing the dusty torus' around supermassive black

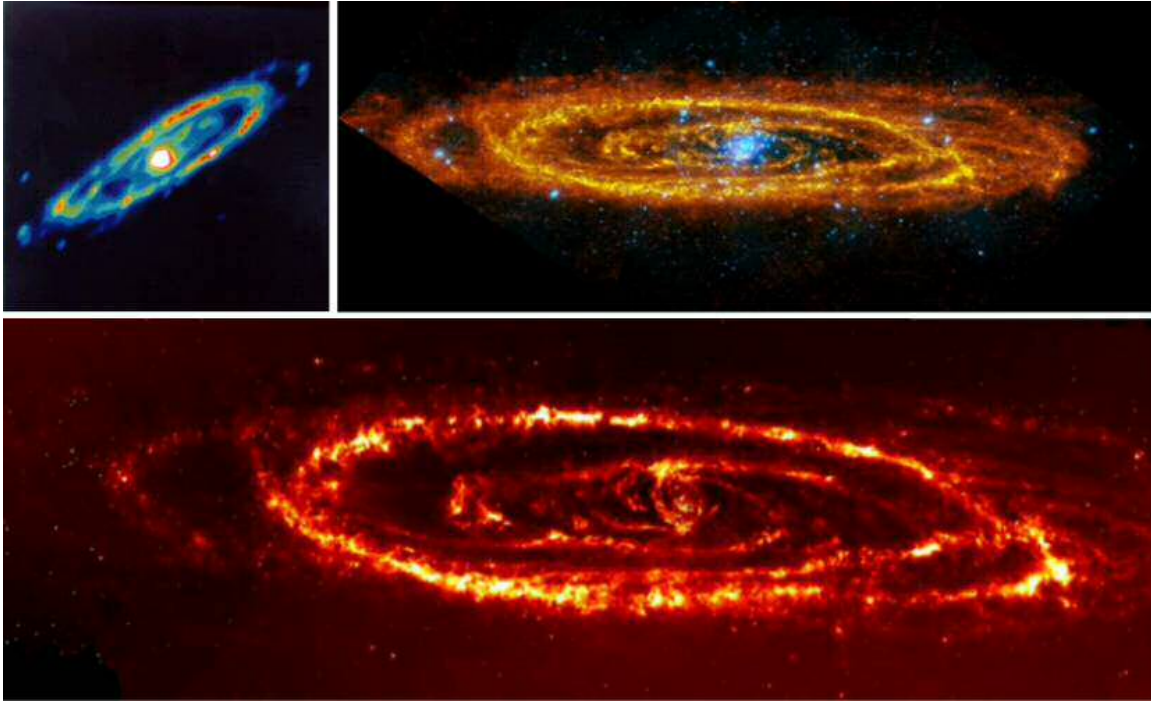


**Figure 1.4.** Observations of the Andromeda galaxy, as observed by IRAS (top left), Herschel (top right) and Spitzer (bottom). Credit ESA and NASA.

holes, allowing the identification of heavily dust obscured AGN (Mushotzky, 2004). Asteroids and comets also radiate energy in the mid infrared. The far infrared is where warm and cold dust takes centre stage. Dust filled galaxies, which may be too faint to observe in the optical, appear bright due to emission from their dust component. The centre of our own galaxy dominates many far infrared full sky surveys, as we stare into the plane of the Milky Way. Beyond the far infrared lies sub-millimetre astronomy, bridging the gap between infrared and radio astronomy and allowing the coldest dust in the Universe to be observed.

One of the key benefits to observing in the far-infrared for extragalactic astronomers is the effect of negative K-correction. As galaxies become more distant, their apparent brightness to us, an observer, decreases. However, the shape of the dust emission peak is such that when one observes on the longer wavelength side of the peak, increasing the redshift of a source shifts our observing wavelength towards the peak of the dust emission. This effects essentially cancels out the dimming of sources with increasing redshift, allowing us to easily observe galaxies out to relatively high redshifts. The far infrared regime is also suited to detecting gravitational lenses. Massive foreground galaxies or galaxy clusters can bend and magnify the light

of coincident background galaxies, making distant galaxies that might otherwise be impossible to detect, bright enough to see. The effect of negative K-correction mitigate the effect of the dimming of light due to distance, allowing us to detect more distant galaxies.

Yet there are many problems that come with far infrared astronomy. Source confusion is a big issue, as infrared observations detect a high density of sources on the sky. Infrared telescopes suffer from poor resolution, causing the blending of sources, making it difficult to identify individual galaxies on the sky. Both of these contribute to difficulties in identifying the correct counterpart to infrared sources at other wavelengths. Simple nearest neighbour methods are often not accurate enough at identifying the correct counterparts, so more complex methods must be implemented.

There have been a number of infrared and sub-millimetre telescopes which have helped advance the area of infrared astronomy in the last few decades. Below I discuss some of the key ones.

The Infrared Astronomy Satellite (IRAS) (Neugebauer et al., 1984), a collaboration between the United States, Netherlands and Great Britain, was the first infrared space observatory to map the entire sky. Over 10 months of operation it mapped 96% of the sky in infrared, at 12, 25, 60 and 100 micrometres, with a resolution between 30 arcseconds and 2 arcminutes. In total it detected around 350,000 infrared sources, including infrared bright merging galaxies, as well as observing the core of our own galaxy for the first time.

The Infrared Space Observatory (ISO) (Kessler et al., 1996), designed and operated by the European Space Agency, was the follow up to IRAS. It launched in 1995 and operated for 28 months, making over 26,000 observations of infrared sources between 2.4 and 240 micrometres.

The Spitzer Space Telescope (Werner et al., 2004) was a NASA infrared space telescope. It operated primarily between its launch in 2003 and when it ran out of liquid helium in 2009; however two of the instruments are still operating at their initial capabilities as they do not require cooling. It covered a photometric range of 3-160 micrometres. Spitzer is part of the Great Observatories program, which consists of four space telescopes covering four different areas of the electromagnetic spectrum, to provide a panchromatic view of the Universe. Spitzer has made a number of significant

discoveries in many fields of astronomy, including the first direct observation of an exoplanet

The Submillimetre Common-User Bolometer Array (SCUBA) (Holland et al., 1998), is the name given to two generations of submillimetre instruments that have been on the James Clark Maxwell Telescope. Both instruments observe simultaneously at 450 and 850 micrometres and have beam sizes of 8 and 13 arcseconds at 450 and 850 micrometres respectively. SCUBA-2 features more pixels than its predecessor, allowing it to scan the sky over 100 times faster than SCUBA-1. SCUBA makes use of the negative K-correction, the effect of distant galaxies appearing brighter in the far infrared due to the shifting of the dust spectral energy distribution peak. This makes SCUBA particularly effective at studying high redshift galaxies.

## 1.7 HERSCHEL

The Herschel Space Observatory (Pilbratt et al., 2010) was a European Space Agency telescope, which observed in the far infrared and submillimetre. It operated from its launch in 2009 to 2013, when its supply of liquid Helium coolant ran out. Its primary mirror has a diameter of 3.5 metres, making it the largest single mirror ever launched in to space.

The design of a space based infrared telescope was proposed to the European Space Agency in the 1980's, initially given the name the Far Infrared and Submillimetre Telescope (FIRST). It was accepted by ESA as part of their Horizons 2000 program, alongside other spacecraft including Planck, Rosetta and Gaia. Herschel was launched in 2009 on-board an Ariane 5 launcher, alongside the Planck satellite, before entering its orbit at L2 6 months later.

Herschel is equipped with 3 detectors: the Photodetecting Array Camera and Spectrometer (PACS), the Spectral and Photometric Imaging Receiver (SPIRE) and the Heterodyne Instrument for the Far Infrared (HIFI).

The Photodetecting Array Camera and Spectrometer (PACS) (Poglitsch et al., 2010) is the shorter wavelength photometer on-board Herschel and also features a spectrometer. The photometer can observe at three photometric bands, centred at 70, 100 and 160 micrometres. PACS can use two camera arrays, allowing it to observe in two bands at once; one can choose either of the two shorter wavelengths to observe, alongside the longest one. The detectors are kept at 0.3 Kelvin. The photometer has

a field of view of  $3.5' \times 1.75'$  and pixel sizes are  $6.4'' \times 6.4''$  for the longest band and  $3.2'' \times 3.2''$  for the two shorter bands. The only observing mode with PACS is the scan map technique, in which the spacecraft is slewed across the sky at either 10, 20, or 60 arcseconds per second.

The Spectral and Photometric Imaging Receiver (SPIRE) (Griffin et al., 2010) is the longer wavelength photometer inboard Herschel, as well as being a spectrometer. The photometer carries out broad-band photometry on three bands, centred at 250, 350 and 500 micrometres, whilst the spectrometer covers between 194 and 671 micrometres. The 250, 350 and 500 micrometre beams have mean Full Width Half Maximum (FWHM) values of 18.1, 25.2 and 36.6 arcseconds respectively, which are very similar to pre-launch predictions. In this mode an area of the sky is scanned at 30 or 60 arcseconds per second. The area is scanned twice in perpendicular directions. Herschel can use scan mapping for either SPIRE or PACS separately, or use both instruments simultaneously in so called parallel mode, providing data from all three SPIRE bands and both PACS bands.

The Heterodyne Instrument for the Far Infrared (HIFI) (de Graauw et al., 2010) is a very high resolution spectrometer on-board Herschel. It provides continuous coverage in five bands between 480 and 1250 GHz and in 2 bands between 1410 and 1910 GHz. The scientific goals of HIFI were based on three areas of interest: 1) the study of water lines, to study cold water; 2) to study the molecular complexity of the Universe; and 3) observations of ionised Carbon [CII]. In-orbit tests indicate that HIFI worked close to or exceeded pre-launch results.

## 1.8 HERSCHEL SURVEYS AND COMPLEMENTARY SURVEYS

### 1.8.1 HERSCHEL-ATLAS SURVEY DATA

The Herschel ATLAS (Eales et al., 2010a) is the largest open-time project carried out on the Herschel Space Observatory. In full it covers nearly  $600 \text{ deg}^2$  of the sky, including three fields covered by the GAMA survey on the celestial equator, a field near the North Galactic Pole and a field near the South Galactic Pole. The fields were chosen to both minimise the cirrus emission in the fields and to maximise

the complementary data from other surveys. Herschel ATLAS has surveyed in 5 passbands, centred on  $100\mu\text{m}$ ,  $160\mu\text{m}$ ,  $250\mu\text{m}$ ,  $350\mu\text{m}$  and  $500\mu\text{m}$ , utilising the parallel mode on Herschel which allows observations using both the PACS and SPIRE instruments. The beams have a FWHM of approximately 9, 13, 18, 25 and 35 arcseconds respectively.

In our work, we use data from the internal data release, Phase 1 (Valiante et al., 2016). The catalogue was produced following the method laid out in Rigby et al. (2011), which was initially done for the Science Demonstration Phase data, but extended to the entire Herschel ATLAS survey. The SPIRE sources are identified by the source extraction routine MADX, which was developed for the Herschel ATLAS survey. The local background is then subtracted from the maps, before being filtered by the PSF. Reliable sources are included if it is detected at a significance level of at least  $5\sigma$  in one of the SPIRE bands. Only the  $250\mu\text{m}$  priors are used for all the catalogues. This may exclude bright, high redshift sources which are bright at  $500\mu\text{m}$  but faint in the other bands, but this is found to be low. The average  $5\sigma$  detection limits for the SPIRE bands, which are the only data we use in our work, are 33.5, 37.7 and 44.0 mJy/beam, for  $250\mu\text{m}$ ,  $350\mu\text{m}$  and  $500\mu\text{m}$  respectively. Full details on the source extraction for the Herschel ATLAS catalogues can be found in Rigby et al. (2011).

The fields are covered by a number of already complete and future surveys in a wide range of wavelengths. The fields are covered by at least one of three spectroscopic surveys, namely the Sloan Digital Sky Survey, the Galaxy And Mass Assembly Survey and the 2dF Galaxy redshift survey. They will provide spectroscopic redshifts for a large fraction of the Herschel ATLAS sources, as well as other data derived from the spectra. In the near infrared, the GAMA fields have been covered by the VISTA Kilo-degree Infrared Galaxy Survey (Edge et al., 2013), which will soon also cover the SGP fields.

Some of the key scientific goals of the Herschel ATLAS survey are:

- Measurements of the luminosity and dust mass functions of galaxies in the local Universe, down to low dust masses.
- To observe dust and obscured star formation and to study how it has changed over the history of the Universe.

- To better understand the cause and details of the far infrared-radio correlation observed in star forming galaxies.
- To utilise Herschel data to improve or aid work done with the Planck satellite, including the removal of cirrus emission and improved spectral energy information.
- To detect a significant number of gravitational lenses and to recreate the lens and lensed galaxy profiles, allowing us to study how lenses and distant galaxies have evolved over the history of the Universe.

### 1.8.2 HERSCHEL-GOODS

The Great Observatories Origins Deep Survey (GOODS) (Dickinson et al., 2003) is a set of extremely deep observations, made with a number of telescopes across a wide range of wavelengths. It has covered two areas of the sky, centred on the Hubble Deep Field North ( $0.002\text{deg}^{-2}$ ) and the Chandra Deep Field south ( $0.11\text{deg}^{-2}$ ). The CANDELS project is a deep imaging survey of both fields carried out by the Hubble Space Telescope, with the aim to study the evolution of galaxies out to distant redshifts. Utilising the Wide Field Camera 3 instrument, CANDELS is able to observe objects in the infrared as well as in the optical, providing a panchromatic view on the early Universe.

As part of the GOODS project, both the north and south fields have been observed with the Herschel Space Observatory, as part of the Herschel-GOODS survey (Elbaz et al., 2011). Whilst the Hubble space telescope is able to observe the optical emission from stars, Herschel has observed the emission from stars, which has been re-radiated by dust in the infrared. The Herschel-GOODS catalogue was built by first detecting galaxies in the Herschel images at  $100$  and  $160\mu\text{m}$ , based on prior positions of sources derived from a Spitzer telescope  $24\mu\text{m}$  catalogue (Elbaz et al., 2011). This technique provides accurate positions for the Herschel sources, allowing them to be better matched to other catalogues. One disadvantage is that any Herschel sources which are not first detected by Spitzer will be missed, but Magnelli et al. (2013) estimate this to be  $\leq 4\%$  of the total sources at  $160\mu\text{m}$ .

The Herschel-GOODS sources were selected at  $160\mu\text{m}$  at  $>3\sigma$ ; however, the Herschel-GOODS survey doesn't provide images at the longer Herschel wavelengths:

250 $\mu\text{m}$ , 350 $\mu\text{m}$  and 500 $\mu\text{m}$ . These flux values have been obtained from the HERMES survey (Oliver et al., 2012) at the positions of the Herschel-GOODS sources. This sample is expected to resolve around 75% of the extragalactic background radiation at both 100 and 160 $\mu\text{m}$  (Magnelli et al., 2013).

Some of the key scientific goals of the GOODS and Herschel GOODS surveys are:

- To study the evolution of galaxies, including their stellar populations and output, over the history of the Universe.
- To locate dust-obscured AGN.
- To resolve the majority of star formation density in the Universe up to redshift  $z \approx 4$ .
- To detect both 'normal' galaxies out to high redshift and the most extreme galaxies, including Luminous Infrared Galaxies (LIRGS) ( $L > 10^{11} L_{\odot}$ ) and Ultra Luminous Infrared Galaxies (ULIRGS) ( $L > 10^{12} L_{\odot}$ ).

### 1.8.3 VIKING SURVEY DATA

The VISTA Kilo-degree Infrared Galaxy Survey (VIKING) (Sutherland, 2012, Edge et al., 2013) is currently being undertaken by the VISTA telescope at the European Southern Observatory (ESO). When complete it will have covered over 1500 deg<sup>2</sup> of the sky in five near infrared bands: Z(0.878 $\mu\text{m}$ ), Y(1.021 $\mu\text{m}$ ), J(1.254 $\mu\text{m}$ ), H(1.646 $\mu\text{m}$ ) and  $K_s$ (2.147 $\mu\text{m}$ ). This will be combined with data from the Kilo Degree Survey (KIDS) (de Jong et al., 2015), which will provide photometry in four optical bands. The covered areas will include the South Galactic Pole area and the GAMA 9h, 12h and 15h fields, all of which are covered by Herschel ATLAS. VIKING is expected to be around 2 magnitudes deeper than the Sloan Digital Sky Survey.

Some of the key scientific goals of the VIKING survey are:

- To study galaxy evolution and clustering out to redshift  $z=1.2$ .
- To get improved photometric redshifts of sources for the study of gravitational lensing.

- To measure stellar masses of galaxies, allowing the relationships between stellar mass, star formation and halo mass to be studied.
- To improve galaxy-star separation, based on the colour of objects.

#### 1.8.4 SUBARU DEEP FIELD (SDF)

The Subaru Deep Field (SDF) (Kashikawa et al., 2004) is an ultra deep optical survey using 8.2 metre Subaru telescope. Targeted at a seemingly empty area of the sky, the ultra deep image contains hundreds of thousands of galaxies, out to great distances. The survey covers an area near the North Galactic Pole, approximately  $0.34 \text{ deg}^2$  in size, which overlaps with the area covered by Herschel ATLAS. The SDF covers five broad-band filters: B(4460Å), V(5484Å), R(6295Å), i'(7641Å), z'(9037Å) as well as two narrow-band filters, NB816(8150Å) and NB921(9196Å). The limiting magnitudes of each band at  $3\sigma$  in a  $2''$  aperture are B = 28.45, V = 27.74, R = 27.80, i' = 27.43, z' = 26.62, NB816 = 26.63, and NB921 = 26.54 in the AB magnitude system. This depth allows galaxies out to redshifts of  $\approx 4-5$  to be detected. In addition, our SDF catalogue contains near infrared counterparts from the UKIRT telescope, providing J and K band data for many of the sources. These chosen bands are suited to detecting Lyman-break galaxies, which are high redshift star forming galaxies which have significant breaks in their flux due to the Lyman limit, a result of the absorption of photons with wavelength less than  $912\text{\AA}$  by neutral gas in the ISM. This is a key technique in identifying high redshift galaxies.

Some of the key scientific goals of the Subaru Deep Field survey are:

- To construct the largest sample of Lyman-break galaxies at  $z \approx 4-5$
- To study a large sample of high redshift galaxies

## 1.9 THESIS OUTLINE

The main aim of this thesis is to study the properties of galaxies detected with the Herschel Space Observatory. I aim to understand how the properties of these galaxies have changed with redshift and how these changes link to the evolution of galaxies as a whole.

The thesis chapters are laid out as follows:

- **Chapter 2:** I identify reliable near infrared counterparts to Herschel sources, using the likelihood ratio technique.
- **Chapter 3:** Using these identifications I find evidence that up to 40% of Herschel sources at high redshift are gravitationally lensed.
- **Chapter 4:** I utilise radio data to find a sample of accurate identifications to Herschel sources. Using the source matching statistics I test the gravitational lensing result I found in the last chapter. I also study the K magnitude-redshift plot of the galaxies and find that they form a relatively homogeneous population.
- **Chapter 5:** I study the star forming properties of two samples of Herschel galaxies by plotting them on the galaxy main sequence and the Kennicutt-Schmidt relation. I find that our galaxies follow both relationships, as found in other works. I find that the starburst galaxies in our samples lie on the same Kennicutt-Schmidt relationship as main sequence galaxies.
- **Chapter 6:** I measures the relative contributions and shapes of the bulge and disc components of a sample of Herschel-GOODS galaxies. I find that a significant fraction of the Herschel galaxies exhibit pseudo-bulges with low Sersic indices; however we find little or no correlation to between the bulge shape and the star forming properties of our galaxies.
- **Chapter 7:** Summarises the work presented in this thesis.

# 2

## Near infrared surveying with VIKING

*“Light thinks it travels faster than anything but it is wrong. No matter how fast light travels, it finds the darkness has always got there first, and is waiting for it.”*

– Terry Pratchett

### 2.1 INTRODUCTION

The power of studying galaxies comes through observing them at multiple wavelengths. Each wavelength of light represents a different process within a galaxy and it is only by studying them in every wavelength that we can get a complete picture. With the advent of the Herschel Space Observatory (Pilbratt et al., 2010), a large fraction of the sky has now been imaged in the sub-millimetre regime to an unprecedented depth. Identifying the optical and near infrared counterparts for this huge influx of Herschel sources is now a key priority to allow us to study these galaxies in detail.

Identifying the correct counterparts in other catalogues to sub-millimetre sources is made difficult by the large beam size and hence low angular resolution of sub-millimetre surveys, as well as source confusion, the result of sub-millimetre surveys detecting a high density of sources (Blain et al., 1998). Both of these issues mean that traditional source matching methods such as the nearest neighbour method are

innaccurate. Instead, recent methods have focused on including other information on the source, such as the brightness, to improve the accuracy of the source matching. One of the most popular techniques is the likelihood ratio technique (Sutherland & Saunders, 1992) which incorporates the offset and brightness of the two sources to determine a likelihood that the sources are associated with each other.

The VIKING survey (Edge et al., 2013) is a near infrared survey which covers the three GAMA fields which lie on the equator, centred at 9 hours, 12 hours and 15 hours of right ascension. These three fields are also covered by the Herschel ATLAS survey, making it a promising near infrared survey to match to the Herschel catalogue to provide ancillary data and improved positions. We refer the reader to Section 1.8.3 for more details on the VIKING survey.

The likelihood ratio technique has been used previously to match the Herschel ATLAS Phase 1 and VIKING data (Fleuren et al., 2012, hereafter F12). They perform their analysis over the GAMA 9-h field, consisting of 22,000 Herschel sources. Their results show that this method is very effective at matching the submillimetre and near infrared sources together, with 51% of Herschel sources having a reliable VIKING counterpart above the VIKING survey limit. We want to take this work one step further by performing the same analysis as performed by F12, but over all three of the GAMA fields, approximately tripling the number of Herschel-VIKING matched sources. This large sample sources will allow the study of the Herschel submillimetre selected galaxies in greater detail, through using near infrared data to derive accurate Spectral Energy distributions (SEDs) for the Herschel sources. Accurate SEDs can be used to study the old stellar population of the galaxies, identify and study the foreground galaxies in gravitational lensing systems and to estimate photometric redshifts of the galaxies. Matching to near infrared galaxies also provides more accurate positions to the Herschel sources, allowing the Herschel sources to be further matched to catalogue of other wavelengths.

Other works have reliably matched Herschel catalogues to optical data, provided by the Sloan Digital Sky Survey (SDSS) (Smith et al., 2011). Using the likelihood ratio technique they find that approximately 37% of Herschel 250 $\mu$ m selected sources have a reliable SDSS counterpart, significantly less than when matching Herschel sources to near infrared VIKING sources. As well as finding fewer reliable

matches when using optical rather than near infrared sources, it is not clear how accurate the optical matches are. Smith et al. (2011) estimate a false identification rate using a simple formula and information on their reliably matched sources; however, we are able to directly compare two samples of optical and near infrared galaxies which have been matched to the same Herschel sources. This will allow us to answer the question of what fraction of Herschel sources are matched to the same source in both the VIKING near infrared and optical SDSS samples, and where they are matched to different sources, what causes two different sources to be matched in the optical and near infrared.

In this chapter we use near infrared VIKING data to find reliable counterparts to Herschel ATLAS sources. In Section 2.2 I introduce the data used in this chapter. In Section 2.3 I detail the method used to match sources together and in Section 2.4 I present the results of this source matching routine. In Section 2.5 I compare these source matching results to that which matched the Herschel ATLAS sources to the optical SDSS. The conclusions are presented in Section 2.6.

## 2.2 DATA

As part of the Herschel ATLAS survey, three fields located on the equator were observed, known as the GAMA fields. These three fields are centred on right ascensions of 9h, 12h and 15h, and as a result take these positions as their names, GAMA 9-h, 12-h and 15-h. Each field has an approximate size of 50 square degrees. These have been observed with Herschel using both the SPIRE and PACS instruments simultaneously, a function on Herschel known as parallel mode, and have been observed at  $100\mu\text{m}$  and  $160\mu\text{m}$  with PACS and  $250\mu\text{m}$ ,  $350\mu\text{m}$  and  $500\mu\text{m}$  with SPIRE. We only consider Herschel ATLAS sources with a S/N of 4 sigma or higher in the  $250\mu\text{m}$  band. This final source count in each field can be seen in Table 2.1. More details on the Herschel ATLAS data can be found in Section 1.8.1.

VIKING is a near infrared survey that covered 1500 square degrees of the sky, including the three equatorial GAMA fields also covered by Herschel ATLAS. It observed in five near infrared bands, Z, Y, J, H and K, with a limiting magnitude of around  $K_s = 20.5$  in the AB system. For this work we use the 4th data release, dated 30/05/2014. We remove all sources which are flagged as saturated and noise in the

VIKING catalogue. Because the Herschel ATLAS and VIKING fields do not completely overlap, a mask was created to only include sources located in areas covered by both the VIKING and Herschel ATLAS surveys.

In order to reduce the number of false matches, we remove unwanted stars from the catalogue of VIKING sources. We first filter out stars using a parameter called *PStar* which is included in the VIKING catalogue, which gives the probability of a source being a star based on the shape of its light profile (Findlay et al., 2012). We hence remove any sources with a value of  $PStar \geq 0.95$ , following the method of Fleuren et al. (2012). Next, we remove any remaining stars based on their colour, using a colour-colour plot of (g-i) against (J-K), based on the method laid out in Baldry et al. (2010). The two populations are concentrated in two different areas of the diagram, with an area in-between where we find a mix of both objects, but with a very low object count; the galaxies and stars can hence be separated by a defined locus. The value for the g and i magnitudes are not present in the VIKING data and hence the sources must be matched to a dataset such as the SDSS to get these values, but this is currently beyond the scope of this work. Instead we adopt a conservative separation based solely on the (J-K) magnitudes, where any object with a value greater than 0.21 are classed as galaxies and any object with a value less than -0.34 as stars, following the logic in Fleuren et al. (2012). This will ignore the objects in between the distributions, but this is only around 0.001% of the overall population. The final VIKING source counts for each field can be seen in Table 2.1.

		GAMA 9 Field	GAMA 12 Field	GAMA 15 Field
N	H-ATLAS	20,259	21,897	23,480
sources				
N	VIKING sources	1,268,404	1,064,791	1,464,168
Area of	VIKING	55.28	56.08	70.81
field (deg <sup>2</sup> )				

**Table 2.1.** The number of sources in both the Herschel ATLAS and VIKING surveys over the three GAMA fields. These are the final counts after removing sources that are likely stars and sources not in areas covered by both surveys.

## 2.3 SOURCE MATCHING

The likelihood ratio technique (Sutherland & Saunders, 1992, Smith et al., 2011, Fleuren et al., 2012) is a statistical tool for matching sources in different catalogues together, when there is a need for more rigorous analysis than a simple nearest neighbour. The method is derived from Bayes theorem in order to first calculate the probability that two sources are associated based on their position and magnitude. The method also allows the calculation of the probability of each possible candidate in one catalogue to a every source in a second catalogue.

The technique relies on the ratio between the probabilities of two situations: the probability that the two sources, with magnitude  $m$  and separation  $r$ , are associated, and the probability that they aren't. This is given by

$$L = \frac{P(r, m, \text{Associated})}{P(r, m, \text{NotAssociated})} = \frac{P(m, c, x, y, id)}{P(m, c, x, y, \text{chance})} \quad (2.1)$$

where  $L$  in this equation is referred to as the 'likelihood',  $m$  is the brightness magnitude,  $c$  is the colour and  $x$  and  $y$  represent the position. The probability that two sources are associated depends on the separation of the two sources and the brightness magnitude of the potential counterpart. Sutherland & Saunders (1992) define several terms:  $q(m)$ , the probability distribution of true counterparts as a function of magnitude  $m$ ;  $f(r)$ , the probability distribution of the source positional errors as a function of separation  $r$  between the sources; and  $n(m)$ , the density distribution of background sources as a function of magnitude  $m$ . The probability that the candidate source is an unrelated background source depends on the density distribution of background sources, defined as  $n(m)$ . Equation 2.1 can be written as

$$\text{Likelihood} = L = \frac{q(m)f(r)}{n(m)} \quad (2.2)$$

The likelihood values have only the limitation that they must be greater than zero. By assigning a lower limit of the likelihood of each possible counterpart one could decide which matches are the likely true counterparts and which are likely random associations. One could decide that the source with the highest likelihood is the true association. However, in many cases there will be more than one likely match for each primary source and one must decide which is the most probable true counterpart. The probability of each source being the true counterpart is calculated

and compared to every other possible counterpart. The probability of each source is referred to as the 'Reliability' and is given by the equation:

$$P(\text{Associated}|r, m) = \text{Reliability} = \frac{L_j}{\sum_i L_i + (1 - Q_0)} \quad (2.3)$$

which compares the likelihood of each possible secondary source,  $j$ , with the sum of the likelihoods of all possible secondary sources,  $i$ .  $Q_0$  is the probability for a random source of finding a genuine counterpart above the survey limiting magnitude. The derivation and use of  $Q_0$  is discussed in detail in Section 2.3.2. To identify a true counterpart one must apply a limiting probability or reliability value, over which a source is deemed to be a true match. A source with a reliability less than this is said not to be associated. We apply a minimum probability/reliability value of 0.8, which means that we cannot be certain within reasonable doubt that any single source with a probability less than 0.8 is the true counterpart. The use of the value of 0.8 is used following the logic set out by Smith et al. (2011), which keeps contamination rate low, whilst ensuring that only one K-band source dominates the Herschel emission. We then remove all sources with a reliability less than this value, leaving us with a catalogue of primary sources with reliable secondary source counterparts.

By measuring the distributions  $q(m)$ ,  $n(m)$  and  $f(r)$ , the likelihood for each source being associated can be calculated. We describe the calculation of each distribution below. For clarity sake, we define the two catalogues that we are matching together as the Primary catalogue and the Secondary catalogue. In this example we use the term 'Primary' to define the sources in the catalogue whose nearest neighbours we will find and 'Secondary' to define the sources we will try to match to the primary sources. That is to say, for each primary sources we expect to have one or more possible secondary source associated with it, which we will evaluate to find which is the most likely counterpart.

### 2.3.1 ESTIMATING $F(R)$

Logic says that the closer two sources are by their position, the more likely they are to be associated. Galaxy surveys in the submillimetre typically have large positional errors associated with them, so sources may be expected to be separated by a larger distance in the two catalogues. The probability distribution of positional errors,  $f(r)$ , is defined as:

$$f(r) = \frac{1}{2\pi\sigma^2} \exp\left(\frac{-r^2}{2\sigma^2}\right) \quad (2.4)$$

where  $r$  is the separation of the primary and secondary sources in arcseconds and  $\sigma$  is the positional uncertainty. The positional uncertainty depends on the Signal to Noise (S/N) and the Full width Half Maximum (FWHM) of the observation. We follow the method used by Smith et al. (2011) and calculate  $\sigma$  using the equation

$$\sigma = 0.655 \frac{FWHM}{SNR} \quad (2.5)$$

where the value of 0.655 is derived in Smith et al. (2011) from Herschel ATLAS data,  $FWHM$  is the Full Width Half Maximum and  $S/N$  is the signal to noise ratio of the Herschel source in the  $250\mu m$  band. In the case of Herschel the FWHM is given by the mean SPIRE  $250\mu m$   $FWHM = 18.1''$ , and the signal to noise is calculated from the  $250\mu m$  band for each source individually. We also set a minimum value of  $\sigma$  of 1 arcsecond, due to minimum positional uncertainties associated with SPIRE.

### 2.3.2 ESTIMATING $n(m)$ AND $q(m)$

The background density distribution,  $n(m)$ , is calculated by constructing a magnitude distribution of all secondary sources. This is then divided by the total area of the survey, to give a distribution of secondary sources, per magnitude, per arcsecond<sup>2</sup>, over the entire field. To calculate  $q(m)$  we follow the procedure of Ciliegi et al. (2003); we first calculate the magnitude distribution of all secondary sources within a set distance of all primary sources,  $total(m)$ . We use a separation distance of 10 arcseconds, which will include 99.996% of real counterparts assuming Gaussian errors (Fleuren et al., 2012). This distribution is background subtracted according to Equation 2.6 to give the distribution of  $real(m)$ .

$$real(m) = total(m) - (n(m)N_{Primary}\pi r^2) \quad (2.6)$$

where  $n(m)$  is our distribution of background sources,  $r$  is the separation radius and  $N_{Primary}$  is the number of primary sources. Finally this distribution is normalised to give our distribution of  $q(m)$ :

$$q(m) = \frac{real(m)}{\Sigma_m real(m)} Q_0 \quad (2.7)$$

where  $\Sigma_m real(m)$  is the sum over all magnitude bins.  $Q_0$  is the normalising factor, which is an estimate of the probability of finding a counterpart to a primary source in the secondary survey, above the limiting survey magnitude. To calculate  $Q_0$  we follow the method in F12, where  $(1 - Q_0)$  is estimated by counting how many primary sources do not have a secondary source within  $X$  arcseconds of their position, referred to as 'blanks'. The value of  $X$  must be large enough to encompass as many real counterparts as possible whilst limiting the number of random associations.

The number of true blanks is equal to the number of observed blanks plus the number of true blanks which have incorrectly been matched to a background source. In order to calculate this, we follow the method in F12:

$$\bar{S}_t = \bar{S} + [\bar{S}_t \times \frac{R}{N}] \quad (2.8)$$

where  $\bar{S}_t$  is the number of true primary blanks,  $\bar{S}$  is the observed number of blanks,  $R$  is the number of random positions and  $N$  is the total number of primary sources and random positions.

To estimate the number of incorrectly matched true blanks we place a number of circles with random positions over the field, equal to the total number of primary sources. The number of circles without a secondary source within them gives us a value of 'random position blanks'. Using this number of random position blanks and re-arranging Equation 2.8, the fraction of true primary blanks can be estimated by the equation:

$$\bar{S}_t = \frac{\bar{S}}{1 - R/N} = \frac{\bar{S}}{\bar{R}/N} \quad (2.9)$$

where  $\bar{S}$  is the observed number of blanks and  $\bar{R}$  is the number of random blanks. Dividing by  $N$ , the total number of primary sources, gives us the fraction of Herschel sources that are true blanks. This is given by the following equation:

$$1 - Q_0 = \frac{\bar{S}_t}{N} = \frac{\bar{S}}{\bar{R}} \quad (2.10)$$

The value of  $Q_0$  here is dependant on the search radius, which we do not want,

so we repeat the simulation for search radii between 1 and 15 arcseconds. A model of the dependence of true blanks on the radius between the two sources is derived in F12 and shown here in Equation 2.11. The first term of the equation denotes the probability that the counterpart to the source is too faint to detect, given by  $(1 - Q_0)$ . The second term denotes the probability that the counterpart lies outside the search radius, given by  $(1 - F(r))$ . Finally the third term assumes that the two possibilities are independent of each other and that both events can occur. This gives the function:

$$(1 - Q_0) + (1 - F(r)) - (1 - Q_0)(1 - F(r)) = 1 - Q_0F(r) \quad (2.11)$$

where

$$F(r) = 1 - \exp\left(\frac{-r^2}{2\sigma^2}\right) \quad (2.12)$$

$\sigma$  here is the positional uncertainty of sources over the whole field, which is estimated as  $\sigma = 2.4''$  by Smith et al. (2011). The value of  $Q_0$ , independent of radius, can then be calculated by fitting the model curve to the data, as seen in Figure 2.1 as an example.

## 2.4 SOURCE MATCHING RESULTS

### 2.4.1 SOURCE MATCHING STATISTICS

We have built upon the work done by F12 to find reliable near infrared counterparts to sources in the Herschel ATLAS survey. Using the same technique we have been able to find reliable counterparts to the Phase 1 Herschel ATLAS sources in the three GAMA fields.

In the 9-h field there are 20,259 Herschel ATLAS sources and 1,268,404 VIKING sources. This results in 15,873 Herschel ATLAS sources with at least one nearby VIKING source within 10 arcseconds. Applying our minimum reliability of 0.8, we find that 9,231 of these matches are reliable and hence 45.6% of Herschel ATLAS sources have a reliable VIKING counterpart in the GAMA 9-h field.

In the 12-h field there are 21,897 Herschel ATLAS sources and 1,064,791 VIKING sources. This results in 17,658 Herschel ATLAS sources with at least one

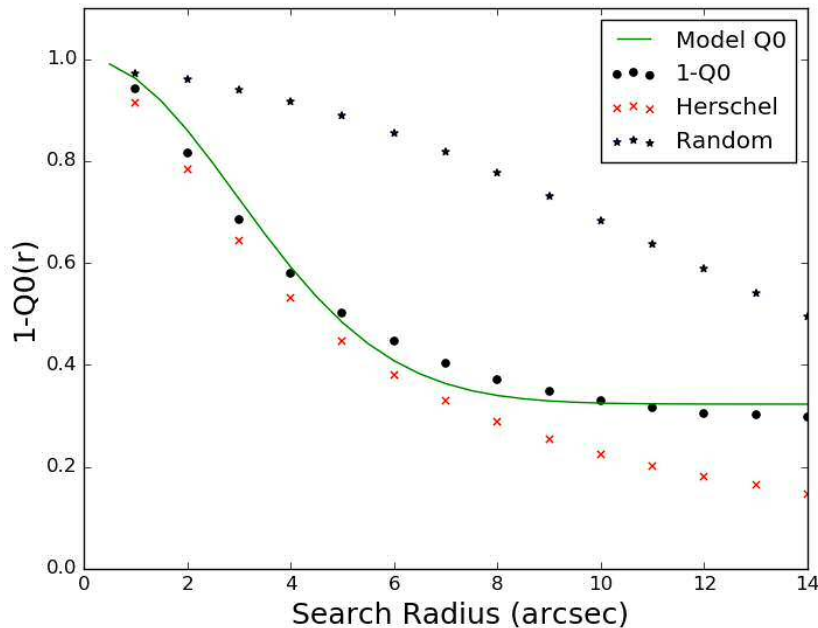


**Figure 2.1.** An example plot used to estimate the value of redshift dependant  $Q_0$  for the GAMA 9-h field. The black dots located at integer radius values in arcseconds, from 1 to 15, are calculated as the number of Herschel blanks (red crosses) divided by the number of random blanks (black stars). The green line is the best fit line to the points of  $1 - Q_0$ .

nearby VIKING source within 10 arcseconds. We find that 11,295 of these matches are reliable and hence 51.6% of Herschel ATLAS sources have a reliable VIKING counterpart in the GAMA 12-h field.

Finally, in the 15-h field there are 23,480 Herschel ATLAS sources and 1,464,168 VIKING sources. This results in 19,300 Herschel ATLAS sources with at least one nearby VIKING source within 10 arcseconds. We find that 12,310 of these matches are reliable and hence 52.4% of Herschel ATLAS sources have a reliable VIKING counterpart in the GAMA 15-h field.

The results of our source matching process can be seen in Table 2.2. F12 perform the same analysis on the GAMA 9-h field, using the Herschel ATLAS Phase 1 data alongside an older VIKING release data. They analyse 22,000 Herschel ATLAS sources in the GAMA 9-h field, with 18,989 of those having at least one nearby VIKING source within 10 arcseconds. They find that 11,294 of these ATLAS sources have a reliable counterpart, resulting in 51% of Herschel ATLAS sources having a reliable VIKING counterpart. This is in line with what we find from our analysis of

	GAMA 9 Field	GAMA 12 Field	GAMA 15 Field
H-ATLAS sources	20,259	21,897	23,480
VIKING sources	1,268,404	1,064,791	1,464,168
Area of field ( $deg^2$ )	55.28	56.08	70.81
Herschel ATLAS sources with a VIKING source within $10''$	15,873	17,658	19,300
Herschel ATLAS sources with a reliable VIKING match	9,231	11,295	12,310

**Table 2.2.** The results of our source matching between the Herschel ATLAS and VIKING catalogues over all three GAMA fields.

the three GAMA fields and is very close to the combined reliable source matching over all three fields of 50.3%.

One point to note is the relatively low fraction of reliable matches in our analysis of the 9-h field compared to that of F12 and indeed compared to the other two fields in our analysis. We used a data set from a later VIKING data release compared to F12, which might explain the differences. Comparing our number of Herschel ATLAS sources with at least one nearby counterpart to F12, we see that we have significantly less in the GAMA 9-h field, a value of 15,873 compared to 18,989. This suggests that it is our number of VIKING sources that is causing this lower fraction. Indeed, where we have 1,268,404 VIKING sources over the field, F12 have 1,376,606.

We can compare the values of  $Q_0$  calculated from our analysis, those found by F12 and the  $Q_0$  values found by Bourne et al. (2016) by matching Herschel and SDSS sources. For the 9-h, 12-h and 15-h GAMA fields, we find  $Q_0$  values of 0.677, 0.709 and 0.738 respectively. F12 find a similar value of  $Q_0=0.72$  for the GAMA 9-h field. However, when matching Herschel sources directly to optical SDSS, the measured value of  $Q_0$  by Bourne et al. (2016) drops to 0.519. Bourne et al. (2016) found that 39% of the Herschel sources have a reliable SDSS counterpart over all three GAMA fields, compared to the value of 50% of Herschel sources with reliable VIKING counterparts that we find and 51% found by Fleuren et al. (2012). It is reassuring to note that we derive a similar result to F12, whilst it's interesting to

see that matching to the deeper near infrared VIKING data, compared to the SDSS data, provides a higher probability of finding counterparts to Herschel sources. We study this further in Section 2.5.

### 2.4.2 LIKELIHOOD METHOD FALSE ID ESTIMATION

In order to estimate the number of false IDs by our likelihood ratio technique, we follow the method used by Smith et al. (2011). The number of false IDs is calculated from all the sources with a reliable ID, given by

$$N_{False} = \sum_{R \geq 0.8} (1 - R) \quad (2.13)$$

where we sum the value of (1-Reliability) for all sources with a reliable counterpart. We find false ID rates of 5.9%, 5.2% and 5.13% for the GAMA 9-h, 12-h and 15-h fields respectively. These are in line with Smith et al. (2011), who found a value of 4.2% for the GAMA 9-h field. Our average reliability values are also slightly lower at 0.941, 0.948 and 0.949 for the three fields compared to the value of 0.958 by Smith et al. (2011), which is likely the cause for the increase in the false detection rate.

### 2.4.3 ADVANTAGES AND DRAWBACKS OF THE LIKELIHOOD RATIO METHOD

The likelihood ratio method provides a statistical approach to matching catalogues of sources together and offers an advantage over a nearest neighbour method. The inclusion of the brightness of the two sources results in a more powerful technique for finding the correct associations. Traditional methods of matching sources based on their separation alone rely on both catalogues having accurate positions. The large beam size of Herschel results in inaccurate positions of the sources, making the likelihood method favourable over using the nearest neighbour method.

Whilst the likelihood method offers advantages over other source matching procedures, there are drawbacks to the technique. The method makes the assumption that the source in the primary catalogue consists of only one source and is not the result of multiple sources blended together. Herschel suffers from source blending, due to the poor resolution of Herschel combined with high source density. Scudder

et al. (2016) presented evidence that many Herschel sources actually consist of multiple unresolved sources. A single Herschel source with multiple nearby VIKING counterparts may therefore actually be multiple Herschel sources blended together, each with their own reliable VIKING counterpart.

Recent work by Scudder et al., 2016 studied the multiplicity of a sample of 360 Herschel sources, selected at  $250\mu\text{m}$ , in the COSMOS field. They select Herschel sources with at least one nearby source in the Spitzer 3.6 and  $24\mu\text{m}$  catalogues. They conclude that of their sample, 95% consist of more than one 'strong' component, each contributing at least 10% to the total flux of the Herschel source. They also find that for the faintest Herschel sources, the brightest component contributes the majority of the flux, but at large Herschel fluxes, the brightest component only contributes 45 percent of the total flux. This result suggests that a significant number of our Herschel sources actually consist of flux contributions from multiple sources. This is a concern, as it suggests that many of our reliably matched Herschel-VIKING sources may be incorrect, as the Herschel source may in reality consist of multiple Herschel sources, each of which should be matched to a VIKING source.

The effect of multiplicity was studied in relation to the likelihood ratio technique by Bourne et al. (2016). They studied the effect when matching Herschel and optical SDSS catalogues together over the three GAMA fields. To estimate the number of Herschel sources with multiple components, they use a technique of studying the likelihood value of potential counterparts to the Herschel sources, rather than the reliability. The reliability only considers the single source which is most likely to be the match to the Herschel source, but does not consider the effect of multiple components. We follow this same technique to estimate the effect of multiplicity in our work of matching Herschel and VIKING sources together. For a Herschel source with a single possible VIKING counterpart, the likelihood value which relates to a reliability of  $R > 0.8$  is 1.292 for the GAMA 9-h field, 1.164 for the GAMA 12-h field and 1.048 for the GAMA 15-h field. We apply these likelihood cuts to all our possible VIKING counterparts and find that 49,034 VIKING sources over the three fields fulfill this minimum likelihood criteria. Of these sources, 9,856 (20.1 percent) have reliabilities less than 0.8. These are candidates for Herschel sources which are comprised of multiple, blended galaxies, though a number of these will also comprise of merging systems and coincident nearby background sources. This is larger than

the value found by Bourne et al. (2016) over the three GAMA fields of 13.0 percent; however, the difference is likely due to the increased depth of VIKING, allowing it to see a larger fraction of counterparts to the Herschel sources.

This incorrect source matching also has a significant effect when we begin using the photometry of our sources to study the physical properties of the galaxies, such as the star formation rate, stellar mass, dust mass, etc. Multiplicity of the Herschel sources will result in submillimetre photometry which is sum of the contribution from several sources. As the submillimetre emission is mainly from the dust component of galaxies, those sources that consist of multiple sources will appear to have dust properties which are a combination of all the contributing sources. When we therefore try to fit model SED's to the SDSS and Herschel fluxes, we will fit incorrect models, as the SDSS fluxes will represent emission from a single galaxy, yet the Herschel fluxes will represent emission from multiple sources. This will also affect those redshift estimates calculated from the Herschel photometry, discussed later in this chapter. Multiple sources at different redshifts will likely broaden and distort the dust emission peak, which will cause the estimated redshifts to be incorrect.

Finally, the likelihood ratio method struggles with source matching merging galaxies or two galaxies which are close together on the sky. The likelihood ratio method identifies the single most reliable counterpart, which causes problems if there are two or more sources with high probabilities of being the true counterpart. If for example there are two identical secondary sources near one primary source, both at the same distance and both with the same magnitude, the likelihoods for both may be very high but the reliabilities of each source would be 0.5. Both sources would be rejected and no probable counterpart would be identified.

#### 2.4.4 USES OF THE HERSCHEL-VIKING MATCHED CATALOGUES

Our final matched catalogue provides 32,836 Herschel sources, over the three GAMA fields, which now have reliable near-infrared counterparts from the VIKING survey. The depth of the VIKING survey allows us to study the near-infrared properties of the dusty, star forming Herschel galaxies out to redshift  $z \approx 1.5$ . Such a catalogue of sources over a wide range of redshifts provides ample opportunity for future studies, which it seems appropriate to discuss.

Our Herschel-VIKING matched catalogues have been used in recent work (Negrello et al., 2017) to help study gravitational lenses in the Herschel ATLAS data. They identify possible lensed Herschel galaxies, based on their bright  $500\mu\text{m}$  fluxes. If these are indeed lensed galaxies, then there must exist either a cluster of galaxies in the foreground, or more likely a massive early-type galaxy, acting as the lens. If the Herschel galaxy is lensed by a foreground early-type galaxy, then one may be able to see the lensing galaxy in the VIKING K-band data, which would detect the stellar component of the early-type galaxy. By estimating the redshift of this VIKING galaxy, and comparing it to an accurate redshift estimate of the Herschel source, one can determine whether these are the same galaxy or whether they are likely a lensing system. I am a named author on this paper, based on the use of my Herschel-VIKING matched catalogues.

If the VIKING source is not a lens, but is the real counterpart of the Herschel source, the VIKING photometry can be used to help estimate accurate photometric redshifts of the Herschel sources. Work done to estimate redshifts from the Herschel photometry alone (Pearson et al., 2013) have been shown to be less accurate than optical and near-infrared estimated photometric redshifts (see Chapter 3). Combining the near-infrared photometry of the VIKING sources with optical photometry, one can produce more accurate photometric redshifts.

The VIKING matched sources not only provides photometry, but more accurate positions for the matched Herschel sources. In the section above, we state the need for using the likelihood method to match the submillimetre Herschel and near-infrared VIKING counterparts, due to the relatively inaccurate Herschel positions. However, with the improved VIKING positions it will be easier and more accurate when matching this catalogue to other data, such as optical catalogues.

Finally, the ancillary near-infrared data will help provide an insight in to the properties of the Herschel galaxies. The Herschel far-infrared data provides information on the dust, and hence re-radiated radiation from young stars, allowing the star forming properties of the galaxy to be studied. The near-infrared VIKING data on the other hand traces the older stellar component of galaxies. The depth of VIKING will allow further study in to the stellar properties of the star forming Herschel galaxies, out to a significant redshift, for a large number of sources.

	GAMA 9 Field	GAMA 12 Field	GAMA 15 Field
Reliable Herschel ATLAS- VIKING matches	9231	11295	10595
Reliable Herschel ATLAS- SDSS matches	8228	8535	9855
Reliable SDSS and VIKING counterpart	5954	7196	7684
SDSS and VIKING the same	5791	6994	7460
SDSS and VIKING different	154	202	224
Reliable SDSS, no VIKING	2283	1339	2171
Has unreliable VIKING	1434	1065	1436
No nearby VIKING	849	274	735
Reliable VIKING, no SDSS	3286	4099	4625
Has unreliable SDSS	1787	2472	2553
No nearby SDSS	1499	1627	2072

**Table 2.3.** Results of matching both the SDSS and VIKING sources to the Herschel ATLAS catalogue, split over the three GAMA fields. We define reliable matches as those with a reliability of 0.8 or greater. The SDSS and VIKING sources are determined as being the same if they are within 1 arcsecond of each other.

## 2.5 DO VIKING AND SDSS FIND THE SAME IDENTIFICATIONS?

The Herschel ATLAS sources in the Phase 1 catalogues have been matched to their optical counterparts in the SDSS catalogue (Bourne et al., 2016). Here I study the source matching results between the two methods of matching to the VIKING catalogue and to the SDSS catalogue. All three GAMA fields have now been matched to the SDSS catalogues, using the same likelihood ratio technique that we have used above to match to the VIKING catalogue.

There are 20,259 Herschel ATLAS sources in the GAMA 9-h field, 21,897 in

the 12-h field and 23,480 in the 15-h field, resulting in a total of 65,636 sources in total. In this analysis we combine the statistics of each field together, but the individual statistics for each field can be seen in Table 2.3. Over all three fields, 32,836 or 50.0% of sources have a reliable VIKING counterpart. In contrast, only 26,618 or 40.0% of Herschel ATLAS sources have a reliable SDSS counterpart.

### 2.5.1 SOURCES DETECTED WITH VIKING AND SDSS

Of the total 65,636 Herschel ATLAS sources, 20,897 or 31.8% have both a reliable VIKING and SDSS counterpart. In the vast majority of these cases, we determine the VIKING and SDSS sources to be the same. Our requirement for the sources to be the same is that the VIKING and SDSS positions are within 1 arcsecond of each other.

This analysis results in 582 or 2.8% of these 20,897 Herschel ATLAS sources being matched to different sources in the SDSS and VIKING catalogues. A similar analysis done by Fleuren et al. (2012) finds that 2.1% of Herschel sources are matched to different SDSS and VIKING counterparts in the Herschel ATLAS Science Demonstration Phase data.

The cause of these different matches is likely due to sources in either catalogue being too faint to detect, resulting in another nearby source being identified as the most reliable source. It could also be that we are observing a system of multiple galaxies, where the SDSS and VIKING source matching procedures are identifying different sources in the system as the most reliable ones. To test what the causes are of identifying different sources, we visually inspect the SDSS cutouts at the positions of the 154 Herschel sources in the GAMA 9-h field, which have different SDSS and VIKING counterparts. We separate the images into 6 categories:

1. Those where there are a significant number of galaxies around the Herschel position
2. Those where there is a single bright galaxy at the Herschel position
3. Those where there is a single faint galaxy at the Herschel position
4. Those where there are 2 or 3 galaxies at the Herschel position, which visually look to be possible mergers or interactions

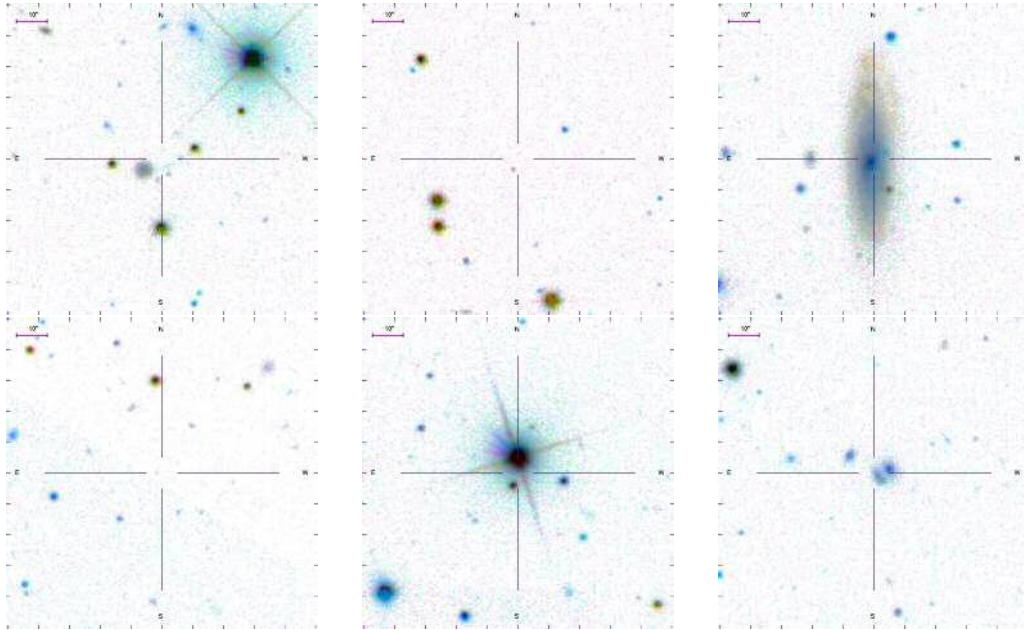


**Figure 2.2.** Cutout images from the Sloan Digital Sky Survey, representing the six categories that we split our sources with different VIKING and SDSS counterparts in to. *From top left, moving clockwise:* Multiple possible galaxies, single small galaxy, single large galaxy, possible merger or interaction, star or artifact and difficult to identify.

5. Those where there is a star or artifact at the Herschel position
6. Those where none of the above options is clear, typically because no galaxy is visible near the Herschel position

The statistics for 154 Herschel GAMA 9-h sources are given in Table 2.4. We find that in 20.1% of cases, matching to the different sources is likely due to multiple sources near the Herschel position or possible merging systems. In this case, the Herschel source is likely being matched to different sources in the images. We stress that our identification of possible mergers is entirely visual, based on one or more of the sources having a disturbed shape or apparent overlapping of the sources. A rigorous test is beyond the scope of this work, instead we are mainly interested in knowing that there are multiple nearby sources.

In the majority of cases, the cutout image shows a single dominant galaxy at the Herschel position. In around 9% of cases, this is a single large, bright galaxy, which is likely to be the true counterpart. In this case, it is possible that both VIKING and SDSS are identifying this galaxy as the best counterpart, but the positions assigned to the galaxy by both surveys are different. In the case of the smaller galaxies, it is

Identified category	Number of Galaxies	Percentage of sample
Multiple galaxies	22	14.3%
Single large galaxy	14	9.1%
Single small galaxy	54	35.1%
Possible merger or interaction	9	5.8%
Star or artifact	6	3.9%
Unlear/Difficult to see	49	31.8%

**Table 2.4.** Table of the different categories of SDSS cutout images at the positions of those Herschel sources with different SDSS and VIKING sources in the GAMA 9-h field.

likely that the VIKING sources are not visible in the SDSS image, probably because they are red, either due to being dusty galaxies or being at high redshifts. In a small number of cases, there is either a star or artifact on the image. In these cases, it may be that either the SDSS or VIKING is incorrectly matching to this, whilst in the other survey we are matching to another source on the image. Finally, in around one third of cases it is not obvious which of the other categories the cutout images fall in to. This is most often due to there being no clearly visible SDSS galaxy near the Herschel position.

We conclude that in the different identifications between the SDSS and VIKING catalogues are due to mixture of mergers, cases of multiple nearby sources, a star or artifact on the image, and cases where the SDSS source is not visible in the VIKING image or vice versa. Removing stars and artifacts should be relatively easy to do and improve the matching process, but the other situations are not easy to fix. We conclude that analysis like this, to identify whether Herschel sources have different SDSS and VIKING counterparts, should be conducted before using both sets of photometry together to avoid erroneous results.

### 2.5.2 SOURCES ONLY DETECTED WITH SDSS

There are 5,721 sources that have a reliable SDSS counterpart, but not a reliable VIKING match. Of these Herschel sources, 3,863 have at least one nearby VIKING galaxy with a reliability less than  $R < 0.8$ , our minimum reliability value. Of these less than reliable sources, 31.7% have reliability between 0.5 and 0.8. These less than reliable sources are the result of one of several possible situations. They

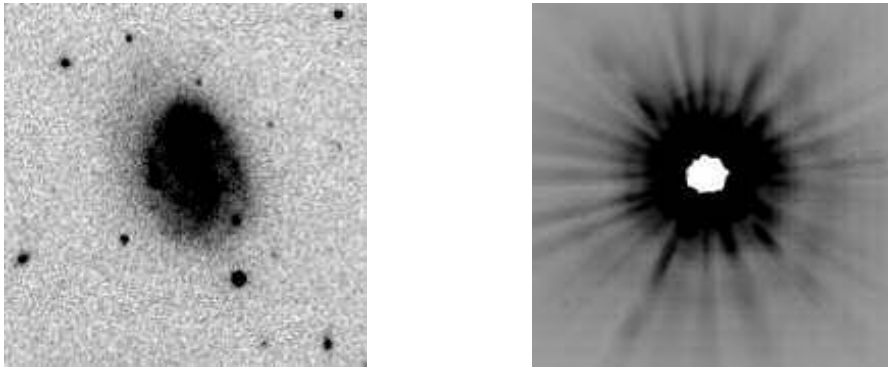


**Figure 2.3.** Two cutouts from the VIKING survey at the positions of Herschel sources, with reliable SDSS counterparts, but no nearby VIKING source. The image on the left shows a bright nearby galaxy imaged with VIKING, whilst the image on the right shows a bright star or artifact which has incorrectly not been removed.

could be sources that are completely unrelated to the Herschel ATLAS source, causing none of them to have a reliability over 0.8. However, if there is more than one reliable source, such as in the case of a merging system, it's likely that no one source has a reliability above the minimum threshold.

We find that the remaining 1,858 sources have a reliable SDSS counterpart, but there is no VIKING source within 10 arcseconds. The VIKING survey is deeper than SDSS, so it is unlikely that we are missing the VIKING counterpart due to it being at a high redshift. To test what is causing this, we select several of the Herschel sources with a SDSS counterpart, but no VIKING, and check the VIKING images at the source position. In Figure 2.3 we show cutout images at the positions of two such sources. It is clear from the image on the right that there is some artifact in the image, or possibly a star, which is creating an issue in our source matching procedure. We note this in the previous section, when we match to different VIKING and SDSS sources, that often the SDSS source is an artifact or star. This is likely the cause of a number of our missing VIKING detections, which we have filtered to remove stars. The image on the left seems to show a bright near-infrared source, yet the catalogue does not contain any detection or information around this position. We observed this in a number of cutout images around Herschel positions. This is an issue with the VIKING catalogue, which seems to be missing several clear sources which appear in the cutout images. It is therefore likely that the number of Herschel sources with an SDSS counterpart, but no VIKING, is in fact inflated by incompleteness of the

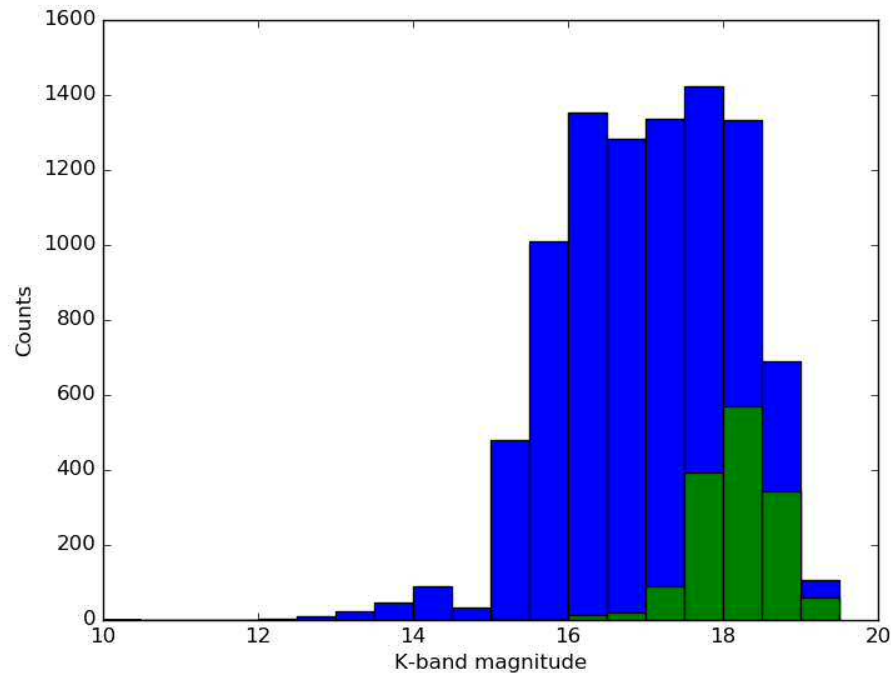


**Figure 2.4.** K-band distributions of all our VIKING sources which have been reliably matched to a Herschel source (blue) and of those VIKING sources who have been reliably matched to a Herschel source, but where there is no nearby SDSS source (green)

VIKING catalogue, despite it covering that area of sky.

### 2.5.3 SOURCES ONLY DETECTED WITH VIKING

Conversely, there are 12,110 sources with a reliable VIKING counterpart but without a reliable SDSS match. We repeat the same analysis as above and find there are 6,882 Herschel ATLAS sources with a reliable VIKING counterpart, but no reliable SDSS counterpart. Of these sources, 28% have reliabilities between 0.5 and 0.8, suggesting that many of these sources may have SDSS counterparts, but they are below the reliability threshold.

The remaining 5,228 sources have no nearby SDSS source. To understand why we do not detect the SDSS counterparts, I have plotted the K-band magnitudes of the VIKING sources in Figure 2.4. The VIKING sources with a reliable Herschel ATLAS counterpart are plotted in blue and represent our full sample of Herschel-VIKING matched galaxies. On top of this are plotted those VIKING galaxies, who have

been reliably matched to a Herschel galaxy, but for who there is no nearby SDSS galaxy. The plot clearly shows that those galaxies without an SDSS counterpart are towards the faintest end of the distribution. We can estimate the redshift of these galaxies, using the K magnitude-redshift relationship (see Section 4.8 for the K magnitude redshift diagram built from a sample of Herschel ATLAS galaxies). The majority of our non-SDSS counterpart galaxies have a K magnitude value of 17.5 or greater (19.35 in AB magnitudes, as plotted in Figure 4.10), which corresponds to a redshift of  $z \approx 1.0$ . The redshift distribution of SDSS sources reliably matched to the Herschel-ATLAS catalogue can be seen in Smith et al. (2011), which clearly shows the inability of the SDSS to find counterparts to the Herschel sources beyond  $z \approx 1.0$ . It is therefore likely that those sources with a VIKING counterparts, but no nearby SDSS source, are due to VIKING's ability to detect galaxies at high redshifts.

## 2.6 CONCLUSIONS

The key aim of this work was to use a robust statistical method to find reliable near infrared counterparts to sources in the Herschel ATLAS survey. We built upon the work of F12, performing the same analysis and producing catalogues of Herschel and VIKING matched sources over the three equatorial GAMA fields. We find similar source matching results. Both pieces of work indicate that around half of all Herschel ATLAS sources have a reliable counterpart in the VIKING survey. We also find that approximately a further third of all the Herschel ATLAS sources have at least one nearby VIKING source, but with a reliability below our minimum requirement. These sources are a mixture of background unrelated sources and true matches, whose reliability is simply too low for them to be identified as the true counterpart. We estimate that between 2-5% of these matches are false.

The Herschel ATLAS sources have been matched to the SDSS catalogue as part of the data release, allowing us to compare the effectiveness of matching Herschel data to both optical SDSS and infrared VIKING data. In each of the three fields, we find a higher fraction of Herschel ATLAS sources with reliable VIKING counterparts than SDSS. 18.4% of the Herschel sources have a VIKING counterpart with  $R > 0.8$ , but no SDSS counterpart with  $R > 0.8$ , whilst 8.72% of Herschel sources have a reliable SDSS counterpart, but no reliable VIKING counterpart. This leads to just under one third of Herschel ATLAS sources having both a reliable VIKING and

SDSS counterpart. Interestingly in 5% of cases the VIKING and SDSS sources are not the same, a result of incorrect source matching by one method or the possibility of identifying different sources in a merging system. We conclude that the matching the Herschel ATLAS catalogue to the near infrared VIKING catalogue is more effective than to the optical SDSS catalogue.

We now have a sample of Herschel-VIKING matched sources. One possible use of this data is to potentially identify and study gravitational lenses. The Herschel sources are expected to lie at relatively high redshifts, out to  $z \approx 3$ , making it suitable for detecting gravitationally lensed galaxies. The VIKING survey on the other hand is expected to detect galaxies at lower redshifts, including large elliptical galaxies with dominant old stellar populations, which are likely to lens distant galaxies. Therefore, it is possible that a number of galaxies in our Herschel-VIKING matched catalogue are gravitational lensing systems. In the next chapter we will use this sample of galaxies to attempt to identify a sample of gravitational lenses.

# 3

## Gravitational lensing identification with VIKING

*“You have no responsibility to live up to what other people think you ought to accomplish. I have no responsibility to be like they expect me to be. It’s their mistake, not my failing.”*

– Richard Feynman

### 3.1 INTRODUCTION

In the previous chapter, we matched a catalogue of near-infrared galaxies from the VIKING survey and a catalogue of submillimetre galaxies from the Herschel-ATLAS survey. The VIKING galaxies are expected to lie at relatively low redshift and for some of them to have significant old stellar populations. Some of these VIKING galaxies may be large elliptical galaxies, which act as gravitational lenses to more distant galaxies. The Herschel-ATLAS survey on the other hand detects galaxies out to a higher redshift and is powerful at detecting gravitationally lensed galaxies. Therefore, a sample of Herschel-VIKING matched galaxies may contain a number of gravitational lensing systems which we can identify and study.

Gravitational lenses provide a view of distant and less luminous galaxies, that would otherwise be difficult or impossible to observe. It is the result of the bending of light from a background galaxy by a foreground lens, typically either a galaxy cluster or early type galaxy, which has the effect of both increasing the brightness

of the background galaxy, often bringing it above the detection limit of a survey and increasing its apparent size. Resolving distant galaxies down to small scales allows their light profile to be studied in detail. The decomposition of galaxy light profiles into their separate components, such as the bulge and disc, is beginning to provide a more detailed and informed view of how star forming galaxies have evolved. Gravitational lensing allows a population of distant, faint and small galaxies to be decomposed into their light profile components, something which has been difficult before now.

Searching for gravitational lenses in the submillimetre has two advantages over other wavelengths. Submillimetre surveys benefit from the effect of negative K-correction. Normally, galaxies appear fainter as they increase in distance from us, the observer. However, due to the shape of the dust emission peak, the submillimetre fluxes of galaxies remain relatively constant for galaxies of increasing redshift, out to a certain limit. This means we can easily observe galaxies out to relatively high redshifts.

The other reason is that submillimetre surveys are very effective at identifying gravitationally lensed galaxies due to the steep drop in the count of un-lensed submillimetre galaxies at bright flux densities, as seen in Figure 3.1. The magnification boosting of gravitationally lensed sources at high redshifts creates a bump in the distribution at bright flux densities, providing a method of easily identifying a significant number of lensed galaxies in the Herschel data (Negrello et al., 2010). Figure 3.2 shows a prediction, based on the model of Cai et al. (2013), of the number of observed lensed and unlensed sources as a function of redshift, for galaxies with  $500\mu\text{m}$  fluxes above 30mJy and 53mJy. The plot shows that for Herschel sources with  $S_{500} > 52\text{mJy}$ , above redshift  $z \approx 3$ , the majority of Herschel sources are lensed, suggesting there is a significant population of gravitationally lensed galaxies that might be observed with Herschel. This method is expected to find lensed sources at a surface density  $\approx 0.5 - 2\text{deg}^{-2}$ , resulting in the possibility of a catalogue of 1,000 lenses from the Herschel ATLAS survey (González-Nuevo et al., 2012). Large samples of lensed galaxies are needed to provide a fuller and more complete view on galaxies over a range of redshifts, so any additional methods for identifying gravitational lenses in the Herschel catalogues will help contribute towards a significant catalogue of gravitationally lensed galaxies.

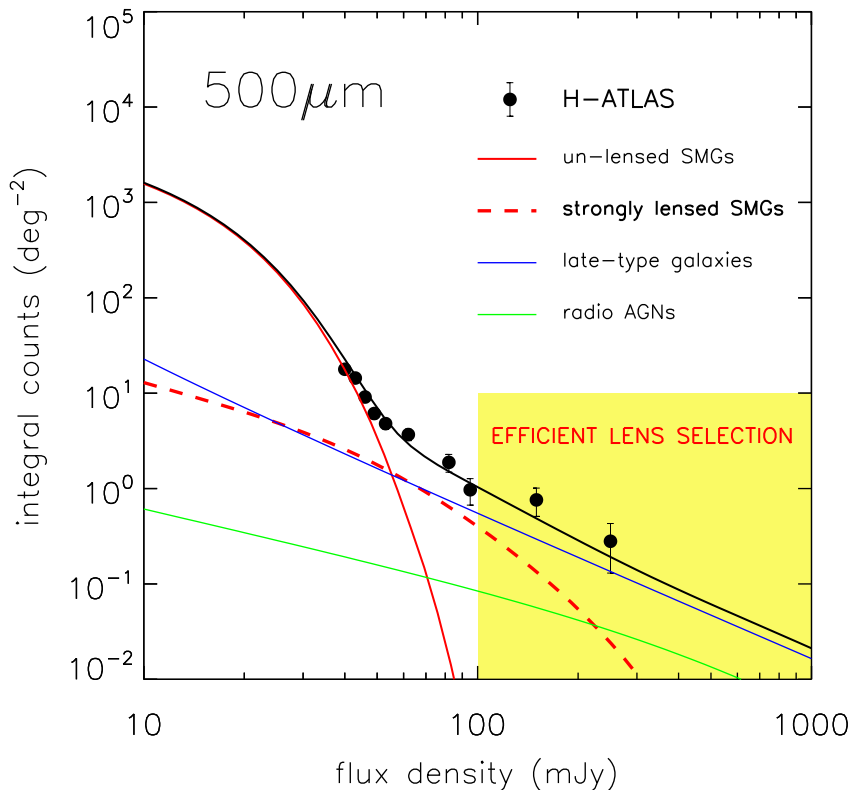


**Figure 3.1.** The 500 $\mu\text{m}$  source counts of three galaxy populations: high redshift submillimetre galaxies, low redshift late type galaxies and radio galaxies powered by AGN. Strongly lensed SMG’s are dominant over un-lensed SMG’s above 100mJy, providing an easy method of selecting lensed SMG’s from Herschel data. This figure is from Negrello et al. (2010).

Another technique used to estimate the number of gravitational lenses is the angular cross correlation method (Wang et al., 2011, González-Nuevo et al., 2014). Gravitational lensing causes an apparent angular cross-correlation between two populations of sources, with distinct redshift distributions, as seen in Figure 3.3. Here, the lower redshift population traces the lens systems and the high redshift population is the lensed galaxies. The cross correlation studies the excess in probability of finding nearby sources in two populations, relative to a random distribution of background sources. Both Wang et al. (2011) and González-Nuevo et al. (2014) find evidence of lensing induced cross correlation between Herschel and SDSS samples of galaxies.

Large samples of gravitational lenses have several uses. To fully characterise

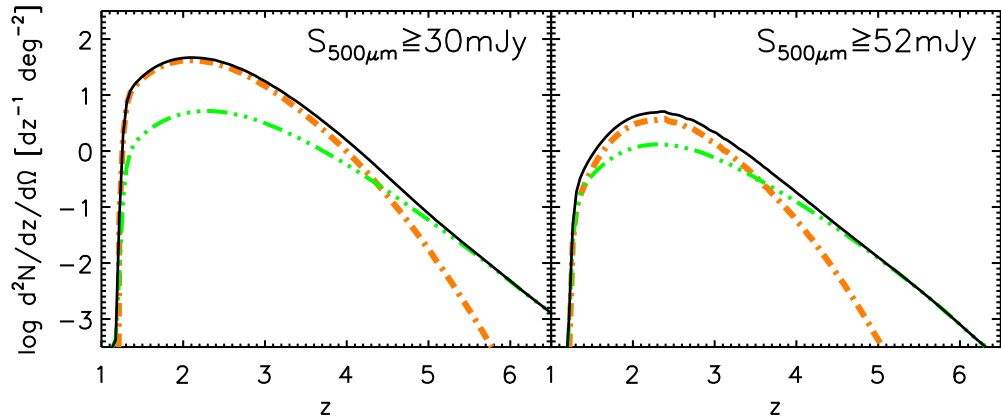


**Figure 3.2.** The counts of predicted lensed (green line) and unlensed (orange line) sources as a function of redshift, above the flux limits given in the upper right of each plot. The black line is the sum of the two distributions. This plot is from private communications with Gianfranco De Zotti.

populations of galaxies, one needs a large, representative sample. Lensing magnifies the image of the distant source, allowing the galaxy to be measured down to small scales. This allows the study of how the morphology of galaxies changes over time; however, large samples are needed to provide reliable results and make conclusions. Cosmological parameters, such as the dark matter and dark energy content of the Universe, can be constrained by studying large samples of galaxies (Eales, 2015). There is hence a strong incentive to identify large populations of gravitational lenses. The method by Negrello et al. (2010) was predicted to discover around 100 gravitational lenses with  $F_{500\mu m}$  over the entire Herschel ATLAS field, which covers around  $600\text{deg}^2$ . Adjustments to this method by González-Nuevo et al. (2012) attempted to push this number to 1,000 lenses, resulting in 2 lenses per square degree on average. However, as both these methods rely on identifying lenses based on their excess  $500\mu m$  fluxes, they are potentially missing a large number of lensed sources who do not fulfill this requirement. The angular cross correlation method is able to provide estimates on the fraction of lensed galaxies in a sample, enabling the testing of various cosmological models. However, it does not provide details on the lensed galaxies themselves, as the  $500\mu m$  excess method does. This means there is no opportunity to directly study lensed galaxies, in terms of their morphology for example.

We therefore identify a different method for identifying gravitational lenses in submillimetre Herschel catalogues, based on the likelihood ratio method described in the previous chapter. Similarly to the angular cross-correlation method, we look to

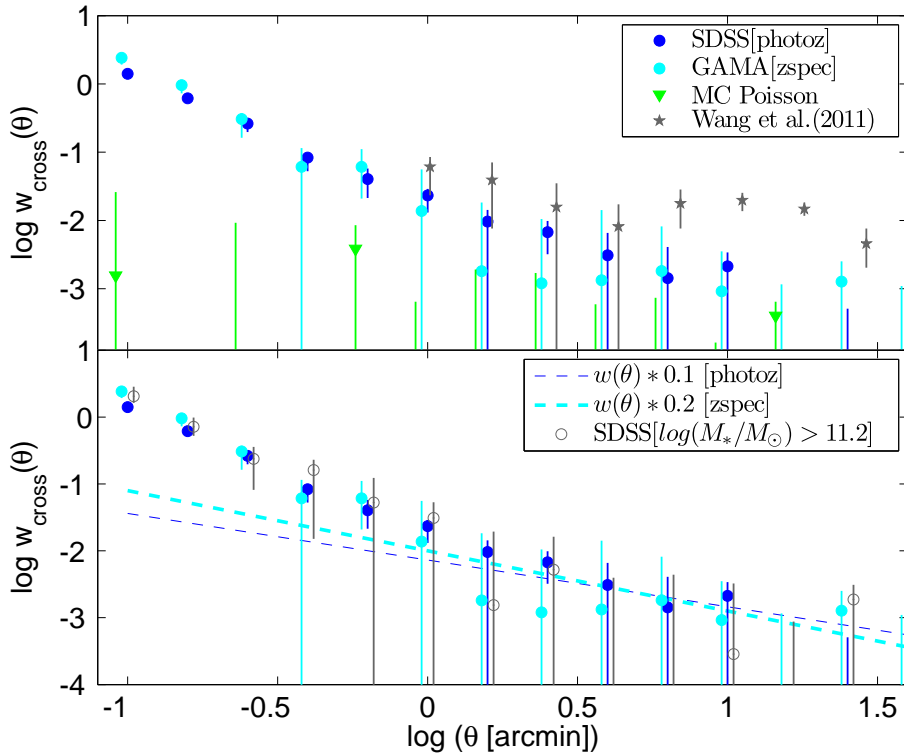


**Figure 3.3.** *Top:* Cross correlation between the Herschel ATLAS sample and two samples of photometric SDSS (blue circles) and spectroscopic GAMA (cyan circles) foreground galaxies. *Bottom:* Comparison of the measured cross correlations and the auto correlation function of the foreground lens samples. This plot is from González-Nuevo et al. (2014).

highlight an overdensity of foreground sources, in our case from the VIKING survey, around the positions of Herschel sources. VIKING is able to detect galaxies at higher redshifts than surveys such as the SDSS, making it better suited to detect the lensing galaxies of Herschel sources. It is also suited to detect the foreground lensing galaxies, which are typically elliptical galaxies with bright K-band emission due to their older stellar populations. The likelihood method is able to estimate the fraction of Herschel sources with a nearby VIKING counterpart above the survey limit. This value should go to zero for Herschel galaxies above the limiting redshift of the VIKING survey; however, cases of gravitational lensing will increase this value. If we ensure the redshift distributions of the two sample do not overlap, then any reliable associations between the catalogues or excess sources above the background density must be due to gravitational lensing systems.

There are several benefits to this method. Firstly, it is able to identify lenses

which may be missed by the method of Negrello et al. (2010), as it does not rely on the Herschel sources having excess  $500\mu\text{m}$  fluxes. This should allow us to discover fainter lensed galaxies, providing details on a different population of lensed galaxies. Secondly, although this method is similar to the angular cross-correlation method, in that we are identifying excess VIKING sources around the Herschel positions, it is able to provide details on the individual lensed galaxies. Those Herschel galaxies, beyond the redshift limit of the VIKING survey, which have reliable VIKING counterparts are likely to be gravitational lens systems. This allows us to study these sources and identify them for follow up observations. This also allows us to visually inspect the possible lensing cases to ensure our method is correct and to study erroneous or interesting cases.

In this chapter, I use the result of Chapter 2 to estimate the number of gravitational lenses, in the Herschel ATLAS data, over the three GAMA fields. In Section 3.2.1 we describe the method to estimate the photometric redshifts of our Herschel galaxies and show the final redshift distributions. In Sections 3.3 and 3.4 we use the results of our source matching to estimate the number of gravitational lenses in the Herschel ATLAS fields. In Section 3.5 we study other gravitational lensing works, which cover the GAMA fields, to test whether our method finds similar results. In Section 3.6, we study the SED's of the most likely gravitational lenses identified in our work, to try to find evidence of a lensing system. In Section 3.7 we study the morphology of the VIKING sources in our most likely lensing systems, to test whether the majority of them have elliptical light profiles, giving further evidence that they are lensing galaxies. In Section 3.8 we highlight the possible sources of error. Finally, we present the conclusions in Section 3.9.

## 3.2 REDSHIFT DISTRIBUTIONS

### 3.2.1 ESTIMATING HERSCHEL PHOTOMETRIC REDSHIFTS

Our method of identifying gravitational lens systems requires us to know the redshifts of the Herschel galaxies. To estimate the photometric redshifts of our Herschel sources, we follow the method outlined in Pearson et al. (2013). They created an averaged Spectral Energy Distribution (SED) from 40 bright Herschel ATLAS sources

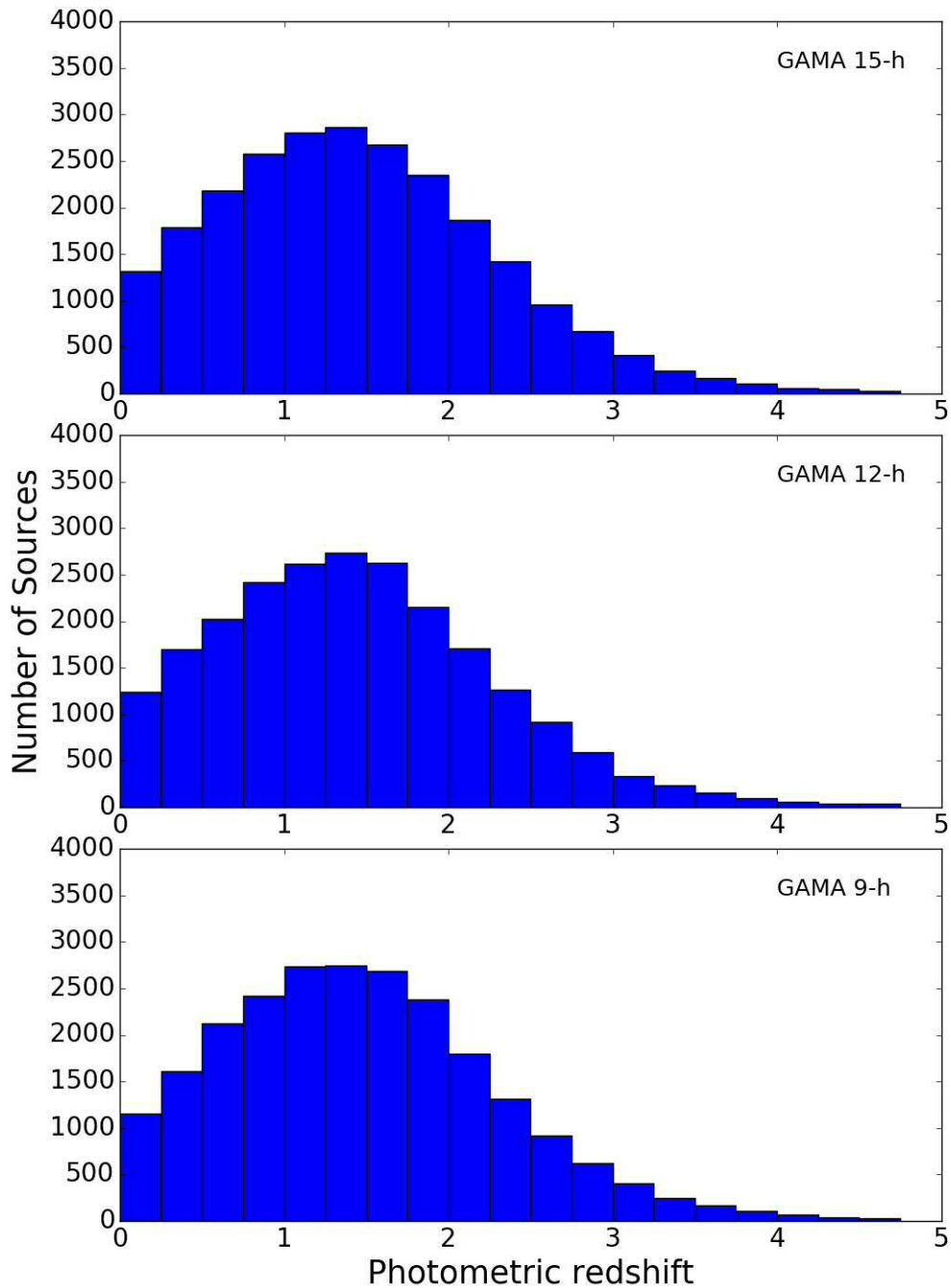


**Figure 3.4.** Photometric redshift distributions of the sources in the three GAMA fields. The three plots are the distributions for the three GAMA fields, the 9-h, 12-h and 15-h, from bottom to top. The redshifts are estimated using the 3 fluxes from the SPIRE instrument on board Herschel, at wavelengths centred at  $250\mu\text{m}$ ,  $350\mu\text{m}$  and  $500\mu\text{m}$

in the Phase 1 catalogue, each of which had known CO or optically determined spectroscopic redshifts. A model SED, consisting of both a hot and a cold component, was fit to the rest-frame SEDs of the 40 galaxies. The temperatures of the two components and the ratio of hot to cold dust mass were free variables, whilst they used a fixed value of Beta  $\beta = 2$ , based on the measured typical value for Herschel galaxies (Eales et al., 2012). Their best fit model is found with a hot dust temperature value of  $T_h = 46.9K$  and a cold dust component with a temperature  $T_c = 23.9K$ . The ratio of cold to hot dust mass is found as 30.1. This averaged SED was then fit to the Herschel SPIRE flux values of sources with unknown redshift, noting how much they need to shift the SED in wavelength to get the best fit, giving the redshift of the source.

Error analysis suggests the method is relatively reliable. When only the Herschel SPIRE fluxes are used (centred at  $250\mu\text{m}$ ,  $350\mu\text{m}$  and  $500\mu\text{m}$ ), the accuracy of the redshifts increases beyond approximately  $z > 1$ . Above this redshift, at least one data point lies on either side of the peak of the dust emission in typical galaxies, significantly increasing the accuracy of the fit. Below this redshift, all three data points lie on the Rayleigh-Jeans tail, making normalising the best fitting curve less accurate.

We use the same technique on our Herschel ATLAS catalogue. The photometric redshift distribution of our Herschel sources, estimated using the Pearson et al. (2013) method, is shown in Figure 3.4.

### 3.2.2 REDSHIFT DISTRIBUTIONS OF THE HERSCHEL AND VIKING SAMPLES

For this method to work, we must ensure that the redshift populations of the two catalogues are distinct. We rely on the fact that the VIKING survey is shallower than the Herschel survey, resulting in the maximum VIKING redshift being lower than the maximum Herschel redshift. A simple test of this can be done by studying a K magnitude-redshift diagram of the Herschel sources. In Section 4.8 we plot the K-z diagram for a sample of Herschel ATLAS galaxies, which have been matched to sources from the Subaru Deep Field catalogue, providing near infrared K band magnitudes. Our limiting K-magnitude of the VIKING survey is  $K \approx 20.5$  in the AB system, which according to the plot relates to a redshift of  $z \approx 1.5$ . On the other

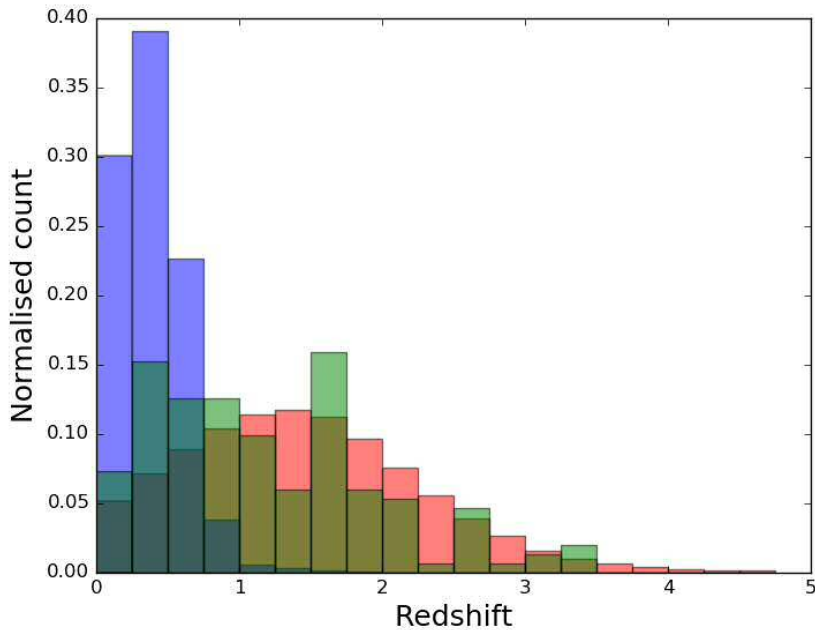


**Figure 3.5.** Normalised distributions of the VIKING and Herschel sources. The VIKING sample, whose redshifts are the photometric redshifts of the best matched SDSS source, is shown in blue. The red distribution shows the Herschel sources over the GAMA fields, whose redshifts have been estimated photometrically from the Herschel fluxes alone. The green distribution is redshift distribution of Herschel sources in the NGP field. These photometric redshifts were estimated from the optical and near infrared using the public code HyperZ, which is discussed in Section 4.6.

hand, the redshift distributions in Figure 3.4 shows that Herschel detects sources out to  $z \approx 5$ . This suggests that for the highest redshift Herschel sources, we should not be able to find the true counterparts in the VIKING survey. We further test that there is a distinction in redshifts of the two surveys, by more accurately measuring redshift values of the VIKING catalogue and directly comparing it to those in the Herschel survey.

We show the redshifts distributions of the Herschel and VIKING sources in Figure 3.5. The redshifts of the VIKING sources are from the best matched SDSS counterpart, whose redshifts have been estimate photometrically and are publicly available as part of the Herschel ATLAS data release. This method provides the most accurate redshifts for the VIKING sources; however, the SDSS survey is shallower than the VIKING survey, so we are almost certainly missing redshifts for the deepest, highest redshifts VIKING sources. In Figure 2.4 we showed that the VIKING sources

with the faintest K-magnitude values failed to be matched to their SDSS counterpart. However, this is a small fraction of the total VIKING catalogue and for a small range of the VIKING K-magnitude values. We therefore must conclude that our distribution of redshifts for our VIKING sample is missing those VIKING sources at the highest redshifts, but we do not expect these to extend to significantly higher redshifts.

We also show the distributions of redshifts of the Herschel ATLAS galaxies. The red distribution shows photometric redshifts of the Herschel galaxies, estimated from the Herschel photometry alone, shown in Figure 3.4 and discussed in Section 3.2.1. The green distribution shows the redshifts of the Herschel galaxies estimated photometrically, after matching to optical Subaru Deep Field counterparts, which is discussed in Section 4.6. We matched the Herschel galaxies to a sample of deep Subaru Deep Field galaxies, providing optical and near infrared photometry for the Herschel sources. The photometric redshifts were then estimated using the public code HyperZ. This provides a sample of Herschel galaxies, with accurate photometric redshifts, though missing the highest redshift galaxies due to the limiting depth of the SDF survey.

We can see that at low redshifts, the Herschel and VIKING sources overlap in redshift. This is expected, as neither survey selects galaxies based on redshift. The VIKING survey detects sources out to  $z \approx 1.5$ , agreeing with our estimate from the K magnitude-redshift diagram. The Herschel sources can be seen to have redshifts which peak around  $z \approx 1.5$ , but extend out to  $z \approx 4.5$ . It is clear that we should not be able to detect the true VIKING counterpart to any Herschel source with a redshift greater than 2, whilst it is likely that this limit is closer to  $z=1.5$ . We can use this fact to help identify lenses, by finding Herschel ATLAS sources at redshifts greater than 2, which have reliable VIKING counterparts.

### 3.3 DENSITY OF VIKING SOURCES AROUND HERSCHEL SOURCES

As discussed previously, it might be possible to detect a significant number of gravitationally lensed galaxies with the Herschel ATLAS survey. The work in the previous chapter has shown that a significant fraction of Herschel sources have a reliable VIKING counterpart. In the majority of cases we expect these counterparts

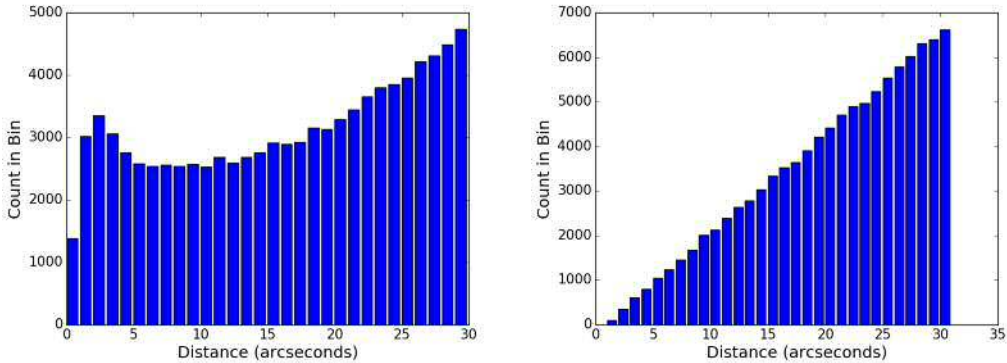


**Figure 3.6.** *Left:* The distribution of all VIKING sources around the positions of the Herschel ATLAS sources, on the GAMA 9h field. *Right:* The distribution of VIKING sources around **random** positions on the GAMA 9h field.

to be the case of us detecting the same galaxy with both surveys, identifying the true counterpart. However, the shallower depth of the VIKING survey means that, for Herschel sources at high redshift, we could instead be detecting a foreground VIKING lensing galaxy and a background Herschel lensed galaxy. We can therefore use our source matching results to estimate the number of gravitationally lensed galaxies in the Herschel ATLAS catalogue.

### 3.3.1 RESULTS

We begin by finding the distribution of distances of VIKING sources around Herschel sources in expanding annuli, 1 arcsecond in radius, centred on the Herschel positions. We would expect a peak in the distribution at small radii from associated sources, whether these are the true associations or gravitational lensing systems. Following the work of F12, we search out to a maximum distance of 15 arcseconds; objects separated by an angular distance greater than this are likely to be unrelated. The distributions for all sources on the GAMA 9h field can be seen in the left hand plot of Figures 3.6. The bump in the distribution around 3 arcseconds is due to associations of sources in both catalogues, whether these are due to gravitational lensing or finding the true counterparts. Random associations do not peak at any specific distance and so contribute towards the overall background distribution of matched sources.

We repeated this with randomly placed Herschel positions (i.e. a set of random positions over the entire field), for each of the GAMA fields, shown in the right hand plots in Figure 3.6 for the GAMA 9h field. As expected, with random associations there is no peak in associations at any separation of sources. In order to estimate the number of either lens systems or true counterparts from our distributions, we subtracted the distribution of randomly placed sources from our distribution of Herschel sources. The top left hand plot in Figures 3.7, 3.8 and 3.9 show these background subtracted distributions for all sources in the GAMA 9h, 12h and 15 fields respectively.

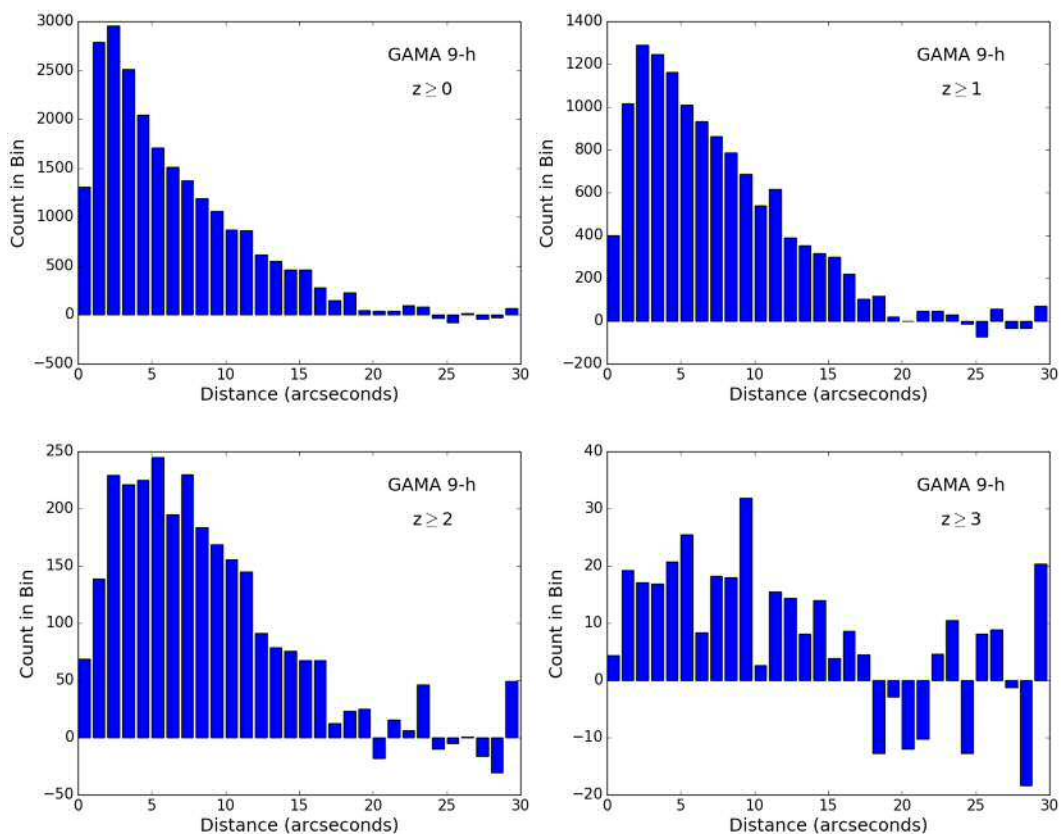


**Figure 3.7.** The background subtracted distribution of VIKING sources around the positions of the Herschel ATLAS sources on the GAMA 9-h field. Each plot denotes a minimum redshift requirement for Herschel sources. The minimum redshift of Herschel sources is  $z > 0$ ,  $z > 1$ ,  $z > 2$  and  $z > 3$ , from left to right, top to bottom.

The remaining peak in the distribution after removing background associations is either due to seeing the same source in both catalogues or due to a gravitational lensing system. There is no way from these plots to determine what fraction of the

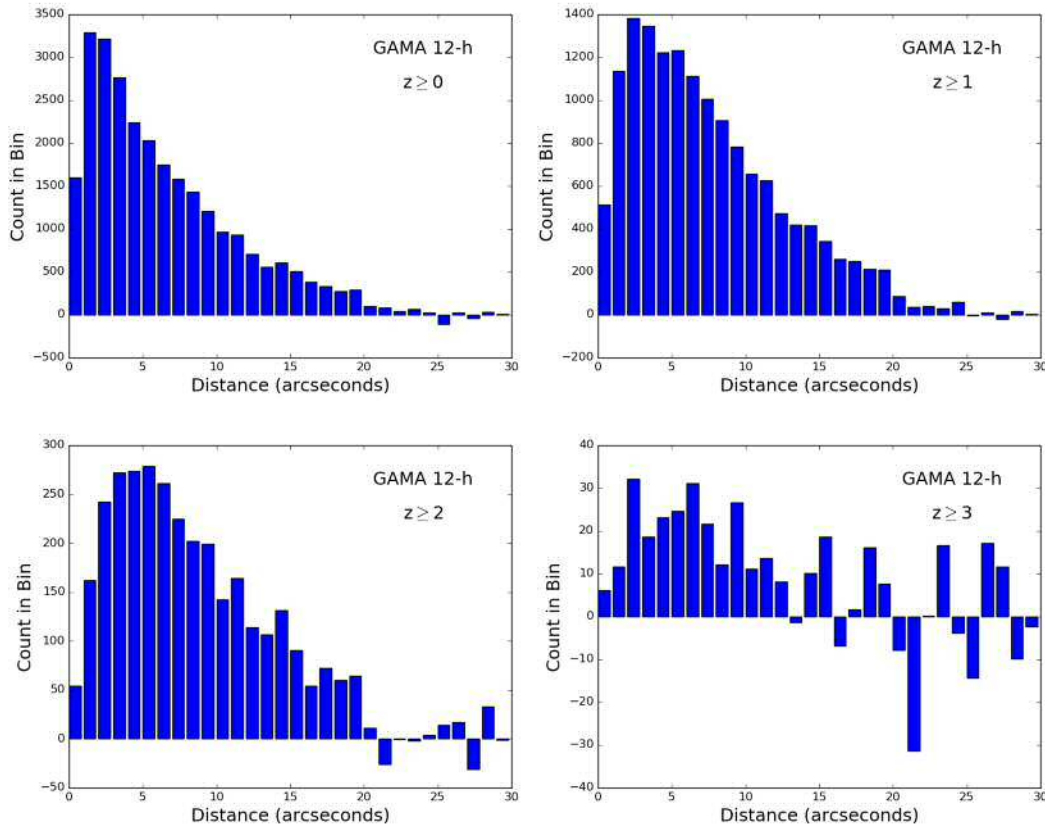


**Figure 3.8.** The background subtracted distribution of VIKING sources around the positions of the Herschel ATLAS sources on the GAMA 12-h field. Each plot denotes a minimum redshift requirement for Herschel sources. The minimum redshift of Herschel sources is  $z > 0$ ,  $z > 1$ ,  $z > 2$  and  $z > 3$ , from left to right, top to bottom.

sources belong to lens systems and which are true counterparts.

To make this distinction, we now take the redshifts of our sources in to consideration. Our initial theory is that the VIKING survey is not as deep as Herschel ATLAS. If this is the case, the VIKING survey should not theoretically be able to see the real counterparts to the Herschel ATLAS sources at high redshift.

To test this, we repeated the analysis above, after splitting our Herschel ATLAS sources into four redshifts bins:  $z > 0$ ,  $z > 1$ ,  $z > 2$  and  $z > 3$ . The distributions for these can be seen in Figures 3.7, 3.8 and 3.9. The photometric redshifts are estimated using a two component black body fitting routine, as discussed in detail in Pearson et al. (2013), and in context of our work in Section 3.2.1. The distribution of redshifts of the Herschel ATLAS sources is show in Figure 3.4.

It can be seen that the bump in the distribution still exists at all redshifts.

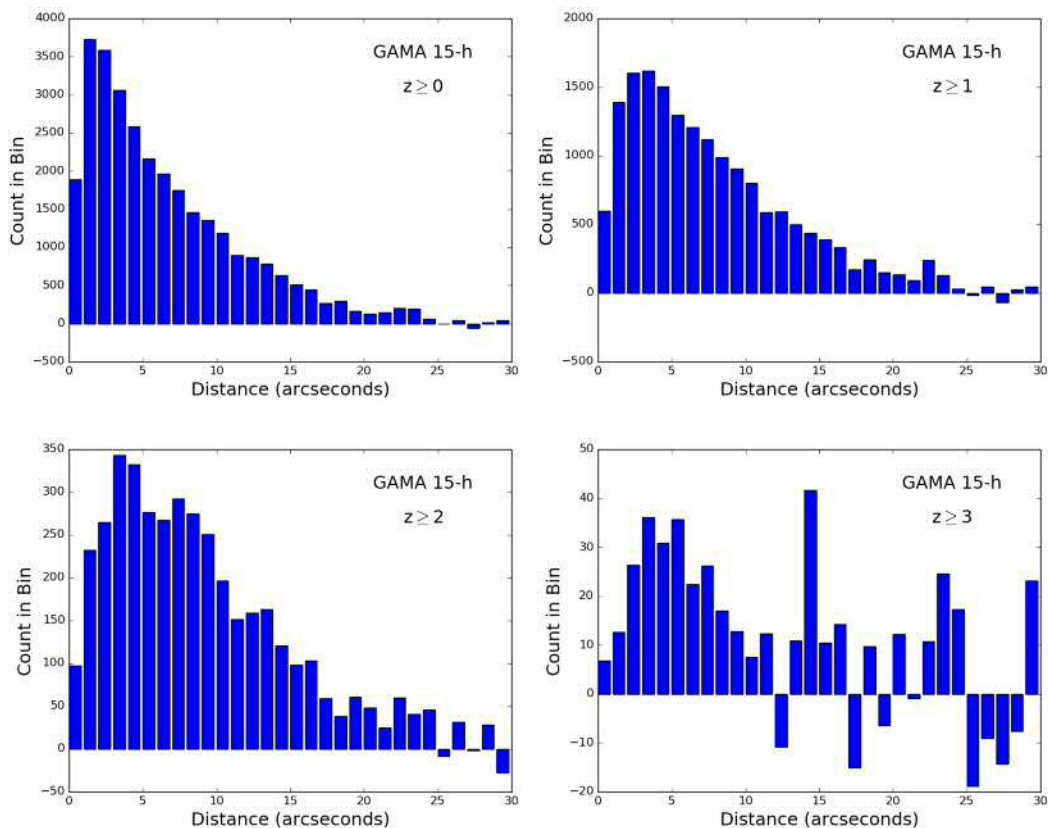


**Figure 3.9.** The background subtracted distribution of VIKING sources around the positions of the Herschel ATLAS sources on the GAMA 15-h field. Each plot denotes a minimum redshift requirement for Herschel sources. The minimum redshift of Herschel sources is  $z > 0$ ,  $z > 1$ ,  $z > 2$  and  $z > 3$ , from left to right, top to bottom.

The plots of redshifts  $z > 3$  are clearly starting to run in to small number statistics, but the bump at low radii is still clearly visible. As the Herschel ATLAS survey should be able to see deeper than VIKING, at high redshift, we shouldn't be able to see the real VIKING counterparts to the Herschel ATLAS sources at  $z > 1.5$  (Section 4.8). However, the redshift dependant source density plots show that we do in fact see nearby VIKING counterparts to Herschel ATLAS sources. The peak in the distribution at low separation is still distinguishable from background noise, suggesting that we are indeed finding a significant number of Herschel ATLAS sources with VIKING matches beyond redshift  $z > 3$ . This is a surprise as the VIKING survey should not be deep enough to see the true counterparts to the Herschel ATLAS sources. This suggests that we might be seeing a large number of lensing systems over the three fields.

We note that the width of the distributions appears to get wider with increasing redshift. This may be a sign that we are incorrectly matching to unrelated background sources at high redshift, as we fail to see the true VIKING counterpart. However, one possibility is that we are detecting a gravitational lensing system and that the distance between lens and lensed galaxies is greater than that between the true counterparts in the Herschel and VIKING surveys. In this case, we would expect the distribution to widen with increasing redshift as we detect a larger fraction of lenses in our Herschel data. We analyse this further in Section 3.4.1.

### 3.4 ESTIMATING HOW MANY HERSCHEL SOURCES HAVE AN ASSOCIATED VIKING COUNTERPART

In our previous source matching work we calculated the value of  $Q_0$ , an estimate of the probability of finding a counterpart to a Herschel source in the VIKING catalogue. We would expect the value of  $Q_0$  to fall to zero for high redshift Herschel sources, beyond the detection limit of the shallower VIKING survey. A non-zero value of  $Q_0$  is therefore an indication that we may be detecting a sample of gravitational lenses.

The method of calculating the value of  $Q_0$  is worked through in detail in Section 2.3 and refreshed upon here. Rather than  $Q_0$ , the value of  $1 - Q_0$  is instead calculated, the probability of a Herschel source **not** having a nearby VIKING counterpart, known as a 'blank'. If we assume that the VIKING survey is not deep enough to see the counterparts to high redshift Herschel galaxies, then we would assume that with increasing redshift the number of blanks would increase and hence  $Q_0$  would fall to zero. If however our data contains a number of lensed galaxies, then we would expect  $Q_0$  to be non-zero for all redshifts.

The number of VIKING sources around the Herschel sources in 1 arcsecond annuli up to maximum for 15 arcseconds is counted. The labelling of a source as a blank is radius dependant. A Herschel source with a VIKING source 10 arcseconds away will be a blank up to 10 arcseconds, then a non-blank from 10-15 arcseconds. The value of  $1 - Q_0$  is given as the number of Herschel blanks in total, divided by the total number of Herschel sources, as a function of radius. This is given in the following equation:

$$1 - Q_0 = \frac{\bar{S}_t}{N} = \frac{\bar{S}}{\bar{R}} \quad (3.1)$$

where  $\bar{S}_t$  is the number of true primary blanks,  $N$  is the total number of primary sources and random position,  $\bar{S}$  is the observed number of blanks and  $\bar{R}$  is the number of random blanks. To estimate the number of random blanks over the field, an equal number of random apertures to Herschel sources are placed over the Herschel fields and the number of blanks per annulus are calculated.

The value of  $1 - Q_0$  is calculated as a function of radius, in  $1''$  steps, to make it independent of radius. A model of the dependence of true blanks on the radius is given by Equation 3.2. The first term of the equation denotes the probability that the counterpart to the source is too faint to detect, given by  $(1 - Q_0)$ . The second term denotes the probability that the counterpart lies outside the search radius, given by  $(1 - F(r))$ . Finally the third term assumes that the two possibilities are independent of each other and that both events can occur.

$$(1 - Q_0) + (1 - F(r)) - (1 - Q_0)(1 - F(r)) = 1 - Q_0F(r) \quad (3.2)$$

where

$$F(r) = 1 - \exp\left(\frac{-r^2}{2\sigma^2}\right) \quad (3.3)$$

The values of  $1 - Q_0$  are plotted in Figure 3.10, for all three GAMA fields, and the function given in Equation 3.2 is fit to the data points. The values of  $Q_0$  and  $\sigma_{pos}$  are estimated from the forms of the best fit function and are given in Table 3.1.

For  $z > 0$  we find similar  $Q_0$  values as F12, who find a value of 0.7342 for all sources above redshift  $z=0$ , though we allow the value of  $\sigma_{pos}$  to be free whereas they fix it to a value of 2.4 arcseconds. We also find that the value of  $\sigma_{pos}$  for our three fields is only slightly higher than the fixed value of 2.4 arcseconds used by F12. The difference in  $Q_0$  in the GAMA 9-h field, which was the focus of their work and part of this work, is likely due to the different catalogues used. We use updated versions of both VIKING and Herschel ATLAS catalogues, which will subsequently lead to different results.

We follow the same procedure as in Section 3.3 and repeat our analysis, but

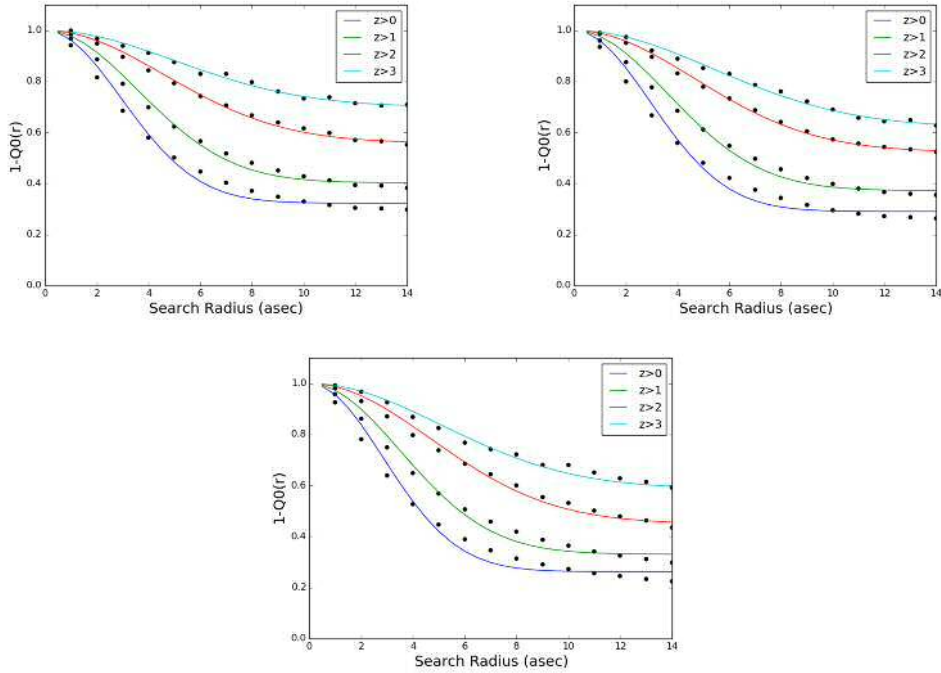


**Figure 3.10.** Plots used to estimate the value of redshift dependant  $Q_0$  for the three GAMA fields, GAMA 9-h, 12-h and 15-h from right to left, top to bottom. The black dots located at integer radius values in arcseconds, from 1 to 15, are calculated as the number of Herschel blanks divided by the number of random blanks. The blue line is for Herschel sources with redshifts  $z>0$ , green for  $z>1$ , red for  $z>2$  and light blue for  $z>3$ .

now for sources with  $z>0$ ,  $z>1$ ,  $z>2$  and  $z>3$ . Figure 3.10 shows the redshift dependant  $Q_0$  plots for the GAMA 9-h, 12-h and 15-h fields respectively. The  $Q_0$  and  $\sigma_{pos}$  values can be found in Table 3.1.

The  $Q_0$  values for each field decrease with increasing redshift, suggesting that most of the low redshift Herschel ATLAS sources are matched to the true counterpart, which is expected. However, at redshift  $z>3$ , the values of  $Q_0$  are all non-zero, meaning that some of the Herschel ATLAS sources have VIKING counterparts above the survey limit. It isn't expected that VIKING can see this deep, based on the K magnitude-redshift diagram, suggesting that these matched sources are due to gravitational lensing.

From this result, we can make an estimate on the number of gravitational lenses in the Herschel ATLAS data. We assume, as discussed previously, that any Herschel source above redshift  $z \approx 2$  with a VIKING counterpart is part of a gravitational lensing system. For each of the three GAMA fields, we calculate the total number of

Field	Min redshift	NSources	$Q_0$ value	$\sigma_{pos}$ (arcseconds)
G09	0.0	18356	0.67686	2.9470
	1.0	12606	0.59694	3.5952
	2.0	4177	0.44060	4.6021
	3.0	628	0.30000	5.0064
G12	0.0	19955	0.70927	2.9406
	1.0	13484	0.62764	3.6110
	2.0	4553	0.47603	4.6399
	3.0	674	0.38038	5.3582
G15	0.0	21446	0.73763	2.8488
	1.0	14497	0.66916	3.5044
	2.0	5000	0.54937	4.6779
	3.0	759	0.41252	5.0843

**Table 3.1.** Table of  $Q_0$  and  $\sigma_{pos}$  for Herschel sources over the three individual GAMA fields.

sources above redshift 2 multiplied by the value of  $Q_0$ . This results in a total of 6,754 sources, which should have a nearby VIKING counterpart above the survey limit. The three GAMA fields consist of around 30% of the total Herschel ATLAS survey, meaning that over all the Herschel ATLAS fields there could be 22,500 gravitational lenses.

### 3.4.1 LENS-LENSED GALAXY SEPARATION

At the end of Section 3.3 we highlighted the fact that our distribution of separations of Herschel and VIKING sources increase in width with increasing redshift. One possibility for this is that we are detecting a number of lens systems at high redshifts, and that the lens-lensed source separation is on average greater than the separation distance of real Herschel-VIKING counterparts. If this is the case, we would expect the distribution to get wider with increasing redshift as we begin to detect a higher fraction of gravitational lenses in our data. A similar result can be seen in Table 3.1 where the value of  $\sigma_{pos}$ , the mean positional uncertainty of the Herschel sources, increases with increasing redshift. This may be due to the same reason that our Herschel-VIKING source separation distribution increases with increasing redshift.

To investigate, we study the sample of gravitational lenses observed by Negrello

et al. (2017), who identified a number of gravitational lenses in the Herschel ATLAS data and identify the optical SDSS counterparts. Studying the separation of their sources, we see that 19 of the Herschel and SDSS sources are separated by between 0.4 and 2.0 arcseconds whilst 6 are separated by larger values up to  $r = 5''$ . From Figure 3.7 we can see that the peak in the distribution for the sources above  $z = 2$ , which we propose are gravitationally lensed, is at around 5 arcseconds. This agrees with 6 of the confirmed lenses in Negrello et al. (2017); however, the fact that the other 19 confirmed lenses are at shorter distances (less than 2 arcseconds) suggests that there is no relationship between the distance of the lens and lensed sources in our data.

### 3.4.2 HIGH S/N SOURCES

One possible source of error in this data would be if the redshift estimates were incorrect. In order to test this possibility we repeat the same process but only for galaxies which have a signal to noise of  $10\sigma$  or greater in the  $350\mu\text{m}$  band. These galaxies should have more reliable flux measurements, which should improve the accuracy of the photometric redshifts. If the redshifts were incorrect then we would expect the  $Q_0$  values from this data set to be different to those derived for the whole data set. The values of  $Q_0$  and  $\sigma_{pos}$  can be seen in Table 3.2. Figure 3.11 shows the same plot for Herschel sources with s/n of at least  $10\sigma$  in the  $350\mu\text{m}$  band.

As can be seen the values of  $Q_0$ , for the minimum redshift bins of  $z=0$ ,  $z=1$  and  $z=2$ , are typically the same for the 10 sigma sources as for the whole catalogue. However, not only are the  $Q_0$  values for the minimum redshift of  $z=3$  bin still non-zero, but they actually increase for the 12-h and 15-h fields. This increase may be due to the fact that the majority of gravitational lenses are the brightest galaxies at the longer Herschel wavelengths, as shown by Negrello et al. (2010). However, this result does imply that even the high redshift Herschel sources with the most reliable photometric redshift consist of a high fraction of gravitational lenses, which in turn gives weight to previous result that a large fraction of all Herschel sources at high redshift are lensed.

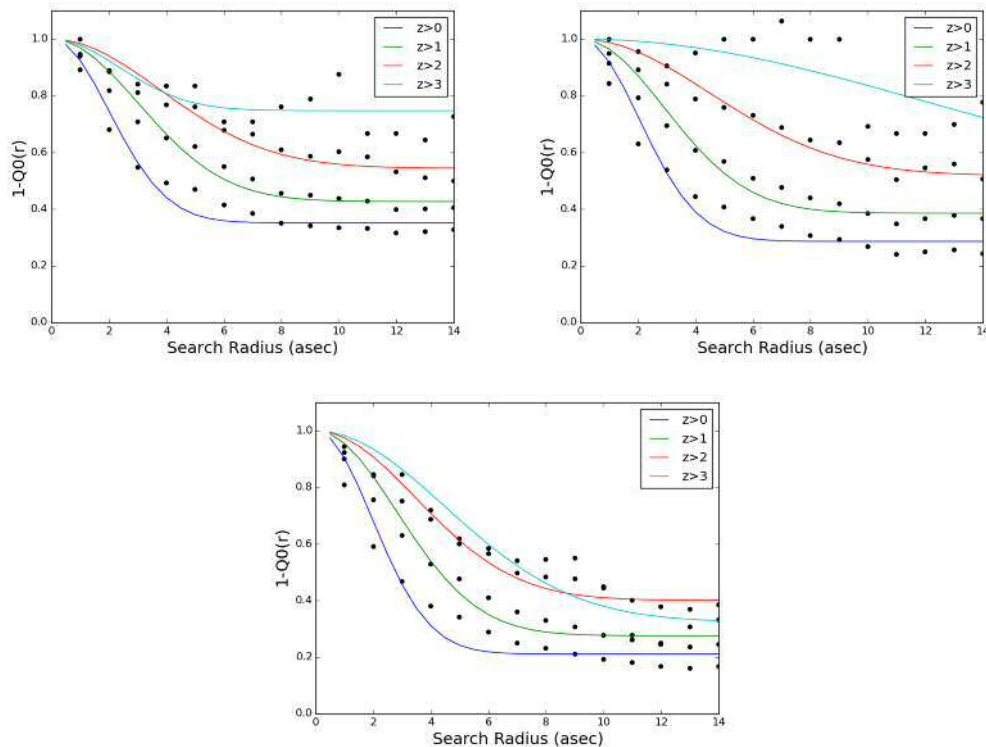


**Figure 3.11.** The  $Q_0$  plots for the GAMA 9-h, 12-h and 15-h fields. Only sources with a 350 micron S/N above 10 are plotted, in order to only include sources in the analysis with the most reliable photometric redshifts.

### 3.4.3 ANALYSIS

It is clear that a very high fraction of Herschel ATLAS sources have counterparts in the VIKING catalogue, many more than we would expect. If our assumptions on the accuracy of the Herschel redshifts and the depth of VIKING are correct, then up to half of all high redshift Herschel ATLAS sources are gravitationally lensed. Although it has been predicted by galaxy models that many high redshift Herschel sources are lensed (Cai et al., 2013), there has been little observational evidence to back them up until now.

The results of Wang et al. (2011) and González-Nuevo et al. (2014) suggest that a significant fraction of Herschel sources are gravitationally lensed, based on a strong correlation between the spatial distributions of high redshift Herschel galaxies and low redshifts SDSS galaxies. We attempt to compare our gravitational lensing result found above, to those in González-Nuevo et al. (2014) (referred to as GN14 from here on), to see whether we are both observing the same effect.

We want to compare the estimated number of sources, within 15 arcseconds of

Field	Min redshift	NSources	Q <sub>0</sub> value	$\sigma_{pos}$ (arcseconds)
G09	0.0	438	0.64808	2.0065
	1.0	322	0.57295	3.0100
	2.0	168	0.45562	3.7890
	3.0	27	0.25238	2.3534
G12	0.0	452	0.71336	2.0366
	1.0	319	0.61405	2.9119
	2.0	156	0.48202	4.4865
	3.0	23	0.56673	12.097
G15	0.0	557	0.78866	1.9655
	1.0	388	0.72389	2.8142
	2.0	197	0.59890	3.4630
	3.0	26	0.67569	4.4737

**Table 3.2.** Table of Q<sub>0</sub> and  $\sigma_{pos}$  for Herschel sources over the three individual GAMA fields. Only sources with a 350 micron s/n above 10 are plotted.

our Herschel sources, as calculated from the results of GN14 and from our Q<sub>0</sub> analysis. to do this, we calculate the number of secondary sources around our Herschel sources as estimated by both the method of González-Nuevo et al. (2014) and by our Q<sub>0</sub> method. We focus on the GAMA 9 field. GN14 calculate the values of  $w(\theta)$ , the value of the angular cross-correlation function, for a range of values of theta. We use this value to estimate the number of secondary sources which we would expect to find near our Herschel sources, which is given as

$$n_{GNMethod} = \int_0^{15} 2\pi\theta \langle n \rangle (1 + w(\theta))d\theta \quad (3.4)$$

where  $w(\theta)$  is the value of the angular cross-correlation function,  $\langle n \rangle$  is the surface density of sources within the search area and  $\theta$  is the search radius. We integrate this function out to 15 arcseconds, the maximum radius we calculate our value of Q<sub>0</sub> out to.  $\langle n \rangle$  is our mean density of VIKING sources over the field, which in the GAMA 9-h field is equal to  $1.79 \times 10^{-3} deg^{-2}$ . We estimate the value of  $w(\theta)$  from the work in GN14, who calculate a value down to a radius of  $\theta \approx 19$  arcseconds, which we extrapolate to  $\theta=15$  arcseconds and estimate a value of  $w(15'')=0.09$ . Here we have made the big assumption that the  $w(\theta)$  function as shown in GN14 for SDSS sources is representative of the  $w(\theta)$  function for the VIKING survey.

Inserting these values in Equation 3.4, we calculate a value of  $n_{objects}=1.4$ , the

number of secondary sources around our Herschel sources as estimated by the method of González-Nuevo et al. (2014).

We can now calculate the number of VIKING sources around Herschel positions, estimated using our  $Q_0$  method, and compare the two values. The number of nearby VIKING sources should equal the background number, plus the fraction of Herschel sources with a counterpart in the VIKING catalogue, which is our value of  $Q_0$ . We therefore estimate the number of nearby secondary sources to Herschel positions as

$$n_{Q_0Method} = \pi\theta^2 < n > + Q_0 \quad (3.5)$$

where  $\theta$  is the search radius, which equals 15 arcseconds and  $< n >$  is the mean number of sources within the search area. From Equation 3.5, we estimate the number of nearby VIKING sources around Herschel positions as  $n_{Q_0Method}=1.72$  using our  $Q_0$  method.

The values estimated by our two methods, of  $n_{objects}=1.4$  and  $n_{objects}=1.72$ , are very similar. This is strong evidence that our method is detecting an excess of sources around the Herschel positions, agreeing with the work of González-Nuevo et al. (2014). This excess of secondary sources is evidence of gravitational lensing if we assume we are not detecting the true counterparts to the sources.

### 3.5 COMPARISON TO LENS CANDIDATES IN OTHER WORK

Gravitational lenses have been searched for in the GAMMA fields by Negrello et al. (2017). They selected possible lensed sources in the Herschel ATLAS data based on their 500 $\mu$ m fluxes, following the method set out in Negrello et al. (2010). In brief, the number count of un-lensed dusty star-forming galaxies is expected drop steeply at 500 $\mu$ m flux densities  $> 100mJy$ , revealing a population of lensed galaxies along with populations of low redshift spirals, blazars and other contaminants, which are easily identified and removed. Negrello et al. (2017) identify 80 lens candidates over the three GAMMA fields and the North and South Galactic Pole fields. We focus on the 26 sources identified in the GAMMA fields.

They confirm 11 of the GAMMA field candidates to be lenses, based on the identification of multiple images, arcs, or by the detection of two sources at different

redshifts along the line of sight. They identify 3 'likely' lenses, based on the existence of a low redshift optical or near infrared counterpart, which is at a significantly lower redshift than the Herschel source. This is the same process that we have used to identify lenses and so offers a way to study the accuracy of our method. Another 11 sources are identified as 'unclear', based on their lack of foreground optical/NIR counterparts. These sources may have foreground counterparts below the detection limit of the counterpart survey, or may be unlensed, bright, high redshift galaxies. Finally, 1 source is confirmed to not be a lens, which we do not include in our analysis (Iverson et al., 2013). Redshifts for the Herschel sources are from a mix of spectroscopic surveys and calculated from the Herschel photometry, following the method laid out in Pearson et al. (2013) - the same method that we use to estimate redshifts for our Herschel sources.

Our work identifies possible gravitational lensing systems, based on reliably matching low redshift VIKING sources to Herschel sources in the GAMA fields. We can therefore compare our possible gravitational lenses to the candidate lenses identified in Negrello et al. (2017). We begin by seeing how many of the Negrello lens candidates are identified as possible lenses in our work. We define possible lenses as Herschel sources which have a reliable counterpart. If these Herschel sources are at a distance beyond the detection limit of the VIKING survey, then we must be studying a lensing system.

### 3.5.1 RESULTS

HATLAS id	Lens Rank	Herschel redshift (Negrello)	Herschel redshift (myself)	Reliable counterpart?
<b>GAMA 9</b>				
HATLASJ083051.0+013225	A	3.634	2.79	N
HATLASJ085358.9+015537	A	2.089	1.88	Y
HATLASJ091043.0-000322	A	1.786	1.73	N
HATLASJ090740.0-004200	A	1.577	1.25	N
HATLASJ090311.6+003907	A	3.042	3.26	Y
HATLASJ091840.8+023048	C	2.581	2.67	Y
HATLASJ091304.9-005344	A	2.626	2.57	Y
<b>GAMA 12</b>				
HATLASJ114637.9-001132	A	3.259	2.76	N
HATLASJ113526.2-014606	C	3.128	2.17	N
HATLASJ121334.9-020323	B	<i>1.89</i>	1.92	Y
HATLASJ121301.5-004922	B	<i>2.35</i>	2.37	Y
HATLASJ120709.2-014702	C	<i>2.26</i>	2.39	N
HATLASJ120319.1-011253	C	<i>2.70</i>	2.73	N
HATLASJ115101.7-020024	C	<i>1.81</i>	1.73	Y
HATLASJ115112.2-012637	B	<i>2.22</i>	2.18	Y
HATLASJ120127.6-014043	C	<i>3.80</i>	4.16	N
HATLASJ120127.8-021648	C	<i>1.50</i>	1.57	N
HATLASJ121542.7-005220	C	<i>2.48</i>	2.46	Y
HATLASJ115820.1-013752	C	2.191	2.33	N
<b>GAMA 15</b>				
HATLASJ142935.3-002836	A	1.027	0.91	Y
HATLASJ142413.9+022303	A	4.243	4.25	Y
HATLASJ141351.9-000026	A	2.478	2.83	Y
HATLASJ144608.6+021927	C	<i>4.10</i>	4.30	Y
HATLASJ144556.1-004853	C	<i>2.51</i>	2.55	Y

**Table 3.3.** Table of lens candidates identified in Negrello et al. (2017), which we have attempted to find counterparts for in our gravitational lensing work. The Herschel redshifts from Negrello et al. (2017) are spectroscopic where available, with the remainder having photometric redshifts (identified in italics). The Herschel redshifts estimated in our work are estimated from the Herschel fluxes alone.

We find that 14 of the 24 sources have a reliable VIKING counterpart. 13 of these Herschel sources have redshifts  $z > 1.5$ , suggesting that the VIKING counterparts are unlikely to be the true counterparts, but are likely to be lenses. Of the 14 sources, 9 are given a lens rank A or B, meaning that they are either confirmed or likely lenses, whilst the remaining 5 sources are unclear based on the analysis by Negrello et al. (2017). This confirms that our method of identifying low redshift reliable counterparts to our high redshift Herschel sources is effective at identifying lensed sources. The remaining 10 sources do not have reliable counterparts in our analysis, either because the likelihood of all possible sources are too low to identify a single reliable counterpart, or because the distance to the VIKING source is greater than 10 arcseconds (this occurs because our source density histograms identify possible lenses out to 30 arcseconds, but our reliable source matching only searches out to 10 arcseconds).

We conclude that we are able to identify two thirds of the same lenses identified using the  $500\mu\text{m}$  selection method. The method of Negrello et al. (2017) is only able to identify lensed Herschel sources whose  $500\mu\text{m}$  flux is greater than  $100\text{mJy}$ , whilst our method is applicable to the entire Herschel catalogue, offering the opportunity to identify a significant number of gravitational lenses in the Herschel ATLAS catalogue.

### 3.6 STUDYING THE SPECTRAL ENERGY DISTRIBUTIONS OF POSSIBLE LENSES

Our hypothesis states that those high redshift Herschel sources, with a reliable VIKING counterpart, are gravitationally lensed systems. In this scenario, the VIKING source is a foreground galaxy, lensing the Herschel source behind it. If this is the case, then there should be no relationship between the near infrared/optical and submillimetre photometry, as they come from two different sources. We can therefore test whether our sources are gravitational lenses by checking whether we can accurately fit a model SED to the shorter and longer wavelength photometry.

We use the model SED fitting routine MAGPHYS (da Cunha et al., 2008) to fit template spectra to our possible lens photometry. Details of MAGPHYS can be found in Section 5.3, but in brief, it generates a library of 25,000 optical and 50,000 infrared

models. It accounts for the energy emitted by stars and that which is absorbed and re-emitted by dust. `MAGPHYS` provides estimates of the physical parameters of galaxies, including their stellar mass, star formation rate and dust mass. It also provides a measurement of how well the model SED was fit to the input photometry, which we will use to determine whether any of our possible lensed galaxies are indeed lens systems.

We define two samples of galaxies to test. First, we create a sample of galaxies in the GAMA 9 field which are identified as possible lenses. These are Herschel galaxies with reliable near-infrared VIKING and optical SDSS counterparts. The Herschel sources have photometric redshifts, estimated from the Herschel fluxes alone, of  $z > 2.5$ . We only include Herschel sources with a signal to noise of  $10\sigma$  or greater in the  $350\mu\text{m}$  band, following the logic set out in Section 3.4.2. This ensures that we are using the sources with the most accurate photometric redshifts. The optical counterparts have spectroscopic redshifts from the SDSS catalogue. In total, this produces a catalogue of 7 sources. Our second sample, named non-lens galaxies, consists of Herschel sources, with reliable VIKING and SDSS counterparts, but with Herschel photometric redshifts of  $z < 0.2$ . Any optical counterpart to a Herschel source at this low redshift is likely to be the same source and not a gravitational lensing system. Our non-lensed galaxies are therefore a control sample to compare to, which consists of 39 sources. We expect the reduced chi squared values, from fitting model templates to our photometry, of our non-lens galaxies to be lower than our lensed galaxies.

We are forced to use the short wavelength photometry from the SDSS counterparts to the Herschel sources, rather than from VIKING, because we use the submillimetre galaxy prior ranges in `Magphys`, which should fit our high redshift Herschel sources better, as discussed in Section 5.3 and Rowlands et al. (2014). Unfortunately, the VIKING filters are not currently available to use with the submillimetre galaxy prior ranges in `Magphys`. As our aim is simply to test whether it is more difficult to fit model SEDs to possible lenses than non-lenses, it does not matter whether we use VIKING or SDSS photometry.

Figure 3.12 shows the distribution of reduced chi squared values for our lens and non-lens samples. We see that the reduced chi squared values of our non-lens sample form a distribution at low values, with the majority of sources having a reduced

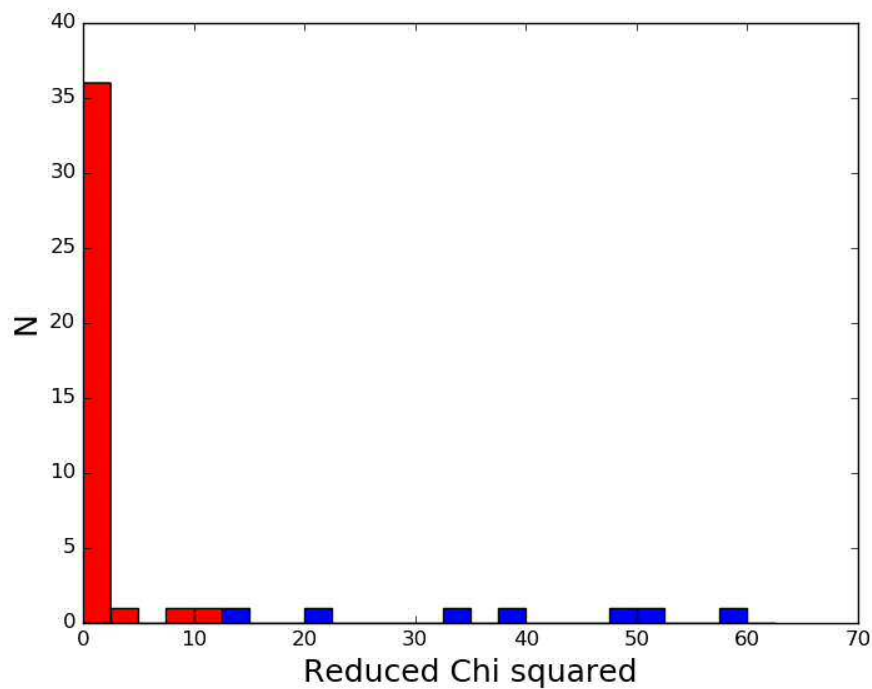


**Figure 3.12.** Distribution of Reduced Chi squared value from fitting model spectra to Herschel galaxies with optical SDSS photometry. Galaxies which are deemed non-lenses are shown in red and those which are possible lenses are in blue.

chi squared value of less than 5. On the other hand, our lensed sources have reduced chi squared values of 10 and greater. The two distributions do not overlap and are clearly distinct. It is clear that the best fit models to the lens sample are significantly worse fit than our non-lens sample, suggesting that our sample of possible lens galaxies are indeed lens systems.

One issue may be if `MAGPHYS` is not as effective at fitting high redshift sources as it is low redshift sources. Rowlands et al. (2014) analyse two samples of Herschel galaxies, one at redshifts  $z > 1.0$  and the other at  $z < 0.5$ . They find that `MAGPHYS` can effectively fit SED's to both high and low redshift galaxies, when using the high redshift SMG galaxy priors.

In Figure 3.13 we show 4 examples of non-lensed and possible lensed best fit SEDs along with the SDSS and Herschel fluxes, to help illustrate why the possible lenses have poorer fits. It is clear from a visual inspection that in the cases of the possible lensed galaxies, the SED does not fit both the SDSS optical and Herschel submillimetre fluxes accurately. In all four possible lens cases, the Herschel flux points lie at wavelengths longer than the dust emission peak, despite the Herschel fluxes appearing to be measuring the dust emission peak based on their shape. This suggests the Herschel fluxes are at a higher redshift than the SED and hence the SDSS fluxes, which backs up our theory that the Herschel sources are in fact distant lensed galaxies and the SDSS sources are foreground lensing galaxies.

We conclude that our possible lensed galaxies show further evidence of being actual lenses, based on the disparity between fitting the optical SDSS and submillimetre Herschel fluxes. We have tested this for those sources with the most reliable photometric Herschel redshifts, reducing the chances of us including Herschel sources at low redshift with true VIKING counterparts. The reduced chi squared values of the possible lensed galaxies are all larger than our non-lensed galaxies and their SED's show clear evidence that the Herschel fluxes belong to a source at a higher redshift than the SDSS source. We take this as further evidence that a significant number of our Herschel sources, which lie at high redshifts yet have a reliable VIKING counterpart, are gravitationally lensed.

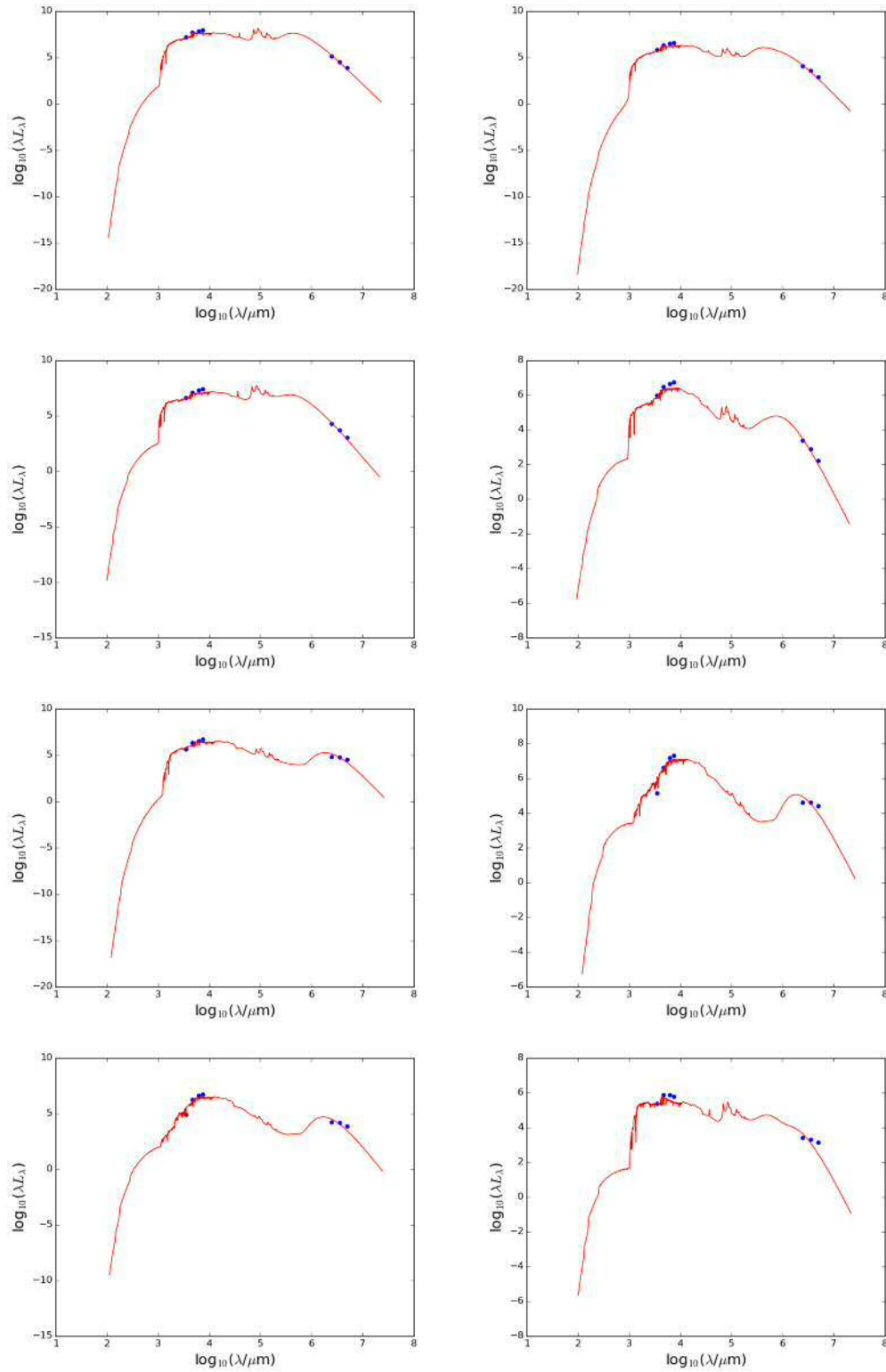


**Figure 3.13.** Example SED fits, using the public code MAGPHYS, to our samples of non-lensed and possible-lensed galaxies. The top four plots show our low redshift, non-lensed galaxies, and the bottom four plots show our possible lensed galaxies. The red line is the best fitting SED and the blue dots are the SDSS and Herschel SPIRE photometry.

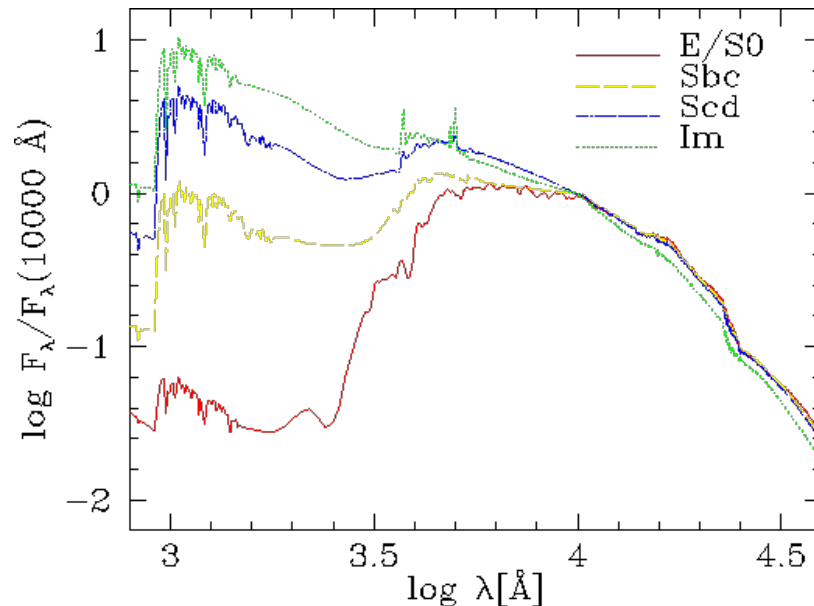


**Figure 3.14.** The mean spectra of local galaxies, as created by Coleman et al. (1980), which are used by HyperZ to estimate the photometric redshifts of galaxies. This figure is from Bolzonella et al. (2011)

### 3.7 THE SPECTRAL ENERGY DISTRIBUTIONS OF POSSIBLE LENSES

Gravitational lensing is the bending of light from a background source, by some foreground mass. This foreground mass is typically either a galaxy cluster or a massive elliptical galaxy. The analysis of lensing by clusters is beyond the scope of this work; however, we can test whether there is any correlation between the possible lenses identified in this chapter and the morphology of the VIKING counterpart, which may be lensing the Herschel galaxy.

We use the public code HyperZ (Bolzonella et al., 2011), which can estimate photometric redshifts of sources with optical and near-infrared photometry. The code fits a range of model galaxy spectra to the input galaxy photometry, selecting the best type of galaxy SED (choosing from four types of galaxy morphology) and shifting in redshift to find the best fit. The model galaxy SEDs can be seen in Figure 3.14. We run HyperZ on a sample of our possible lens galaxies, identified in the previous sections, and note how many of the VIKING counterparts are best fit by an elliptical galaxy SED. Full details on HyperZ can be found in Section 4.6 where we use it to a greater extent.

We begin by building a sample of possible lenses to run through HyperZ. We select Herschel galaxies, with reliable VIKING counterparts and reliable SDSS counterparts. This provides us with the five near-infrared VIKING photometric bands and four optical SDSS photometric bands: u, g, r and i. We refine this list down to only include Herschel sources with photometric redshifts, estimated from the Herschel fluxes, of  $z > 2.0$ . This should ensure we do not include Herschel galaxies where we have identified the true VIKING counterpart. We also ensure the Herschel galaxies have  $S/N_{350} > 10$ , to only include the most reliable Herschel redshifts. Our final sample consists of 47 galaxies which we run through HyperZ.

HyperZ fits three galaxy spectra types: Elliptical (E), Spiral (Scd and Sbc) and Irregular (Im). Of our 47 galaxies, we find that 2 of the VIKING galaxies are best fit with an Elliptical galaxy SED, 13 are best fit with a Spiral galaxy SED and 32 with an Irregular galaxy SED. If our lensing result is correct, we would expect the majority of our foreground galaxies to be best fit with the SEDs of elliptical galaxies, which are known to be the main morphology type of lensing galaxies. It is unclear why we find that the majority of foreground galaxies are irregular in morphology and so we cannot conclude anything from this analysis.

### 3.8 POSSIBLE SOURCES OF ERROR

Faced with the prospect of detecting a significantly high number of lenses over the Herschel ATLAS fields, many more than we would initially expect, we must consider the sources of error that may lead to this surprising result. There are two assumptions that we have made for this work that could have a big effect on our final results: is our assumed value of the depth of the VIKING survey correct and are our redshift values accurate?

Our assumption that the VIKING survey is not deep enough to see the high redshift Herschel ATLAS counterparts may be incorrect. The redshift distribution of Herschel ATLAS sources suggests that Herschel can see galaxies at greater redshifts than VIKING, based on its K-magnitude limit. However, it could be that our estimated photometric redshifts for our Herschel ATLAS sources are incorrect. If our redshifts are overestimated, then it follows that the Herschel ATLAS sources at high redshift with reliable VIKING counterparts are actually low redshift sources with reliable counterparts. To estimate the photometric redshifts, we follow the method

of Pearson et al. (2013), who fit a modified two component black body profile to measured Herschel ATLAS fluxes. Their analysis suggest that using this method to estimate the redshifts of high redshift sources is relatively accurate.

However, estimating redshifts using only the submillimetre fluxes is not ideal. Like all photometric redshifts methods, it relies on building model galaxy spectra which can be fit to the flux data points of galaxies. The method in Pearson et al. (2013) uses Herschel ATLAS galaxies of known spectroscopic to build a single spectra, that represents the average spectrum of Herschel galaxies. It is this average spectra which is fit to galaxies to estimate the photometric redshift. However, this makes a fundamental assumption that all Herschel galaxies and the properties of the dust in them are the same. It could be that the properties of dust vary with redshift, so using a single spectrum on all galaxies would be incorrect. It may also be that some of the galaxies are undergoing starburst phases or other extreme events that will significantly alter their spectra.

These factors contribute towards inaccuracies in estimating the redshifts using solely the submillimetre flux values. Our redshifts are only a problem if the higher redshift sources are incorrect, as it is these sources that give us the best evidence that there is a large population of lensed galaxies. However, Pearson et al. (2013) suggest that it is these high redshift sources that have the most accurate information. To confirm or disprove our gravitational lensing results, we further look in to the accuracy of this redshift estimation method in Chapter 4.

### 3.9 CONCLUSIONS

We studied a technique of estimating the number of gravitational lenses present in the Herschel ATLAS data using the results of our source matching technique in the previous chapter. The theoretical limit to how distant a galaxy can be detected with VIKING is around redshift  $z=1.5$ . We postulate that in any system where the Herschel ATLAS source that has a reliable counterpart and is further than redshift  $z \approx 1.5$ , the VIKING source must be lensing the distant Herschel source. We first plot histograms of the density of VIKING sources around all Herschel sources, split in to four redshift bins. We find that in each of the three GAMA fields, there still exists a significant population of Herschel ATLAS sources with redshift greater than 2.0, which have at least one nearby VIKING source. After removing the background level

of sources, this statement is still true, suggesting these Herschel ATLAS sources have nearby VIKING sources which are in some way physically related to the Herschel sources.

Using the value of  $Q_0$  from our likelihood ratio source matching, we can quantify the fraction of sources with an associated VIKING galaxy as a function of redshift. We find that approximately 44-55% of Herschel ATLAS galaxies between  $z=2-3$  have an associated VIKING source. Even for sources with redshift higher than 3.0, we find that between 30-41% of sources have an associated VIKING source. This is further confirmed when we tested the value of  $Q_0$  for only the sources with the most reliable photometric redshifts, and found values of  $Q_0$  between 0.25 and 0.68. These values suggest that a large fraction of the Herschel ATLAS sources could be lens systems, where we have identified the nearby lens in the near infrared VIKING catalogue.

We conclude that there are three possible explanations for this gravitational lensing result: (1) A significant fraction of high redshift Herschel sources in our catalogue are gravitationally lensed, (2) The VIKING survey can see much deeper than we first thought, causing us to detect the Herschel galaxies themselves, (3) Our estimated redshifts of the Herschel sources are incorrect and so many of the Herschel sources that we believe are at high redshift with counterparts are in fact at low redshift. We test this result and these three possibilities further in Chapter 4.

# 4

## Accurate optical identifications for Herschel ATLAS sources

*"For dust thou art, and unto dust shalt thou return."*

*– Genesis 3:19, The Bible*

### 4.1 INTRODUCTION

In Chapter 2 we matched two catalogues of near infrared VIKING and submillimetre Herschel ATLAS sources together, using the likelihood ratio technique. This produced a large catalogue of matched sources, which we used in Chapter 3 to identify a large sample of possible gravitational lenses using a new method. We also used this sample to study the accuracy of matching submillimetre sources to optical catalogues, finding that around 5% of optically matched sources may be incorrect. We will now try to improve upon our method of matching optical and submillimetre sources together and test how accurate our new source matching method is.

Far infrared and submillimetre surveys are cursed by inaccurate astrometry. The cause of this is down to two things: poor resolution and high source density. The large beam size of most far infrared telescopes causes low resolution, making it difficult to find accurate positions of sources. The large beam size combines with the high background source density to cause source confusion, often resulting in the sources blending together. As a result, it is very difficult to match far infrared catalogues to other wavelengths using a simple nearest neighbour method.

The solution to this is to use an intermediary step. The far infrared sources are first matched to a catalogue of radio sources, before being matched to other wavelengths. The more accurate positions of the radio sources can be assigned to the associated far-infrared sources, giving them accurate astrometry. It is favourable to match far infrared sources to radio catalogues for several reasons. The source density of radio surveys is typically lower than optical surveys. As a result, it is much easier to find the true radio counterparts to the far infrared sources than it is to find the optical counterpart, which will have a higher number of unrelated background sources. Another benefit is due to the far infrared-radio correlation, a fundamental relationship between the far infrared and radio emission of star forming galaxies (Ivison et al., 2010). Whilst not fully understood, the origin of this relationship is believed to be due to the lifetime of hot, young stars. These stars emit ultraviolet radiation during the lives, which is absorbed by dust in the interstellar medium and re-emitted in the far infrared. These same stars are very short lived and so quickly go supernova, releasing large amount of radio emission, mainly through synchrotron emission. Therefore, as long as the length of the star formation phase is longer than the lifetime of these stars, a strong correlation between far infrared and radio emission of these stars is observed. This relationship results in a very high fraction of far infrared galaxies having radio counterparts. To a lesser effect, it also allows us to include a brightness term in our source matching procedure, as the brightness of the radio and far infrared sources is strongly correlated, improving the reliability of matching sources together.

In this chapter, we find accurate and reliable optical counterparts to Herschel data, by utilising radio data as an intermediary step. This will provide a catalogue of Herschel sources with optical counterparts, which can be used to build SEDs of the Herschel galaxies. In turn, these SEDs can be used to estimate accurate photometric redshifts and estimate the properties of the galaxies through SED fitting. We use the likelihood ratio technique, outlined in Fleuren et al., 2012, Sutherland & Saunders, 1992 and in Section 2.3. This will create a large sample of deep data, with both optical and submillimetre photometry. We will use this catalogue to study the properties of the Herschel sources, to understand more about the properties of submillimetre selected galaxies. We will also study them in terms of the redshift-K magnitude diagram, which may give some indication of the size of the Herschel galaxies.

We showed in Chapter 2 that directly matching submillimetre and optical catalogues is not as reliable as matching to near infrared catalogues. A common technique to improve matching optical and submillimetre samples is to first match the submillimetre sources to radio sources, providing more accurate positions, before matching to the optical sources. We will test whether this method is more accurate by comparing it to the results of directly matching optical and submillimetre sources. We will evaluate those Herschel sources which are matched to different optical sources by the two methods to understand what may cause this difference.

In section 4.2 I introduce the data used in this chapter. In Section 4.3 I detail the method used to match sources together and in Section 4.4 I present the results of this source matching routine. In Section 4.5 I compare these source matching results to those found when directly matching Herschel sources to optical and near infrared catalogues. In Section 4.6 I test the accuracy of redshifts estimated from the Herschel fluxes alone, to test the reliability of our gravitational lensing result in Chapter 3. In Section 4.8 I study the K magnitude-redshift plot of our Herschel sources. The conclusions are presented in Section 4.9.

## 4.2 DATA

For information on the Herschel ATLAS survey and catalogue, please refer to Sections 1.8.1 and 2.2.

### 4.2.1 SUBARU DEEP FIELD (SDF) DATA

For information on the Subaru Deep Field survey, we refer the reader to Section 1.8.4.

### 4.2.2 VERY LARGE ARRAY (VLA) DATA

Supplementary data of a section of the North Galactic Pole (NGP) was obtained by Rob Ivison in the radio, using the Very Large Array (VLA). The VLA is a radio interferometer consisting of 27 radio antennas, each of 25 metres in diameter. We use a 1.4GHz map, approximately  $1.4 \text{ deg}^2$  in size, which was created using the VLA 'A' configuration. This map covers a fraction of the area covered by the Herschel ATLAS survey and fully covers the area covered by the SDF.

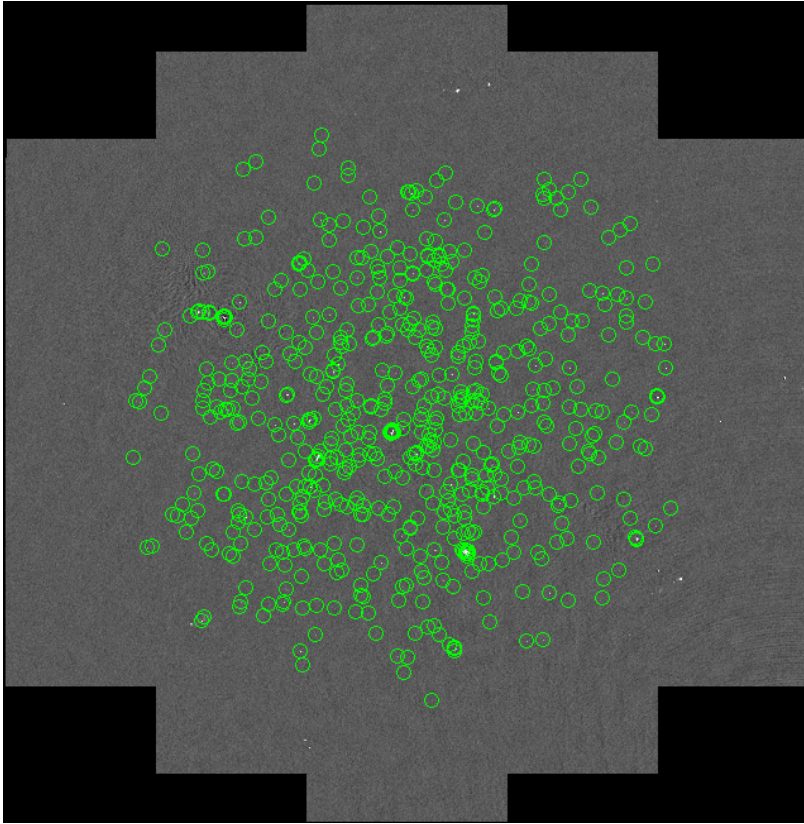


**Figure 4.1.** VLA map of the area covered by both the Herschel ATLAS and Subaru Deep Field surveys. Sources detected at 5 sigma are highlighted by green circles. Fewer sources are detected as a function of radius from the centre of the map, due to the decreasing sensitivity.

A feature of many large radio maps is a fall off in sensitivity as one moves further from the centre of the map. This is due to the primary beam, which offers high sensitivity at the centre but falls off as a Gaussian like profile towards the edges of the map. This results in a reduction of fainter source counts towards the edges, giving false statistics on the distribution of galaxies by brightness. This can be seen in Figure 4.1, where the number of sources detected decreases with increasing radius from the centre of the map. We only consider sources within 25 arcminutes of the centre of the map, which encapsulates all detected sources on the map. This reduced VLA field contains 602 detected sources in total.

### 4.3 MATCHING HERSCHEL AND SUBARU CATALOGUES

We need to match our catalogue of submillimetre Herschel sources to their optical/near infrared counterparts in the Subaru Deep Field. As discussed previously,

the large positional errors of submillimetre surveys makes it difficult to accurately match these sources to short wavelength catalogues. To solve this, we first match our Herschel sources to a catalogue of VLA radio sources to get accurate positions. We can then accurately match these sources to our optical and near infrared catalogue using a simple nearest neighbour method. Here I describe how to perform this source matching procedure.

### 4.3.1 MATCHING HERSCHEL ATLAS TO VLA

We begin by matching our Herschel ATLAS catalogue to the VLA radio sources. We use the likelihood ratio technique to match our radio and far infrared sources. This method is preferred to the simple nearest neighbour method for surveys with high background source densities, as it assigns reliabilities for each possible counterpart, allowing us to determine which if any is the true counterpart. A detailed description of this technique is given in Section 2.3 and we refer the reader to this for more information. We detail the significant changes to the likelihood method, due to the properties of the data we use, below.

The VLA radio observations suffer from varying sensitivity, depending on the angular distance from the centre of the map. This results in fainter objects, which would be detected in the centre of the primary beam, not being detected at the edge of the map. This would bias our  $q(\text{flux})$  and  $n(\text{flux})$  distributions and give us false probabilities for faint sources. To avoid this we build two separate distributions of  $q(\text{flux})$  and  $n(\text{flux})$  from our VLA sources: one distribution for bright sources ( $\text{Flux}_{\text{radio}} \geq 1000\text{mJy}$ ) and one for faint sources ( $\text{Flux}_{\text{radio}} < 1000\text{mJy}$ ). For our bright sources, we build the distributions from all the sources over the entire map. For the faint sources, the distribution is built from sources at the centre of the map, out to a radius corresponding to a flux sensitivity of 90% of the the maximum sensitivity. This high sensitivity region provides a significant number of sources in our sample whilst keeping the sensitivity above a reasonable value. The primary beam shape is assumed to be Gaussian, with a Full Width Half Maximum (FWHM) of the beam given by:

$$FWHM[\text{arcmin}] = \frac{45}{\text{Frequency}[\text{GHz}]} \quad (4.1)$$

and the formula for a Gaussian is given by:

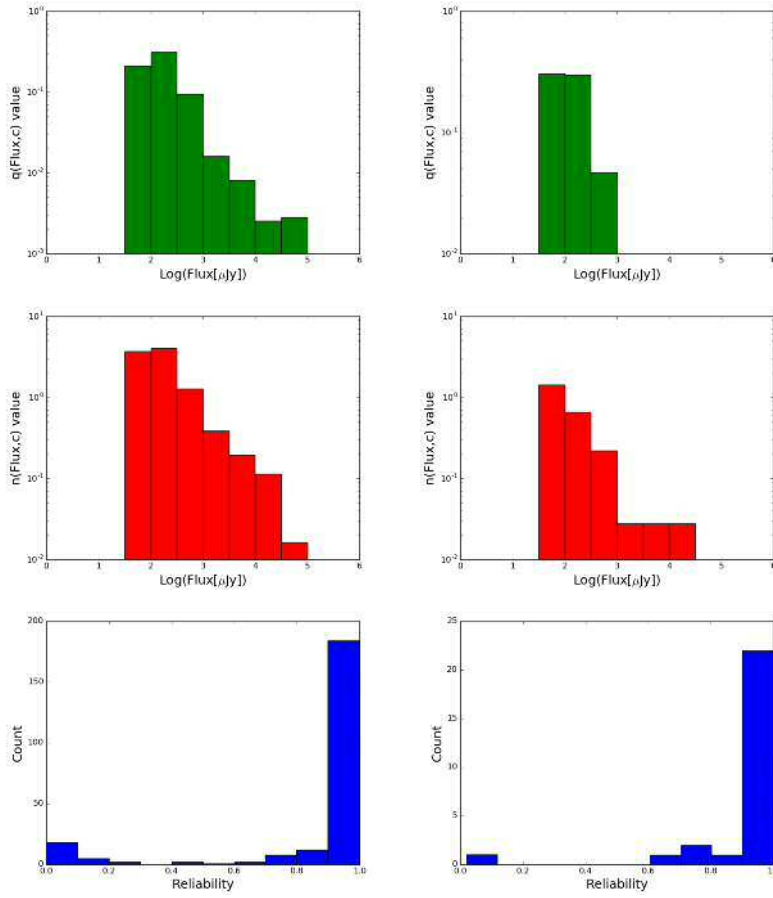


**Figure 4.2.** *Top row:* The  $q(\text{Flux}, c)$  distributions for all Herschel sources (left) and those in the more sensitive central area (right). *Middle row:* The  $n(\text{Flux}, c)$  distributions for all Herschel sources (left) and those in the more sensitive central area (right). *Bottom row:* The distribution of reliabilities for all Herschel sources (left) and those in the more sensitive central area (right).

$$\text{FluxSensitivity} = 0.9 = \exp\left[\frac{-r^2}{2\sigma^2}\right] \quad (4.2)$$

From this we are able to calculate the radius at which there is a drop in sensitivity down to 90% of the maximum. For the VLA data, this corresponds to a radius of 6.266 arcminutes. Within this radius, there are 39 Herschel ATLAS sources and 87 VLA sources. We build the  $q(\text{flux})$  distribution for the faint sources using these 39 Herschel ATLAS sources, following the method in Section 2.3.2. We similarly build the  $n(\text{flux})$  distribution for faint sources from these 87 VLA sources.

The distribution  $q(\text{flux})$  depends on the normalising factor,  $Q_0$ . This is an estimate of the probability of finding a counterpart to a Herschel ATLAS source

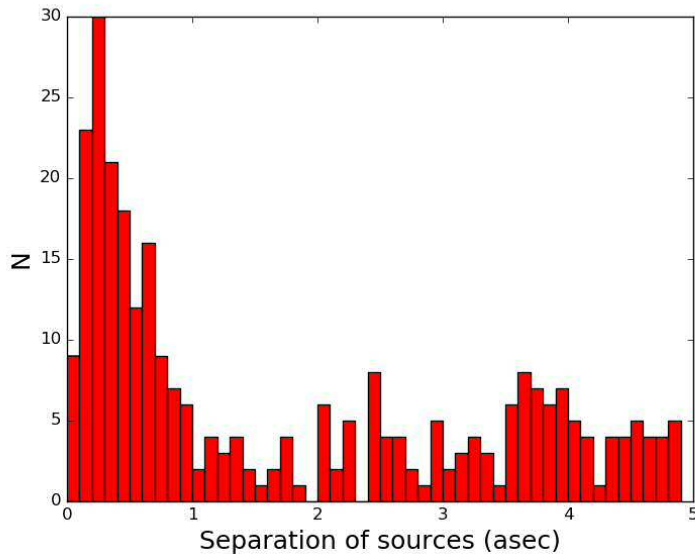


**Figure 4.3.** The distribution of separations of Herschel sources and SDF sources. The separation values are between the optical SDF positions and the radio VLA positions.

in the VLA survey, above the limiting survey flux and above the  $5\sigma$  survey limit, which corresponds to a flux density of  $\approx 50\mu\text{Jy}$ . We calculate the value of  $Q_0$  as done previously in Section 2.3.2. However, we must use a similar method of calculating  $Q_0$  from only the centre region of the map, as we did above for  $n(\text{flux},c)$  and  $q(\text{flux})$ . The value of  $Q_0$  is therefore calculated only from the sources around the centre of the VLA map, over which the sensitivity is 90% or higher. We cannot utilise the trick we used before for splitting sources into bright and faint ones as  $Q_0$  is not magnitude dependant and so would create a bias for the brighter sources. We derive a  $Q_0$  value of 0.645 over the centre of the map, a value which we use for all the sources. Finally, we estimate the reliability of each SDF source, following the method set out in Section 2.3.

#### 4.3.2 MATCHING HERSCHEL ATLAS TO SUBARU DEEP FIELD

The likelihood ratio method, as used to match Herschel ATLAS to VLA sources, is used when there may be some difficulty in identifying the correct counterparts, typically due to high background source density. Being able to include the flux of the source in addition to the separation of the sources provides more accurate matches. However, when both catalogues have accurate positions it is more

appropriate to use a simple nearest neighbour approach. This is the case when we want to match sources in our optical Subaru Deep field (SDF) catalogue and our Herschel ATLAS sources, which now have accurate VLA positions. When using the nearest neighbour method, the nearest SDF source to each Herschel ATLAS source is considered the most likely associated candidate. This is viable assuming the background density of SDF sources is relatively low, which reduces the chances of falsely associating to a random source, which is the case with our data.

The maximum search radius around each Herschel ATLAS source must be chosen to enclose a high fraction of true counterparts whilst keeping the number of background SDF sources to a minimum. Figure 4.3 shows the histogram of separations of SDF sources around all Herschel sources, out to 5 arcseconds. The drop in counts at  $r=1$  arcsecond suggests the majority of true identifications are within this radius and so we set this as our maximum search radius.

It is also possible that some apertures have multiple sources within them, which could be the result of one of several scenarios. It may be that these multiple counterparts consist of the true association and one background source. It may be that both sources are background sources, which whilst extremely unlikely is still possible. However, it may also be that the Herschel ATLAS source is in fact two interacting or merging systems. We study any cases of two or more sources within our search radius in detail to better understand what the cause of this is.

## 4.4 SOURCE MATCHING ANALYSIS

### 4.4.1 HERSCHEL ATLAS TO VLA MATCHING STATISTICS

Over the area covered by both the VLA and Herschel ATLAS, approximately  $0.34 \text{ deg}^2$ , there are 675 Herschel ATLAS sources and 602 VLA sources. Of our Herschel ATLAS sources, 243 have at least one nearby VLA source, with 196 of these being reliable matches (reliability  $> 0.8$ ). We therefore find that 29.0% of our Herschel ATLAS sources have a reliable nearby VLA counterpart.

The value of  $Q_0$  gives an estimate of the chance of finding a VLA source to a Herschel source above the survey sensitivity limit. In the central area, in which the sensitivity of the map is above 90%, we find a  $Q_0$  value of 0.645. This suggests that if we had similar sensitivity across the entire map, around two thirds of the Herschel

ATLAS sources would have a nearby VLA counterpart.

We follow the method used by Smith et al., 2011 to estimate the number of false ID's from the likelihood ratio method on the Herschel ATLAS and VLA data. We calculate:

$$N_{False} = \sum_{R \geq 0.8} (1 - R) \quad (4.3)$$

from which we expect 4.11 false identifications in our sample of 196 galaxies, corresponding to a contamination rate of 3.32%. For comparison, Bourne et al., 2016 find a contamination rate of 4.7% when directly matching Herschel ATLAS sources to SDSS counterparts over the three GAMA equatorial fields.

As part of our analysis we study those sources which are within the central region of our VLA map, where our sensitivity is above 90% of that at the centre. We find that 23 of the 39 Herschel sources in this area have reliable VLA counterparts. We expect a similar fraction of source across the field to have reliable radio counterparts. We can therefore predict that 59% of Herschel sources have a reliable radio counterpart above the 5 sigma limit, only slightly lower than our value of  $Q_0$  estimated over the entire field. The final source matching statistics can be found in Table 4.1.

#### 4.4.2 HERSCHEL ATLAS TO SDF MATCHING STATISTICS

There are 196 Herschel ATLAS sources which have previously been matched to VLA sources, but only 164 of these are in the area covered by the SDF map. The SDF catalogue contains 35,117 sources over the common area of the SDF and VLA maps. Of these 164 Herschel ATLAS sources, 149 have one nearby SDF counterpart and two Herschel ATLAS sources each have two nearby SDF sources. The final source matching statistics can be found in Table 4.1.

The two Herschel-VLA matched sources which have two possible SDF counterparts are of interest. The sources have the Herschel ID's HATLAS\_J132413.8+271934 and HATLAS\_J132459.2+272726. Figure 4.4 shows the SDF image of the two Herschel ATLAS sources with two possible associations. In both images it seems as if the SDF galaxies may in some way be physically connected to each other. We show the redshift and separation of the Subaru sources in Table 4.2. The redshifts of the

Sub-sample	Number
Herschel Sources (entire VLA field)	675
Herschel Sources (central VLA region)	39
VLA sources (entire VLA field)	602
VLA sources (central VLA region)	87
SDF sources	35,117
Herschel sources with nearby VLA source (entire region)	243
Herschel sources with reliable VLA source (entire region)	196
Herschel sources with nearby VLA source (central region)	26
Herschel sources with reliable VLA source (central region)	23
Herschel-VLA matched sources in SDF covered area	164
Herschel-VLA sources with one nearby SDF source	149
Herschel-VLA sources with two nearby SDF source	2

**Table 4.1.** Table of the source matching statistics when matching the Herschel and VLA catalogues together and then by matching this sample to the SDF catalogue.

	SDF Photometric Redshift	VLA-SDF separation (arcsec)
HATLAS_J132413.8+271934	2.26	0.849
	2.30	0.905
HATLAS_J132459.2+272726	1.485	0.223
	1.53	0.639

**Table 4.2.** Those Herschel sources with two possible SDF counterparts and their properties.

both pairs of SDF sources suggest that they are likely merging or interacting, based on their very similar redshifts. The benefit of using a nearest neighbour method over the more complex likelihood method is that mergers and interactions are much easier identified. As both sources are very close to the radio positions and of similar brightness, the likelihood method would allocate similar probabilities to both sources, causing both sources to be eliminated by our minimum reliability requirement. The nearest neighbour method, however, allows us to easily identify such systems and analyse them on a one-by-one basis, if desired.

A possibly interesting result is that of our 164 Herschel sources with a reliable VLA counterpart over the SDF area, 13 or 8% do not have any nearby K-band SDF

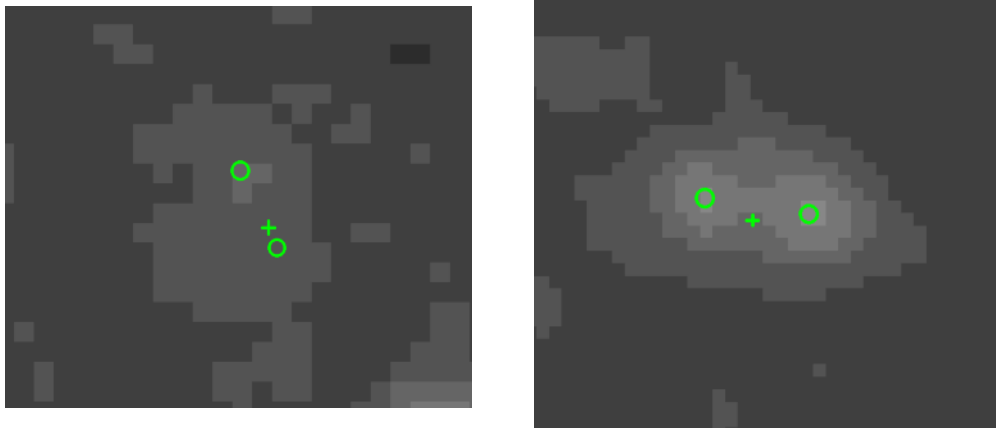


**Figure 4.4.** The two Herschel sources which have two nearby Subaru counterparts. We identify the two SDF counterparts with circles and the VLA position with a cross.

counterparts. This is likely because at high redshift, the K-band is observing the rest-band optical emission, which will be faint if these galaxies are dusty. These two effects will be the two likely causes for the missing infrared counterparts.

To estimate the number of false ID's using the nearest neighbour method we place a number of random apertures over the SDF image and count how many sources are detected in those apertures. To avoid small number statistics we place 1,000 apertures, detecting 28 sources inside the 1 arcsecond radius apertures. Normalising this then multiplying by our 149 apertures with at least one source inside, we get an estimated number of false identifications as 4 sources, or a false detection rate of 2.6%.

## 4.5 USING RADIO DATA AGAINST DIRECTLY MATCHING

So far we have discussed the need to use radio sources as a middleman when matching submillimetre and optical/near-infrared sources together. However, there currently aren't radio surveys covering all of the Herschel ATLAS fields at the depth needed to see the counterparts to the sources. As a result, Herschel ATLAS sources are normally directly matched to optical and near infrared catalogues, resulting in some of the issues discussed in our work in Chapter 3, Bourne et al. (2016) and Smith et al. (2011). As we have radio data, we are able to accurately find the true counterparts for a small sample of Herschel sources. We can also directly match this sample to our K-band selected Subaru Deep field sources, similarly to how we matched Herschel

and VISTA VIKING sources together in the previous chapter. Using these source matching results, we can determine how accurate our method of directly matching Herschel sources to near infrared catalogues is, compared to using radio data as an intermediary.

We perform the following steps to test our source matching methods:

1. Create a sample of SDF sources which are similar in properties to the VISTA VIKING catalogue, by only selecting SDF sources with a K-band magnitude less than the VIKING K-band limit.
2. Using the likelihood method, match this SDF sample to the Herschel ATLAS catalogue. This creates our **Herschel-SDF** sample.
3. Compare this sample to our previously created Herschel-VLA sample. We check how many of our Herschel-SDF galaxies are also present in the Herschel-VLA catalogue.
4. Compare this sample to our previously created Herschel-VLA-SDF sample. We check how many of our Herschel-SDF galaxies are present in the Herschel-VLA-SDF catalogue.
5. Finally, determine in how many cases are the Herschel sources matched to different SDF sources by the two different methods and what causes these discrepancies?

Here we go through each of these steps in more detail. We begin by creating a catalogue from our SDF sources which mimics the VISTA VIKING survey. This enables us to directly compare our results to those found in Chapter 3. Because the SDF survey is deeper than VIKING, we remove any SDF sources from the catalogue with an AB K-magnitude greater than the  $K=20.4$ , the VIKING survey completeness limit. This leaves us with a catalogue of 2,473 SDF sources. We match our Herschel ATLAS catalogue to this SDF sample using the likelihood ratio method, which is the same method we used to match the Herschel ATLAS and VISTA VIKING catalogues together in Section 2.3. We find that 142 of our Herschel sources have a reliable SDF counterpart, resulting in reliable matches for 36.0% of Herschel sources. We refer to this sample of 142 reliably matched sources as the 'Herschel-SDF' sample.

The next step is to find how many of our Herschel-SDF sources have reliable radio counterparts. We compare our sample of Herschel-VLA matched sources from Section 4.3.1, consisting of 196 sources, to our Herschel-SDF catalogue. Of our 142 sources in the Herschel-SDF sample, 68 are also present in the Herschel-VLA matched sample, resulting in 47.9% of the Herschel-SDF sources having a reliable radio counterpart. This means that over half of our Herschel-SDF sample do not have a reliable radio counterpart. This is comparable to our previous result in matching Herschel and VLA sources together, which found that in the central, most sensitive area of the VLA map, 59% of Herschel sources have a reliable radio counterpart. Some of our Herschel-SDF sources will not have a radio counterpart due to decreased sensitivity towards the outer edge of the VLA map, which likely explains our decrease in the number of reliable matches. The fraction of sources with a radio counterpart is not something we are interested in for this work, but we include it here for reference.

Next, we want to find how many of our Herschel sources in the Herschel-SDF sample also have a SDF counterpart in the Herschel-VLA-SDF sample. Our Herschel-VLA-SDF sample, where we have excluded all SDF sources with a K-band magnitude  $K > 20.4$ , contains 70 sources. Of the 68 Herschel-SDF sources that we previously found that also exist in the Herschel-VLA-SDF sample, and 70 Herschel-VLA-SDF sources, there are 53 sources that are common in both catalogues. This means that in 78.0% of cases where we directly match the Herschel sources to the SDF catalogue, we are correctly identifying that there is a reliable nearby counterpart, as found in our Herschel-VLA-SDF sample. The 15 Herschel-SDF sources without a match in the Herschel-VIKING-SDF catalogue are likely to be incorrect matches, as they are not found in our reliable sample of Herschel-VIKING-SDF sources.

Our final check is to see how many of these 53 sources are matched to the same SDF source and how many are matched to different ones. This statistic will tell us how accurate source matching Herschel catalogues directly to optical or near infrared surveys is. Of the reliable matches from both methods, we check which SDF sources are the same. We find that of the 53 sources present in both the Herschel-SDF and Herschel-VLA-SDF catalogues, 50 have the same SDF source. This means that in 3 cases, or 5.67%, we are associating a different SDF source to a Herschel source when we match optical catalogues directly to Herschel catalogues and when we use radio data as an intermediate step. The final source matching statistics can be seen in

Field	Number of Sources
Number of Herschel Sources	394
Number of SDF sources	2473
Herschel-SDF matched sources	142
Herschel-SDF sources with a VLA counterpart	68
Herschel-SDF with VLA counterpart which itself has a SDF counterpart	53
Both SDF sources are the same	50

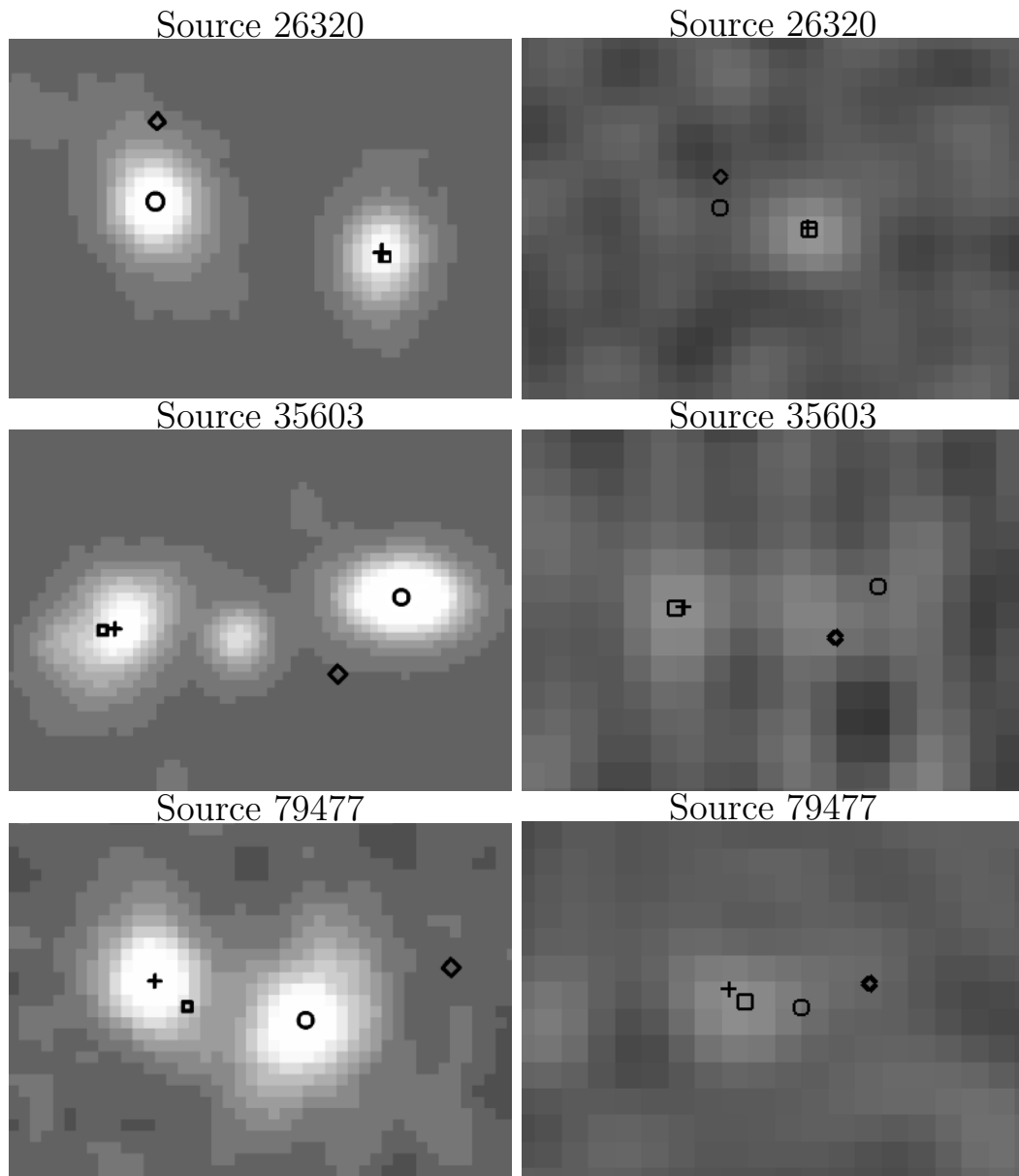
**Table 4.3.** The statistics of matching a sample of Herschel sources to the Subaru Deep Field catalogue. We compare the results of two methods: directly matching the two catalogues and using an intermediate step of first matching to a radio catalogue to get improved positions for our Herschel sources.

Table 4.3.

We study these 3 cases in more detail, to understand what causes this discrepancy in source matching. In Figure 4.5 we show SDF and VLA cutout images of the 3 sources. On each image we show the positions of the Herschel source, the position of the most reliable VLA radio source and the positions of the two different SDF sources. We have labelled each image with the Herschel source number.

**Source 26320 - Incorrect Match** - In this situation, there are two nearby SDF galaxies. There is only one nearby apparent radio galaxy, which is at the same position as the SDF source which we reliably match to in our Herschel-VLA-SDF sample. The Herschel-SDF matched source is much closer to the Herschel position, so it is no surprise that we match to this SDF source, instead of the one we match to our VLA source. The photometric redshift of the Herschel-SDF source is  $z = 0.51$ , derived from the SDF photometry, whilst the redshift of the Herschel-VLA-SDF source is  $z = 0.69$ . This makes it unlikely that these two sources are interacting or merging, but are coincidentally near each other on the sky. The reliability of the SDF source which we identify in our Herschel-VLA-SDF method, as measured in our Herschel-SDF method, is 0.05638, whilst the Herschel-SDF match has a reliability of 0.91966, making it the clear best match via this method. In this situation, we must conclude that, assuming that the radio source is the true counterpart, then directly matching to the SDF source results in an incorrect match.

**Source 35603 - Merger system** - In the SDF image, we see there are three



**Figure 4.5.** *Left:* Subaru Deep Field images showing those Herschel galaxies where the most likely SDF source is different in our two source matching methods. *Right:* VLA images of the same sources. Diamonds indicate the positions of the Herschel ATLAS sources, squares are the reliable VLA positions, crosses show the SDF source when first matched to a radio source and circles indicate the SDF source when we match Herschel ATLAS directly to Subaru.

close optical sources. The two SDF sources that we match to are the two similar sources at the far left and right of the image. Inspecting the VLA image, we see that the SDF source which we match to in our Herschel-VLA-SDF sample is at the same position as the VLA source, making this a likely correct match. On the other hand, the SDF source we match to in our Herschel-SDF sample is much closer to the Herschel position. The two possible SDF sources both have photometric redshifts of 0.365, making it very likely that they are in some way interacting or merging. The third SDF source, which lies in between the other two, is at redshift 0.355, making it also likely to be part of this merger or interaction. We therefore put this case down as a merger system, which is likely the cause of the disparity in our source matching technique.

**Source 79477 - Merger System** - There are two close optical sources, which are each identified as the possible SDF source by the two methods. The Herschel position lies offset to both sources, but is significantly closer to the position of the Herschel-SDF position, which is likely why the direct method matched to a different SDF source. There is a bright radio source at the Herschel-VLA-SDF position, but no apparent radio source near the Herschel-SDF position. The sources both lie between redshifts 0.71-0.75, which along with a seemingly bright region between the two sources in the optical image, suggest the galaxies might be merging or interacting. The reliability of the SDF source which we identify in our Herschel-VLA-SDF method, as measured in our Herschel-SDF method, is 0.14005, whilst the Herschel-SDF match has a reliability of 0.82753, making it the clear favourite, though only just above the *Reliability* > 0.8 limit we impose. We therefore conclude that this case is probably a merging/interacting system, which is the cause of our different source matching.

Our analysis above identifies 2 merger or interacting systems and 1 incorrect matching results by the Herschel-SDF method. Therefore, only 1 of the cases is due to incorrect matching between the Herschel and SDF catalogues, where there is no easy way to identify that the sources matches might be incorrect, such as the case with merger systems. This suggests that only 1.89% of source matches are incorrect when we directly match Herschel and near-infrared sources, due to reasons that we cannot control. A further 3.77% are false due to merger systems, which if we cannot identify will cause a significant increase in our rate of false ID's. This results in a total incorrect ID rate of 5.66%.

In Smith et al., 2011 they derive the fraction of optical SDSS to Herschel false ID's. They estimate that 4.2% of their source matches are incorrect, similar to the false-ID rate that we estimate above. For comparison, we can also estimate the false ID rate following the method of Smith et al., 2011 to estimate the number of false ID's from our direct Herschel-SDF source matching. We calculate:

$$N_{False} = \sum_{R \geq 0.8} (1 - R) \quad (4.4)$$

from which we expect 3.811 false identification, or 6.35%. This is a slightly larger false ID rate than that estimated by us and Smith et al., 2011, but is less than one source within our estimates.

We can see that merging or interacting systems cause problems for the likelihood method. 3.77% (2/53) of our direct Herschel-SDF matches are incorrect due to identifying the wrong source in a merging system. We discussed in the previous chapter the problems with merger systems and the likelihood ratio method, where the reliabilities of both sources may be less than the required 0.8, resulting in neither source being reliably matched. However, we can also see that the opposite occurs, where we reliably match to the incorrect source in the merging/interacting pair. From our analysis above, it is clear that when matching submillimetre to optical or near infrared catalogues that it is beneficial to match to radio sources as an intermediary. If the radio identifications are correct, then 5.66% of ID's are incorrect when matching submillimetre and optical directly, due a mix of incorrect matching and merger systems. We conclude that using radio data as an intermediary in matching submillimetre and optical significantly improves the accuracy of the identifications, yet the current lack of deep radio coverage of the Herschel fields means that this is not always possible at this time.

## 4.6 TESTING OUR PHOTOMETRIC REDSHIFTS WITH HYPERZ

Part of this work is to test the results found in Chapter 3. To summarise, we took sources in the Herschel ATLAS and VISTA VIKING surveys, which were matched together, over the three GAMA fields. We found that a significant number of the Herschel ATLAS sources, with estimated photometric redshifts up to  $z=3$ , had

reliable VIKING counterparts. This is surprising as it was thought that VIKING was not deep enough to see galaxies out to such high redshifts. One solution to this problem would be if these sources are actually gravitational lens systems, where the VIKING counterparts we are finding are in fact lensing the distant Herschel sources. However, this would indicate that a significant fraction of Herschel ATLAS sources are lensed, much more than expected.

We concluded this previous work by proposing three scenarios: 1) that a high fraction of Herschel ATLAS could indeed be lensed; 2) that our estimated redshifts of the Herschel ATLAS sources could be wrong; 3) that VISTA VIKING could be deeper than we expect and so we are in fact detecting the real counterparts. With the Subaru Deep Field data we can now detect the reliable, high redshift counterparts to a sample of Herschel ATLAS sources. The Subaru data provides us with optical photometry of our Herschel sample. Photometric redshifts are typically estimated by fitting model SED's to the observed photometry of sources. The key to finding accurate redshifts with this method is to therefore have a combination of many data points to fit the models to and to have data points around distinct features in galaxy SED's. The Lyman break is one such feature. The absorption of the photons with wavelengths shorter than  $912\text{\AA}$  by neutral Hydrogen causes a sharp and steep drop in the SED of a galaxy.

With this sample of SDF matched Herschel sources we can do two things: 1) test the accuracy of our method to estimate redshifts for Herschel sources using their submillimetre fluxes; 2) get a better estimate on how deep VIKING can observe. By doing this, we can try to determine which of the three scenarios is true for our previous work.

#### 4.6.1 HYPERZ

To estimate redshifts using optical and near infrared photometry, we use the public code HyperZ (Bolzonella et al., 2011). HyperZ is a SED fitting routine, within the wavelength range of  $91\text{\AA}$  to  $9.74\text{mm}$ . A catalogue of template SED's are individually fit to the observed photometry of each galaxy; each template is adjusted in amplitude and redshift to find the best fit. The best fitting template is determined by a simple chi squared calculation:

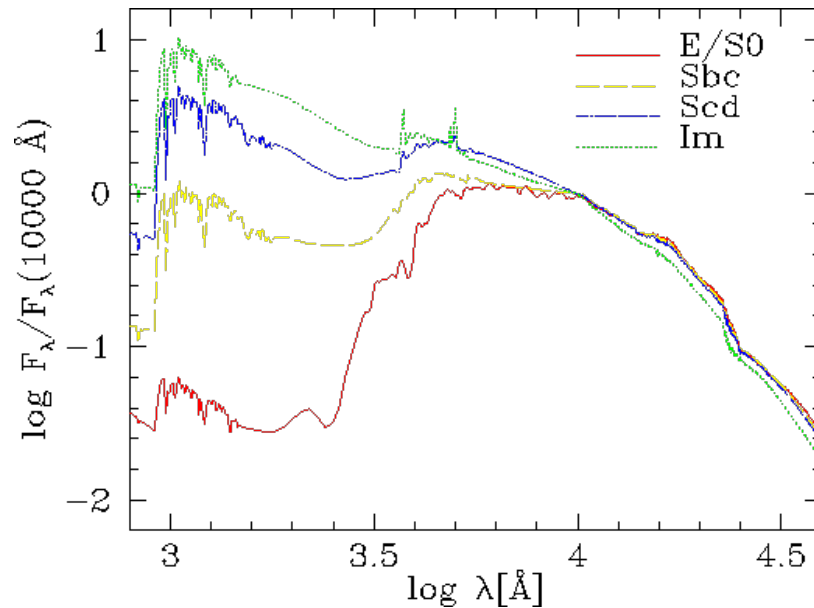


**Figure 4.6.** The mean spectra of local galaxies, as created by Coleman et al., 1980, which are used by HyperZ to estimate the photometric redshifts of galaxies. This figure is from Bolzonella et al., 2011

$$\chi^2 = \sum_{i=1}^{N_{Filters}} \left[ \frac{F_{obs,i} - F_{temp,i}(z)}{\sigma_i} \right]^2 \quad (4.5)$$

where  $F_{obs,i}$ ,  $F_{temp,i}$  and  $\sigma_i$  are the observed flux, template flux and their uncertainty respectively, in each filter  $i$ .

By default, HyperZ uses two sets of spectra. It uses the mean spectra of local galaxies from Coleman et al., 1980. These four template SED's, plotted in Figure 4.6, are the mean spectra for local E, Sbc, Scd and Im galaxies. It also uses the GISSSEL98 (Galaxy Isochrone Synthesis Spectral Evolution Library) spectra of Bruzual A. & Charlot, 1993. These galaxies are simulated from a number of simulated samples of stars that follow stellar tracks, which when combined with initial mass functions and star formation rates, provide a simulated galaxy SED. A Miller & Scalo, 1979 IMF is used. The star formation rates depend on the morphology of the galaxy SED type: a burst-like star formation model is applied to starburst galaxies; exponential models are applied to elliptical and spiral galaxies, with varying timescales; and a constant star formation rate model is applied to irregular galaxy models.

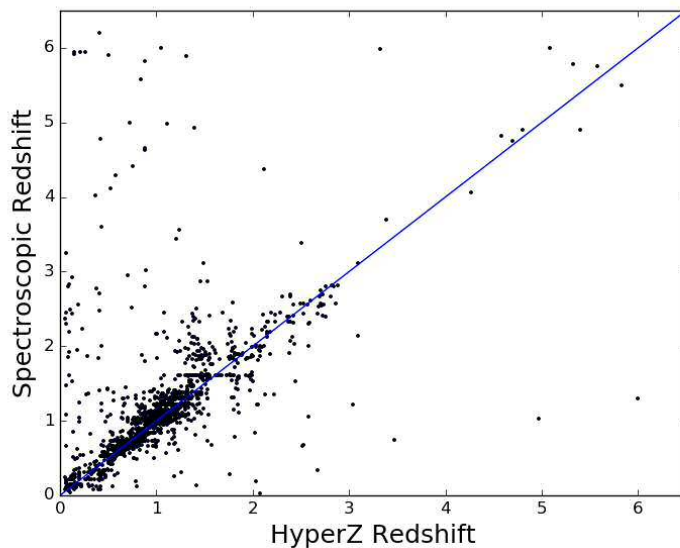


**Figure 4.7.** Comparison of the photometric HyperZ redshifts and spectroscopic redshifts for a sample of CANDELS galaxies. The blue line indicates a line of gradient unity.

#### 4.6.2 TESTING THE ACCURACY OF HYPERZ

We base our analysis on the assumption that the HyperZ estimated redshifts are accurate, allowing us to measure and compare the accuracy of the Herschel photometry estimated redshifts. To test this assumption, we use a sample of galaxies from the HST CANDELS survey which have been run through HyperZ. These galaxies span a wide range of redshifts, out to  $z \approx 6$ , providing a good representative sample to test the accuracy of HyperZ. This sample consist of 34,930 galaxies. The HyperZ redshifts have been estimated from the filters: U CTIO (3570Å), HST WFC F606W (6000Å), HST WFC F814W (8210Å), HST F125W (12516Å) and HST F160W (15392Å).

A fraction of these sources also have spectroscopic redshifts, which we use to judge the accuracy of the HyperZ method. These redshifts come from the Chandra Deep Field South (CDFS) spectroscopic redshift catalogue, a collection of spectroscopic redshift samples over the CDFS. This catalogue consists of 10,354 sources with spectroscopic redshifts. We match these two catalogues together to produce a catalogue of sources with photometric HyperZ redshifts and spectroscopic redshifts. We remove those sources with erroneous and missing redshifts by either method. This results in a final catalogue of 1,463 sources.

We show a plot of the comparison of the two redshifts in Figure 4.7. As

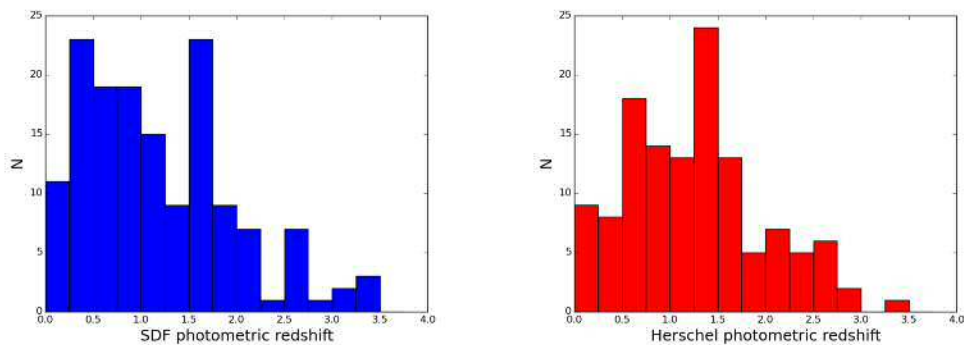


**Figure 4.8.** Redshift histograms of our SDF matched Herschel sources. The plot on the left is the redshifts estimated using the Subaru photometry and the plot on the right is from using the Herschel photometry.

can be seen, over all redshifts there is a relatively good correlation between redshifts estimated by both methods. There is scatter on the plot, mainly at high spectroscopic redshifts but low HyperZ redshifts. This suggests that HyperZ sometimes estimates sources to be at lower redshifts than they have in reality. We measure the Spearman rank coefficient of 0.714 and a dispersion standard deviation of 1.12 about the line of unity. We conclude that our redshifts estimated using HYPERZ are relatively accurate, based on the strong correlation seen in Figure 4.7, though a number of incorrect fits are expected.

### 4.6.3 REDSHIFT FITTING RESULTS

We estimate the photometric redshifts of our Herschel sources that have been matched first to radio sources in the VLA catalogue, then to optical sources in the Subaru Deep Field. This Herschel-VLA-SDF sample consists of 166 sources. We begin by estimating the photometric redshifts of these sources from the Herschel fluxes alone, following the method laid out in Section 3.2.1. In brief, we generate a template SED from a sample of Herschel galaxies with spectroscopic redshifts (Pearson et al., 2013). This template is then fit to our galaxies of unknown redshifts, shifting the template in redshift until the best fit is found. It is the accuracy of this redshift estimation method that we are trying to test.

We use HyperZ to estimate the photometric redshifts from the optical and near infrared photometry of the same 166 sources. We fit templates to the optical B, V, R, i and z photometry and the near infrared J and K bands. Of the 166 sources,

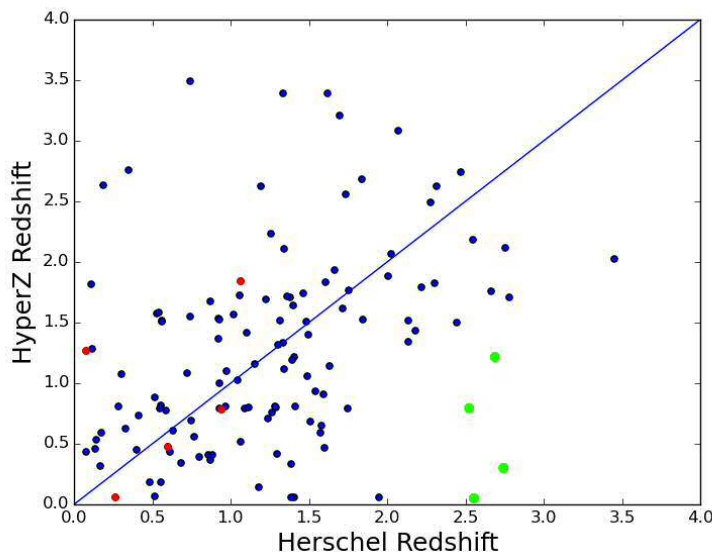


**Figure 4.9.** A plot of the SDF photometric redshifts against the Herschel photometric redshifts, of our SDF matched Herschel matched sources. The blue line indicates a gradient of unity. The red points are those sources who have  $F_{350}/E_{350} > 10$ . Green points indicate our sample of possible lenses, as studied in Section 4.7.

HyperZ is able to determine redshifts for 127 of them, all of which we include in our analysis. The photometric redshift distribution of our sample, estimated from the SDF data, can be seen in Figure 4.8, alongside the distribution of redshifts of the same sample estimated from the Herschel fluxes. We derive similar distributions from both methods, though it appears the peak of the distribution of redshifts estimated from the Herschel fluxes is offset towards a higher value. This may be an indication that we are overestimating the redshifts when calculated from the Herschel fluxes, implying that the sources may actually be the true counterparts at low redshift.

To test the accuracy of our Herschel photometric redshifts, we plot the Herschel photometric redshifts against the SDF HyperZ redshifts in Figure 4.9. The significant scatter on the plot suggests that the redshifts estimated from the Herschel fluxes alone are inaccurate. There is some indication that there is a weak correlation between the redshifts of both methods, confirmed by a Spearman rank correlation coefficient of 0.365; however, it is clear from this plot that we cannot consider our Herschel estimated redshifts as accurate.

This analysis brings our gravitational lensing result from Chapter 3 in to question. From Figure 4.9 we can see that there is a poor correlation between our redshift

Source ID	$z_{Herschel}$	$z_{SDFredshift}$	$F_{350}/E_{350}$	Negrello counterpart	SDF morphology
30072	2.745	0.3	7.86	No	Im
79063	2.558	0.05	8.18	No	Im
157887	2.688	1.22	5.84	No	S
209793	2.52	0.795	3.53	No	Im

**Table 4.4.** Table of our possible lenses, identified from Figure 4.9.

values estimated from the Herschel fluxes alone and from the SDF optical fluxes. This raises questions about our earlier gravitational lensing result, as incorrect redshift values may indicate that we are detecting the true counterparts to the VIKING sources, rather than gravitational lensing systems. We tested this result previously by only including those Herschel sources with a flux to error ratio at  $350\mu\text{m}$  of  $F_{350}/E_{350} > 10.0$ , whose redshifts are expected to be more accurate due to having more reliable flux values. We test this by highlighting in red all of the sources in our SDF sample which obey this condition in Figure 4.9. They have a Spearman rank correlation coefficient of 0.400, not significantly greater than when we include all sources. It is difficult to conclude anything for certain with 5 sources, but there is no obvious evidence that the higher signal to noise sources have more accurate redshifts.

We must conclude from this that it is not clear whether the gravitational result from Chapter 3, that a significant fraction of high redshift Herschel sources are lensed, is correct. Whilst our work does agree with other studies who predict such a significant fraction of Herschel should be lensed, our estimates of the redshifts of the Herschel sources are relatively unreliable, as seen from the work in this chapter. If a significant fraction of the Herschel sources which we estimate to be at high redshift in Chapter 3 are in fact at low redshift, then any VIKING counterparts are probably simply us observing the actual Herschel source with VIKING.

## 4.7 POSSIBLE LENSES IN THE SUBARU DEEP FIELD

In Figure 4.9 we showed the photometric redshift values, of a number of Herschel sources, estimated by two different methods: redshifts estimated from the Herschel photometry and redshifts estimated from the optical and near-infrared SDF

photometry. Inaccuracies in our Herschel estimated redshifts causes significant scatter in the plot. However, it may be that some of the outliers in our plot are in fact evidence of gravitational lensing. In gravitational lensing systems, a foreground mass magnifies the image of a background source. This foreground mass is often a massive early type galaxy. These galaxies consist of older stellar populations, making them appear bright in the near infrared, but faint in the submillimetre due to their low dust content. On the other hand, the distant lensed galaxies are dusty, making them bright in the far infrared, but the K-band at high redshifts traces the optical or UV, which is absorbed by dust. Therefore, we may detect the lensing galaxy in the SDF survey and the lensed galaxy in our Herschel ATLAS sample.

We investigate those sources which we observe to have low redshifts estimated from their SDF photometry and high redshifts estimated from their Herschel photometry. These are candidates for gravitational lensing systems in our data. We begin by selecting those galaxies with a minimum Herschel estimated redshift. Lensed galaxies must be at a high enough redshift to be lensed by a foreground galaxy. The method of estimating redshifts from the Herschel photometry increases in accuracy with increasing redshift, as described in Pearson et al., 2013. It is for these reasons that we only study those galaxies with a minimum Herschel estimated redshift of  $z = 2$ . We select those sources with SDF redshifts less than  $0.5 \times z_{Herschel}$ . We base this on the gravitational lens sample in Negrello et al. (2017), where the maximum ratio between the SDF and Herschel photometric redshifts is 0.446. This highlights four galaxies as possible gravitational lenses, denoted on Figure 4.9 as green points. We list these sources and their properties in Table 4.4.

We begin by checking the value of  $S/N_{350}$ . Sources with low  $S/N_{350}$  values have less reliable photometric redshifts, due to less certain flux values. One of our sources has a value  $S/N_{350}$  less than 5, which may be considered unreliable; however, the other three sources have relatively large values and are at redshift  $z > 2$ , increasing the reliability of the redshift estimates.

Next, we check whether any of our possible lenses have been confirmed as lenses in other works. In Negrello et al., 2017, we identified a sample of lenses in the NGP Herschel ATLAS field, consisting of 24 sources. These sources were selected as having 500 micron fluxes greater than 100mJy. We match this catalogue to our possible lenses, but find no matches - the cause of this due to none of our possible

lenses exhibiting a  $500\mu\text{m}$  flux above 100mJy.

To test whether these are lensing systems, we can study the optically identified galaxy, which we assume to be the lensing galaxy. As stated above, these are expected to be massive early type galaxies, with bright k-band emission and low submillimetre dust emission. If they are lensing the Herschel galaxies, we would therefore expect their morphologies to be elliptical in nature. We study the morphology of the best fit SED from our HyperZ redshift estimation of the four galaxies. We find that three of our galaxies were best fit by the SED of an irregular galaxy, whilst one was best fit with the profile of a spiral galaxy. This gives no indication that the SDF galaxies are foreground, early type lensing galaxies. However, we did use this method in Section 3.7, for a sample of known and possible lenses, and got a similarly negative result, suggesting that studying the morphology of the template fit to galaxies using HyperZ is not reliable.

We conclude that there is no evidence that any of these galaxies are indeed lenses. The foreground galaxies show no signs of being typical lensing galaxies and the sources have not been identified as lenses in other literature. Further observations to provide spectroscopic redshifts for the Herschel sources would clarify this result, but we must instead conclude that there is no evidence that any of these galaxies are gravitationally lensed.

## 4.8 K-MAGNITUDE REDSHIFT RELATION

The K-band magnitude and redshift relation (henceforth referred to as the K-z relation) is a strong correlation between the K band magnitude of radio galaxies and their redshift. It is the result of the small range of absolute magnitudes of radio galaxies. This relationship has been studied before in detail with many samples of radio galaxies (Longair & Lilly, 1984, Eales et al., 1997), but we can now explore where our VLA matched Herschel sources lie on this plot. This will allow us to indicate the highest redshift sources that the VIKING survey can observe, which may provide answers to our gravitational lensing result in the previous chapter. The plot will also give us some information on the Herschel galaxies. Their position on the plot and their distribution can give some indication of how homogeneous the galaxies are and how large they are compared to other galaxy samples.

Figure 4.10 shows the positions of our 149 Herschel ATLAS sources, with SDF

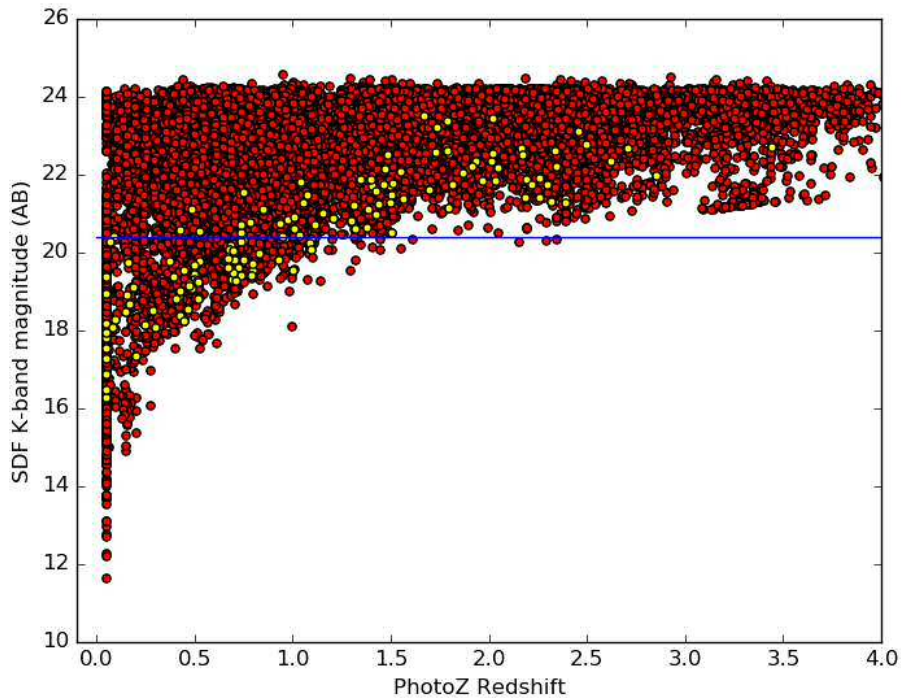


**Figure 4.10.** A plot of the K-magnitude against the redshift of our SDF matched Herschel ATLAS galaxies, shown in yellow. The red points are every other galaxy in the Subaru Deep field. The blue line indicates the completeness limit of the VISTA VIKING survey at a K-magnitude of 20.4. All magnitudes are AB magnitudes.

counterparts, on a K-z relation plot. We also plot the positions of **all** the Subaru sources. We can see from the plot that the Herschel matched sources are some of the brightest sources in the K-band at any given redshift, suggesting that the Herschel galaxies in our sample are some of the highest stellar mass galaxies. They also form a relatively tight correlation, indicating that there is not a wide range of stellar masses of Herschel galaxies. The dispersion of our galaxies is equal to 0.81 magnitudes when we consider the entire redshift range. This is comparable to the dispersion of radio galaxies found by other authors, such as a standard deviation of 0.5 found by Longair & Lilly, 1984. This distribution of galaxies on the K-z diagram paints a picture of Herschel galaxies being a rather homogeneous population of some of the most massive galaxies in the universe.

We have plotted the VISTA VIKING K-band limit on the plot. From this plot we can estimate that VIKING can see galaxies to around  $z \simeq 1.25$ . In Chapter 3 we

predicted that VIKING would not be able to see the real counterparts of high redshift Herschel galaxies, based on initial predictions on the depth of the VIKING survey. This result shows that our assumption was correct, with the VIKING survey only being able to see the true counterparts to Herschel sources out to around  $z \simeq 1.25$ ; any matched sources above this limit are likely to be lens systems. However, in Section 4.6 we showed that the photometric redshifts estimated from the Herschel photometry are relatively inaccurate. It is therefore unclear as to whether the gravitational lensing result we find is correct, as we are left with the two possibilities that either we are detecting a large fraction of gravitational lenses or that our redshifts are incorrect.

## 4.9 CONCLUSIONS

The key aim of this work is to find accurate optical and near infrared counterparts for Herschel ATLAS sources for the first time. We utilised a small area of sky at the north galactic pole which has been covered by surveys using Herschel the VLA and the Subaru telescope. We utilised the technique of first matching our submillimetre Herschel sources to the radio VLA catalogue, providing us with accurate positions for the Herschel catalogue. The matching procedure was performed using the likelihood ratio technique, finding that 29% of our Herschel sources have a reliable VLA radio counterpart. We then matched these Herschel sources, with radio counterparts, to the optical Subaru Deep Field catalogue. Of the Herschel-VLA matched sources, we find that 92% have at least one reliable optical counterpart.

We then tested the accuracy of matching far infrared sources directly to optical or near infrared sources. This is a common practice when an intermediate data set, such as our radio VLA sources, is not available. We directly match our Herschel ATLAS sample to the Subaru deep field catalogue and compare the source matching results to our previous result when we take the intermediary step of matching to radio sources. We find that 142 of our Herschel ATLAS sources have a reliable Subaru Deep Field counterpart, compared to 149 when utilising the radio positions. Of these, 53 sources are common in both samples, with 50 of these Herschel sources having the same reliable Subaru source. The remaining 3 Herschel sources identify different SDF sources as their reliable counterparts. Two of these incorrect identifications are identified as likely mergers or interactions, whilst one is simply an incorrect identification. This suggests that 5.66% of Herschel sources may have incorrect counterparts when

matched directly to optical or near-infrared catalogues, agreeing with the false ID rate found by other works.

We test the surprising result in Chapter 3 where we found that a significant fraction of Herschel sources are gravitational lenses. We postulated that if our Herschel photometric redshifts were incorrect then this result would be false. To test this we estimated the photometric redshifts of a sample of Herschel galaxies, both from the Herschel fluxes alone and from the optical and near-infrared photometry. We found that the redshifts from both methods agreed little, suggesting that our Herschel estimated redshifts may not be reliable.

Finally we study the K magnitude-redshift diagram for our sample of Herschel sources. We find that the Herschel galaxies have some of the brightest K band magnitudes at any redshift, indicating they have some of the biggest stellar populations. The tightness of the distribution of magnitudes also suggests that Herschel galaxies are all very similar.

We estimate that the VIKING survey can only detect sources out to  $z \simeq 1.25$  and so it would not be able to detect the true counterparts to high redshift Herschel sources. It is unclear whether the gravitational lensing result from Chapter 3 is correct or not, as it is not clear how reliable our Herschel photometric redshifts are. In the Chapter 3 we stated three possibilities of the cause of this surprising gravitational lensing result: (1) A significant fraction of high redshift Herschel sources in our catalogue are gravitationally lensed; (2) The VIKING survey can see much deeper than we first thought, causing us to detect the Herschel galaxies themselves; (3) Our estimated redshifts of the Herschel sources are incorrect, so many of the Herschel sources that we believe are at high redshift with counterparts are in fact at low redshift. Our K magnitude-redshift diagram disproves point 2, as we can see that the VIKING survey can only see sources out to redshift  $z \simeq 1.25$ . Our analysis of the Herschel photometric redshifts suggest that point 3 may be correct and that our redshifts may be inaccurate; however, we cannot prove this conclusively. We must therefore conclude that either a significant fraction of high redshift Herschel sources are lensed, our estimated Herschel photometric redshifts are incorrect, or some combination of both scenarios.

We now have a catalogue of around 150 Herschel sources with optical SDF counterparts, out to redshift  $z \approx 4$ , which cover a wide period of galaxy evolution.

---

We would now like to study these sources in detail to better understand them and submillimetre galaxies over this period of time in general. Having both submillimetre and optical photometry allows us to accurately estimate the properties of these galaxies, including the star formation rate, stellar mass and dust mass. In the next chapter, we will estimate these properties using the public code MAGPHYS. We will study whether these galaxies are different from optically selected galaxies by investigating them in terms of the galaxy main sequence and Kennicutt-Schmidt relation. Furthermore, we will try to understand the role of extreme star forming starburst galaxies in global star formation in the Universe.

# 5

## The properties of Herschel ATLAS galaxies

*"Not all those who wander are lost."*

– J. R. R. Tolkien, *The Lord of the Rings*

### 5.1 INTRODUCTION

In the previous chapter, we matched two samples of optical SDF and submillimetre Herschel galaxies together. The combination of optical and submillimetre photometry offers the ability to accurately estimate the properties of these galaxies, including their star formation rate and dust and stellar mass. We hope to investigate whether these submillimetre selected galaxies are different from optically selected galaxies. We will also investigate the extreme star forming galaxies known as starbursts, to help better understand their role in global star formation in the Universe.

It is long established that the peak in star formation in the Universe occurred around redshift  $z=2$  (Schreiber et al., 2015). But whilst the question of when stars in the Universe formed is easy to answer, the question of where they formed is still unclear. The hierarchical model of galaxy formation suggests that mergers play a large role in galaxy evolution. Mergers between gas rich galaxies create short but significant bursts in star formation, which last  $\approx 0.11Gyr$  (González et al., 2011). Could it be that these rare and extreme events have been the cause of the majority of star formation in the Universe? On the other hand, if galaxies do not have merger

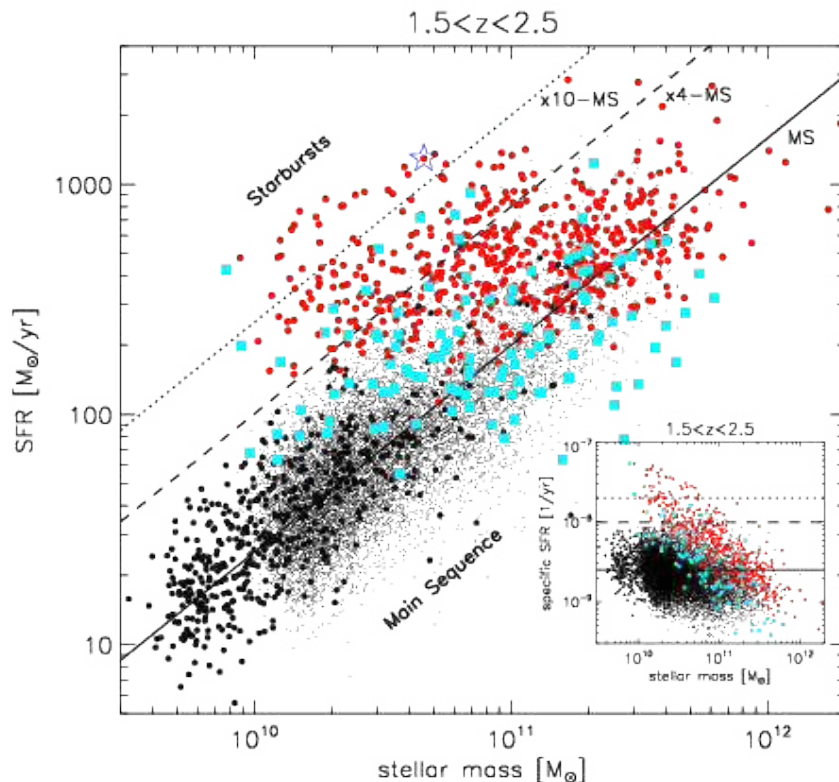


**Figure 5.1.** The galaxy main sequence at  $1.5 < z < 2.5$ . The four samples plotted are a shallow (red filled circles) and deeper (cyan squares) PACS-COSMOS sources, a BzK-GOODS sample (black filled circles) and a sample of BzK-COSMOS sources (black dots). The main sequence (MS) for star-forming galaxies at  $z \approx 2$  defined by Daddi et al. (2007) is plotted as a solid black line, while the dotted and dashed lines represent 10 and 4 times the main sequence (along the Star Formation Rate axis), respectively. This figure is from Rodighiero et al. (2011).

rich histories, then there must be another process through which the majority of stars form. In Eales et al. (2015), we find that the majority of stars in the Universe have formed in disc like galaxies, before being quenched and transformed in to elliptical galaxies at later times. This suggests that the majority of stars may be formed in the Universe through continuous and gradual star formation.

The galaxy main sequence (Noeske et al., 2007) is the relationship between the star formation rate and stellar mass of galaxies, and is one of the key ways of studying how star formation has changed over time. It is an indication of how the star formation rate has changed per stellar mass, with redshift. The galaxy main sequence plot from Rodighiero et al. (2011) can be seen in Figure 5.1 for galaxies from several surveys which lie between redshifts  $1.5 < z < 2.5$ . The relationship between stellar mass

and star formation rate exists for galaxies at  $z \simeq 0$  (Brinchmann et al., 2004),  $z \simeq 1$  (Noeske et al., 2007, Salmi et al., 2012, Rodighiero et al., 2011) and higher (Daddi et al., 2009). However, several authors have shown that the main sequence evolves with redshift, with galaxies at the same mass having higher star formation rates with increasing redshift (Noeske et al., 2007, Speagle et al., 2014). It is clear that galaxies in the past were much more active at forming stars.

Hints on the cause of this increased star formation can be found by studying the overall scatter of the main sequence. An increase in scatter with redshift may indicate that there was a higher fraction of extreme star forming galaxies in the past; however, the scatter has been shown to be relatively constant up to redshift  $z=6$  (Speagle et al., 2014). This implies that the evolution of the main sequence with redshift must be due to a more ordered effect, such as an increased star formation efficiency or a larger gas supply. The consistently small scatter of the main sequence paints a picture of homogeneity amongst star forming galaxies, each of which steadily forms stars over the history of the Universe, whilst spending a small fraction of their lives above the main sequence. We want to see if Herschel galaxies lie on the main sequence plot and to measure their scatter around it. These two factors will help us determine whether submillimetre selected galaxies have similar star forming properties to optically selected galaxies and whether they exhibit a similar level of homogeneity.

Whilst the overall scatter of the main sequence has been shown to remain relatively constant, much work has been done to study those galaxies which lie significantly above the main sequence. These galaxies, termed starbursts (Rodighiero et al., 2011), are undergoing a short term increase in star formation due to some event, most likely a merger or interaction. The question has been asked whether it is by main sequence galaxies or starbursts that the majority of stars in the Universe have been formed. Rodighiero et al. (2011) studied two samples of Herschel galaxies: a mass selected sample of galaxies from the GOODS survey and a star formation rate selected sample from the COSMOS survey. They define starburst galaxies as those galaxies which lie more than 4 times above the galaxy main sequence, based on offsets in the Gaussian distribution of specific star formation rates (the ratio between the star formation rate and stellar mass) of the galaxy samples. They studied the starburst galaxies in both samples and showed that these extreme star forming galaxies only

represent 2% of the number of galaxies and  $\sim 10\%$  of the total star formation between  $1.5 < z < 2.5$ . This further backs the model of homogeneous galaxies dominating star formation throughout the Universe, with merger-driven starburst phases only lasting a short period of time ( $\approx 20 \text{ Myrs}$ ). The work by Rodighiero et al. (2011) focuses on those galaxies between redshifts  $1.5 < z < 2.5$ , the peak in star formation in the Universe. In this chapter we will track the contribution of Herschel starburst galaxies over a significant fraction of the history of the Universe, by studying them over a larger redshift range. We will test what fraction of our galaxies are starbursts and investigate what fraction of total star formation is provided by the starburst galaxies. This will help us answer the question of how large a role Herschel starburst galaxies have had on star formation through the history of the Universe.

The Kennicutt-Schmidt relationship (Kennicutt, 1998) is a correlation between the star formation surface density and gas surface density of star forming galaxies. The equation is given by:

$$\Sigma_{SFR} \propto \Sigma_{gas}^n \quad (5.1)$$

Alternative versions of the relationship have been derived between the overall star formation rate and gas mass of galaxies. The Kennicutt-Schmidt relation gives an indication of how efficient galaxies are at forming stars from their gas. Galaxies with higher star formation rates per gas mass ( $SFE = SFR/M_{Gas}$ ) are by definition more efficient at forming stars. The gradient of the Kennicutt-Schmidt relationship, the value of  $n$  in Equation 5.1, typically takes a value of around 1.4, meaning galaxies with a higher gas density have higher star forming efficiencies. There is evidence that the star formation rates per gas mass of galaxies, the star formation efficiency, increases with redshifts (Rowlands et al., 2014, Santini et al., 2014), which has been proposed to be due to an increased gas fraction with increasing redshift (Combes et al., 2013).

There are two possible causes for starbursts to have increased star formation rates: an increase in star formation efficiency (the number of stars formed per unit gas mass) and an increase in the total gas mass. An increase in star formation efficiency in mergers, and hence starbursts is believed to be the result of an increase in the number of dense molecular clouds (Young & Scoville, 1991). Several works (Sargent et al., 2013, Daddi et al., 2010b) have found evidence of starburst galaxies exhibiting

higher star formation efficiencies than main sequence. However, other works find no evidence of increased star formation efficiency in starbursts, creating a confused picture (Scoville et al., 2016, Santini et al., 2014). In this work we will study the star formation efficiency of Herschel galaxies. We will compare the star formation efficiency of starburst and main sequence galaxies to determine whether Herschel starburst galaxies have higher star formation rates per stellar mass due to increased star formation efficiency, or due to some other reason such as increased gas mass.

In Section 5.2 I introduce the data used in this chapter. In Section 5.3 I describe the public code `MAGPHYS` and how we use it to derive the properties of our galaxies. In Section 5.5 I study these galaxies in terms of the galaxy main sequence and begin to study the role of starbursts in star formation. In Section 5.6 I study the galaxies in terms of the Kennicutt-Schmidt relation. The conclusions are presented in Section 5.7.

## 5.2 DATA

We perform our analysis on two sets of Herschel sources: the Herschel ATLAS and Subaru Deep Field (SDF) matched sources, hereafter referred to as Herschel-SDF, and sources in the Herschel-GOODS survey. We perform the same analysis on both sets of data.

### 5.2.1 HERSCHEL-SDF

The sample of Herschel ATLAS and SDF matched sources is the same sample that we analysed in Chapter 4. This sample consists of Herschel galaxies, which have first been matched to a sample of VLA radio sources, providing accurate positions for the Herschel sources. These galaxies were then matched to the catalogue of optical Subaru Deep Field sources, resulting in a catalogue of 149 Herschel-VLA-SDF matched sources. Full details on this set of data and the source matching process can be found in Chapter 4.

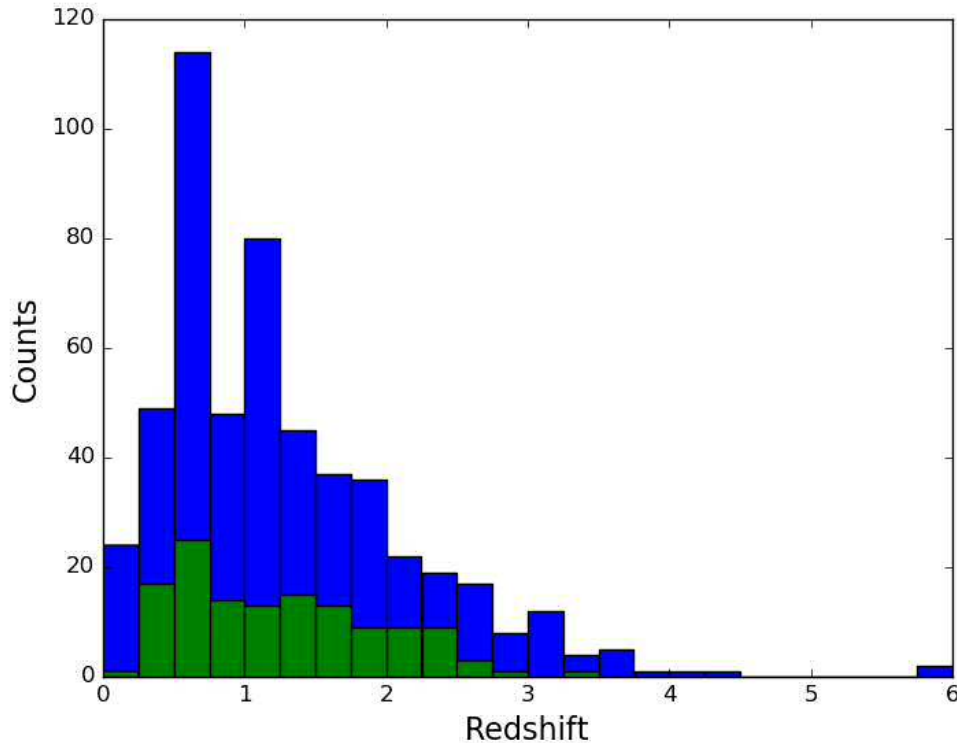


**Figure 5.2.** The redshift distribution of our two galaxy samples. The Herschel-SDF galaxies, whose redshifts are estimated photometrically from the SDF and Herschel photometry, are shown in green. The Herschel-GOODS galaxies, whose redshifts have been estimated photometrically or spectroscopically, are shown in blue.

### 5.2.2 HERSCHEL-GOODS

General details on the Herschel-GOODS survey are given in Section 1.8.2. The structural parameters<sup>1</sup> of the CANDELS sample have been measured by van der Wel et al. (2012). They fit single Sersic profiles to the  $H_{F160W}$  selected objects, measuring the parameters of the best fitting Sersic profile, including the total magnitude, half-light radius, Sersic index, axis ratio and position angle. These values provide structural information for our sample of Herschel-GOODS and CANDELS matched galaxies.

For redshifts, we use the spectroscopic values where available. If there is no spectroscopic redshift for the sources, we use the photometric redshift given as part

<sup>1</sup>In this work, we use the term 'structural parameters' to describe the spatial features of a galaxy's light profile. These include, but are not limited to, the Sersic index of the bulge and disc component, the bulge to disc ratio and the inclination of the galaxy light profile.

of the Herschel-GOODS public data release. If a source still has no available redshift, we use the photometric redshifts given in the CANDELS catalogue of galaxies (Hsu et al., 2014). This results in 314 (60%) of the Herschel-GOODS sources having a spectroscopic redshifts. The redshift distribution of our final sample can be seen in Figure 5.2, along with redshift distribution of the Subaru Deep Field sample.

For this work, we analyse the profiles of galaxies on the CANDELS F160W image, which was taken in the infrared H-band centred around  $1.6\mu\text{m}$ . The publicly available H-band image doesn't cover the entire field that the Herschel and GOODS catalogues are built from so we remove any source that is not covered in this image. The final count of sources in our catalogue is 439. This is the same sample of galaxies that we analyse in Chapter 6.

### 5.3 MAGPHYS

Both the Herschel-SDF and Herschel-GOODS samples of galaxies have been observed in the optical, infrared and submillimetre, allowing us to estimate their physical properties <sup>2</sup> using spectral energy distribution fitting. Having both optical and infrared photometry allows us to accurately account for the majority of stellar emission, enabling us to get reasonable estimates of the physical properties of our galaxy samples. We use the public SED fitting routine, MAGPHYS (da Cunha et al., 2008) to estimate the physical properties of our galaxies. MAGPHYS produces a spectral library of 25,000 optical emission models and 50,000 infrared dust emission models, between  $912\text{\AA}$  and 1mm. This wavelength range covers our SDF, GOODS and Herschel bands. These two libraries are linked together to produce SED's for galaxies across the full wavelength range. One of the key features of MAGPHYS is its ability to account for all the energy absorbed by dust in birth clouds and the ISM, and how this energy is re-radiated in the far-infrared. It is assumed that all the light absorbed by dust is re-emitted and that stellar light is the only significant source of dust heating.

The optical libraries are calculated by latest stellar population synthesis code from Bruzual & Charlot (2003), which computes the light produced by the stars in

---

<sup>2</sup>Throughout this thesis, we use the term 'physical properties' to refer to the stellar, dust and gas properties of galaxies. These include, but are not limited to, values such as the star formation rate, stellar mass, gas mass and dust mass.

galaxies. The library consists of models created from a range of stellar parameters, such as metallicities and star formation histories. A Chabrier (2003) initial mass function is assumed. The attenuation of starlight by dust is accounted for using the model of Charlot & Fall (2000), which accounts for the different attenuation by young and old stellar populations.

The infrared libraries account for the light emitted by dust in the ISM. This emission is attributed to three components of dust in the ISM: polycyclic aromatic hydrocarbons (PAH's), which emit at wavelengths around 3-20  $\mu\text{m}$ ; small dust grains, which are heated by the ultraviolet light from young, hot stars; and big dust grains.

Our galaxy samples tend to consist of high redshift submillimetre galaxies (SMG). This is a problem for the default parameter prior ranges of MAGPHYS, the range of values that each parameter can take, as the prior ranges are often too constrained for these extreme galaxies. We instead use a modified versions of the prior ranges which are better suited for SMG's. The full list of changes can be found in Appendix A of Rowlands et al. (2014), but in brief they include: an extension in the range of cold dust temperatures; an increase in birth cloud timescales, the time before stars move from their birth clouds to the ISM; and changes to the star formation history, to account for the more extreme lives of these objects. The libraries also allow the generation of templates out to a higher redshift.

These spectra are then fit to each galaxy, producing Probability Distribution Functions (PDF) for a multitude of parameters of the galaxies, including star formation rate, stellar mass, dust mass and dust luminosity. We take the median value of the probability distribution function as the value of each galaxy parameter. Our final samples consist of 453 Herschel-GOODS galaxies and 124 Herschel-SDF galaxies.

## 5.4 ESTIMATING THE GAS MASS

MAGPHYS is unable to provide gas mass estimates for galaxies. As part of this work, we want to study our galaxies in terms of the Kennicutt-Schmidt relation, a relationship between the star formation rate and gas mass of galaxies. Traditionally the atomic gas mass is measured by observing the 21cm line, an emission line which is the result of a change of energy state of neutral hydrogen atoms. Molecular hydrogen, from which stars form, is more difficult to observe due to its lack of emission. Instead the amount of CO is traced, which is believed to exist alongside molecular hydrogen,

though in a much lower quantity. The CO 1-0 emission line is converted to molecular hydrogen through a constant known as the X Factor (see Bolatto et al., 2013 for a review), according to the equation:

$$N(H_2) = X_{CO}W(CO) \quad (5.2)$$

where  $N(H_2)$  is the column density,  $X_{CO}$  is the X factor and  $W(CO)$  is the integrated line intensity. The reliability of this method is unknown; there is evidence that the relationship depends on metallicity (Boselli et al., 2002) and that it can also vary between different galaxy types and regions within the galaxies (Bell et al., 2007). One possible cause for this is the relative rate of photodissociation of CO and  $H_2$  molecules in clouds, as molecular hydrogen is better at self-shielding from ultraviolet radiation than carbon monoxide (Glover & Mac Low, 2011).

Another method of estimating the gas mass is from the dust mass of galaxies, a method which has been around for several decades (Hildebrand, 1983, Boselli et al., 2002, Eales et al., 2010b). The gas mass is estimated by assuming a dust to gas ratio, which typically takes the value of DGR=0.01. This method could provide gas mass estimates for millions of galaxies for which getting CO gas estimates is unfeasible. The error in this measurement is estimated to be around 30% when using Herschel estimated dust masses (Eales et al., 2012). The reliability of directly converting dust mass to gas mass has been brought in to question by several works which have shown that the ratio depends on metallicity, similar to the X factor method discussed above (Lisenfeld & Ferrara, 1998, Draine et al., 2007, Sandstrom et al., 2013). As metallicity has been shown not to be universal, converting between dust and gas mass without considering the metallicity can result in incorrect dust mass measurements.

The Fundamental Metallicity Relation (FMR) (Mannucci et al., 2010) provides the solution to this problem. The FMR is a relationship which forms a tight surface in 3D space between the metallicity, star formation rate and stellar mass of galaxies. It has been shown to have a tight dispersion in metallicity of 0.05dex. The relationship between the stellar mass and metallicity has been known for decades (Lequeux et al., 1979), whilst recent work has shown that the star formation rate also correlates with stellar mass and metallicity (Mannucci et al., 2010, Rémy-Ruyer et al., 2014). The relationship has been shown to hold up to redshift  $z \approx 2.5$ , but there is evidence that it evolves beyond this (Mannucci et al., 2010). The metallicity value estimated with

the FMR can then be used in the conversion of gas to dust mass as discussed above, providing a more accurate conversion. Using this method, one can therefore estimate the gas mass from the dust mass, star formation rate and stellar mass of a galaxy.

With no CO measurements for our galaxy samples, we must estimate the gas mass from the dust mass. We use the FMR to estimate the gas mass from the dust mass, based on evidence that the conversion ratio depends on the metallicity of the galaxy. There is evidence that for our highest redshift galaxies, at  $z > 2.5$ , the FMR does not hold, which will affect our gas mass estimates; however, only a small fraction of our galaxies lie above redshift  $z = 2.5$  (30/452 of our Herschel-GOODS sample and 4/124 of our Herschel-SDF sample). Below we discuss the method and results of using the FMR to estimate gas masses of our galaxies, as well as estimating the accuracy of the technique.

#### 5.4.1 FUNDAMENTAL METALLICITY RELATIONSHIP

The Fundamental Metallicity Relationship method is laid out in Santini et al. (2014) and Mannucci et al. (2010). The FMR from Mannucci et al. (2010) is based on several samples of galaxies with measured metallicities, stellar masses and star formation rates. They use galaxies over a range of redshifts:  $0.07 < z < 0.3$  (SDSS),  $0.5 < z < 2.5$  (multiple sources) and  $3 < z < 4$  (multiple sources). Details of how the parameters for each sample were calculated are available in Mannucci et al. (2010) and a plot of the FMR from Mannucci et al. (2010) can be seen in Figure 5.3.

We begin by estimating the metallicity of all the galaxies in both our samples. The metallicity depends on the stellar mass and star formation rate, according to the equation from Mannucci et al. (2010):

$$Metallicity = 8.90 + 0.47 \times (Mu - 10.0) \quad (5.3)$$

where  $Mu$  is given as

$$Mu = \log_{10}(M_*) - \alpha \log_{10}(SFR) \quad (5.4)$$

$M_*$  is the stellar mass of the galaxy in solar masses and SFR is its star formation rate in solar masses per year. We use the values of star formation rate and stellar mass estimated for our galaxies using MAGPHYS.  $\alpha$  in the equation is a free

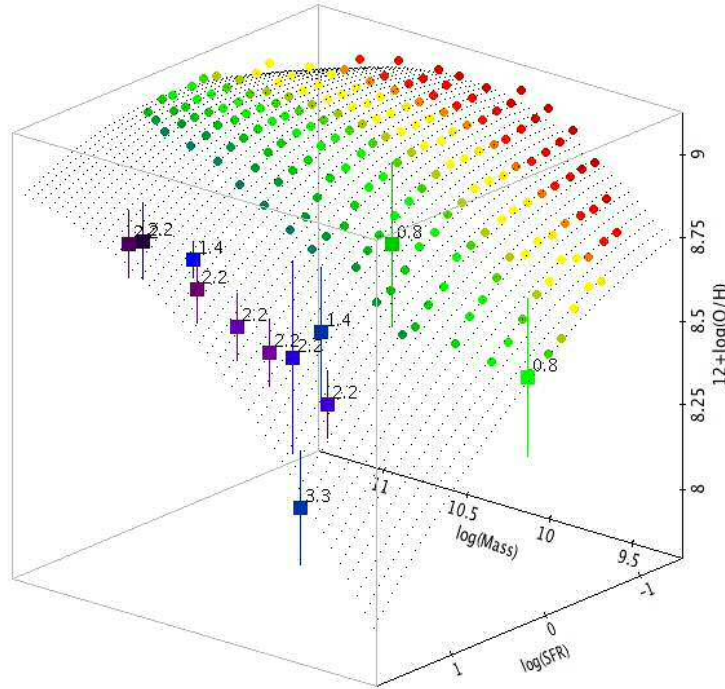


**Figure 5.3.** The Fundamental Metallicity Relationship, which shows the 3D surface relationship between the metallicity, star formation rate and stellar mass of SDSS galaxies. Circles without error bars are the median values of metallicity of local SDSS galaxies in bins of  $M^*$  and SFR. The colour coding also indicates SFR. The square dots are the median values of high redshift galaxies, whose labels give their redshifts. The black dots show a second-order fit to these SDSS data, extrapolated toward higher SFR. This figure is from Mannucci et al. (2010)

parameter, which is found to have a value  $\alpha=0.32$  by Mannucci et al. (2010). The metallicity values of our galaxies can be seen in Figure 5.4.

The metallicity value is then used to calculate the dust to gas ratio used in the following equation, given in Santini et al. (2014):

$$DGR = 0.01 \times 10^{(Z-Z_0)} \quad (5.5)$$

where  $Z$  is the metallicity and  $Z_0$  is the solar metallicity, which has a value of 8.69. This assumes that the FMR does not evolve with redshift. This assumption has been shown to be true out to redshift  $z = 2.5$  by Mannucci et al. (2010). Only 34 of our 576 galaxies lie above this redshift, so the FMR will hold for the vast majority

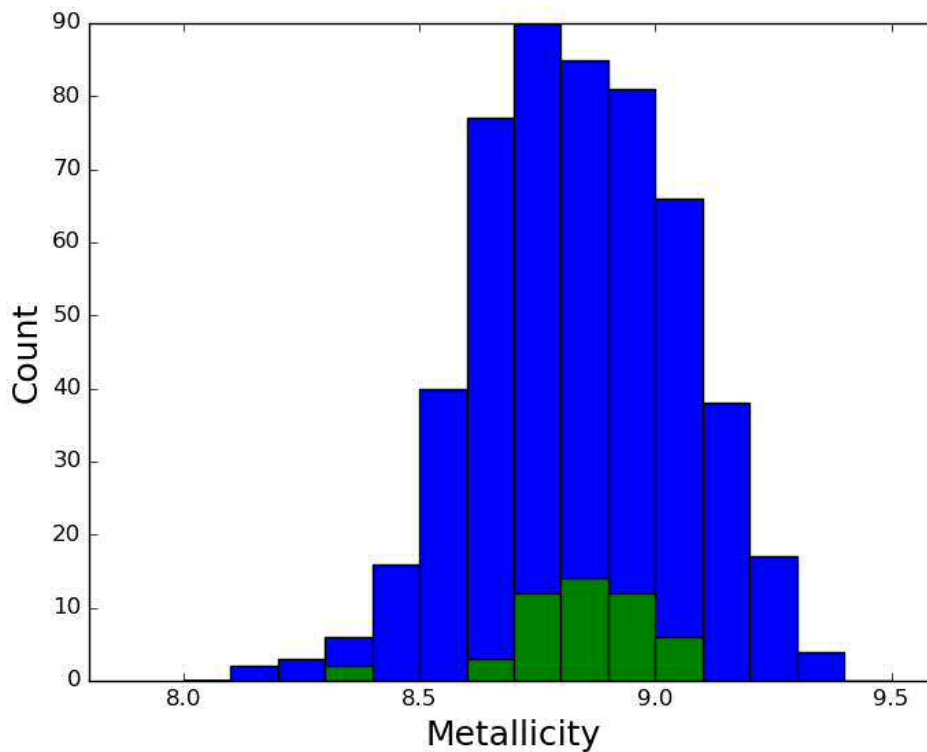


**Figure 5.4.** A histogram of the metallicities of our galaxies, calculated using Equation 5.3. Our Herschel-GOODS sample is shown in blue and our Herschel-SDF sample in green.

of our galaxies. We test this further, later in this section. The gas mass here is the total gas mass, the sum of atomic and molecular gas.

We can compare our results to the gas values we would get if we estimated them from the dust mass and a universal gas-to-dust ratio method. The typical dust-to-gas ratio value used is  $DGR=0.01$ . If the metallicity in Equation 5.5 is set to the Milky Way value of 8.69, the dust to gas ratio comes out as 100, agreeing with this more simple method. Our mean metallicity values are 8.838 and 8.829 for the Herschel-GOODS and Herschel-SDF samples respectively, putting them slightly above the Milky Way metallicity value of 8.69. However, this is in agreement with the mean metallicity value of Herschel selected GOODS galaxies found by Santini et al. (2014) of  $Z_{MEAN} \approx 8.9$ . These metallicity values result in mean gas to dust mass ratios of 71.1 and 72.6 for the Herschel-GOODS and Herschel-SDF samples respectively.

Source ID	$z$	$M_*$ [ $10^{10} M_\odot$ ]	SFR [ $M_\odot/yr$ ]	$M_{Dust}$ [ $10^8 M_\odot$ ]	$M_{Gas-FMR}$ [ $10^{10} M_\odot$ ]	$M_{Gas-CO}$ [ $10^{10} M_\odot$ ]
GN20	4.05	23	2000	14	16.5	15
BzK-21000	1.52	7.8	220	2.0	11	8.9

**Table 5.1.** The properties of the two sources, studied by Magdis et al. (2011), that we use to test the FMR.

#### 5.4.2 ACCURACY OF THE FMR

Here we study the accuracy of the Fundamental Metallicity Relationship. The scatter of the FMR is  $\approx 0.06dex$ , forming a tight relation, whilst the scatter is reduced for those galaxies with higher star formation rates. Galaxies out to high redshifts have been shown to follow a single mass-metallicity relationship (Mannucci et al., 2009), whilst data out to  $z \approx 2.5$  are consistent with a single FMR, as defined in Mannucci et al. (2010). There is evidence that galaxies at  $z \approx 3.3$  have metallicities about 0.6dex lower than the FMR defined by SDSS and  $0.5 < z < 2.5$  galaxies. This is likely in part due to observational biases, as discussed in Mannucci et al. (2010), but is also likely due to some type of galaxy evolution in the high redshift Universe. We might therefore expect our highest redshifts galaxies to have over-estimated gas masses; however, only 6.0% of our galaxies lie at redshifts  $z > 2.5$ .

We find no tests of the accuracy of the FMR for submillimetre, high redshift galaxies. We therefore perform a simple test ourselves, by using the FMR to calculate the gas masses of a sample of sources with known accurate CO gas masses, and compare the two values. We find no CO observations for any of the galaxies in either of our GOODS or SDF samples, from which we could estimate the gas mass. Instead we look for work which has studied high redshift Herschel galaxies in other fields, which have gas mass estimates from the CO luminosities, dust masses, star formation rates and stellar masses. Magdis et al. (2011) study two galaxies in the GOODS North field, the starburst GN20 and normal star forming galaxy BzK-21000, in order to better understand gas-to-dust ratios and the CO to H<sub>2</sub> conversion method. We use these two galaxies as a small sample to test the accuracy of the FMR in estimating gas masses. The stellar masses of GN20 and BzK-21000 are given in Daddi et al. (2009) and Daddi et al. (2010a) respectively, the star formation rates are estimated by Magdis et al. (2011) using the total IR luminosity. The dust masses of the two

galaxies are estimated by Magnelli et al. (2012) by fitting the dust models of Draine & Li (2007). The physical properties of both galaxies are given in Table 5.1.

Following the FMR method detailed above, we estimate the metallicity, dust-to-gas ratio and hence gas mass of these two galaxies. The values of  $M_{Gas}$  that we calculate from the FMR can be seen in Table 5.1, alongside the values estimated from the CO luminosities. We see that the values are in good agreement, suggesting that the FMR method is accurately estimating the gas mass of these Herschel sources. It is also reassuring to note that it correctly estimates the gas mass for our high redshift source, GN20, a concern which was discussed in Mannucci et al. (2010) and above. This result, combined with the analysis done by Mannucci et al. (2010), leads us to believe that we are accurately estimating gas masses for our galaxy samples using the FMR.

## 5.5 THE GALAXY MAIN SEQUENCE

Previous work by Rodighiero et al. (2011) studied the main sequence for two samples of Herschel matched galaxies; mass selected from the GOODS survey and star formation selected from the COSMOS survey. They studied galaxies between redshifts  $1.5 < z < 2.5$ , the peak of star formation in the Universe. We build upon this work by also studying our sample of SDF galaxies. These galaxies have been matched to bright radio counterparts in the VLA survey, by making use of the far infrared-radio correlation. This is believed to be the result of active star formation in galaxies, which produces UV emission from young hot stars, which is absorbed and re-emitted by dust in the infrared, and radio emission from the resulting supernovae. This implies that these galaxies are currently undergoing significant star formation.

In Figure 5.5 we show the star formation rate against stellar mass of our samples of Herschel-SDF and Herschel-GOODS galaxies in six redshift bins. We have plotted a redshift dependant version of the main sequence on each plot, as well as the lines of 4 and 10 times these main sequence lines, to indicate possible starbursts as defined by Rodighiero et al. (2011). The redshift dependant main sequence is given in Speagle et al. (2014), who derived the best fitting main sequence from the combination of 25 studies of the galaxy main sequence. They select works with: at least 50 galaxies or more than 2 data points if stacked; details of how the galaxies were fit and their parameters estimated; and published no earlier than 2007, when

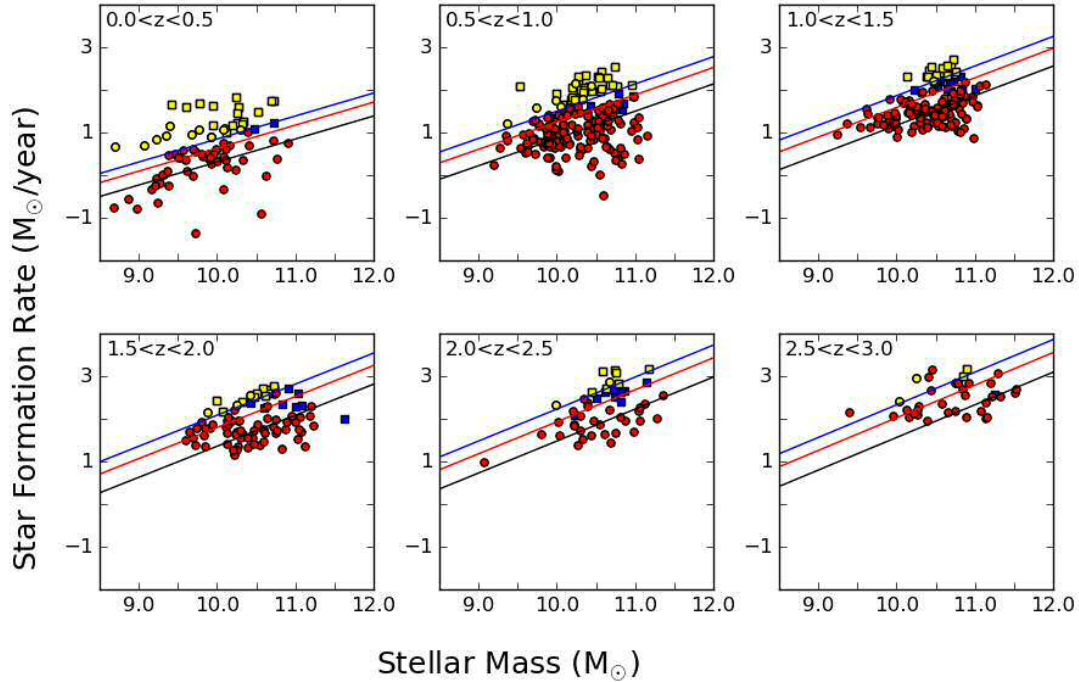


**Figure 5.5.** Galaxy main sequence plots for our two galaxy samples which have been binned by redshift. The black line is the redshift dependant main sequence from Speagle et al. (2014) and the red and blue lines are 4 times and 10 times the main sequence respectively. The red circles and blue squares are the Herschel-GOODS and Herschel-SDF galaxies respectively, which lie below the  $10 \times MS$  line. The yellow circles and squares are the Herschel-GOODS and Herschel-SDF galaxies respectively, which lie above the  $10 \times MS$  line and hence are designated starbursts following the definition in Rodighiero et al. (2011).

the idea of a galaxy main sequence began. The data have all been converted to a set of common calibrations. This work provides one of the most comprehensive measurements of the form of the galaxy main sequence, for a wide range of galaxy types and redshift, making it well suited to our analysis. The main sequence is derived from these data out to  $z \approx 6$  and is given by the following equation:

$$\log_{10}\psi = (0.84 - 0.026t)\log_{10}M_* - (6.51 - 0.11t) \quad (5.6)$$

where  $\psi$  is the star formation rate in solar masses per year,  $M_*$  is the stellar mass in solar masses and  $t$  is the age of the Universe in Giga-years at the redshift of the source.

It is expected that our Herschel-GOODS sample is more complete than the

Herschel-SDF sample (Eales et al., 2015). We measure the scatter of our main sequence in each redshift bin around the best fit main sequences from Speagle et al. (2014), as we do not have enough data points in each redshift bin to fit our own main sequence. We calculate the standard deviation of displacements in star formation rate of each source from the redshift dependant main sequence lines. A larger scatter than in other works may suggest that our galaxy sample is less homogeneous or have a higher fraction of starbursts. We find a scatter of 0.672dex at  $0 < z < 0.5$ , 0.571dex at  $0.5 < z < 1$ , 0.443dex at  $1 < z < 1.5$ , 0.556dex at  $1.5 < z < 2$ , 0.557dex at  $2 < z < 2.5$  and 0.465dex at  $2.5 < z < 3$ . The scatter in our main sequence is relatively consistent above redshift  $z=1$ , but is slightly higher at  $z < 1$ . Several authors have shown that the galaxy main sequence has a scatter of around 0.3dex for all redshift bins and all star forming galaxies (Salmi et al. (2012) for  $0 < z < 1.3$  and Schreiber et al. (2015) for  $0 < z < 4$  galaxies). The main reason why our main sequence has a higher scatter than other papers is likely because we are not measuring the scatter around a main sequence derived from our galaxies, but instead we use the best fit main sequence from Speagle et al. (2014). Our Herschel-SDF sample detects significantly more starburst galaxies than main sequence, a likely result of malmquist bias, the preferential detection of brighter objects at increasing distance. This will also cause us to calculate a significantly higher dispersion value, as the majority of the galaxies are not main sequence galaxies, but instead lie significantly away from the main sequence lines.

We see that there is an evolution in our galaxies as they shift upwards with increasing redshift. This agrees with the work of Speagle et al. (2014), who derived redshift dependant main sequence lines to account for this. This increase in star formation rate per stellar mass shows that some process is slowly lowering the star formation rate in the Universe towards the present day.

### 5.5.1 STARBURST GALAXIES

Those sources that lie on the main sequence at a given redshift are steadily forming stars. However, those which are significantly above are deemed to be starbursts, defined as having at least 10 times larger star formation rates than the main sequence line (Rodighiero et al., 2011).

In Table 5.2 we show the number of starburst and main sequence galaxies for

	Redshift	N main sequence galaxies	N starburst galaxies
Herschel-GOODS			
	0-0.5	49	12
	0.5-1.0	144	7
	1.0-1.5	112	1
	1.5-2.0	63	3
	2.0-2.5	29	2
	>2.5	28	2
Herschel-SDF			
	0-0.5	2	16
	0.5-1.0	8	28
	1.0-1.5	14	14
	1.5-2.0	8	12
	2.0-2.5	11	7
	>2.5	2	2

**Table 5.2.** A table of the number of main sequence and starburst galaxies in each redshift bin in the Herschel-GOODS and Herschel-SDF samples.

both data sets in each redshift bin. It is interesting to note that despite the Herschel-SDF sample being smaller than Herschel-GOODS, there are more starbursts in most redshift bins. The cause of this is likely because the SDF data covers a larger area of sky and the Herschel ATLAS flux limit is much brighter than for Herschel-GOODS. Malmquist bias is likely causing us to miss many of the fainter sources, whilst still observing the bright starburst galaxies, which explains our higher ratio of starburst to main sequence galaxies. The Herschel-GOODS sample on the other hand has a fainter flux limit and is expected to resolve  $\approx 50\%$  of the total infrared background into individual galaxies at  $250\mu\text{m}$  (Eales et al., 2015).

Of our Herschel-GOODS galaxies, only 27 of the 425 galaxies or 6.0%, are starbursts, agreeing with the work of Rodighiero et al. (2011) who found that starburst galaxies only represent 2% of mass selected galaxies. We calculate the amount of star formation in our starburst galaxies as a fraction of the total star formation, over all redshifts in the Herschel GOODS sample. The GOODS sample is more complete so will provide a more accurate estimate. Our sample of GOODS starburst galaxies contribute 11.7% of the total star formation of the Herschel-GOODS sample. This is comparable to the value estimated by Rodighiero et al. (2011), who found that 10% of the star formation density is due to starburst galaxies. Our sample of GOODS galaxies is not complete however, as we are missing the faintest sources;

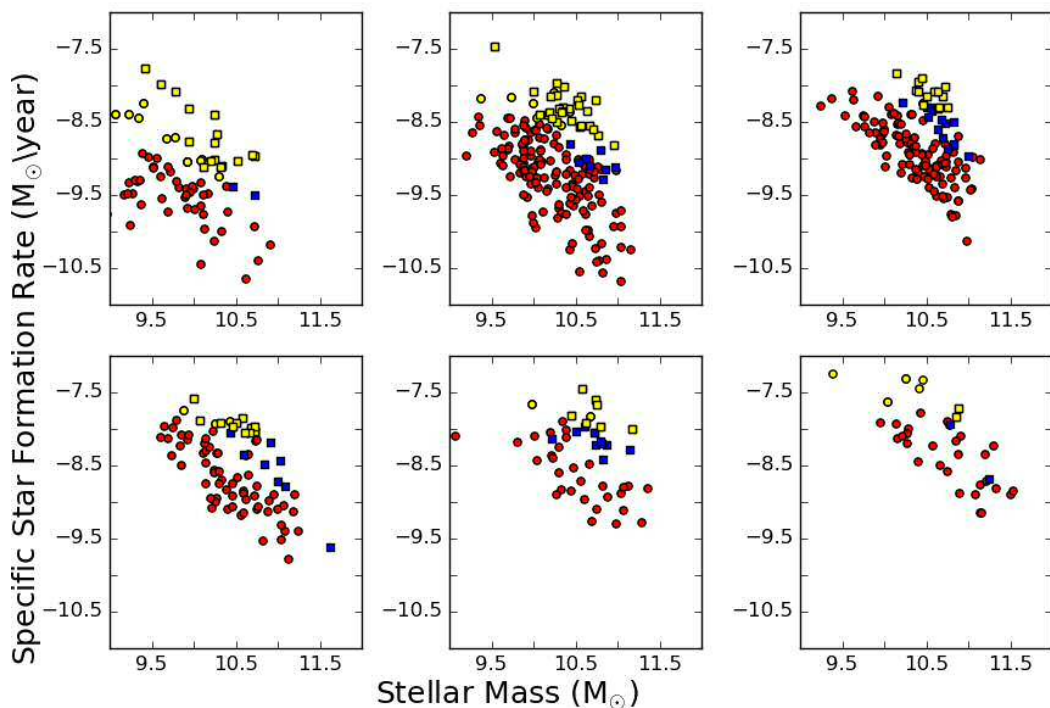


**Figure 5.6.** The galaxy main sequence of our galaxy samples, showing the specific star formation rate. The red circles and blue squares are the Herschel-GOODS and Herschel-SDF galaxies respectively, which lie below the  $10 \times MS$  line. The yellow circles and squares are the Herschel-GOODS and Herschel-SDF galaxies respectively, which lie above the  $10 \times MS$  line and hence are designated starbursts following the definition in Rodighiero et al. (2011).

these missing sources are almost certainly main sequence galaxies, which would lower our fraction of star formation density in the Universe by starburst galaxies. If we make the assumption that Herschel-GOODS detects 50% of the star formation in the Universe (Eales et al., 2015), then we can expect our measured fraction of the total star formation contributed by starburst galaxies to drop to  $\approx 6\%$ . These results agree with other evidence to suggest that the majority of star formation in the Universe is from steady star forming main sequence galaxies and not from extreme star forming galaxies. We use these samples of starbursts in the next section to study whether they exhibit higher star formation efficiencies than the main sequence galaxies.

In Figure 5.6 we show the plot of specific star formation rate ( $SFR/M_*$ ) against stellar mass of our two galaxy samples. We have again binned the galaxies into 6 redshift bins and have plotted all the starburst galaxies as yellow points. By definition, our starburst galaxies are those with the highest star formation rate per

stellar mass for any given stellar mass. We see that the specific star formation main sequence has a negative gradient, as found by other authors (Rodighiero et al., 2010) and shifts upwards with increasing redshift, implying galaxies formed more stars per stellar mass in the past.

## 5.6 THE KENNICUTT-SCHMIDT RELATION

There are two key questions we hope to answer about our two galaxy samples, by studying the Kennicutt-Schmidt relation. Firstly, do our galaxies defined as 'starbursts' in the previous section have higher star forming efficiencies than those which are classed as 'main sequence' galaxies? We have seen from our galaxy main sequence plots that starburst galaxies in general have higher star formation rates. However, it is not known whether this is due to them having more gas to form stars from or whether they are more efficient at forming them. Secondly, we want to investigate whether the star forming efficiency of galaxies evolves with redshift. The peak in star formation occurred around  $z \approx 2$  and has been declining ever since. The cause of this decline may be due to an exhaustion of gas in the ISM, or due to a decrease in star forming efficiency, either due to a reduction in galaxy interactions or some other reason.

In Figure 5.7 we have plotted the Kennicutt-Schmidt relation for our Herschel-GOODS and Herschel-SDF galaxies, which have been binned by redshift. The star formation rates plotted are those estimated with MAGPHYS and the gas mass values were estimated from the dust mass using the fundamental metallicity relation. Those galaxies defined as main sequence are plotted in red and blue for the Herschel-GOODS and Herschel-SDF samples respectively, whilst those galaxies defined as starbursts are plotted in yellow. The first thing to note is that whilst our Herschel-SDF galaxies on average have higher gas masses and star formation rates than the Herschel-GOODS sample, both populations overlap each other, suggesting there is no fundamental difference between the galaxies in both samples.

We can see both samples evolve with redshift, with galaxies having increasing star formation rate per gas mass with increasing redshift, implying that the star formation efficiency of our Herschel galaxies is increasing with redshift. This implies that the conditions for star formation were different in the past than they are today. Increasing star formation efficiency with increasing redshift has been seen by

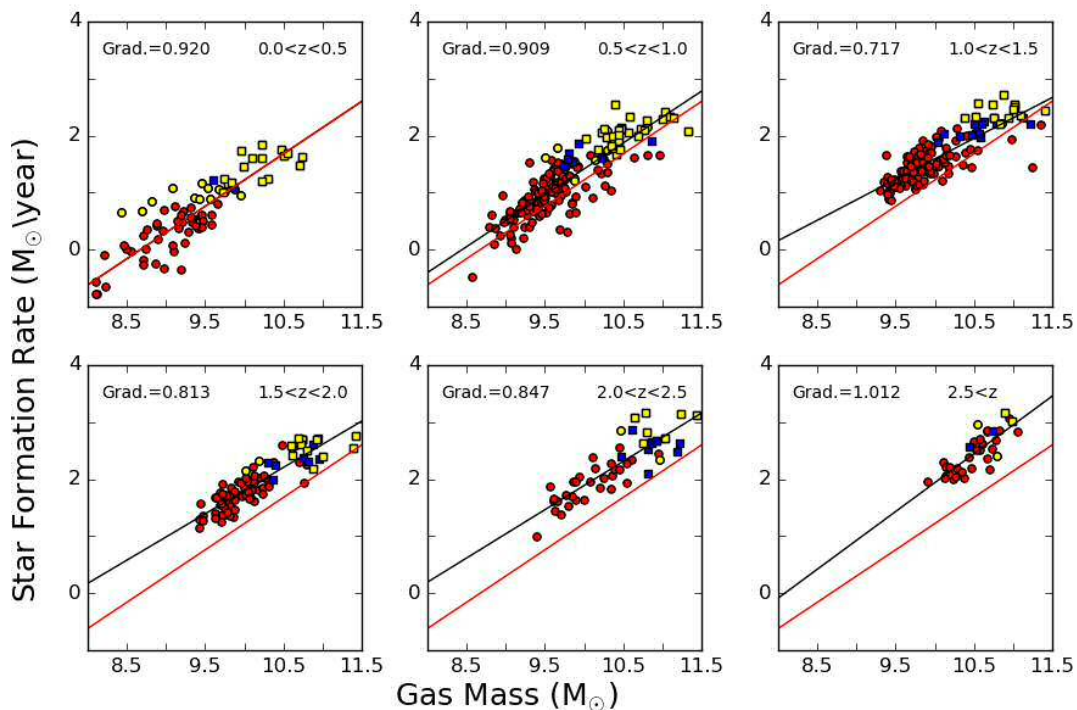


**Figure 5.7.** The Kennicutt-Schmidt plot for our two galaxy samples, where the galaxies have been binned by redshift, which is given in the upper right of each sub-plot. The red circles and blue squares are the Herschel-GOODS and Herschel-SDF galaxies respectively, which lie below the  $10 \cdot M_{\text{MS}}$  line. The yellow circles and squares are the Herschel-GOODS and Herschel-SDF galaxies respectively, which lie above the  $10 \cdot M_{\text{MS}}$  line and hence are designated starbursts following the definition in Rodighiero et al. (2011). The lines of best fit to the galaxies are plotted are the black lines, whilst the line of best fit for the  $0 < z < 0.5$  bin is shown in red in each sub-plot. The gradient of each line of best fit is given in the upper left of each sub-plot.

several authors before (Combes et al., 2013, Santini et al., 2014, Rowlands et al., 2014, Scoville et al., 2016). A similar study by Santini et al. (2014) found similar evidence for an evolving star formation efficiency, based on a sample of Herschel galaxies matched to GOODS and COSMOS galaxies. They estimate the gas masses using the Fundamental Metallicity Relationship, using dust masses derived using the spectral energy distribution templates of Draine & Li (2007). They derive the stellar mass from the fitting the photometry to the models of Bruzual & Charlot (2003), the same technique that we use through the code MAGPHYS. The star formation rates are estimated using the calibrations given in Santini et al. (2009), which estimates the star formation rate directly from the total infrared luminosity. They find that the

star formation efficiency consistently increases between  $0 < z < 2.5$ , with galaxies at  $z \approx 2$  forming stars with an efficiency of 5 times greater than the present day main sequence galaxies. We have shown that this trend appears to exist for our sample of Herschel-SDF galaxies, though this sample detects a smaller fraction of main sequence galaxies, so we cannot say for certain whether all of the galaxies increase their star formation efficiency or whether there are a larger fraction of starburst galaxies,

Scoville et al. (2016) show that the star formation efficiency increases for a sample of galaxies out to redshift  $z \approx 4.5$ . They similarly find that galaxies at high redshift have star formation efficiencies  $\approx 5$  times larger than at low redshifts. This increase in efficiency with redshift applies to both the main sequence and starburst galaxies. This is important as it implies that it is a similar physical process which is occurring in both main sequence and starburst galaxies to increase the star formation efficiency. This further backs the idea that the increase in star formation around  $z = 2$  is not due to an increase frequency of mergers, and hence starbursts, but due to all galaxies being more star forming efficient in the past. The reason for this increase in star formation efficiency has been suggested to be due to an increase in dispersive gas motions due to an increase gas infall rate, creating a higher number of compression in the ISM gas and hence leading to increased star formation rates (Scoville et al., 2016). Similarly, Rowlands et al. (2014) suggest that it could be due to increased gas density; local ULIRGs have been shown to have high density gas components, which are likely responsible for the increased star formation efficiency (Greve et al., 2009).

Santini et al. (2014) also showed that the gradient of best fit lines in each redshift bin decreases with increasing redshift, from 1.45 in the local Universe to 0.76 at  $z \approx 2$ . However, we see evidence of the gradient increasing in the bins of  $z > 1.0$ , although our lower redshift bins have steeper slopes, giving a confused picture of whether the gradient of our Kennicutt-Schmidt plot evolves or not. Our measured gradients are also shallower than those in Santini et al. (2014) except in the highest redshift bin.

### 5.6.1 THE STAR FORMATION EFFICIENCY OF STARBURST GALAXIES

In the previous section we identified starburst galaxies in both of our Herschel samples. One key question we are able to investigate is whether the starburst galaxies are more efficient at forming stars than main sequence galaxies. We can see in Figure

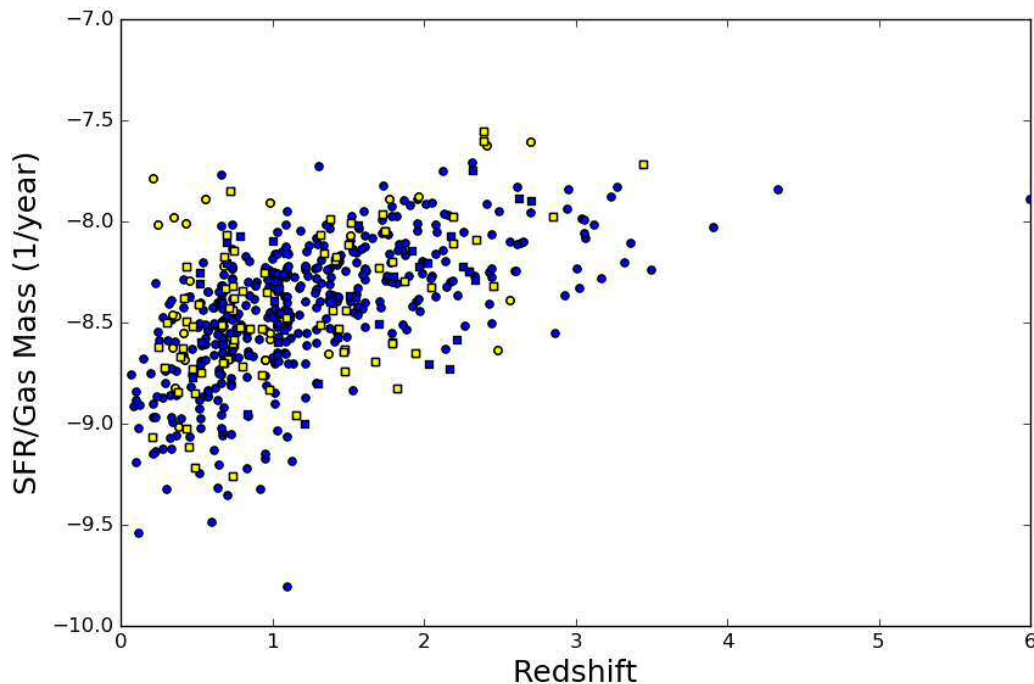


**Figure 5.8.** Plot of the star forming efficiency ( $SFR/M_{GAS}$ ) for our two galaxy samples. The star formation rate was estimated using MAGPHYS whilst the gas mass was estimated from the dust mass using the fundamental metallicity relation. Herschel-SDF galaxies are plotted as blue squares and Herschel-GOODS and blue circles. Those galaxies identified as starbursts in Figure 5.5 are plotted as yellow squares (Herschel-SDF) and yellow circles (Herschel-GOODS).

5.7 that in each redshift bin, the starburst galaxies are typically those with the largest gas mass and star formation rate. However, we **do not** see strong evidence that they have higher star formation rates per gas mass, compared to the main sequence galaxies. Both main sequence and starburst galaxies lie very closely to the same best fit lines, implying that starbursts do not have increased star formation efficiencies over main sequence galaxies.

We can further test our result by plotting the star formation efficiency ( $SFR/M_{Gas}$ ) of our two galaxy samples as a function of redshift, shown in Figure 5.8. We have plotted the main sequence galaxies in blue and those defined as starbursts in the previous section in yellow. We can see that not only do galaxies contain more gas at higher redshifts, but they also form their stars much more efficiently. It appears that the relationship is beginning to peak around  $z = 2$ , which may correlate with other works which show that star formation peaked in the Universe around this redshift.

The key result of main sequence and starburst galaxies having the same star formation efficiencies has also been found in other works. Santini et al. (2014) noted that their starburst galaxies do seem to follow the same star formation law as all other galaxies for their Herschel-GOODS sample. We note that we see this in both our Herschel-GOODS and Herschel-SDF samples, providing further evidence that starburst galaxies are no more efficient at forming stars than main sequence galaxies. Scoville et al. (2016) also found that galaxies on and above the main sequence have similar star formation efficiencies. At all redshifts, they find that the cause of increased star formation in starburst galaxies is due to an increase in gas mass, a result which we also find.

Our result and that of Santini et al. (2014) and Scoville et al. (2016) are in contrast to other works, which find starburst galaxies to be more efficient than those on the main sequence. Magdis et al. (2012) studied a small sample of submillimetre galaxies and a sample of 4000 stacked main sequence galaxies, and estimate their gas masses through using the dust-to-gas ratio and CO luminosity method. They find that main sequence galaxies have lower star formation efficiencies than starburst galaxies with the same star formation rates; however, we note that their result only considers two starburst galaxies, whilst our work considers  $> 100$ . Genzel et al. (2010) find a similar result, for a sample of galaxies between  $0 < z < 1.5$ . They find starburst galaxies are forming stars 4-10 times more efficiently than normal star forming galaxies, which they explain is likely due to gas compression and higher fractions of dense gas, which is believed to be the case in starburst galaxies (Papadopoulos & Geach, 2012). This physical process of denser gas leading to increased star formation efficiency, typically attributed to increased gas flows from the intergalactic medium, has been proposed to explain the trend for increasing star formation efficiency with increasing redshift for all galaxies (see Section 5.6 above). If this is true for all galaxies due to increased gas inflow, then it is logical that the same would occur for galaxy mergers. However, the fact that we see different results in these two scenarios suggest that increased gas density may not be the only process which is affecting the star formation efficiency of galaxies, or that the gas density is not changed by equal amounts by mergers and gas inflow.

Our finding that starburst galaxies are on average no more efficient at forming stars than main sequence galaxies is a key result, as it implies that the increased star

formation rates observed per stellar mass of starburst galaxies, as seen in the galaxy main sequence in Figure 5.5, is not due to an increase in star forming efficiency. Instead, the increase in star formation rate is likely due to an increase in gas mass, which can be seen in Figure 5.7 where the starbursts lie on the same star formation efficiency line as main sequence galaxies, but simply at a higher gas mass. Their increased star formation is in this case due to an increase in gas mass, possibly due to the merging of two galaxies, rather than any increase in star formation efficiency.

## 5.7 CONCLUSIONS

The aim of this work is to study the properties of two samples of Herschel galaxies, in terms of four key properties: their star formation rate, stellar mass, gas mass and dust mass. Both samples contain galaxies out to redshift  $z \approx 3$ , covering the peak in star formation history of the Universe.

We began by plotting both samples on a plot of star formation rate against stellar mass. We find that our galaxies tend to lie on the redshift dependant main sequences derived by Speagle et al. (2014). Following this redshift dependant main sequence, our galaxies shift to higher star formation rates per stellar mass with increasing redshift. We find that in our Herschel GOODS sample, which resolves around 48% of the total infrared background at  $250\mu m$  (Eales et al., 2015), only 7.5% of the galaxies are starbursts, which contribute around 11% of the total star formation. This suggests that the majority of stars in the Universe have formed in steady star forming main sequence galaxies rather than starbursts.

We plotted our galaxy samples on the Kennicutt-Schmidt plot of gas mass against star formation rate. Our galaxies form a relatively tight correlation. We find that the Kennicutt-Schmidt relation of our galaxies shifts upwards to higher star formation rates with increasing redshift. This implies that galaxies were on average more efficient at forming stars in the past. This has implications for the star formation evolution in the Universe, as it suggests that the decrease in star formation density in the Universe over time has been due to gas exhaustion in galaxies.

We also note that our starburst galaxies, identified from the plot of star formation rate against stellar mass, appear to lie on the same best fit line as the main sequence galaxies, implying that starburst and main sequence galaxies have the same star forming efficiency. However, they do have higher gas masses and star formation

rates than the main sequence galaxies. This is clear evidence that the star formation rate of starburst galaxies is not due to increased star formation efficiency, but is instead due to increased gas masses from which the starburst galaxies can form more stars.

We conclude that starburst galaxies are simply the more extreme versions of main sequence galaxies. The increase in star formation rate per stellar mass of starburst galaxies is due to an increase in available gas to form stars, not of an improved star formation efficiency. Galaxies as a whole, however, have become less star forming efficient over time, which is likely the cause for the drop in star formation density in the Universe since  $z \approx 2$ , rather than a decrease in the number of mergers or interactions.

We now have a sample of Herschel-GOODS galaxies with estimates for their star formation rates, stellar masses, dust masses and gas masses. In this chapter we studied where they lie on the main sequence and the Kennicutt-Schmidt plot, investigating the role of starburst galaxies on the total star formation in the Universe. The GOODS survey provides good resolution images of the galaxies, allowing the profiles of many of the galaxies to be accurately measured. An interesting question that we would like to answer is whether the light profiles of galaxies is related to their star formation properties. In the next chapter, we will measure the light profiles of the Herschel-GOODS galaxies and see if they relate to their star forming properties.

# 6

## Analysing the profiles of Herschel galaxies

*”’Curiouser and curiouser!’ Cried Alice”*

– Lewis Carroll, *Alice’s Adventures in wonderland*

### 6.1 INTRODUCTION

In the previous chapter we estimated the star forming properties of a sample of Herschel-GOODS galaxies, specifically studying their position on the galaxy main sequence, Kennicutt-Schmidt plot and the role of starburst galaxies in star formation. The Herschel-GOODS survey provides high resolution images of the galaxies, allowing us to measure the light profiles of the galaxies. This can provide information on the bulge and disc components of the galaxies. One interesting question is whether the light profile of our Herschel-GOODS galaxies is related to the star forming properties, estimated in the previous chapter.

For centuries, astronomers have known the importance of studying the shape of galaxies. Hubble’s popularised tuning fork diagram gives a broad illustration of the different shapes that galaxies can be. Each galaxy can be assigned to one of four types: spiral, elliptical, lenticular or irregular. Learning why galaxies were different shapes and how this affected their intrinsic properties became key to understanding how galaxies have evolved over the history of the Universe. As telescopes and instruments have improved, we have been able to study the light profiles of galaxies at a much

higher resolution, allowing us to decompose galaxies into their individual components. Where once each galaxy could be separated into one of a few simple types, there now exist a wide range of sub-varieties built from these individual components, such as the disc, bulge and spiral arms. It is these individual components that define where the galaxy lies on Hubble's tuning fork, yet much more can be learnt when one studies the individual components in detail.

The two dominating components of most galaxies are the bulge and disc. It has been known for a long time that the disc of a galaxy is best fit by an exponential model (de Vaucouleurs, 1958 Freeman, 1970). These early studies also noted that the bulge component of observed galaxies was best fit with a  $R^{1/4}$  model, known as the de Vaucouleurs model (Kormendy, 1977). These bulges typically have little gas and low star formation rates, but instead house an older stellar population. However, later studies began to note that the bulges of some galaxies were better fit with an exponential profile (Shaw & Gilmore, 1989), which is normally fit to the profiles of galaxy discs. Today the bulges of galaxies are fit with a Sersic  $R^{1/n}$  profile, the generalisation of the de Vaucouleurs model, allowing either a de Vaucouleur or exponential profile to be fit.

It is not just the intensity profile of the bulges which have been shown to be different. Whilst some exponential bulges have low star formation activity, many are very active, showing signs of ongoing star formation and large gas reserves. They are instead much more similar to the properties of discs, often featuring significant levels of star formation, spiral arms and bars. These bulges have been given the name pseudobulges (Kormendy, 1982a, Kormendy, 1982b). The term classical bulge is given to those bulges which do not exhibit such active properties. Several works have tried to quantitatively distinguish between classical and pseudobulges. Traditionally the two populations were separated by their Sersic index, with classical bulges having  $n > 2.5$  and pseudo bulges  $n < 2.5$  (Fisher & Drory, 2008), a method which is reliable in around 90% of cases (Fisher & Drory, 2010). Other definitions focus more on the star forming activity of the bulge, identifying those with significant ongoing star formation as pseudobulges.

The frequency of pseudobulges in galaxies at low redshifts has been studied in detail by several works. Vaghmare et al. (2015) studied a sample of 185 S0 and 31 nearby spiral galaxies, which lie at redshifts  $z < 0.06$ , imaged with the Spitzer

Infra-Red Array Camera. They find that, of their sample of 31 spiral galaxies, 24 or 77% have pseudobulges, whilst 25 or 14% of their S0 galaxies also have pseudobulges. Fernández Lorenzo et al. (2014) find that, of their sample of 189 isolated galaxies, 94% have pseudobulges. Similarly, Fisher & Drory (2011) find that, for a sample of 97 galaxies, only 17% of galaxies more massive than  $10^9 M_\odot$  have classical bulges, whilst 45% have pseudobulges. They also find that those galaxies with pseudobulges have higher star formation rates than those with classical bulges, with 61% of star formation in the local Universe occurs in galaxies with pseudobulges. It is clear that our idea of galaxies having a de Vaucouleurs shaped bulge is incorrect, with a significant fraction of observed galaxies at low redshift featuring an exponential shaped bulge.

The question of how classical and pseudobulges form is debated. Hydroynamical modelling has presented contrasting arguments on the formation of pseudobulges. Debattista et al. (2006) present SPH simulations of disc galaxies, which show that secular processes, help grow exponential bulges. These secular processes are typically found to be the migration of gas and gas clumps to the centre of the galaxy, possibly due to some type of instability around the bulge. Immeli et al. (2004) also show that the migration of gas clumps towards the centre of galaxies increases the star formation rate in the bulge, giving it the properties of a pseudobulge. Classical bulges are thought to form from more extreme events, such as minor mergers which disrupt the dynamics of the core. Aguerri et al. (2001) perform N body simulations between exponential profile bulges and satellites, measuring how the Sersic index of the bulge intensity profile changes after the merger. They find that the Sersic index of the bulge increase proportionally to the satellite mass, with satellites of equivalent mass to the bulge raising the bulge Sersic index  $n$  from 1 to 4. The mergers with several smaller satellites can therefore gradually change the intensity profile of the bulge.

However, there is evidence that the contrary is in fact true and that secular events cannot be entirely responsible for creating pseudobulges. Okamoto (2013) studied two simulated galaxies from the Aquarius project (Springel et al., 2008). These are created with halo masses similar to the Milky Way's. Both galaxies have been identified as having pseudobulges, based on their Sersic index. They find that these pseudobulges do not form through secular processes associated with the galaxy

disc, but instead are formed by starbursts and are already in place by redshift 2-3. These early pseudobulges are disc-like with small scale lengths and already account for at least 70% of the final pseudobulge mass of both galaxies. Guedes et al. (2013) make a similar conclusion, that pseudo-bulges are formed through non-secular processes. They study the evolution of a single, Milky Way-like late-type spiral, using the smoothed particle hydrodynamics code *Eris*, following the evolution from  $z = 90$  to the present day. In their simulations, the bulk of mass of pseudobulges forms around  $z \approx 4$ , from the bars present in galaxies. They see no evidence that processes such as clumping contribute to the bulge formation. This evidence of pseudobulges being in place at moderately high redshifts, with the main disc of the galaxy forming later, suggest that secular processes associated with the disc play a small role in the formation of pseudobulges. These two contrasting results of galaxy simulations presents a confused image of pseudobulge formation.

In this chapter we will study the discs of our Herschel-GOODS galaxies. We will investigate whether our sample of Herschel galaxies primarily exhibits classical or pseudo shaped bulges, in order to determine what fraction of Herschel sources feature a pseudo-bulge. We will study how the fraction of Herschel sources with pseudo-bulges changes with redshift to see if there is some evolution in the galaxy population.

Modern telescopes are beginning to distinguish the bulge and disc components of high redshift galaxies. The Great Observatories Origins Deep Survey (GOODS) survey brings together data from many of the worlds most powerful telescopes to study the evolution of the Universe out to distant redshifts. The project combines data in a wide range of wavelengths to provide a deep view of the Universe. Previous work has been done to decompose samples of GOODS galaxies (van der Wel et al., 2012, Bruce et al., 2012). The GOODS fields have now been covered by several Herschel surveys in the submillimetre, providing a look at the hidden star formation in these galaxies. This Herschel-GOODS catalogue contains around 500 Herschel selected sources which have also been observed with Hubble, providing a view of the two main wavebands in which most of the energy is emitted in the Universe. In the previous chapter we estimated the properties of the GOODS galaxies, including the star formation rate, stellar mass, dust mass and gas mass. There has been little work done to study whether these galaxy properties are linked to the light profiles of the

galaxies, specifically to the relative dominance of the bulge and disc and to the shape of the disc. In this chapter we will test whether there is any such relationship in our Herschel-GOODS sample.

## 6.2 GALFIT

In order to decompose the disc and bulge components of a galaxy, we use the profile fitting program GALFIT (Peng et al., 2010). GALFIT provides automated two dimensional profile fitting for galaxies, by modelling objects using a parametric function. The simplest configuration of GALFIT allows the user to fit a single profile to an image of a galaxy. However the real power of GALFIT comes in fitting multiple components to a single source, providing details on the relative contributions of a galaxy's light from the bulge and disc.

GALFIT is a least squares fitting algorithm. It determines the goodness of fit between the model and data by calculating the value of Chi-squared,  $\chi^2$ , given by the equation:

$$\chi^2 = \sum_{x=1}^{nx} \sum_{y=1}^{ny} \frac{(f_{data}(x, y) - f_{model}(x, y))^2}{\sigma(x, y)^2} \quad (6.1)$$

which loops over an image of size  $nx$  by  $ny$  pixels. The value of  $\sigma$  is the error in each pixel. GALFIT uses a sigma map in the calculation of reduced chi squared. This is an image, the same size as the input data image, which gives one standard deviation of counts in each pixel. This image can either be given by the user or generated by GALFIT from details of the observation. Once the value of  $\chi^2$  has been calculated for a set of input model parameters, it will adjust the values of the parameters to attempt to further decrease the value of  $\chi^2$ .

GALFIT also outputs the value of reduced  $\chi^2$ , defined as  $\chi^2$  divided by the number of degrees of freedom,  $N_{DOF}$ . In the case of fitting an image of a model galaxy to an image of real data, the number of degrees of freedom is given by the number of pixels in the image minus the number of free parameters.

GALFIT is able to generate a number of different profiles, including Sersic, exponential, Gaussian and a de Vaucouleurs. Each profile uses a different set of parameters to create the model. In this work we use with the Sersic profile which has

the following parameters: position on the image, photometric magnitude, effective radius, Sersic index, axis ratio and rotation angle. By default, each of these parameters is able to vary with no limitations. However, one can choose to fix a given parameter or even limit the range of values it can take, ensuring the program does not start searching beyond reasonable values.

The limitations of a minimisation routine such as GALFIT is that the program needs estimates of each parameter to begin with in order for it to start at a realistic point in parameter space. In fact, GALFIT requires initial estimates of the parameters that are reasonably close to the real best fitting values, otherwise it is unlikely to ever find a global or indeed local minima. GALFIT itself offers no method of automatically restarting the fitting procedure of each galaxy at a different point in parameter space, to avoid the problem of getting stuck in a local minimum. This can be a significant problem, one which we discuss later in this chapter.

In addition, GALFIT is also able to generate complex structure in the models to better fit the complex nature of real galaxies. These include adjusting the shape to that of a non-typical ellipse, bending the ellipse to create bar-like patterns and modelling spiral arms. In this work we are not interested in the features of a galaxy beyond the contribution of the bulge and disc and so we do not add any complex structures to our galaxy modelling.

### 6.3 SIMULATING HERSCHEL GOODS GALAXIES

The aim of this work is to use the public code GALFIT to decompose a sample of galaxies into their bulge and disc components. However, before we run GALFIT on our Herschel GOODS data we test the program on a sample of model galaxies for three purposes. First, we need to ensure that we have set up the program correctly and that it is reproducing the characteristics of the model galaxies that we artificially generate. Secondly, we need to check that GALFIT can correctly fit two individual Sersic profiles to galaxies that have two distinct components. This work has been done previously by other authors (Häussler et al., 2007), but testing it ourselves also allows us to check we have set GALFIT up correctly. Finally, it may be possible to do some basic science with the results of these models.

### 6.3.1 SIMULATING TECHNIQUE

To simulate the Herschel GOODS galaxies, we generate a Sersic profile using the equation from Caon et al. (1993):

$$I(r) = I_e e^{(-b_n (\frac{r}{R_e})^{\frac{1}{n}} - 1)} \quad (6.2)$$

where  $I_e$  is the intensity at the effective radius,  $R_e$ ,  $r$  is the radius from the centre of the galaxy and  $n$  is the Sersic index. We use this form of the equation, which depends on the effective radius, as this is a parameter that GALFIT uses, making it easier for us to compare our input parameters and those which GALFIT measures. The parameter  $b_n$  is defined by the equation:

$$b_n = 1.9992n - 0.3271 \quad (6.3)$$

which is given in Capaccioli (1989). This analytical expression for  $b_n$  is an approximation, for Sersic value between  $0.5 < n < 10.0$ . All of our galaxies are simulated with Sersic indexes between these values.

Using this equation, we are able to simulate galaxies with a variety of Sersic indices and effective radii, both of which are free parameters that GALFIT fits to find the best profile. We are also able to simulate galaxies of different brightnesses using the variable  $I_e$ . However, this equation can only generate face on galaxies. To generate inclined galaxies we need to include both an inclination and position angle, which we do by incorporating the equation of an ellipse into our simulations, given by:

$$1 = \frac{((X - X_0) \cos(\theta) + (Y - Y_0) \sin(\theta))^2}{a^2} + \frac{((X - X_0) \sin(\theta) - (Y - Y_0) \cos(\theta))^2}{b^2} \quad (6.4)$$

where  $X_0$  and  $Y_0$  are the position of the centre of the galaxy,  $X$  and  $Y$  are the position we are calculating the profile at.  $\theta$  is the angle subtended by the galaxy on the sky,  $a$  is the semi-major axis and  $b$  is the semi-minor axis.

We calculate the distance of each pixel from the centre of the galaxy using Equation 6.4, then apply our Sersic profile in Equation 6.2 to the array of distances to calculate the counts in each simulated pixel of our galaxy image. We generate images

of size 200 by 200 pixels in order to both accommodate large simulated galaxies and keep running time to a minimum.

One issue with the method above is that we fill each pixel of our image based on the distance from the centre of the pixel to the centre of the galaxy. However, in reality the Sersic profile should be integrated over the whole pixel, as the Sersic profile varies over the scale of a single pixel. Difficulties in integrating the inclined ellipse Sersic profile led us to choose this more simple but less accurate method for estimating the counts in each pixel. However, as a compromise between the two methods we split each pixel into a set of sub-pixels, calculate the counts in each sub-pixel and sum them together. A compromise between run time and increases in accuracy led us to split each pixel into 7 x 7 sub-pixels.

We generate our galaxies with a range of parameters, representing both the typical galaxies in the Herschel GOODS catalogue as well as more unusual galaxies. We fit the Sersic index ( $n$ ), effective radius ( $R_e$ ),  $a$  and  $b$  ellipse parameters, central brightness in counts ( $I_e$ ), the angle of the galaxy profile and the  $X$  and  $Y$  positions of the centre of the galaxy on the sky. For double profiles we generate two sets of these parameters, one of which is applied to the bulge component and one that is applied to the disc component. The range of values we set for each parameter can be seen in Table 6.1.

Parameter	Bulge		Disc	
	Min	Max	Min	Max
X Position [pixels]	99.5	100.5	99.5	100.5
Y Position [pixels]	99.5	100.5	99.5	100.5
$I_e$	0.01	1.01	0.01	1.01
$R_e$ [pixels]	2.0	30.0	2.0	30.0
$n$	3.0	6.0	0.25	2.0
$a$	1.0	1.0	1.0	1.0
$b$	0.2	1.0	0.2	1.0
Angle	0.0	360.0	0.0	360.0

**Table 6.1.** The range of the parameters we use to simulate our galaxies.

We define the brightness in terms of the central intensity, but we can convert this total brightness of the galaxy in counts by integrating over the whole galaxy. This total count value can be converted to an apparent magnitude using the equation:

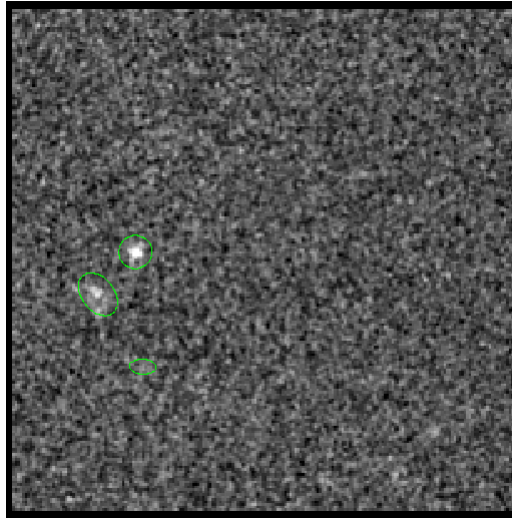


**Figure 6.1.** The cutout region that we inject our simulated sources into. The field contains three background sources which are detected in the GOODS survey and are highlighted by green ellipses.

$$Magnitude = -2.5 \log_{10}(Counts) + M_0 \quad (6.5)$$

where  $M_0$  is the magnitude zero point of the GOODS survey, which has a value of 25.96 in the H-band, allowing us to directly compare the results of our simulation and the Herschel GOODS data. Our range of central brightness values corresponds to a simulated range of magnitudes of approximately  $Magnitude \approx 15 - 25$ . We adjust the total flux of our galaxies to allow for the increase in surface brightness caused by inclining our galaxies.

We next convolve our sources with the Hubble WFC3 Point Spread Function (PSF). As we inject our sources on to the real GOODS image, which by definition has been convolved with the Hubble PSF, we must convolve the simulated images of our galaxies with the PSF as well. We inject the sources into a small, relatively blank, area of sky, cutout from the GOODS WFC3 F160W image which can be seen in Figure 6.1. The size of the cutout area is set to 200 by 200 pixels, or approximately 12x12 arcseconds. The maximum size of our simulated galaxies, whose half-light radius is 30 pixels, will be much smaller than this. This ensures that the whole profile of each simulated galaxy fits on the image, whilst still keeping the runtime of the simulations relatively low.

Using this setup, we generate 1,000 sources, each built from both a classical

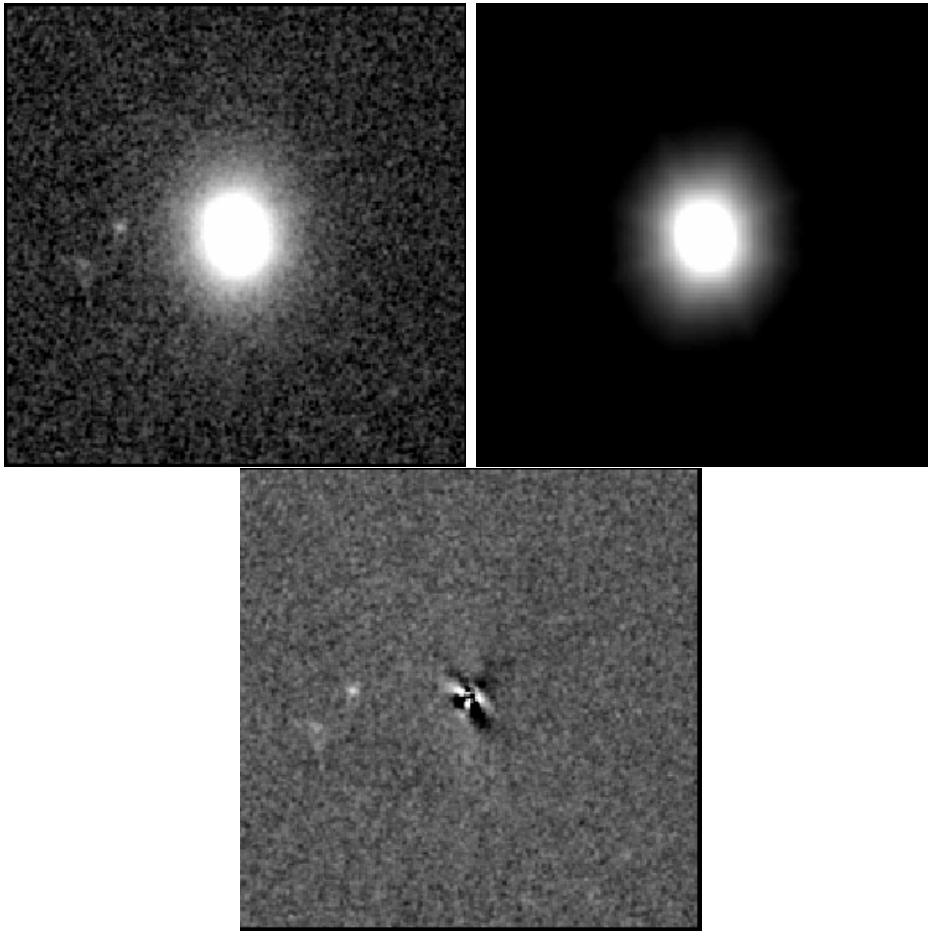


**Figure 6.2.** *Top Left:* An example of a simulated galaxy, which was built from both a bulge and a disc component. *Top Right:* The model galaxy, created by GALFIT, which best fits the profile of our simulated galaxy. The fit has a reduced chi squared value of 1.70. *Bottom:* The residual image after subtracting the model image from the simulated image.

bulge and disc like profile. An example of the simulated galaxy can be seen in Figure 6.2.

## 6.4 RUNNING GALFIT ON SIMULATED SOURCES

We run GALFIT with several configurations to see how robust it is at retrieving the correct characteristics of the simulated galaxies. We run each configuration on the same 1,000 simulated sources, given in Table 6.1, allowing us to directly compare the best fit profiles by each method on the same galaxies. The three configurations we perform with GALFIT are:

1. Fitting a single Sersic profile to the data

2. Fitting two Sersic profiles to the data, fixing the Sersic indices to be  $n=1$  and  $n=4$
3. Fitting two Sersic profiles to a galaxy where both Sersic indices are allowed to vary

### 6.4.1 POTENTIAL PROBLEMS WHEN RUNNING GALFIT

There are several key parts to running sources through GALFIT, each of which can have a serious effect on the accuracy of the final results. Here we discuss these possible problems and the techniques we have used to limit their effect on our final results.

#### **Avoiding local minima**

A problem that can arise with minimisation routines, such as GALFIT, is getting stuck in local minima. Whilst a global minimum exists in parameter space, so too do local minima, points of better fitting than the surrounding parameter space, but that are not the best overall fit. Complex fitting routines use techniques to avoid getting stuck in local minima, but it is still possible for them to fail finding the global minimum. A simple improvement that can be made is to start the program at a variety of different points in parameter space, reducing the chance of getting stuck in local minima. We run the GALFIT routine on our sources a number of times, each at a different set of initial parameters. Because of the large length of time it already takes to run all our sources through GALFIT, we limit ourselves to varying the initial guesses of just two parameters: the ratio of magnitudes of the bulge and disc; and the source Sersic index.

When fitting a single Sersic profile we start at a value of Sersic index of  $n=1$  or 4. We set the initial guess magnitude of this profile to the simulated magnitude. When fitting double profiles to galaxies, we run the routine for five different ratios of the total flux in each profile. Our initial guesses are for 99% of the total flux in the bulge and 1% in the disc, 75% bulge and 25% disc, 50% bulge and 50% disc, 25% bulge and 75% disc and finally 1% bulge and 99% disc. These five combinations are set to give an even spread of starting magnitude parameters guesses, whilst still keeping the running time of the program to a reasonable length. Because our Herschel galaxies

and our simulated galaxies overwhelmingly contain a disc component, we start one of the components as a disc like  $n=1$  profile. We start the other components with initial guess parameters of  $n=1$  or  $n=4$ , representing the classical and pseudobulge profiles.

### Point Spread Function

Using an accurate model of the PSF is vital when trying to finely determine the intensity profile of galaxies. Several authors have used GALFIT on GOODS sources, which has resulted in two different techniques emerging to generate a model PSF of the data. Bruce et al. (2012) begin by using the TinyTim package to generate the PSF for the Hubble Space Telescope. However, they find that compared to a PSF generated from stacked bright stars over the field, the TinyTim PSF seems to underestimate the emission of the PSF at low radii. This has a significant effect on the measured sizes of galaxies, which on average are found to be between 5-10% larger than when the empirical star PSF is used.

van der Wel et al. (2012) find a similar result when they compared the TinyTim generated PSF to a set of stacked images of stars over the field. However, they point out the problems of stacking stars on the field due to the difficulty of identifying the accurate sub pixel positions of the sources. To combat this, they create a hybrid PSF, a combination of both the empirical star model and that generated with TinyTim. They replace the inner pixels of the empirical star PSF with those from the TinyTim PSF. We adopt this hybrid PSF in the GALFIT runs on our Herschel GOODS sources.

### Background Estimation

To find the best fitting model, GALFIT estimates the value of reduced  $\chi^2$  according to Equation 6.1. This calculation incorporates the value of  $\sigma$  of each pixel, defined as one standard deviation of counts, through the sigma or weight map. The sigma map can often be calculated by GALFIT; however, the mosaicked GOODS maps have variable exposure times across them, making automated sigma map creation impossible.

Without this information, we are forced to generate a sigma map ourselves. To do this, we calculate the standard deviation of the pixels around the edge of the cutout image for each individual source. Each source cutout image is  $200 \times 200$  pixels and we estimate standard deviation of the 20 pixel wide outer border, in order to

avoid flux from the source itself. We then set this value as the standard deviation of every pixel in our sigma map. This method is not ideal. The sigma value of each pixel should represent the standard deviation of each individual pixel. However, as we are working with cutout images and are only fitting to a single source on each image, the sigma value is unlikely to vary significantly between the pixels of the cutout images of each source. The sigma value is also only used to scale the chi squared value of the fit. This means it will not affect the final selected best-fit model for each source.

### **Background source masking**

GALFIT finds the best-fit profile(s) of the input image map. In each case, we centre the source we want to fit at the centre of the cutout image map. However, the depth of the GOODS survey means there are often background sources on the images. These sources will cause problems when profile fitting, as GALFIT will try to fit complex and large profiles that cover the source we want to fit and all background sources. By specifying a fitting area only slightly larger than the source we want to fit, we reduce the number of background sources on the image.

However, it is probable that there are still some background sources on the image. In order to avoid GALFIT fitting to these sources, we create a pixel mask file for each individual source. We find the central pixel positions of every sources in the GOODS field from the full GOODS catalogue. We also find their effective radius, ellipticity values and their position angle from the CANDELS catalogue, as found by van der Wel et al. (2012). From these parameters we generate an ellipse at the position of any background source on the cutout image, identifying the position of any pixel that lies within this ellipse. We then exclude all of these pixels in our mask file, which are then not fit to.

Despite being a relatively blank area of sky, there are several obvious sources in the small field that we inject our simulated sources into. We mask three sources that can be seen in Figure 6.1, highlighted by green ellipses. The parameters used to create this ellipse are from the GOODS catalogue of all sources on the field.

### **6.4.2 DOUBLE PROFILE FIT - VARIABLE SERSIC INDICES**

We attempt to fit two intensity profile components to our simulated galaxies. We need to test whether GALFIT is able to accurately fit the correct bulge and disc

components of galaxies. Our sample of 1,000 simulated galaxies was built from a disc-like and bulge-like profile, with realistic magnitudes and effective radii based on the real CANDELS galaxies and with random AB ratios and position angles. We allow all other parameters to vary, whilst starting at several different values of Sersic index and brightness magnitude, as described before. We run our 1,000 sources, built from a disc-like and bulge-like profile, through GALFIT and compare their measured parameters to those used to generate the model galaxies, given in Table 6.1. We supply GALFIT with the initial guess parameters based on those found previously from our single Sersic profile fit, apart from the Sersic index, which we set to  $n=1$  and  $n=4$ . When working on real sources we will not have the parameters of each component to use as initial guesses, but instead, we will use the parameters of the best fit single profile as our initial guess parameters.

Bruce et al. (2012) fix the positions of the bulge and disc profiles to the position of the best fitting single Sersic profile. This reduces the chances of GALFIT fitting to unrealistic positions. To test this, we ran our sources twice in two separate configurations: one where we fix the positions of both components to the positions found by the single Sersic fit and one where we start the parameters at those positions, but allow them to vary. In the case where we allow them to vary, we also add in parameter constraints to the positions of both profiles. We force the positions to take values to within  $\pm 1$  pixels of our initial guess values. This ensures that GALFIT does not fit to unrealistic positions. According to the GALFIT documentation, this can cause problems, as the program can sometimes get stuck in a local minima towards the edge of the boundary between acceptable and restricted values; however, we consider this a worthwhile trade.

Of the 1,000 sources, GALFIT finds a fit for 861 sources when using variable positions. This means GALFIT cannot find a reasonable fit for 139 sources. This is likely due to GALFIT becoming stuck in local minima at the edges of our parameter boundary and hence never finding realistic parameters. We find reasonable fits for 989 of the sources when using fixed positions. The reason for finding fits to more sources is unknown; however, it may be because when we force the positions to stay constant, GALFIT cannot get stuck in any local minima, or because with less varying parameters GALFIT finds reasonable fits more easily.

We begin by comparing the parameters used to simulate our galaxies to those

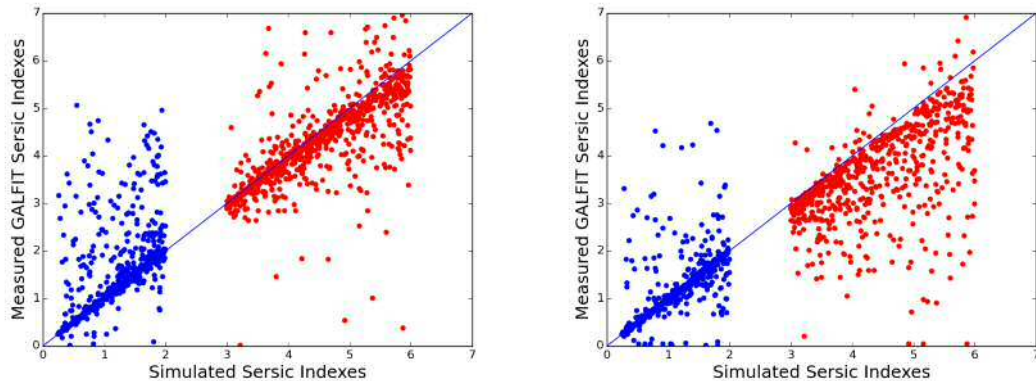


**Figure 6.3.** The measured Sersic indices of our sources against the simulated Sersic indices. Here we have fit two profiles to each of our galaxies, one disc-like and one bulge-like. The most disc-like components are plotted in blue and the most bulge-like are plotted in red. The left hand plot shows the results when using variable positions to fit profiles and the right plot uses fixed positions.

measured by GALFIT. When allowing the Sersic indices of our components to vary, it is sometimes possible that the profile we give disc-like initial guess parameters, incorrectly fits to the bulge component and vice versa. This still provides an accurate fit to the model, but makes it difficult for us to compare the measured to simulated data. In order to fix this we re-arrange our profiles such that the profile with the smallest Sersic index is labelled the 'disc' and the profile with the largest Sersic index as the 'bulge'.

In Figure 6.3 we study how well GALFIT recovers the Sersic indices of both the disc and bulge components. The blue points are the disc like profiles and the red points are the bulge components. The plot on the left shows the results of using variable positions and the one on the right using fixed positions. In both plots we see that the majority of the sources form a tight linear correlation on a line of gradient unity. However, in both plots there seems to be a significant number of outliers. The reason for these outliers is unknown, but a likely cause is that in these cases, GALFIT is becoming stuck in a local minima and hence failing to find the correct fit.

On the other hand, when we use fixed positions the number of outliers for the disc profiles is reduced, but now the Sersic index of the bulge component is being underestimated. If the fixed positions are not the positions of both components, GALFIT will alter the Sersic index and effective radius of the component to try to counter this incorrect position. After much analysis of how well GALFIT recovers the

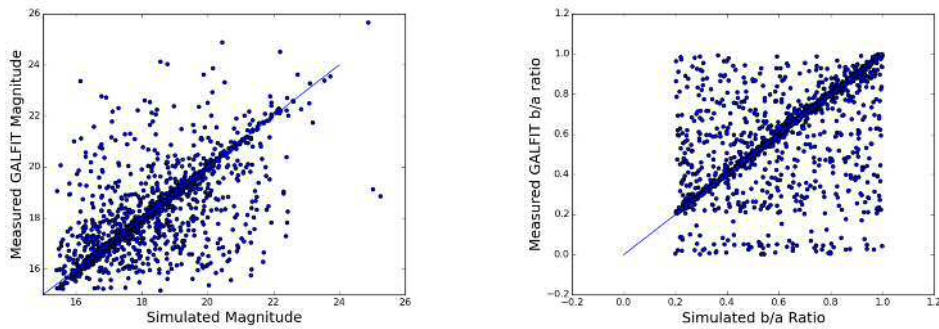


**Figure 6.4.** Left: The simulated against measured magnitudes of our sources when using variable positions to fit our components. Right: The simulated against measured AB ratios of our sources when using variable positions

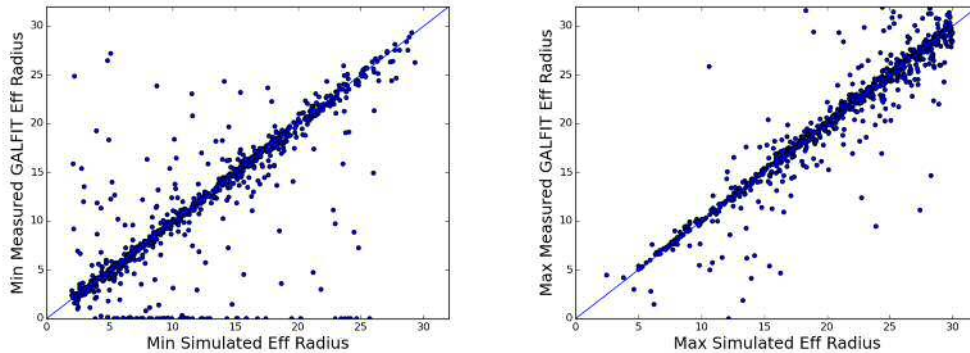


**Figure 6.5.** The simulated against measured effective radii of our sources, when allowing the Sersic indices to vary and using variable positions. We split our components up into the smallest effective radii (left) and largest (right) of each source.

parameters of our simulated galaxies, when using both variable and fixed positions, we decided to always allow the positions of the profiles to vary. By constraining the position parameters we are confident that the profile cannot fit to any background source or noisy pixel.

In Figure 6.4 we look at the simulated and measured magnitudes and AB ratios of our galaxies. We see that GALFIT recovers the magnitudes of the majority of the sources, though there are a significant number of outliers. These outliers do not seem to correlate with the magnitude of the components. As with the magnitudes, we note that the majority of the sources form a tight correlation between simulated and measured values of the AB ratio. Again there exists a fraction of the sources which lie off this correlation, causing significant scatter.

In Figure 6.5 we compare the simulated and measured effective radii of both

components. As GALFIT often switches around the components that it is fitting, we split the effective radius values in to the smallest and largest components, making it easier for us to compare the values. For both the small and large effective radii plots, we see a tight correlation with a small fraction of outliers. There is slightly more scatter at the very smallest and largest radius values.

### 6.4.3 DOUBLE PROFILE FIT - FIXED SERSIC INDEXES

Finally we run the same sample of simulated galaxies through GALFIT, except now we follow the method of Bruce et al. (2012) and force GALFIT to fit two profiles with Sersic indices of  $n=1$  and  $n=4$ . However, our input sample of simulated galaxies were generated with two profiles, a bulge-like components with random Sersic indices between 3.0 and 6.0 and a disc-like components with a Sersic index between 0.25 and 2.0. Each profile has a realistic magnitude and effective radius based on the real CANDELS galaxies and a random ellipticity AB ratio and position angle. Fixing the two profiles to  $n=1$  and  $n=4$  fits the classical model of galaxy profiles, in which a galaxy consists of a spheroidal bulge and a flat disc.

The benefit of fixing the Sersic indices rather than letting them vary is that it provides us two very distinct classical bulge and disc components, allowing us to study the bulge to disc ratio for galaxies more clearly. However, this does assume that all galaxies have a classical bulge and disc component, which as we discuss in Section 6.1, is not the case for a significant fraction of galaxies. Galaxies that have a pseudobulge with Sersic index  $n \approx 1$  will not be fit well; however, in our simulated galaxies we only simulate classic bulges with  $n=3-6$  and do not simulate pseudobulges.

Of the 1,000 simulated sources, GALFIT finds a fit for 644 sources when using variable positions and for 683 of the sources when using fixed positions. As when using variable Sersic indices, we see that GALFIT finds more reasonable fits when using fixed positions than variable; however, in both cases we are now failing to find any fits for one third of the sources, a result of fixing the Sersic indices.

We have now measured the Sersic indexes of our single sample of 1,000 model galaxies using three different methods: fitting a single profile, fitting two profiles with variable Sersic indices and fitting two profiles with Sersic indices fixed at  $n=1$  and  $n=4$ . In Figure 6.6 we can now see the distributions of measured Sersic indices by each method. As we force both components of the fixed Sersic indices to be  $n=1$  and

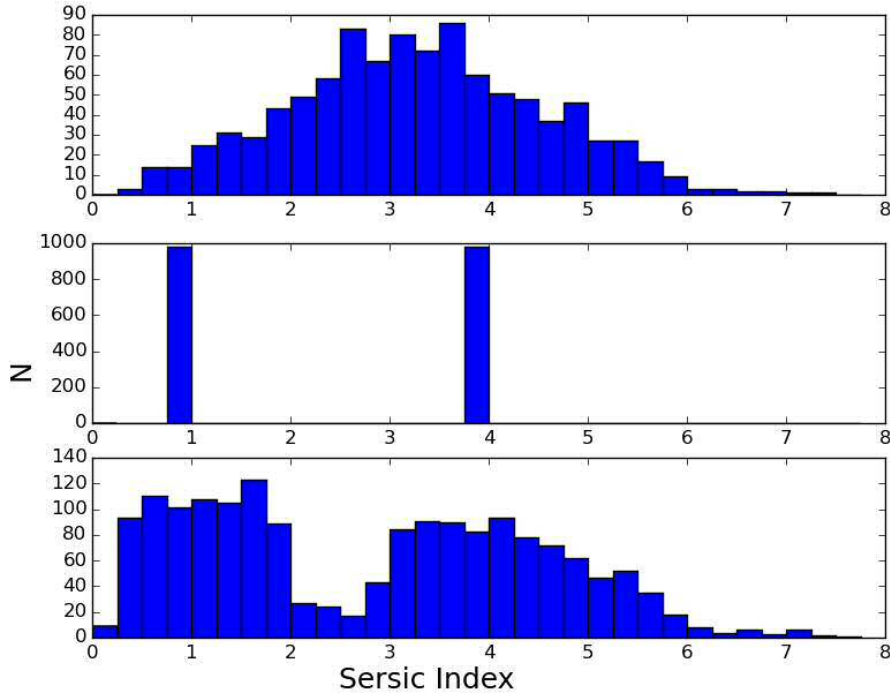


**Figure 6.6.** The histograms of the measured Sersic indices using variable positions. The plots from top to bottom are of Single profiles, two profiles with fixed Sersic indices and fitting two profiles using variable Sersic indices.

$n=4$ , it is not a surprise that our distribution consists of two equal peaks at these values. The single distribution measures the average of the Sersic indices of both components, which is seen by the peak in the distribution around  $n=3$ .

In Figure 6.7 we compare the simulated magnitudes and AB ratios to the measured values, when using fixed Sersic indices. Compared to the same plot when using variable Sersic indices in Figure 6.4, we see that there is much more scatter in the magnitude plots. There is some indication that this scatter increases for fainter sources, indicating that it is much harder to accurately measure the contributions towards the total brightness from each profile. The same is true for the AB ratio, where we a larger scatter in the data. In Figure 6.8 we see the simulated against measured effective radii. Again, compared to the plots using the variable Sersic indices we find there is significantly more scatter when measuring the effective radii of our simulated galaxies when we fix the Sersic index parameter.

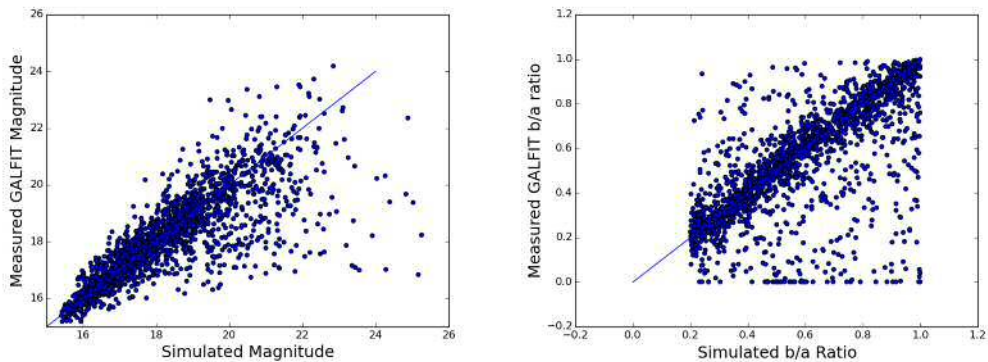


**Figure 6.7.** Left: Comparison of the measured and simulated magnitudes of our galaxies when using fixed Sersic indices. Right: Comparison of the measured and simulated AB ratios of our galaxies.

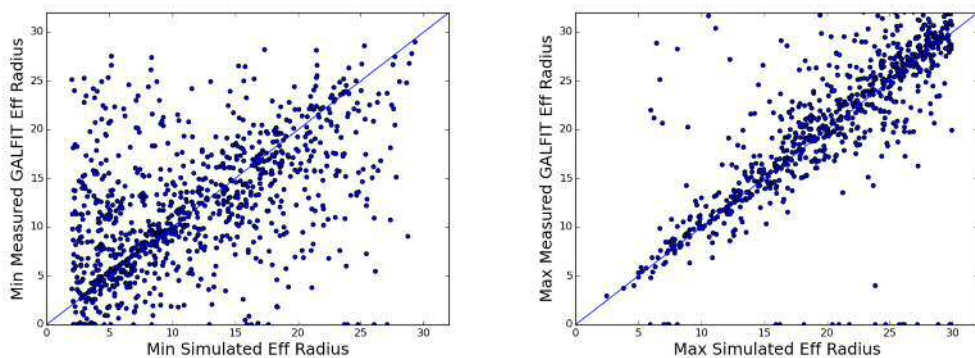


**Figure 6.8.** The simulated against measured effective radii of our sources, when fixing the Sersic indices, using variables positions for our components. We split our components up into the smallest effective radii (left) and largest (right) of each source.

#### 6.4.4 HIGH REDUCED CHI VALUES

GALFIT provides the parameters of the best fitting profile, alongside statistics on the goodness of fit, including the reduced Chi squared value for the model. This value can be used to judge how likely it is that the fit is correct and to compare the goodness of fit of multiple models. The reduced chi value distributions for our single, double variable and double fixed data can be seen in Figure 6.9.

As can be seen, in all three scenarios the reduced chi values reach very large values for a number of the galaxies. Convention says that reduced chi values around a value of 1 are deemed as reliable, yet these distributions show that the majority of our model fits would be considered unlikely. However, from the plots above it is clear that when fitting two profiles to our simulated galaxies, we are correctly finding

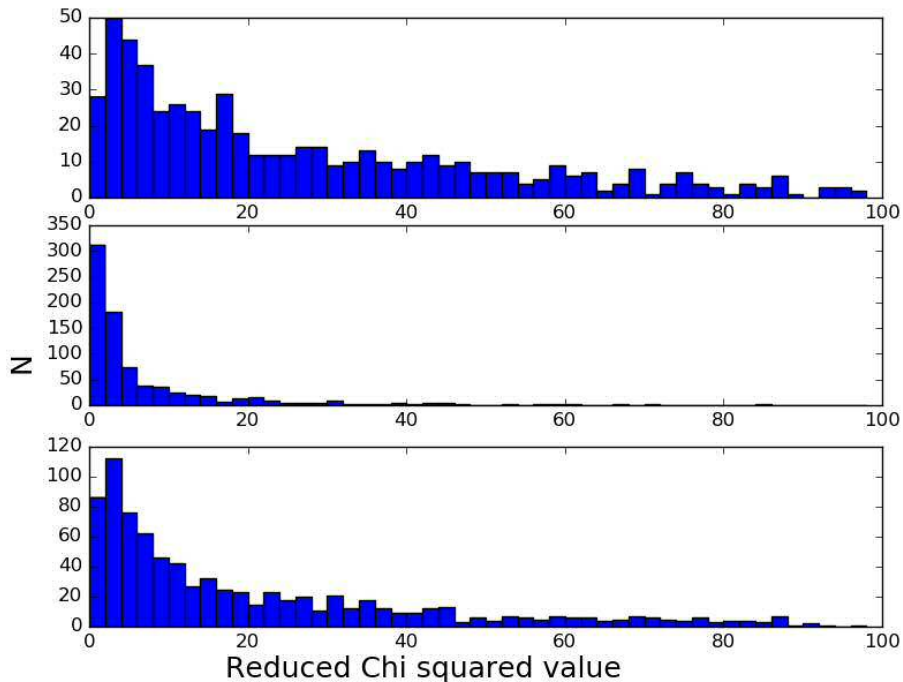


**Figure 6.9.** Histograms of the reduced chi squared values from our fits. The top plot is the values from fitting single Sersic profiles, the middle plot from fitting two profiles with fixed Sersic indices at  $n=1$  and  $n=4$  and at the bottom is from fitting two profiles with variable Sersic indices.

the structural properties of the galaxies. The cause of these high reduced chi squared values is likely due to how we generate our sources. We have noted an artifact in our residual images, produced by subtracting the best fit model from our simulated sources, which can be seen in Figure 6.10. The source of this artifact appears to be due to the method we use to generate sources, where we numerically integrate the Sersic function to calculate the total flux to be binned in to each pixel of our image. Increasing the number of points that we use to integrate over the pixel is likely to reduce this effect, but will increase the time to run our simulations and so is unfeasible to change. This method results in inaccuracies in the total counts in each pixel, resulting in this irregular and unrealistic pattern of counts in our sources.

This issue is likely the cause of our high reduced Chi values, along with our method of creating the sigma map. As a result we are not able to use the reduced chi values to determine whether our models have fit the data well or not. We are also not able to compare our fits to our real data fits, which will not suffer from this issue. However, the fact that we recover accurate models to our simulated galaxies shows that GALFIT is able to correctly measure the properties of multiple profiles.

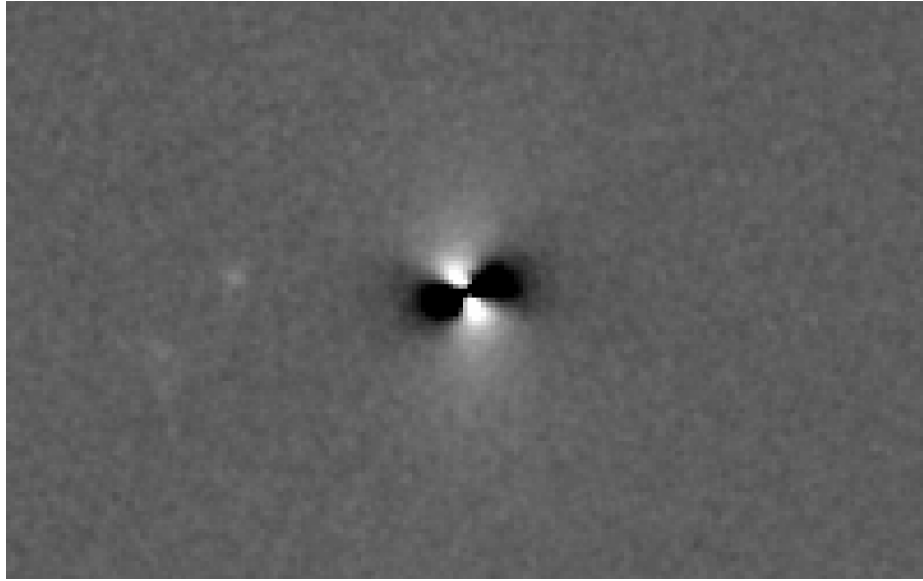


**Figure 6.10.** The artifact left over in the residual GALFIT image of each of our simulated galaxies.

#### 6.4.5 DISCUSSION OF THE SIMULATIONS

We tested the accuracy of GALFIT in finding the parameters of 1,000 simulated sources, built from two Sersic profiles. We tested five different methods to see which recovers the most accurate simulation parameters:

1. Fitting a single profile where the Sersic index and position are allowed to vary
2. Two profiles with fixed positions and fixed Sersic indices
3. Two profiles with fixed positions and variable Sersic indices
4. Two profiles with variable positions and fixed Sersic indices
5. Two profiles with variable positions and variable Sersic indices

From our analysis it is clear that fixing the positions of the profiles isn't wise. The position of the best fit single Sersic profile is rarely the same as the two best fitting individual bulge and disc components. By fixing the positions of components, GALFIT is forced to vary the other parameters to overcome the fact it cannot adjust the position parameter. By allowing the positions to vary, yet constraining them to a small distance from the best fit single Sersic profile position, GALFIT is able to

recover the structural parameters of a galaxy much more accurately, whilst still fitting to realistic positions.

Using fixed Sersic indices results in the parameters other than the Sersic index being less accurately recovered. The cause of this is probably due to GALFIT adjusting these parameters to overcome the fact it cannot adjust the Sersic index parameter, similar to the problem of using fixed positions. When using variable Sersic indices, we find GALFIT is much more accurate at finding the simulated parameters and finding reasonable fits for significantly more sources.

## 6.5 RUNNING GALFIT ON HERSCHEL GOODS GALAXIES

### 6.5.1 FITTING METHOD

Buoyed by the success of accurately identifying both components of our simulated galaxies, we now perform the same analysis on our Herschel GOODS galaxies. The Herschel GOODS sample is the same used in the previous Chapter 5. This is a sample of 525 Herschel galaxies which have been matched to optical sources from the CANDELS survey. Information on this sample of galaxies can be found in Section 5.2.2.

The galaxies have already been fit with single profiles by van der Wel et al. (2012) (hereafter vdW12), which we repeat to ensure that how we run GALFIT over the Herschel GOODS sources is consistent with other works. However, we do not go in to much detail or analysis over the single fit data. We follow the same method we used for our simulated galaxies, so we refer the reader to the previous section for the details on the fitting procedure. However, there are several key differences that we have learnt from our simulated data which we apply to our Herschel GOODS fitting.

When fitting two profiles to a galaxy, we choose to allow the positions of the profiles on the images to vary, unlike the work done by Bruce et al. (2012). The results from our simulated galaxies suggests that fixing the position of the galaxy components to the position of the single Sersic profile produces inaccurate results. We therefore allow the position of both profiles to vary, whilst forcing the positions to remain within  $\pm 1$  pixels of the positions of the best fitting single profile. This

stops the profiles from moving to fit to any background pixels or object which is not correctly masked.

We run our analysis twice, once where we fix the Sersic indices to  $n=1$  and  $n=4$ , in order to determine the contribution of brightness from the bulge and disc component. However we also perform a run where we allow the Sersic indices to vary. There is evidence that a significant fraction of galaxies at low redshifts contain a pseudobulge, with a low Sersic index, rather than a classical  $n=4$  bulge. By allowing the Sersic index of both profiles to vary, we can test whether the Herschel galaxies also exhibit disc like bulges.

### 6.5.2 SINGLE PROFILE FITTING

Like our simulated data, we find that reliable profiles cannot be found for a number of Herschel GOODS sources. Of our 525 sources, we find that 434 sources have a reliable profile when fitting a single Sersic profile, based on a reduced chi squared value close to 1.0. It appears that when using the real Herschel GOODS data we are much more likely to find a reliable profile than when we use our simulated data. We go into details of some of the important differences between the real and simulated data later in this chapter.

Here we analyse the results of our GALFIT fitting routine on the Herschel-GOODS sources. On the following plots, we only show the galaxies for which both we and vdW12 find reasonable fits. We begin by comparing our results of fitting a single Sersic profile to those found by vdW12. We allow the Sersic index value that we fit through GALFIT to vary freely. Figure 6.11 shows the values of Sersic index that we measure on the Herschel GOODS sources compared to those values found by vdW12. We see that in general we form a tight correlation between the two sets of values, though increasing scatter exists with increasing Sersic index.

In Figure 6.12 we compare the values of effective radius and magnitude of the single profiles fit by us and van der Wel et al. (2012). The plot of magnitude shows that we recover their results very well, forming a tight relationship of gradient unity. Our plot of effective radius forms a relatively tight correlation, but unusually the gradient of a line of best fit through the data is not of unity. Compared to Figure 6.12, we underestimate the effective radius at  $R_e < 7$  and over estimate it at values of  $R_e > 7$ . The cause of this disparity is unknown and does not exist in our simulated

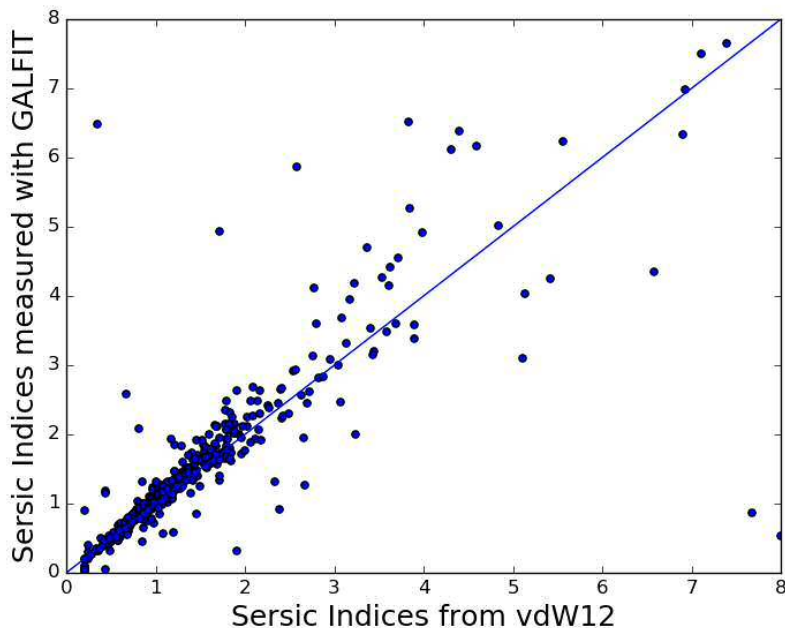


**Figure 6.11.** The measured Sersic indices of our Herschel GOODS galaxies against the Sersic indices found by vdW12

galaxies, which use the exact same process as this real sample of galaxies. We are confident that our parameter measurements are correct, as our work on simulated data correctly measures the parameters and because we use the basic version of GALFIT, whilst van der Wel et al. (2012) use a wrapper for GALFIT which provides less control over how the program is run. Whilst it is unusual that we do not reproduce the same value of radius as found by van der Wel et al. (2012), we do not use the effective radius value in any of our work and it is clear from 6.11 that we are correctly finding the Sersic indices and magnitudes of our real galaxies, which are the two pieces of data that we do use in this work.

### 6.5.3 SELECTING THE BEST DOUBLE PROFILE MODEL

We now run our Herschel GOODS galaxies through GALFIT and attempt to fit two profiles to them, representing a bulge and a disc component. We follow the same method as discussed in Section 6.4.2 and fit two profiles, with both fixed and variable Sersic indices and variables positions that can be within 1 pixel distance of the best fit single Sersic profile. Of our 439 sources, we find fits for 402/439 sources when using variable Sersic indices and 368/439 when using fixed Sersic indices.

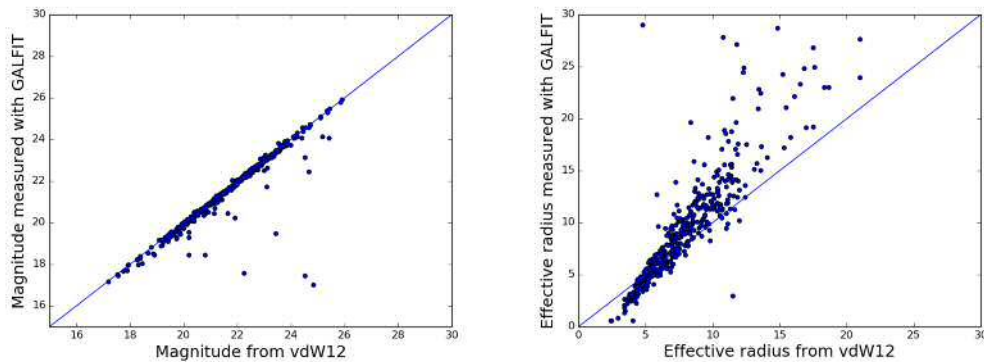


**Figure 6.12.** Left: The measured magnitude of our galaxies against the values found by vdW12. Right: The measured effective radii of our galaxies against the values found by vdW12.

We need to decide whether all of these fits can be deemed reliable, based on their measured parameters and reduced chi squared values. We first remove any source with a high reduced chi squared value. Because we do not fit any galaxy features such as star forming regions, spiral arms or AGN, our reduced chi squared values will always be relatively large, as there are features that we are not fitting to with GALFIT. Faint background sources that are not correctly masked, because they are not identified, will also contribute to an increased reduced chi squared value. In Figure 6.13 we plot the histogram of reduced chi values of our GALFIT run when we use variable Sersic indices and limited positions. There is clearly a peak in reduced chi squared values around 1.0, with an extending tail out to higher values. From the plot, we decide to set the limit for a reliable fit to a reduced chi value of 3.0. This value cuts off the extended tail of our distribution whilst including the peak.

To understand what causes such poor fits, we study 4 galaxies whose best fit profile has a reduced chi squared value of  $> 20.0$ . These are all excluded by our criteria above. We show cutout images of the galaxies, their best fit GALFIT models and the residual images in Figure 6.14. Here we go through each of the 4 sources in detail:

**Galaxy 310** has a reduced chi squared value of 37.50 and appears as a single source in the centre of the image. However, it appears that there is a possible Airy pattern around the source. GALFIT appears to have tried to account for this, as seen in the model image. This is likely to have caused an increased reduced chi squared value as GALFIT will unlikely be able to accurately create a profile to fit

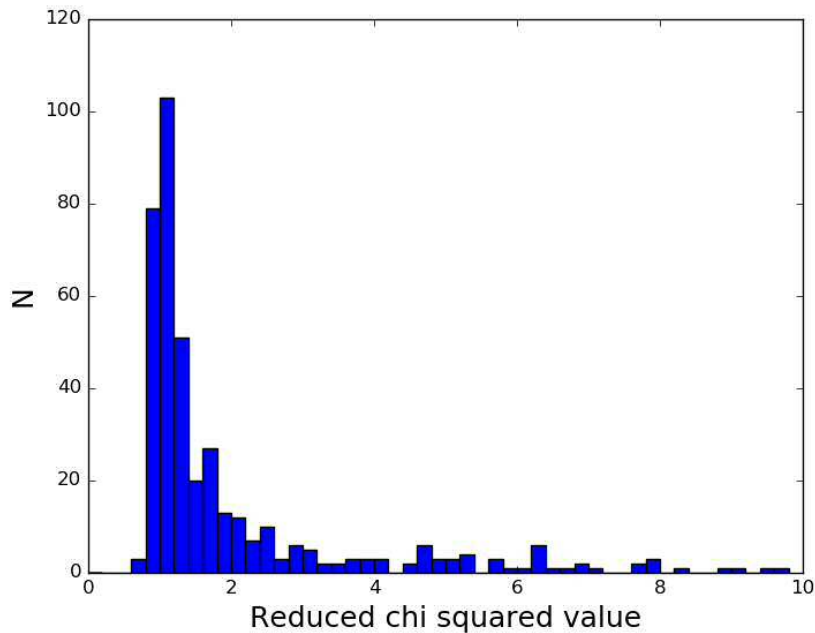


**Figure 6.13.** Histogram of the reduced chi squared values of our Herschel GOODS galaxies when fitting double Sersic profiles with variable Sersic indices.

this component.

**Galaxy 1210** has a reduced chi squared value of 27.65 and appears to be an extended source, with multiple peaks in brightness and is not symmetric. Fitting to sources with multiple components, such as merging or interacting galaxies, will produce poorer fits. This can be seen in the residual image, where the central areas of the source have been poorly fit. Fitting to the non-symmetric background emission around the bright peaks will only further decrease the accuracy of the fit.

**Galaxy 1648** has a reduced chi squared value of 21.54 and appears as a single bright galaxy, with a fainter 'tail' of emission above it on the image. The model image indicates that GALFIT has tried to fit to this background emission, but due to its irregular shape, it is likely that GALFIT has not fit to it very well. This can be seen in the residual image and is almost certainly the cause of the poor fit.

**Galaxy 4520** has a reduced chi squared value of 70.17 and appears to be a source consisting of multiple bright peaks, possibly due to a galaxy merger event. It is clear from the model image that GALFIT has not been able to accurately fit to the two individual bright peaks in the image, but has instead fit a single bright peak. This is confirmed in the residual image.

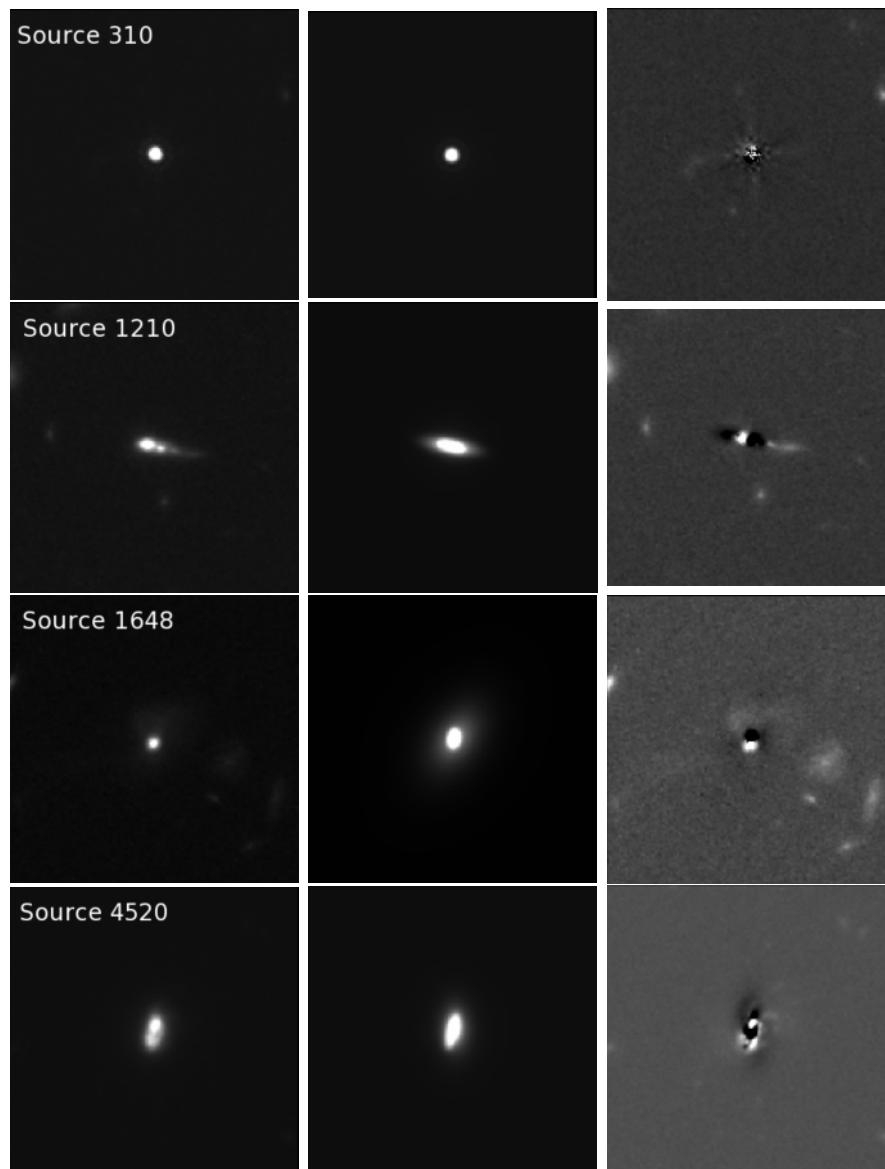


**Figure 6.14.** Example sources whose best fit GALFIT profiles have reduced chi squared values of  $> 20.0$ . The left image shows the actual galaxy, the middle image shows the GALFIT model and the right image shows the residual left after subtracting the model from the actual galaxy.

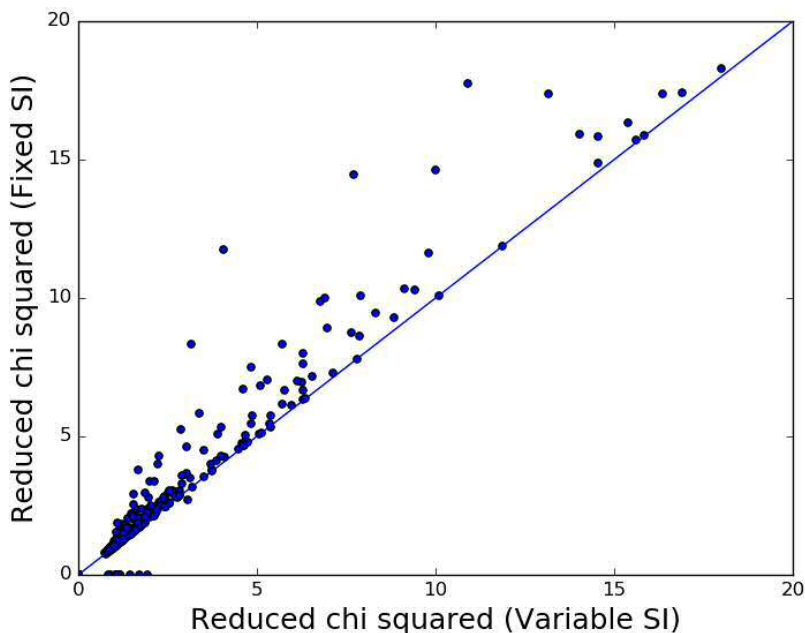


**Figure 6.15.** The reduced chi squared values when using fixed positions against using variable positions of our single profile fit.

We conclude that it is likely that the majority of our galaxies with poor fits from GALFIT are due to unusual or complex source profiles, which GALFIT is not able to correctly fit to.

In Figure 6.15 we plot the reduced chi values from our fixed and variables Sersic index runs against each other. Almost all sources are seen to have a lower reduced chi value when using variable Sersic indices. We expect this, as allowing the Sersic indices to vary should always produce a fit equal to or better than when we fix the Sersic index. We find that 9 of our sources have smaller chi squared values from their fixed Sersic index run than variable Sersic index. The cause of this is likely due these sources getting stuck in local minima, probably a result of constraining the positions of our models to be close to the simulated positions. However, as these few sources only have marginally better fits with fixed Sersic indices, we still include them in our analysis.

Finally, we remove any galaxy from our analysis which has unrealistic structural properties. We reject any profile fit in which one of the profile has an effective radius larger than 100 pixels, the size of our cutout images. Even nearby galaxies in the Herschel GOODS catalogue are smaller than our cutout images. As our position

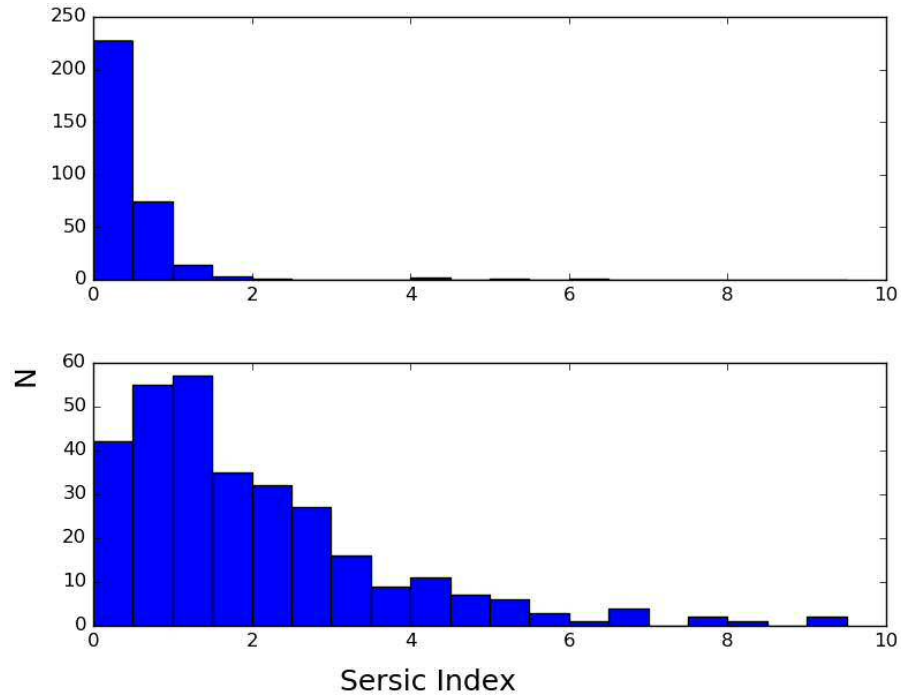


**Figure 6.16.** Histograms of the Sersic indices of the most disc-like (top) and most bulge-like (bottom) profiles. Here we have allowed the Sersic indices to vary.

values are constrained, we do not need to remove any sources based on their position. We also do not remove any source based on unrealistic AB ratio values, angle or magnitude. As we have do not know much about the profiles of our galaxies, if we remove any sources which may be considered unrealistic, we may in fact be removing real sources from our results. This leaves us with a sample of 324 galaxies that have been fit with double profiles, with variable Sersic indices and limited positions. This is our Herschel GOODS sample of galaxies that we will analyse in the rest of this chapter.

#### 6.5.4 DOUBLE PROFILE FITTING

We now analyse the structural parameters found by fitting two independent profiles to our Herschel GOODS galaxies as dicussed above. We begin by studying the distributions of Sersic indices of each profile in Figure 6.16. In this plot we have allowed the Sersic indices of our sources to vary freely. The most obvious feature of these plots, and one of the key results of this work, is that for many of the galaxies, both profiles are best fit with low Sersic indices. This model of two disc like profiles

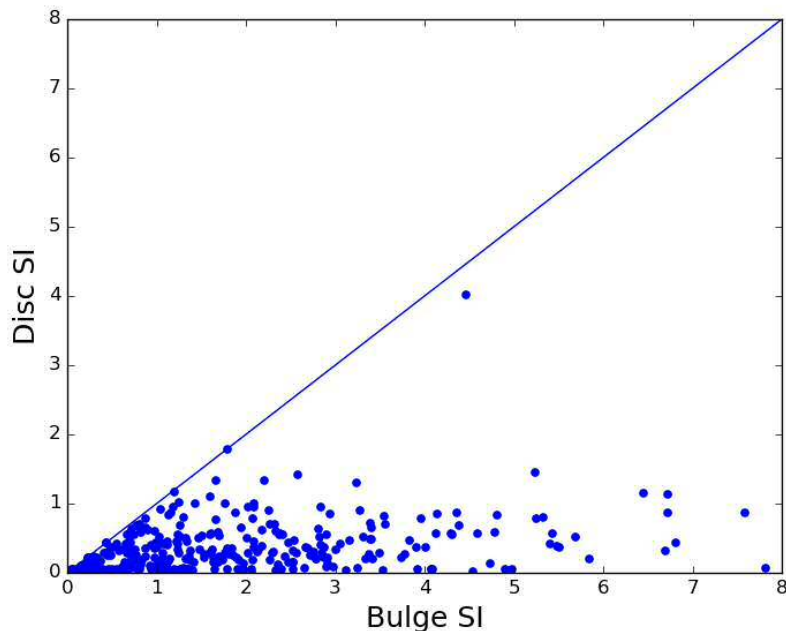


**Figure 6.17.** The Sersic indices of the most disc-like profiles against the most bulge-like.

goes against the idea of classic bulges and suggests a large fraction of star forming galaxies feature disc-like or pseudobulges.

We can see this better in Figure 6.17 where we plot the Sersic index of the bulge component against the Sersic index of the disc component. We define the bulge component as the one with the largest Sersic index. If our galaxies exhibit two disc-like profiles, then our definition becomes blurry; we address this confusion later. The majority of sources have two profiles both with low Sersic indices, occupying the bottom left hand corner of the plot. It is more clear in this plot that indeed both components are often measured as disc-like. We also see a number of sources which have a classical bulge and disc component, with one component having a Sersic index  $n > 2.5$  and one with  $n < 2.5$  respectively. We see one candidate which exhibits two bulge like profiles.

This result agrees with work done at low redshift that finds that many galaxies exhibit disc like bulges, so called pseudobulges. Vaghmare et al. (2015) find that 77% of their sample of spiral galaxies feature pseudobulges, whilst Fisher & Drory (2011) find that 45% of local near-infrared detected galaxies have pseudobulges. The fact that we measure so large a fraction of our galaxies as having disc like bulges at high

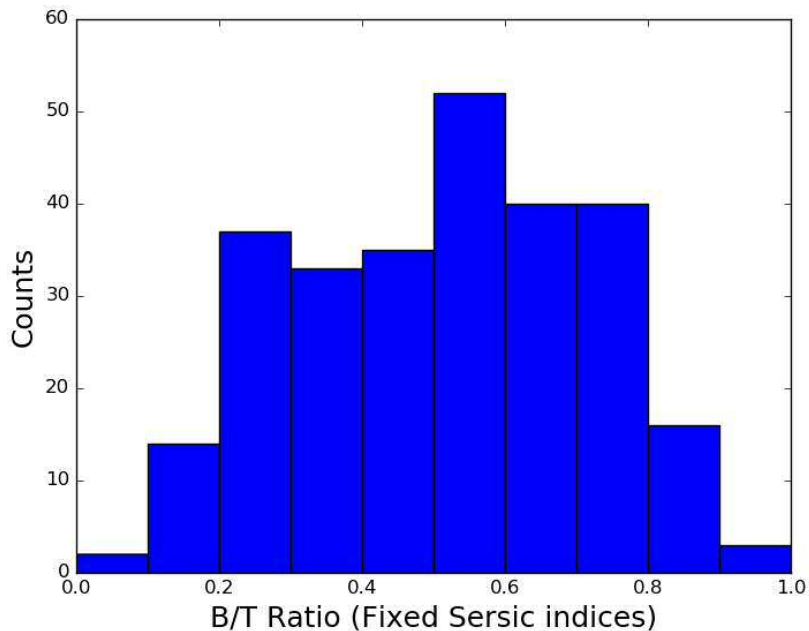


**Figure 6.18.** Histogram of the bulge to total flux ratio's of our Herschel GOODS galaxies, using variable Sersic indices.

redshift is a new result. This would suggest that pseudobulges have existed and been in place for a significant fraction of the age of the Universe, agreeing with the results found from galaxy simulations by Okamoto (2013) and Guedes et al. (2013), who found that pseudobulges were already in place by  $z = 2 - 3$ .

One question to ask is whether these galaxies may be best fit with a single disc like profile, where the second profile is redundant. It may be that the second profile is being fit to a bright star forming region or other feature in the galaxy, rather than to a bulge or disc component. To test if this is the case, we plot ratio of bulge to total flux of our galaxies, which can be seen in Figure 6.18. Only 3 of our sources are bulge dominated, defined as having a B/T ratio greater than 0.9, whilst only 2 of our sources have a bulge component which contributes less than 10% of the total flux of the source. It is clear that very few of our sources have a profile fit in which one of the components contributes little to the overall brightness of the galaxy, suggesting that we are indeed correctly fitting the bulge profiles in our sample.

The plot of single profile Sersic index against the bulge-to-total brightness ratio has been studied for galaxies when a fixed bulge-like and disc-like profile have been fitted to galaxies (Bruce et al., 2012). In galaxies with classical bulges, the fraction

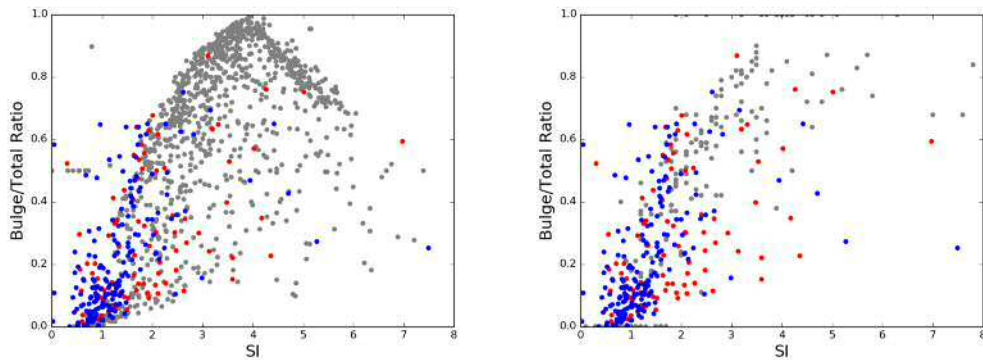


**Figure 6.19.** The plot of measured bulge to total flux ratio against the Sersic index of the best fit single profile, using fixed Sersic indices. Those galaxies which exhibit a bulge with  $n < 2.5$ , labelled as pseudo bulges, are shown in blue. Classic bulges, determined by having a Sersic index of  $n > 2.5$ , are plotted in pink. Left: Our simulated galaxies are plotted as grey points. Right: We plot the CANDELS galaxies studied in Bruce et al. (2012) as grey points.

of light from the bulge is defined as:

$$B/T \text{ ratio} = \frac{F_{Bulge}}{F_{Bulge} + F_{Disc}} \quad (6.6)$$

This forms a relatively tight relationship with the Sersic index of the best fitting single profile. In the left hand plot of Figure 6.19, we show the results of our Herschel GOODS galaxies as well as the results of our simulated galaxies. We have used fixed Sersic indices, at  $n=1$  and  $n=4$ . The Herschel GOODS galaxies appear to form a similar trend as the simulated 'classical' galaxies. However, some of the real galaxies seem to have a lower single Sersic index at a given B/T ratio than the simulated galaxies. This could be some indication that the relationship breaks down for galaxies with pseudobulges. In the right hand plot we show our galaxies plotted along with the CANDELS galaxies from Bruce et al. (2012). Their sample consists of 192 galaxies, whose B/T ratio have been measured in the  $H_{160}$ -band. We see that more of our galaxies are disc dominated, with fewer of our galaxies occupying the graph in the region of  $B/T > 0.5$ . Both samples of galaxies create a similar distribution, though some of our galaxies have a lower Sersic index value at a given B/T ratio, similar to what we see when we compare to our simulated data.

In Figure 6.19, we have also split our Herschel GOODS galaxies up by the Sersic index of their bulge, estimated from the variable Sersic index run. We use the

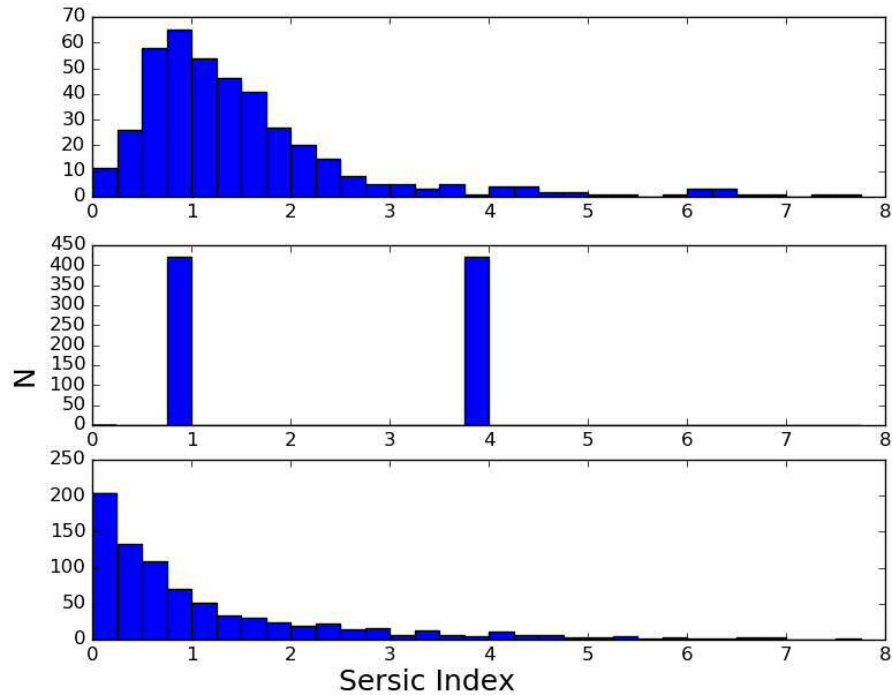


**Figure 6.20.** Histograms of the Sersic indices of our Herschel GOODS galaxies. The distributions are from fitting single Sersic profiles (top), double profiles with fixed Sersic indices (middle) and fitting double profiles with variable Sersic indices (bottom)

definition above and separate our galaxies between classical and pseudobulges at a value of Sersic index  $n=2.5$ . We test whether some of the scatter in the plot is caused by different bulge profiles; however, no such pattern seems to occur in the plot, with both populations overlaying each other.

In Figure 6.20 we show the measured Sersic indices of the single profile fits and the double profile fits, with fixed and variable Sersic indices. Our single profiles form a distribution which peaks at  $n=1$ , implying that the galaxies are all typically disc dominated. Again, we clearly see that when we fit our galaxies with variable Sersic indices, our galaxies are often best fit by two disc-like profiles.

To analyse these galaxies further, we separate them based on their contribution from each profile. For this, we define 'classical bulges' as bulge components with a Sersic index  $n>2.5$  and 'pseudobulges' as those with  $n<2.5$ . We separate our galaxies in to 3 categories:

1. Dominant profile - A galaxy with a component that contributes more than 90% of the total emission

2. Classical Bulge - Those with no dominant component and with a bulge component with  $n > 2.5$
3. Pseudobulge - Those with no dominant component and with a bulge component with  $n < 2.5$

Galaxy Type	Number	Percentage
Galaxies with a dominant profile	5	1.5%
Galaxies with a Classical Bulge	102	31.5%
Galaxies with a pseudobulge	217	67.0%

**Table 6.2.** The statistics of the different types of galaxies that make up our Herschel GOODS sample.

The numbers of each type of galaxy can be seen in Table 6.2. We see that only 5 of our sources have a dominant profile, defined as one which contributes more than 90% of the light from the galaxy. The majority of these are disc dominated, something we expect to detect with Herschel, due to disc galaxies typically being dustier and having significant ongoing star formation. Around one quarter of our sample have no dominant component but do have a classical bulge component, whilst the rest of our galaxies feature a pseudobulge. The majority of the Herschel GOODS galaxies therefore do not follow the classic idea of galaxies having high Sersic index bulges and low Sersic index discs, but instead agree with the observations of galaxies at low redshifts which have disc like, low Sersic index bulges.

One concern is that many of our galaxies may be very disc dominated, exhibiting negligible flux from a bulge component. In this case, forcing GALFIT to fit two profiles may result in two nearly identical profiles being fit to the single disc component of the galaxy, with the total flux of each fit component equalling the flux of the galaxy disc. This would explain why both components of many of our galaxies are disc like. To test this, we plot the effective radius of the two profile components in Figure 6.21. We plot the components with the largest effective radius in the top plot, and those with the smallest effective radius in the bottom plot. From the plot, it is clear that the effective radii of both components are significantly different. The distribution of effective radius of the smallest component peaks at small values, implying that it is likely being fit to a bulge component of the galaxy. The largest effective radius peaks at significantly higher values, which is likely to be the galaxy disc. The

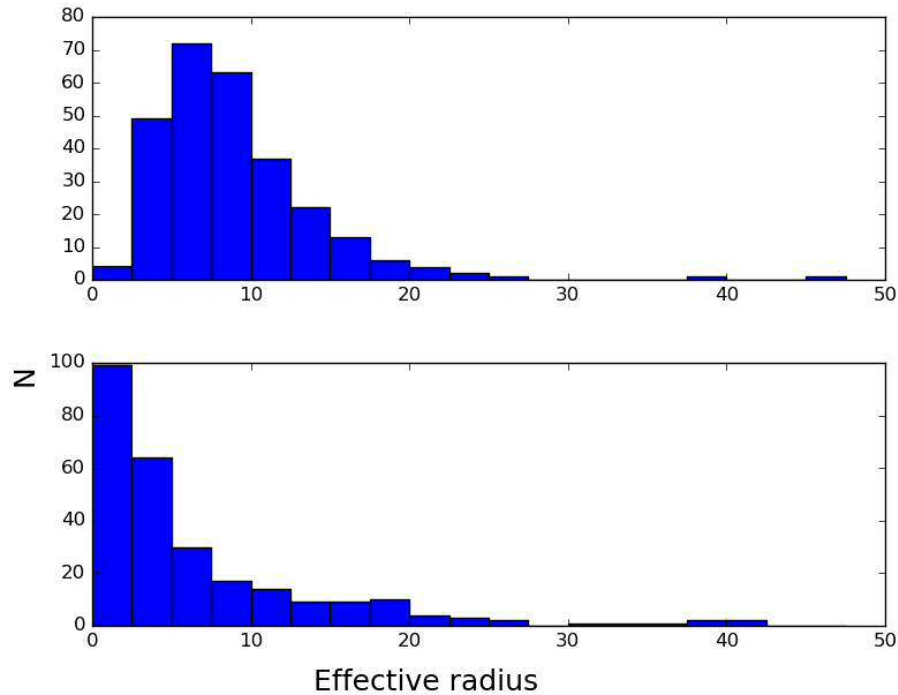


**Figure 6.21.** Histograms of the effective radii of our Herschel GOODS galaxies. The top plot shows the components of each galaxy with the largest effective radius and the bottom shows those with the smallest values.

fact that the effective radii are different implies that we are not simply fitting two profiles to the galaxy disc, but that we are detecting bulges with low Sersic indices.

Previously in this chapter we discussed our results of fitting Sersic profiles to a set of 1,000 simulated galaxies. These galaxies were generated with two components: a disc and a classical bulge. The range of parameters used to generate these profiles can be seen in Table 6.1. When we fit two Sersic profiles to each of these galaxies, allowing the Sersic indices to vary, we find that we accurately recover the input parameters, as seen in Figures 6.3-6.5. This confirms that GALFIT is reliably recovering the bulge and disc components of galaxies, reassuring us that the non-classical bulge result of our Herschel GOODS galaxies is correct. We also ran a sanity check to see whether GALFIT correctly recovered the parameters of a sample of simulated galaxies which were generated with a disc profile and a pseudobulge, both with typical Sersic indices  $n = 1$ . We find that GALFIT does correctly recover both profiles. After these tests and the finding that our result closely matches those found by vdW12 for single Sersic fits to Herschel GOODS sources, we are confident that our conclusion that Herschel GOODS galaxies exhibit disc-like/pseudo bulges is correct.

## 6.6 THE PROPERTIES OF GALAXIES AND THEIR INTENSITY PROFILES

In Chapter 5, we measured the physical properties of our Herschel GOODS galaxies. We estimated values including the star formation rate (SFR), stellar mass ( $M_*$ ) and dust mass ( $M_D$ ) using the public code MAGPHYS. We studied several relationships and correlations between different parameters, such as the star forming main sequence of galaxies and the Kennicutt-Schmidt relationship. Using the data we have found in this chapter on the structure of the same galaxies, we study the relationship between the physical parameters and structural parameters of our Herschel GOODS sample of galaxies.

The majority of our galaxies can be split into two categories: around three quarters feature a disc-like pseudobulge and around one quarter feature a classical bulge. Several works (Fisher & Drory, 2010) suggest that Sersic index alone is only effective at differentiating between pseudo and classical bulges in 90% of cases. However, pseudobulges are expected to be forming many more stars than classical bulges. We can therefore test whether the combination of Sersic index of the bulge and the star formation properties of a galaxy can distinguish between a classical bulge and pseudobulge.

In Chapter 5 we plotted our galaxies in terms of the galaxy main sequence, a relationship between the stellar mass and star formation rate of star forming galaxies. It is interesting to see whether our two different types of galaxy bulges occupy different areas on the plot. In Figure 6.22 we show the galaxy main sequence for our classical and pseudo bulge galaxies. Those galaxies with a bulge with Sersic index  $n > 2.5$ , the so called classical bulges, are plotted in red, and those with  $n < 2.5$  are plotted in blue. We measure the scatter of both populations, about the redshift dependant main sequence lines. The scatter for the classical bulges is 0.521, 0.423 and 0.552 dex for the  $0 < z < 1$ ,  $1 < z < 2$  and  $2 < z < 3$  bins respectively, whilst the pseudobulges have scatters of 0.450, 0.355 and 0.476 dex for the same bins. Over all redshifts bins, the classical bulges have a larger scatter than the pseudo bulges. This implies that galaxies with classic bulges are less homogeneous than pseudobulges and exhibit a large range of star formation rates per stellar mass than pseudobulges.

A similar result was found by Morselli et al. (2016), who studied a sample of 265,000 local SDSS galaxies, with redshifts  $0.02 < z < 0.1$ . They identify galaxies as

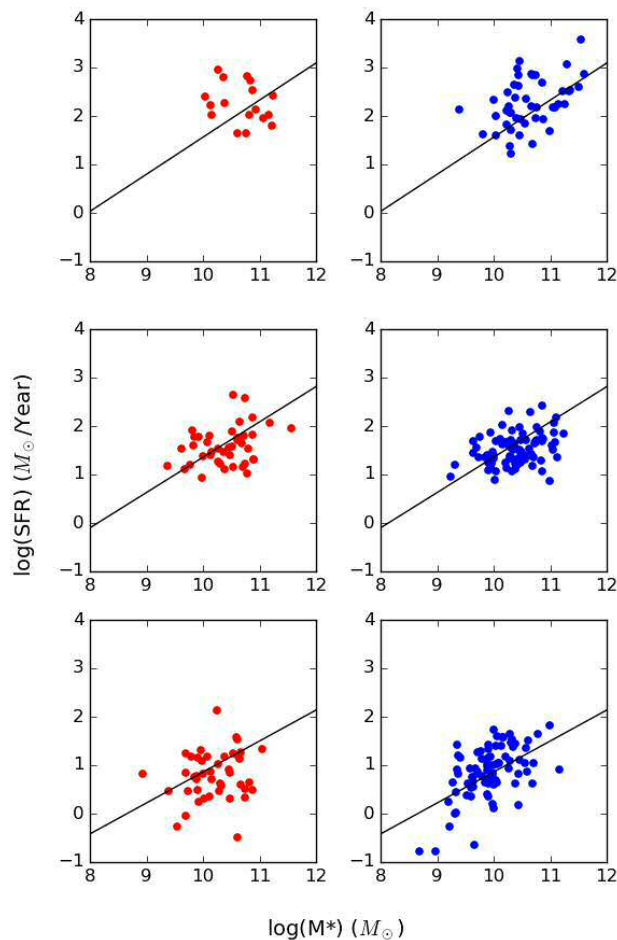


**Figure 6.22.** The galaxy main sequence, built from our Herschel GOODS sample. Galaxies shown in blue have a pseudobulge and those in red have a classical bulge. The bottom row are galaxies binned between  $0 < z < 1$ , the middle row between  $1 < z < 2$  and the top row between  $2 < z < 3$ . The black lines are the redshift dependant main sequence lines, given in Speagle et al. (2014)

pseudo or classical bulges based on their velocity dispersion and the SDSS concentration parameter, defined as the ratio of  $R_{50}/R_{90}$ , the radii containing 50% and 90% of the flux. They find that those galaxies in the outer envelopes of the main sequence are more consistent with being classical bulges, whilst the galaxies in the centre are more similar to pseudobulges. This agrees with our result that pseudobulges follow the main sequence more tightly than classical bulges.

In Figure 6.23 we show histograms of the offsets of our classic and pseudo bulges from the plotted main sequence lines. The mean values of the distributions can be seen in Table 6.3. For the  $0 < z < 1$  bin, our classic bulges lie on average

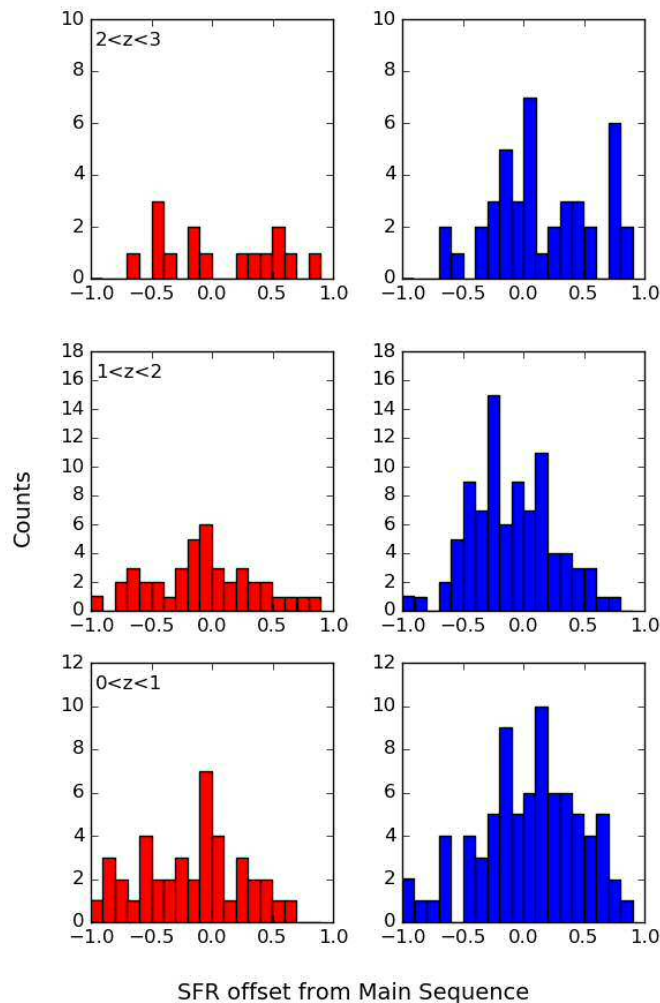


**Figure 6.23.** Histograms showing the displacement in star formation rate of our classic (red) and pseudo bulge (blue) galaxies.

below the main sequence whilst our pseudobulges lie above. For galaxies with redshifts  $1 < z < 2$ , both galaxy samples lie below the main sequence, with the pseudobulges exhibiting more negative offsets on average. Finally, for  $2 < z < 3$  both samples lie above the main sequence, with pseudobulges exhibiting more positive offsets than the classic bulges. We perform a two sample Kolmogorov-Smirnov test, for the pseudo and classical bulges in each redshift bin. We calculate p values of 0.0164, 0.5389 and 0.6084 for the  $0 < z < 1$ ,  $1 < z < 2$  and  $2 < z < 3$  bins respectively, implying that we cannot reject the null hypothesis that samples are drawn from the same distribution for the two highest redshift bins.

Other authors have shown that the scatter of the main sequence is a result of the different intensity profiles of the bulges of star forming galaxies. The cause of

Redshift	Bulge Type	Offset from Main Sequence
$0 < z < 1$	Classic	-0.191
	Pseudo	0.042
$1 < z < 2$	Classic	-0.068
	Pseudo	-0.111
$2 < z < 3$	Classic	0.173
	Pseudo	0.224

**Table 6.3.** The mean values of the offsets of our classic and pseudobulges from the main sequence lines, shown in Figure 6.23

this scatter has been studied before and has been put down to a variety of different properties, including different formation times (Speagle et al., 2014) and mass accretion rates (Dutton et al., 2010, Forbes et al., 2014). We cannot confirm this from our results as we find no significant differences between the pseudo and classical bulge distributions.

We therefore find some evidence, based on the scatter of the classical and pseudo bulge galaxies around the main sequence, that the intensity profile of the bulge does seem to affect the position of the galaxy on the main sequence. This agrees with the work by Morselli et al. (2016), who also found that classical bulge galaxies tend to occupy the outer envelopes of the main sequence, whilst pseudobulge galaxies are more concentrated towards the centre.

Because our galaxies are all very disc dominated, it is difficult to study the evolution of B/T ratio with redshift, as done in Bruce et al. (2012). However, we can study the evolution of the fraction of galaxies with pseudo and classical bulges. In figure 6.24 we plot these fractions against redshift, with classical bulges shown in red and pseudo bulges shown in blue. There is some evidence evolution in the fraction of each bulge type from the earliest to latest times, but there also seems to be little evolution between redshifts  $z \approx 0.75 - 2.25$ . We conclude that there is little evidence that the fractions of pseudo and classical bulges change over time from this plot.

## 6.7 CONCLUSIONS

The aim of this work was to reliably decompose a sample of sources in to their bulge and disc components. We aim to find the contribution of emission of our galaxies from the individual bulge and disc components. We use the public

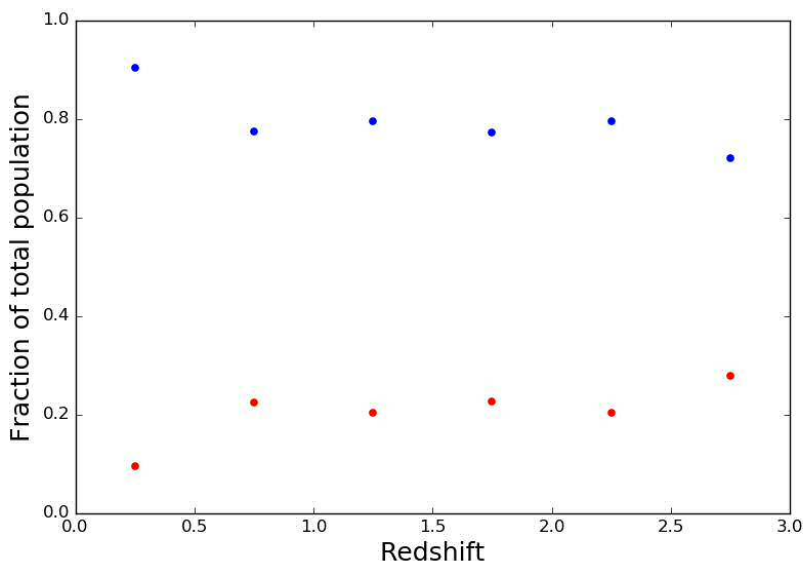


**Figure 6.24.** The redshift evolution of the fraction of our sample with pseudobulges (blue) and classical bulges (red).

code GALFIT to simultaneously fit two profiles. We begin by testing the ability of GALFIT to correctly extract multiple profiles from galaxies. To do this, we simulate 1,000 galaxies built from a bulge and disc component, with various Sersic indices, brightness magnitudes, sizes, inclinations and angles. We find that we are able to accurately measure the parameters of our galaxies, proving that it is able to detect multiple components of galaxies.

We test several setups of GALFIT in order to decide the best method to run on our galaxies. We compare the accuracy of allowing the positions of the components to vary, whilst limiting them to a reasonable range of values and fixing them to the position of the best fitting single Sersic profile. The fixed positions ensures the profiles do not wander away from the galaxy to fit some bright peak in noise, background or un-masked background source. However we find significantly more scatter in the measured parameters when we fixed the positions rather than allowing them to vary. This is not a surprise because the bulge and disc components are unlikely to have the same positional centre as the best fit single profile.

Buoyed by the success of our simulated galaxies, we performed the same analysis on a sample of real galaxies. Our sample consists of galaxies present in both the GOODS and Herschel catalogues, referred to as the Herschel GOODS catalogue. The matched source catalogue consists of 525 sources, which is reduced to 439 when we

remove those that we cannot create cutout images for. The biggest discovery is that the majority of the Herschel GOODS galaxies exhibit bulges with low Sersic indices. We find that over two thirds of our galaxies have bulges with Sersic indices  $n < 2.5$ . It is likely that some of these are so called pseudobulges, with the rest being disc like classical bulges.

This sample of galaxies was analysed in Chapter 5, where their physics properties such as starformation rate, gas mass and stellar mass were estimated. In this chapter we have studied whether any of these parameters are linked to the structural parameters of the same galaxies found in this chapter. We find that some of the scatter in the main sequence is a result of the intensity profile of the bulge, with classical bulge galaxies tending to have a larger scatter than pseudobulges. This was also seen by Morselli et al. (2016), who noted that pseudo-bulge galaxies followed the main sequence much tighter than galaxies with a classical bulge. We study the position of pseudo-bulge galaxies on the galaxy main sequence and find no evidence that they lie at higher star formation rates per stellar mass than classical bulge galaxies, implying that pseudo-bulge galaxies do not form more stars on average than classical bulge galaxies.

# 7

## Conclusions

*”If people sat outside and looked at the stars each night, I’ll bet they’d live a lot differently”*

– Bill Watterson, *Calvin and Hobbes*

### 7.1 THESIS OVERVIEW

The key aim of this thesis was to use data from the Herschel Space Observatory to improve our knowledge of dusty, submillimetre bright galaxies. The areas of the sky covered by Herschel were often chosen to coincide with other surveys, providing a panchromatic view on galaxies. An important part of this thesis covers the method and results of matching Herschel sources to these optical, radio and infrared surveys. Utilising the multi-wavelength photometry we were able to study both the optical and infrared peaks of stellar emission and hence study the complete star formation of Herschel galaxies. We studied the properties of extreme starburst galaxies against those which are quiescently forming stars in order to identify any differences in their star formation histories as a population. Finally, we studied the structural properties of a sample of Herschel galaxies to determine the relative light emission from each of the disc and bulge components. We tested whether there were any correlations between the structural and physical properties of the galaxies.

## 7.2 KEY RESULTS

In Chapter 2 we matched the Herschel ATLAS catalogue to near infrared VISTA VIKING sources over the GAMA equatorial fields and studied the accuracy of this source matching process.

- Around 80% of Herschel ATLAS sources have at least one nearby VIKING source; however, only 49% of Herschel ATLAS sources have a reliable VIKING counterpart. This agrees with the work by Fleuren et al. (2012), who carried out a similar study over a smaller area, in which they find that 50.3% of Herschel sources in the GAMA 9-h field have a reliable counterpart.
- I find values of  $Q_0$ , the fraction of Herschel sources with a VIKING counterpart above the survey limit, of 0.677, 0.709 and 0.783 for the GAMA 9-h, 12-h and 15-h fields respectively. This is similar to the  $Q_0$  value found by Fleuren et al. (2012) of 0.72 for the GAMA 9-h field. Smith et al. (2011) found a  $Q_0$  value of 0.593 when matching the Herschel ATLAS catalogue to Sloan Digital Sky Survey (SDSS) sources, implying that the VIKING survey is much better at finding counterparts to Herschel ATLAS sources than SDSS.
- Whilst 50.3% of Herschel ATLAS sources have a reliable VIKING counterpart, only 40.0% have a reliable SDSS counterpart. 31.8% of Herschel sources are reliably matched to the same sources present in both the VIKING and SDSS surveys, but in 2.8% of cases, Herschel sources are matched to different VIKING and SDSS sources.

In Chapter 3, we use the Herschel-VIKING matched catalogues from the previous chapter. Using this result, we made estimates of the number of gravitational lenses present in the Herschel ATLAS data.

- I find a large number of VIKING sources which are reliably matched to Herschel ATLAS sources out to an estimated redshift of the Herschel ATLAS sources of  $z=3$ . Assuming that VIKING is shallower than Herschel ATLAS, these reliably matched sources cannot be the same source observed with both Herschel and VIKING and so must be gravitational lensing systems. This is a slightly surprising result, as we didn't expect such a large fraction of the Herschel ATLAS sources to be lensed.

- We compare our gravitational lensing result to that found by Wang et al. (2011) and González-Nuevo et al. (2014), who identified gravitational lenses in Herschel data using the angular cross-correlation method. We find that both methods give a similar result for the overdensity of VIKING sources around Herschel sources.
- We compare our results to those found by Negrello et al. (2017). We note that our method identifies 14 of the 24 sources identified by Negrello et al. (2016).

In Chapter 4, we matched the Herschel ATLAS North Galactic Pole field catalogues to optical Subaru Deep Field (SDF) data, using radio data to provide accurate positions.

- I find that 196, or 29.0%, of our Herschel ATLAS sources have a reliable radio VLA counterpart; however this is a lower boundary, as the sensitivity of the VLA map falls off towards the edge of the map, causing many radio counterparts to be too faint to observe. We calculate a value of  $Q_0$  of 0.645 for those sources in the central most sensitive area.
- Of our 196 Herschel-VLA matched sources, we find that 149 have one unique nearby reliable counterpart in the SDF catalogue and 2 sources have two possible nearby counterparts. Therefore, 45 sources do not have a K-magnitude counterpart above the survey limit.
- I tested the accuracy of directly matching Herschel ATLAS sources to near infrared catalogues as opposed to using radio data as an intermediary to first get accurate positions for the Herschel sources. We find that over the entire field there are 60 Herschel ATLAS sources which have a reliable match from both using radio positions and directly matching. Of these 60 sources, 10 are matched to different SDF sources. From the cutout images, we find that 3 of the sources are likely mergers, whilst the other 7 are simply cases of the two methods identifying different sources as the most reliable.
- Using the public code HyperZ we test our photometric redshifts estimated from the Herschel fluxes alone, as used in Chapter 3. We find that our Herschel

estimated redshifts correlate poorly with those calculated from the optical photometry with HyperZ, which are known to be very accurate. We conclude that this is a possible cause of our unusual gravitational lensing result in Chapter 3.

- From the K magnitude-redshift diagram, we note that our galaxies have a similar dispersion to that found by other authors for samples of radio galaxies. It is a relatively small scatter, suggesting that the radio and optical matched Herschel galaxies are relatively homogeneous, with similar stellar masses at all redshifts, and have followed similar evolutionary paths.
- We also show from the K magnitude-redshift diagram that the VIKING survey can observe galaxies out to a redshift  $z \simeq 1.25$ . It is therefore not possible for VIKING to detect the Herschel galaxies at high redshift and so any counterparts may be gravitational lens systems. We conclude that we cannot determine whether the gravitational lensing result from Chapter 3 is correct or not.

In Chapter 5, we study the properties of two samples of Herschel galaxies, the Herschel-SDF and Herschel-GOODS samples, to understand how they have evolved with redshift.

- Our Herschel galaxies agree well with the galaxy main sequence best fit lines given in Speagle et al. (2014). We see an evolution in our galaxies for them to have higher star formation rates per stellar mass with increasing redshift.
- I find that only 7.5% of our Herschel-GOODS galaxies are starbursts, following the definition in Rodighiero et al. (2011), implying that starbursts are relatively rare in the Universe.
- I plotted the two galaxies samples on the Kennicutt-Schmidt relation. We find strong evidence of evolution with redshift, with galaxies shifting upwards towards higher star formation rates per gas mass with increasing redshift. This suggests galaxies in the past were more star forming efficient than today.
- I find similar star forming efficiencies between main sequence and starburst galaxies. This implies that the increase in star formation in starburst galaxies is likely due to an increase in gas mass, or some other effect.

- The relation between dust mass and stellar mass of our Herschel galaxies evolves with redshift. Galaxies of different stellar mass have more similar dust masses at high redshift than in the local Universe. Starburst galaxies consistently have higher dust mass per stellar mass than main sequence galaxies at all redshifts.

In Chapter 6, we measure the relative contributions the bulge and disc components of our sample of Herschel-GOODS galaxies. We study whether the shape of the galaxies correlates to any properties of the galaxies.

- Using a set of simulated galaxies, with a distinct bulge and disc component, we find that we are able to accurately recover both the simulated bulge and disc components and their parameters.
- Of our Herschel galaxy sample, 31.5% of galaxies feature a classical bulge with Sersic index greater than 2.5. However, 67.0% of the galaxies feature a disc like bulge, or pseudo-bulge, with Sersic index less than 2.5. It is clear that the vast majority of our Herschel-GOODS galaxies have disc-like or pseudo bulges.
- We see no evidence of a separation on the galaxy main sequence of those Herschel GOODS galaxies with a classical bulge and those with a disc-like bulge. We also see no separation based on the bulge-to-total flux ratio of the galaxies, implying that the shape of the bulges of galaxies has little effect on its star formation and hence its position on the main sequence.
- We note that the fraction of disc-dominated galaxies with pseudo-bulges has gradually increased from redshift  $z=3$  to the current day, whilst the fraction of classical bulges has decreased.

### 7.3 FUTURE WORK

This thesis has used several different techniques to study how dusty, star forming galaxies have evolved since  $z \approx 3$ . For much of the work, I have utilised the multi-wavelength data available for many of the Herschel surveys to better understand the physical properties and history of these galaxies. To do this, I have often had to first match the Herschel sources to shorter wavelength samples. Whilst the method I have used is not novel, the data I have worked on and the sheer number of sources makes

this work unique. One key result that may indicate a flaw in the current source matching method is that in over 10% of cases, when directly matching Herschel sources to shorter wavelength catalogues, the identifications are probably incorrect. The solution to this is to first match the Herschel sources to radio counterparts, to get more accurate positions of the sources, before matching to shorter wavelength catalogues. Future radio surveys will be able to find the radio counterparts to a significant fraction of Herschel sources across the sky. This will begin to provide, for the first time, accurate radio counterparts for a large number of Herschel sources, allowing us to more easily find reliable counterparts in other wavelengths.

I have continued the work done by other authors, such as van der Wel et al. (2012) and Bruce et al. (2012), in decomposing large populations of high redshift galaxies into their individual components. I have studied the physical properties of a sample of Herschel galaxies in terms of their physical parameters, such as the bulge and disc contribution, shape and size. Whilst the decomposition of galaxies has been studied in detail before, there is much work that can be done in studying the link between the structural parameters of each component and the physical properties of the galaxy overall. Our work finds little correlation between the stellar, dust and gas properties of galaxies and their bulge-disc ratios, but one avenue to pursue would be to study the physical properties of the components individually. It would be interesting to see whether the shape of the bulge does have any effect on the star formation rate and find what properties differ between classical and pseudo-bulges.

## **Appendix A**

### **Herschel-VLA-SDF matched sources table**

Herschel ATLAS ID	Herschel RA	Herschel Dec	F250	F350	F500	E250	E350	E500	Source Separation	Reliability	Radio Flux	Radio Error	Flux
HATLAS_J132522.6+271457	201.344553	27.249202	0.245967	0.099657	0.050849	0.005296	0.005685	0.007075	1.222	0.99438	401.101		70.728
HATLAS_J132505.7+273244	201.27405	27.545615	0.220764	0.089711	0.032434	0.005563	0.005768	0.006669	0.92	0.891431	1481.0		28.0
HATLAS_J132503.8+273318	201.266196	27.555135	0.147929	0.053803	0.011236	0.005161	0.00582	0.006576	0.334	0.998528	1931.0		29.0
HATLAS_J132342.7+272158	200.928041	27.36633	0.118644	0.074786	0.036478	0.005267	0.005516	0.007053	2.351	0.992042	666.751		33.82
HATLAS_J132512.1+271113	201.300671	27.187166	0.115898	0.06424	0.023886	0.005397	0.005598	0.006911	0.42	0.994984	632.756		76.32
HATLAS_J132539.7+271355	201.415555	27.232183	0.111457	0.056031	0.029616	0.005404	0.005617	0.006361	1.023	0.994593	702.129		59.25
HATLAS_J132317.7+273842	200.823743	27.645182	0.104808	0.049137	0.01777	0.005104	0.005667	0.006641	0.683	0.994857	803.777		58.353
HATLAS_J132616.8+273016	201.570385	27.504488	0.104471	0.067884	0.03679	0.005237	0.005712	0.006868	2.257	0.992334	616.137		76.429
HATLAS_J132430.9+274211	201.128979	27.703257	0.095565	0.042395	0.01077	0.005355	0.005785	0.0077	1.177	0.931429	299.431		35.375
HATLAS_J132357.1+272034	200.987978	27.342829	0.084043	0.046639	0.013084	0.005243	0.005905	0.007184	0.794	0.994784	464.975		74.654
HATLAS_J132414.4+272418	201.06029	27.405148	0.084179	0.061	0.033589	0.005139	0.005741	0.006941	2.489	0.996014	166.062		21.975
HATLAS_J132357.6+272924	200.99032	27.490117	0.086173	0.033187	0.010915	0.00536	0.005768	0.007087	1.142	0.998368	1907.0		22.0
HATLAS_J132331.4+272602	200.881119	27.434001	0.080298	0.07649	0.039244	0.005153	0.005699	0.00702	3.858	0.989378	145.226		30.786
HATLAS_J132522.8+273054	201.34531	27.515002	0.081358	0.059271	0.023569	0.005434	0.005681	0.006952	1.276	0.998321	5205.0		26.0
HATLAS_J132338.8+273301	200.911673	27.550481	0.077001	0.035068	0.025089	0.005316	0.00576	0.006965	1.454	0.994071	598.535		39.105
HATLAS_J132604.7+272101	201.51978	27.350461	0.076099	0.054499	0.030734	0.005272	0.005904	0.007489	0.587	0.997597	173.67		56.418
HATLAS_J132615.1+273120	201.563196	27.522348	0.074299	0.023547	0.008021	0.005346	0.005765	0.007065	1.515	0.993978	470.336		80.983
HATLAS_J132351.6+272310	200.965382	27.386198	0.069846	0.044978	0.017094	0.004975	0.005715	0.006743	1.685	0.993687	520.402		26.413
HATLAS_J132422.5+272334	201.093828	27.392784	0.07046	0.044417	0.021087	0.005299	0.006128	0.007282	2.338	0.992084	626.545		21.54
HATLAS_J132317.6+273647	200.823347	27.613173	0.065809	0.030392	0.011052	0.005171	0.005561	0.006743	1.831	0.993402	351.337		80.244
HATLAS_J132437.2+273640	201.155245	27.611134	0.067467	0.050231	0.027365	0.005275	0.005514	0.006779	2.496	0.996001	150.655		20.686
HATLAS_J132412.5+274612	201.052357	27.770172	0.064221	0.055725	0.022497	0.005414	0.005805	0.006842	1.627	0.993792	537.892		41.0
HATLAS_J132537.6+273335	201.407005	27.559888	0.060739	0.046321	0.027947	0.005422	0.005778	0.006843	2.719	0.990656	353.154		42.031
HATLAS_J132322.8+273206	200.845073	27.535187	0.059295	0.050919	0.020151	0.005239	0.005696	0.00635	1.619	0.997074	153.302		38.39
HATLAS_J132520.2+272832	201.334246	27.475672	0.058252	0.024825	0.007848	0.005005	0.005624	0.006835	3.206	0.99645	1227.0		25.0
HATLAS_J132545.7+272243	201.440802	27.378654	0.058425	0.029544	-0.00167	0.00527	0.005743	0.006567	1.822	0.989243	132.779		29.106
HATLAS_J132352.2+273117	200.967747	27.521456	0.05923	0.04051	0.01908	0.005285	0.005773	0.006794	1.323	0.997287	143.993		22.442
HATLAS_J132411.1+272244	201.04632	27.379113	0.061526	0.047897	0.026488	0.005348	0.005701	0.006713	1.023	0.997242	179.478		24.943
HATLAS_J132348.0+272831	200.950076	27.475268	0.053834	0.026421	0.001555	0.005127	0.005952	0.007312	3.156	0.994483	274.562		25.499
HATLAS_J132329.1+272925	200.871503	27.490411	0.055533	0.041103	0.016476	0.005287	0.005688	0.006966	3.484	0.985961	93.134		26.346
HATLAS_J132534.7+271950	201.394828	27.330587	0.052159	0.015103	0.007137	0.005283	0.005883	0.007308	1.129	0.997396	261.154		43.001
HATLAS_J132440.0+272847	201.166872	27.479951	0.050229	0.04139	0.017972	0.005088	0.005574	0.006455	2.377	0.996197	126.744		29.204
HATLAS_J132429.4+270555	201.122557	27.098786	0.051584	0.04947	0.03223	0.005341	0.005732	0.00688	0.642	0.997584	296.976		94.892
HATLAS_J132538.3+274326	201.409862	27.724041	0.051217	0.035301	0.023624	0.005301	0.005889	0.007017	6.467	0.918936	249.488		56.498
HATLAS_J132413.8+271934	201.057866	27.326336	0.050568	0.035233	0.011352	0.005216	0.005629	0.00665	3.339	0.986397	45.665		16.203
HATLAS_J132308.5+272912	200.785478	27.486703	0.053826	0.042985	0.025281	0.005487	0.005737	0.007089	1.166	0.997377	166.304		51.682
HATLAS_J132502.4+274501	201.260326	27.750326	0.050488	0.018967	0.004223	0.005148	0.005882	0.006757	2.245	0.996393	208.769		38.3
HATLAS_J132540.3+272021	201.418014	27.339269	0.051215	0.047215	0.038924	0.005237	0.00583	0.007211	4.374	0.987849	120.697		35.903
HATLAS_J132440.1+272803	201.167406	27.467535	0.048028	0.038849	0.016668	0.005028	0.005656	0.00674	0.301	0.995021	732.671		22.021
HATLAS_J132435.6+272513	201.148369	27.420422	0.047879	0.032609	0.021775	0.005047	0.005517	0.00687	0.247	0.997656	290.529		21.731
HATLAS_J132413.9+274025	201.057978	27.673713	0.04752	0.028101	8.23E-4	0.005047	0.005679	0.006694	5.63	0.964691	117.591		25.33
HATLAS_J132607.6+273610	201.531662	27.60284	0.048269	0.027528	0.001678	0.005185	0.005819	0.00664	1.012	0.997452	239.73		70.703

HATLAS_J132403.8+272247	201.016185	27.37973	0.049799	0.049382	0.03474	0.005144	0.005522	0.006769	2.919	0.995126	142.589	23.337
HATLAS_J132326.2+271554	200.859397	27.265224	0.047995	0.040252	0.030659	0.005207	0.005505	0.00654	4.307	0.98844	210.203	68.397
HATLAS_J132407.1+272512	201.029744	27.420206	0.047954	0.042994	0.039731	0.005252	0.005434	0.00693	1.071	0.996066	107.034	18.948
HATLAS_J132417.4+274238	201.072555	27.710722	0.049806	0.039224	0.035815	0.005426	0.005633	0.006942	1.301	0.9973	278.112	27.744
HATLAS_J132533.3+272852	201.389057	27.481319	0.045126	0.044823	0.045789	0.004966	0.005712	0.006757	3.027	0.989122	96.692	25.089
HATLAS_J132439.8+270814	201.166084	27.137465	0.047526	0.042839	0.020211	0.005317	0.005922	0.007216	6.634	0.815338	353.424	61.646
HATLAS_J132409.0+272312	201.037815	27.386846	0.047791	0.048111	0.046877	0.005344	0.00589	0.007374	1.427	0.997219	149.488	26.709
HATLAS_J132448.2+271710	201.201021	27.286345	0.046177	0.029005	0.008489	0.005158	0.005523	0.006805	1.912	0.993227	355.989	25.375
HATLAS_J132331.1+274609	200.879653	27.76927	0.047162	0.037339	0.026479	0.005315	0.005612	0.007107	2.493	0.991557	328.985	71.906
HATLAS_J132457.0+271834	201.237715	27.309433	0.049263	0.023078	0.019984	0.00542	0.005558	0.006418	0.66	0.997578	135.649	27.404
HATLAS_J132449.6+271124	201.206778	27.19013	0.044577	0.036076	0.024733	0.005133	0.005715	0.006778	3.184	0.994396	182.312	45.464
HATLAS_J132454.8+274158	201.228385	27.699589	0.049423	0.020614	0.004094	0.0054	0.00588	0.007125	3.172	0.994434	192.524	33.839
HATLAS_J132551.9+271839	201.466526	27.310978	0.04627	0.050762	0.034644	0.005254	0.005868	0.006699	0.717	0.997562	151.62	47.345
HATLAS_J132456.5+272749	201.235444	27.463766	0.044971	0.037209	0.027226	0.005286	0.005563	0.006662	1.306	0.997297	124.025	22.469
HATLAS_J132526.9+273924	201.362321	27.656802	0.045442	0.021333	0.01251	0.005275	0.005605	0.006906	6.12	0.943075	104.278	36.502
HATLAS_J132353.9+273955	200.974817	27.665374	0.044975	0.011086	-0.007114	0.005265	0.005606	0.007251	5.566	0.96673	159.254	25.963
HATLAS_J132519.3+272318	201.330452	27.388361	0.043512	0.031144	0.009896	0.005212	0.00565	0.006966	1.783	0.99693	136.79	23.543
HATLAS_J132341.9+272016	200.924906	27.338004	0.043296	0.023865	0.011212	0.005154	0.00592	0.006922	2.796	0.995414	145.329	32.778
HATLAS_J132423.8+272254	201.099336	27.381701	0.044767	0.028599	0.00693	0.005161	0.005692	0.006829	0.823	0.997528	165.766	19.242
HATLAS_J132527.1+272821	201.362971	27.472501	0.043648	0.046127	0.028596	0.005282	0.005808	0.007129	0.456	0.99497	635.259	24.989
HATLAS_J132451.1+271616	201.212912	27.271166	0.041991	0.039245	0.012486	0.00512	0.005631	0.007447	0.385	0.997638	201.525	27.823
HATLAS_J132542.2+271939	201.426055	27.327615	0.043655	0.023045	0.002576	0.005309	0.00588	0.007238	4.63	0.985192	134.336	38.264
HATLAS_J132508.9+271704	201.287443	27.284466	0.042362	0.033472	0.023429	0.005138	0.005688	0.007178	1.989	0.996716	191.341	37.567
HATLAS_J132428.8+273641	201.120173	27.611623	0.043008	0.024715	0.015984	0.005161	0.00558	0.006547	3.067	0.994739	111.559	24.569
HATLAS_J132534.5+272333	201.393861	27.392532	0.042077	0.02158	0.018651	0.00506	0.005424	0.00682	0.734	0.997557	118.272	31.664
HATLAS_J132437.5+272001	201.156319	27.333663	0.041843	0.029547	0.011005	0.005182	0.005498	0.007253	2.069	0.844374	111.666	29.092
HATLAS_J132528.4+272401	201.368715	27.400365	0.041593	0.011951	-0.0055	0.005249	0.005572	0.007071	1.258	0.997325	182.528	25.173
HATLAS_J132431.3+274337	201.130518	27.726953	0.042323	0.020222	0.002303	0.005329	0.005407	0.006778	1.891	0.996822	220.571	25.55
HATLAS_J132534.3+274338	201.393204	27.727364	0.042541	0.023837	0.006309	0.005336	0.005569	0.007322	0.819	0.997529	124.594	40.163
HATLAS_J132510.5+271809	201.293918	27.302615	0.038328	0.040856	0.02079	0.004882	0.005578	0.006515	1.106	0.997408	133.484	30.429
HATLAS_J132439.6+273848	201.165067	27.646763	0.039292	0.03237	0.018265	0.005087	0.005714	0.00664	1.912	0.995855	282.55	20.193
HATLAS_J132446.9+273023	201.195408	27.506571	0.040863	0.028152	0.017753	0.005316	0.005504	0.006971	2.257	0.996376	159.741	17.667
HATLAS_J132508.2+273134	201.284267	27.526172	0.040574	0.029373	0.017391	0.005315	0.005498	0.006608	3.34	0.987094	72.498	24.044
HATLAS_J132301.7+272134	200.757215	27.359623	0.039336	0.026189	0.002126	0.005081	0.005647	0.006388	2.562	0.995885	201.462	69.548
HATLAS_J132425.1+272001	201.104798	27.333852	0.038611	0.033441	0.012043	0.005067	0.005724	0.007523	4.179	0.977887	68.262	21.007
HATLAS_J132415.6+273509	201.065183	27.586088	0.039881	0.0231	0.026725	0.005166	0.005658	0.006857	1.667	0.993721	82.035	16.808
HATLAS_J132525.1+274009	201.354953	27.669366	0.041315	0.032966	0.022624	0.005497	0.005725	0.007195	4.408	0.973886	79.626	22.774
HATLAS_J132403.0+273418	201.012532	27.571701	0.03883	0.02908	0.009227	0.005054	0.005802	0.006881	0.975	0.997468	109.103	20.883
HATLAS_J132307.2+272008	200.780361	27.335808	0.038634	0.028654	0.016039	0.005233	0.005779	0.00689	1.027	0.994589	932.224	98.952
HATLAS_J132338.7+272653	200.91151	27.448224	0.038303	0.021075	-0.004746	0.00511	0.00571	0.006687	1.988	0.993052	85.11	27.237
HATLAS_J132354.5+273442	200.977258	27.57839	0.038699	0.027986	0.026274	0.005248	0.005522	0.007079	4.394	0.974156	76.263	21.06
HATLAS_J132421.6+272103	201.090267	27.350935	0.036731	0.02316	0.014488	0.005093	0.005599	0.007004	6.165	0.940434	102.979	28.685
HATLAS_J132405.9+273330	201.024598	27.558535	0.037544	0.019151	0.009227	0.005275	0.006011	0.00691	1.377	0.870151	54.75	19.571
HATLAS_J132316.3+272922	200.818035	27.489608	0.037224	0.025664	0.011169	0.005298	0.005597	0.006865	3.756	0.99211	270.588	44.734

HATLAS_J132540.5+272835	201.418945	27.476383	0.038165	0.020965	0.005828	0.005388	0.005653	0.00671	4.794	0.951058	570.524	29.426
HATLAS_J132420.9+271002	201.087297	27.167315	0.037111	0.023137	0.014191	0.005324	0.005634	0.006693	3.33	0.845422	6981.0	59.0
HATLAS_J132428.2+274322	201.117755	27.722993	0.037445	0.03147	0.022901	0.005196	0.005636	0.007275	0.8	0.994779	96.502	26.947
HATLAS_J132418.5+272241	201.077086	27.378297	0.037043	0.027967	0.003923	0.005211	0.005531	0.00659	0.726	0.997559	110.644	29.848
HATLAS_J132411.4+273008	201.047744	27.502261	0.039325	0.033258	0.014022	0.005194	0.005571	0.006973	0.906	0.997496	284.746	18.551
HATLAS_J132440.9+274109	201.170713	27.685904	0.036571	0.032557	0.017642	0.005083	0.005573	0.007085	1.336	0.994237	79.603	23.965
HATLAS_J132536.6+273253	201.402528	27.548256	0.036131	0.0139	-0.00642	0.00527	0.005622	0.007566	1.928	0.996783	179.049	41.865
HATLAS_J132418.0+273040	201.075239	27.51136	0.035841	0.023287	0.024907	0.00513	0.005544	0.006574	2.836	0.990121	44.482	15.996
HATLAS_J132459.8+272503	201.249459	27.417691	0.038287	0.020798	0.009096	0.005411	0.005906	0.00665	2.406	0.996152	123.184	18.755
HATLAS_J132413.6+273308	201.057049	27.552395	0.035902	0.032262	0.007193	0.005057	0.005646	0.006595	5.363	0.943163	82.639	21.628
HATLAS_J132352.7+273815	200.96981	27.637595	0.036146	0.034676	0.010817	0.005341	0.005665	0.006884	3.064	0.994748	160.768	27.663
HATLAS_J132517.5+272154	201.323287	27.365225	0.037702	0.019467	0.008971	0.005454	0.005726	0.007245	2.727	0.990623	83.973	27.077
HATLAS_J132414.2+273108	201.059154	27.519077	0.033488	0.025097	0.017161	0.004984	0.005829	0.007029	3.327	0.987191	85.953	20.356
HATLAS_J132449.9+272556	201.208057	27.432371	0.036568	0.043755	0.025933	0.00542	0.00584	0.006911	6.102	0.944118	130.764	28.915
HATLAS_J132308.1+274129	200.784099	27.691495	0.033162	0.022711	0.009526	0.004998	0.005551	0.006579	2.777	0.995455	168.445	60.585
HATLAS_J132413.9+272648	201.0582	27.446701	0.035164	0.013218	0.012068	0.005157	0.005565	0.006718	3.88	0.991441	138.71	24.181
HATLAS_J132449.4+274115	201.205964	27.687731	0.031881	0.040224	0.047368	0.004923	0.005544	0.006975	4.987	0.958777	99.753	27.535
HATLAS_J132448.9+272138	201.204143	27.360573	0.034525	0.029215	0.001651	0.00517	0.005868	0.007159	3.082	0.994698	116.087	20.62
HATLAS_J132551.7+273152	201.465418	27.531172	0.033375	0.015911	0.001664	0.005123	0.005671	0.006823	3.81	0.982802	91.345	28.292
HATLAS_J132543.3+273200	201.430661	27.533576	0.034865	0.045025	0.031839	0.005351	0.005454	0.006573	2.441	0.996096	168.245	28.803
HATLAS_J132400.9+272614	201.003992	27.437222	0.034108	0.014445	0.014097	0.005286	0.005629	0.00702	4.737	0.966355	83.138	23.257
HATLAS_J132438.3+270925	201.159631	27.157075	0.033652	0.017438	-0.007166	0.005244	0.005699	0.006747	2.034	0.996664	247.686	63.359
HATLAS_J132522.8+272245	201.345219	27.379254	0.035053	0.020637	0.003008	0.005449	0.005602	0.006902	1.201	0.994405	82.745	22.097
HATLAS_J132516.5+272227	201.31914	27.374417	0.033442	0.008403	-0.006819	0.005242	0.00577	0.006713	3.022	0.994861	145.307	32.586
HATLAS_J132359.1+271805	200.996568	27.301479	0.033116	0.017878	0.014294	0.005359	0.005928	0.007089	6.632	0.815708	60.776	22.866
HATLAS_J132516.2+271817	201.31753	27.304715	0.032375	0.028015	0.015586	0.005102	0.005505	0.007056	2.428	0.996116	102.742	26.6
HATLAS_J132454.8+272110	201.228505	27.352782	0.031389	0.026227	0.005593	0.005194	0.005561	0.006734	4.415	0.972067	65.127	20.478
HATLAS_J132348.5+273008	200.952458	27.502415	0.033403	0.010826	-0.002819	0.005172	0.005682	0.00657	0.955	0.997477	227.591	30.622
HATLAS_J132514.2+272320	201.309378	27.389004	0.030149	0.030899	0.024857	0.005132	0.005512	0.00716	1.614	0.993814	698.973	22.647
HATLAS_J132409.5+272417	201.039805	27.40489	0.031575	0.018873	0.023649	0.005152	0.005872	0.006907	1.977	0.993078	93.374	23.175
HATLAS_J132510.4+272616	201.293614	27.437815	0.03154	0.012244	-0.002035	0.005268	0.005466	0.006611	2.879	0.989908	76.688	19.131
HATLAS_J132507.3+274444	201.280731	27.745597	0.030407	0.039855	0.02729	0.005297	0.005743	0.00692	0.766	0.997547	114.132	32.226
HATLAS_J132519.8+273332	201.332621	27.559074	0.031381	0.003272	0.008608	0.005343	0.005605	0.006833	2.859	0.995272	197.533	26.923
HATLAS_J132501.1+273113	201.254664	27.520366	0.030168	0.032061	0.006829	0.005211	0.005761	0.006646	2.74	0.990564	76.283	23.782
HATLAS_J132506.6+272648	201.277753	27.446873	0.031209	0.021474	0.007284	0.005357	0.005758	0.006584	0.285	0.997652	249.455	22.062
HATLAS_J132458.6+272920	201.244464	27.489054	0.030281	0.032647	0.024289	0.00525	0.005858	0.007152	3.073	0.988854	74.041	22.547
HATLAS_J132436.3+274038	201.151581	27.677468	0.028804	0.022234	-4.94E-4	0.005239	0.005599	0.006725	1.119	0.957378	69.796	22.398
HATLAS_J132346.4+272246	200.943655	27.379607	0.029412	3.73E-4	8.76E-4	0.005239	0.005858	0.007011	1.824	0.993416	80.626	24.755
HATLAS_J132418.7+273103	201.077976	27.517708	0.029801	0.010647	-0.001083	0.005243	0.0056	0.006865	2.694	0.995632	163.9	19.799
HATLAS_J132412.4+273510	201.051979	27.586184	0.027179	0.019465	0.011826	0.004989	0.005674	0.006706	0.744	0.997554	121.633	26.682
HATLAS_J132347.9+273114	200.949594	27.520743	0.029947	0.011706	0.014745	0.005275	0.005491	0.007083	4.008	0.980369	89.213	26.751
HATLAS_J132546.1+273712	201.442181	27.620203	0.029209	0.018775	0.016779	0.005414	0.005773	0.007183	5.378	0.897357	68805.0	87.0
HATLAS_J132600.9+272149	201.503797	27.363847	0.028017	0.011624	-0.001667	0.005231	0.005772	0.006822	0.545	0.994932	92.354	35.863
HATLAS_J132513.0+273705	201.30456	27.618058	0.029648	0.027783	0.021391	0.005519	0.005487	0.006625	3.363	0.986925	364.344	24.687

HATLAS_J132435.8+273534	201.149235	27.592814	0.027925	0.00499	-0.004235	0.00526	0.00542	0.007236	3.093	0.988741	83.684	14.835
HATLAS_J132537.0+273204	201.404152	27.534629	0.027716	0.021264	0.007722	0.00522	0.005623	0.007405	0.744	0.997554	133.515	34.012
HATLAS_J132559.6+271933	201.498333	27.325968	0.028904	0.02613	0.004526	0.005291	0.005798	0.006666	3.104	0.98867	133.014	63.444
HATLAS_J132435.5+271127	201.147985	27.191013	0.027872	0.024863	0.025652	0.005209	0.005774	0.00708	4.228	0.989091	255.888	40.466
HATLAS_J132357.9+272503	200.991397	27.417506	0.028915	0.004003	0.0099	0.005278	0.005552	0.006937	2.792	0.995423	119.073	20.637
HATLAS_J132410.9+273059	201.04551	27.516442	0.027801	0.017375	0.018026	0.005331	0.005725	0.006743	5.675	0.963153	113.212	19.091
HATLAS_J132327.1+271412	200.863055	27.236862	0.027473	0.019386	0.005625	0.005188	0.005562	0.006551	7.304	0.806579	270.096	78.448
HATLAS_J132451.9+273000	201.216265	27.500134	0.027736	0.023171	0.00955	0.005196	0.005625	0.006973	2.013	0.972464	49.964	14.306
HATLAS_J132423.0+274231	201.096114	27.708604	0.027478	0.025157	0.006689	0.005363	0.005594	0.006904	0.835	0.994753	85.879	26.12
HATLAS_J132550.4+272854	201.460267	27.481763	0.026587	0.031415	0.024684	0.005196	0.005496	0.006847	6.651	0.812404	73.653	27.702
HATLAS_J132424.0+273927	201.100246	27.657532	0.026786	0.034332	0.027124	0.005208	0.005681	0.006662	0.759	0.994808	81.18	19.669
HATLAS_J132553.6+273110	201.473692	27.519489	0.026352	0.011638	0.01134	0.005146	0.005467	0.006503	3.808	0.982818	90.855	31.696
HATLAS_J132359.2+272227	200.996908	27.374308	0.027947	0.006948	0.001902	0.005581	0.005394	0.007072	5.002	0.958263	72.27	22.019
HATLAS_J132505.1+272221	201.271259	27.372648	0.028674	0.00908	0.008035	0.005517	0.005678	0.007028	1.555	0.997125	103.697	19.597
HATLAS_J132441.4+274010	201.172597	27.669601	0.026448	0.020318	0.009613	0.005163	0.005629	0.006604	2.858	0.990012	88.694	23.772
HATLAS_J132324.4+273538	200.851802	27.59407	0.02634	0.014964	0.003631	0.005101	0.005708	0.006989	3.029	0.994844	159.672	39.745
HATLAS_J132330.5+272727	200.877162	27.457622	0.02749	0.027894	0.029978	0.005345	0.005819	0.00718	1.394	0.994157	71.86	26.615
HATLAS_J132334.7+272935	200.894942	27.493101	0.02576	0.024671	0.007165	0.005192	0.005605	0.006794	3.741	0.992186	132.931	33.266
HATLAS_J132442.6+273234	201.177828	27.542932	0.027043	0.016008	0.003503	0.005339	0.00557	0.006625	4.303	0.988473	144.31	18.343
HATLAS_J132417.6+271932	201.073334	27.325557	0.026774	0.019132	0.009813	0.005185	0.005698	0.006517	3.296	0.994035	101.622	23.865
HATLAS_J132517.6+272117	201.323542	27.354958	0.027437	0.020444	0.001373	0.005522	0.005495	0.006659	2.863	0.99526	122.938	25.581
HATLAS_J132339.6+271359	200.915137	27.233261	0.024709	0.032681	0.023992	0.00497	0.005635	0.006675	6.873	0.876364	105.047	37.445
HATLAS_J132416.8+271811	201.070366	27.303087	0.025519	0.022677	0.01254	0.005138	0.005571	0.006952	3.849	0.970884	807.626	76.175
HATLAS_J132400.4+271920	201.002045	27.322366	0.026073	0.013592	-6.05E-4	0.005243	0.005498	0.006976	5.619	0.965028	153.756	35.149
HATLAS_J132417.5+273843	201.073156	27.645419	0.025964	0.023339	0.010825	0.005463	0.005777	0.006922	0.769	0.997546	148.729	22.125
HATLAS_J132406.0+272420	201.025382	27.405769	0.025082	0.018518	0.006496	0.005182	0.005627	0.00687	3.132	0.988503	75.479	20.115
HATLAS_J132338.0+272205	200.908713	27.368226	0.025698	0.02043	0.010816	0.005423	0.005672	0.006667	5.653	0.926292	88.974	28.406
HATLAS_J132456.5+272525	201.235471	27.42366	0.024563	0.013973	0.002819	0.005145	0.005721	0.006879	6.497	0.837658	94.187	18.818
HATLAS_J132410.2+272144	201.042845	27.362401	0.025331	0.026934	0.015252	0.00525	0.005814	0.006899	3.248	0.994194	123.431	32.35
HATLAS_J132428.1+273955	201.117403	27.665412	0.025026	0.013008	0.002969	0.005105	0.005443	0.006747	1.933	0.996333	149.458	25.575
HATLAS_J132449.1+274050	201.20496	27.680803	0.025063	0.019337	0.012817	0.005045	0.005627	0.006807	1.409	0.997231	101.727	25.176
HATLAS_J132504.8+272939	201.270262	27.494268	0.023958	0.011293	0.007814	0.005128	0.005789	0.007132	2.795	0.990313	46.885	17.391
HATLAS_J132516.7+271324	201.319628	27.223389	0.024839	0.015888	0.003458	0.005329	0.005452	0.007211	0.967	0.994644	363.51	40.732
HATLAS_J132434.8+272047	201.145223	27.346522	0.025946	0.010386	0.008267	0.005403	0.005752	0.006659	3.409	0.986572	37.957	15.025
HATLAS_J132500.7+272954	201.25305	27.498547	0.024837	0.025177	0.003531	0.005452	0.005743	0.007248	1.946	0.993152	93.222	22.422
HATLAS_J132523.4+273552	201.347687	27.597927	0.024011	0.02129	0.012509	0.005213	0.005605	0.007464	4.984	0.980216	103.975	29.487
HATLAS_J132500.6+272138	201.252571	27.360601	0.023809	0.015597	-0.007183	0.005239	0.005982	0.007026	2.447	0.996085	140.838	22.154
HATLAS_J132503.3+273531	201.263813	27.592022	0.024687	0.020013	0.016264	0.005198	0.005575	0.00633	3.381	0.993735	142.962	20.652
HATLAS_J132557.6+272555	201.490041	27.432057	0.025596	0.007571	0.005266	0.005273	0.005646	0.006875	3.202	0.994342	220.092	41.268
HATLAS_J132433.3+271626	201.138933	27.274151	0.023595	0.026469	0.031168	0.005164	0.005796	0.00669	3.652	0.984441	95.532	26.222
HATLAS_J132502.4+273446	201.260061	27.579524	0.024095	0.013736	0.022232	0.005237	0.005666	0.006681	3.392	0.986699	91.245	20.213
HATLAS_J132342.3+273739	200.926397	27.62754	0.024686	0.008702	0.009981	0.005538	0.005899	0.007082	6.628	0.816396	65.403	24.149
HATLAS_J132433.0+272913	201.137553	27.487093	0.024272	0.017214	0.009775	0.005287	0.005948	0.006796	3.735	0.992213	116.517	19.457
HATLAS_J132503.4+273934	201.264399	27.659666	0.024857	0.030236	0.017993	0.005477	0.005561	0.006711	3.469	0.986087	64.922	20.879

HATLAS_J132530.8+271245	201.378417	27.212502	0.023067	0.005739	-0.004195	0.00526	0.005732	0.007256	5.748	0.960468	297.608	50.971
HATLAS_J132420.6+274627	201.086068	27.774175	0.02481	0.007192	-0.011508	0.005466	0.005657	0.007025	5.435	0.970528	129.685	34.211
HATLAS_J132445.1+272100	201.188038	27.350191	0.023388	0.008714	-0.002434	0.005247	0.005721	0.006547	3.814	0.982749	71.833	18.566
HATLAS_J132403.5+273226	201.014572	27.540542	0.021426	0.020534	0.01997	0.004948	0.005847	0.006846	3.082	0.988803	50.639	16.891
HATLAS_J132428.3+272658	201.118271	27.449512	0.023134	-0.002765	-9.23E-4	0.005172	0.005557	0.00692	1.538	0.99394	74.177	22.242
HATLAS_J132422.0+273234	201.091926	27.542927	0.024122	0.004006	0.009076	0.005454	0.00568	0.006579	3.617	0.984781	690.185	18.984
HATLAS_J132303.8+273500	200.765899	27.583547	0.022212	0.017903	0.031639	0.005268	0.005984	0.007303	2.711	0.997244	1297.619	80.727
HATLAS_J132355.3+272309	200.980591	27.386034	0.02144	0.016098	0.005434	0.005051	0.005577	0.006944	2.464	0.991659	63.829	22.61
HATLAS_J132505.7+273406	201.274122	27.568394	0.022412	0.020437	0.020072	0.005283	0.00562	0.006568	5.556	0.932515	45.123	16.349
HATLAS_J132503.1+272154	201.263254	27.365053	0.023026	0.020349	0.010756	0.005389	0.00576	0.007217	4.569	0.970502	66.943	22.877
HATLAS_J132442.0+271400	201.175157	27.23352	0.023559	0.017884	0.006613	0.005502	0.005732	0.006583	3.331	0.98716	77.592	28.308
HATLAS_J132443.6+272143	201.181774	27.361945	0.022584	0.014993	0.014458	0.005426	0.005793	0.006855	1.914	0.993224	79.659	21.812
HATLAS_J132350.0+271757	200.958714	27.299285	0.02461	0.022127	0.007213	0.005398	0.005954	0.006989	3.994	0.990749	140.394	34.739
HATLAS_J132431.1+274054	201.129766	27.681669	0.022447	0.013401	0.007195	0.005085	0.00563	0.006755	5.111	0.977921	105.028	24.244
HATLAS_J132405.4+273741	201.022605	27.628147	0.020772	0.029001	0.012614	0.005085	0.005834	0.006725	2.368	0.991989	59.344	21.257
HATLAS_J132530.7+272346	201.378311	27.39612	0.021734	0.001399	0.011322	0.00512	0.005537	0.006648	5.634	0.96453	136.89	26.279
HATLAS_J132459.2+272726	201.246877	27.45747	0.023146	0.02535	0.014602	0.005416	0.005886	0.006728	1.99	0.993047	95.006	19.939
HATLAS_J132433.6+271735	201.140213	27.293252	0.021176	0.006807	-0.008891	0.005137	0.005729	0.007083	3.721	0.983751	54.632	19.889
HATLAS_J132556.2+272245	201.484337	27.379258	0.020875	0.011712	0.012054	0.00519	0.006047	0.007293	6.127	0.963417	2160.0	44.0
HATLAS_J132457.3+271305	201.23892	27.21821	0.02177	0.008384	-0.004638	0.005283	0.005724	0.006508	0.882	0.997506	179.577	46.132
HATLAS_J132419.8+272441	201.082574	27.411545	0.021159	0.030665	0.021664	0.005258	0.005515	0.006741	1.679	0.993085	73.231	19.221
HATLAS_J132410.1+272608	201.042436	27.435694	0.021286	0.00237	0.010291	0.005237	0.005606	0.007379	2.876	0.989924	90.565	18.874

# Bibliography

- Aguerri, J.A.L., Balcells, M., Peletier, R.F., 2001, *A&A*, 367, 428, <http://adsabs.harvard.edu/abs/2001A%26A...367..428A>
- Arendt, R.G., Odegard, N., Weiland, J.L., et al., 1998, *ApJ*, 508, 74, <http://adsabs.harvard.edu/abs/1998ApJ...508...74A>
- Baldry, I.K., Robotham, A.S.G., Hill, D.T., et al., 2010, *MNRAS*, 404, 86, <http://adsabs.harvard.edu/abs/2010MNRAS.404...86B>
- Baugh, C.M., 2006, *Reports on Progress in Physics*, 69, 3101, <http://adsabs.harvard.edu/abs/2006RPPh...69.3101B>
- Bell, E.F., Wolf, C., Meisenheimer, K., et al., 2004, *ApJ*, 608, 752, <http://adsabs.harvard.edu/abs/2004ApJ...608..752B>
- Bell, T.A., Viti, S., Williams, D.A., 2007, *MNRAS*, 378, 983, <http://adsabs.harvard.edu/abs/2007MNRAS.378..983B>
- Benson, A.J., 2010, *Phys. Rep.*, 495, 33, <http://adsabs.harvard.edu/abs/2010PhR...495...33B>
- Blain, A.W., Ivison, R.J., Smail, I., 1998, *MNRAS*, 296, L29, <http://adsabs.harvard.edu/abs/1998MNRAS.296L..29B>
- Bolatto, A.D., Wolfire, M., Leroy, A.K., 2013, *ARA&A*, 51, 207, <http://adsabs.harvard.edu/abs/2013ARA%26A..51..207B>
- Bolzonella, M., Miralles, J.M., Pelló, R., 2011, *Hyperz: Photometric Redshift Code, Astrophysics Source Code Library*

- Boselli, A., Lequeux, J., Gavazzi, G., 2002, *A&A*, 384, 33, <http://adsabs.harvard.edu/abs/2002A%26A...384...33B>
- Bourne, N., Dunne, L., Maddox, S.J., et al., 2016, *MNRAS*, 462, 1714, <http://adsabs.harvard.edu/abs/2016MNRAS.462.1714B>
- Brinchmann, J., Charlot, S., White, S.D.M., et al., 2004, *MNRAS*, 351, 1151, <http://adsabs.harvard.edu/abs/2004MNRAS.351.1151B>
- Bruce, V.A., Dunlop, J.S., Cirasuolo, M., et al., 2012, *MNRAS*, 427, 1666, <http://adsabs.harvard.edu/abs/2012MNRAS.427.1666B>
- Bruzual, G., Charlot, S., 2003, *MNRAS*, 344, 1000, <http://adsabs.harvard.edu/abs/2003MNRAS.344.1000B>
- Bruzual A., G., Charlot, S., 1993, *ApJ*, 405, 538, <http://adsabs.harvard.edu/abs/1993ApJ...405..538B>
- Cai, Z.Y., Lapi, A., Xia, J.Q., et al., 2013, *ApJ*, 768, 21, <http://adsabs.harvard.edu/abs/2013ApJ...768...21C>
- Caon, N., Capaccioli, M., D'Onofrio, M., 1993, *MNRAS*, 265, 1013, <http://adsabs.harvard.edu/abs/1993MNRAS.265.1013C>
- Capaccioli, M., 1989, In: Corwin, H.G., Jr., Bottinelli, L. (eds.) *World of Galaxies (Le Monde des Galaxies)*, 208–227, <http://adsabs.harvard.edu/abs/1989woga.conf..208C>
- Casey, C.M., Narayanan, D., Cooray, A., 2014, *Phys. Rep.*, 541, 45, <http://adsabs.harvard.edu/abs/2014PhR...541...45C>
- Chabrier, G., 2003, *PASP*, 115, 763, <http://adsabs.harvard.edu/abs/2003PASP..115..763C>
- Charlot, S., Fall, S.M., 2000, *ApJ*, 539, 718, <http://adsabs.harvard.edu/abs/2000ApJ...539..718C>
- Ciliegi, P., Zamorani, G., Hasinger, G., et al., 2003, *VizieR Online Data Catalog*, 339, 80901, <http://adsabs.harvard.edu/abs/2003yCat..33980901C>

- Coleman, G.D., Wu, C.C., Weedman, D.W., 1980, *ApJS*, 43, 393, <http://adsabs.harvard.edu/abs/1980ApJS...43..393C>
- Combes, F., García-Burillo, S., Braine, J., et al., 2013, In: Wong, T., Ott, J. (eds.) *Molecular Gas, Dust, and Star Formation in Galaxies*, vol. 292 of *IAU Symposium*, 303–306, <http://adsabs.harvard.edu/abs/2013IAUS..292..303C>
- da Cunha, E., Charlot, S., Elbaz, D., 2008, *MNRAS*, 388, 1595, <http://adsabs.harvard.edu/abs/2008MNRAS.388.1595D>
- Daddi, E., Dickinson, M., Morrison, G., et al., 2007, *ApJ*, 670, 156, <http://adsabs.harvard.edu/abs/2007ApJ...670..156D>
- Daddi, E., Dannerbauer, H., Stern, D., et al., 2009, *ApJ*, 694, 1517, <http://adsabs.harvard.edu/abs/2009ApJ...694.1517D>
- Daddi, E., Bournaud, F., Walter, F., et al., 2010a, *ApJ*, 713, 686, <http://adsabs.harvard.edu/abs/2010ApJ...713..686D>
- Daddi, E., Elbaz, D., Walter, F., et al., 2010b, *ApJ*, 714, L118, <http://adsabs.harvard.edu/abs/2010ApJ...714L.118D>
- de Graauw, T., Helmich, F.P., Phillips, T.G., et al., 2010, *A&A*, 518, L6, <http://adsabs.harvard.edu/abs/2010A%26A...518L...6D>
- de Jong, J.T.A., Verdoes Kleijn, G.A., Boxhoorn, D.R., et al., 2015, *A&A*, 582, A62, <http://adsabs.harvard.edu/abs/2015A%26A...582A..62D>
- de Vaucouleurs, G., 1958, *ApJ*, 128, 465, <http://adsabs.harvard.edu/abs/1958ApJ...128..465D>
- Debattista, V.P., Mayer, L., Carollo, C.M., et al., 2006, *ApJ*, 645, 209, <http://adsabs.harvard.edu/abs/2006ApJ...645..209D>
- Di Matteo, P., Bournaud, F., Martig, M., et al., 2008, *A&A*, 492, 31, <http://adsabs.harvard.edu/abs/2008A%26A...492...31D>
- Dickinson, M., Giavalisco, M., GOODS Team, 2003, In: Bender, R., Renzini, A. (eds.) *The Mass of Galaxies at Low and High Redshift*, 324, <http://adsabs.harvard.edu/abs/2003mgllh.conf..324D>

- Draine, B.T., Li, A., 2007, *ApJ*, 657, 810, <http://adsabs.harvard.edu/abs/2007ApJ..657..810D>
- Draine, B.T., Dale, D.A., Bendo, G., et al., 2007, *ApJ*, 663, 866, <http://adsabs.harvard.edu/abs/2007ApJ...663..866D>
- Dunne, L., Eales, S.A., 2001, *MNRAS*, 327, 697, <http://adsabs.harvard.edu/abs/2001MNRAS.327..697D>
- Dutton, A.A., van den Bosch, F.C., Dekel, A., 2010, *MNRAS*, 405, 1690, <http://adsabs.harvard.edu/abs/2010MNRAS.405.1690D>
- Eales, S., Rawlings, S., Law-Green, D., Cotter, G., Lacy, M., 1997, *MNRAS*, 291, 593, <http://adsabs.harvard.edu/abs/1997MNRAS.291..593E>
- Eales, S., Dunne, L., Clements, D., et al., 2010a, *PASP*, 122, 499, <http://adsabs.harvard.edu/abs/2010PASP..122..499E>
- Eales, S., Smith, M.W.L., Auld, R., et al., 2012, *ApJ*, 761, 168, <http://adsabs.harvard.edu/abs/2012ApJ...761..168E>
- Eales, S., Fullard, A., Allen, M., et al., 2015, *MNRAS*, 452, 3489, <http://adsabs.harvard.edu/abs/2015MNRAS.452.3489E>
- Eales, S.A., 2015, *MNRAS*, 446, 3224, <http://adsabs.harvard.edu/abs/2015MNRAS.446.3224E>
- Eales, S.A., Smith, M.W.L., Wilson, C.D., et al., 2010b, *A&A*, 518, L62, <http://adsabs.harvard.edu/abs/2010A%26A...518L..62E>
- Edge, A., Sutherland, W., Kuijken, K., et al., 2013, *The Messenger*, 154, 32, <http://adsabs.harvard.edu/abs/2013Msngr.154...32E>
- Elbaz, D., Dickinson, M., Hwang, H.S., et al., 2011, *A&A*, 533, A119, <http://cdsads.u-strasbg.fr/abs/2011A%26A...533A.119E>
- Fernández Lorenzo, M., Sulentic, J., Verdes-Montenegro, L., et al., 2014, *ApJ*, 788, L39, <http://adsabs.harvard.edu/abs/2014ApJ...788L..39F>
- Findlay, J.R., Sutherland, W.J., Venemans, B.P., et al., 2012, *MNRAS*, 419, 3354, <http://adsabs.harvard.edu/abs/2012MNRAS.419.3354F>

- Fisher, D.B., Drory, N., 2008, *AJ*, 136, 773, <http://adsabs.harvard.edu/abs/2008AJ...136..773F>
- Fisher, D.B., Drory, N., 2010, *ApJ*, 716, 942, <http://adsabs.harvard.edu/abs/2010ApJ...716..942F>
- Fisher, D.B., Drory, N., 2011, *ApJ*, 733, L47, <http://adsabs.harvard.edu/abs/2011ApJ...733L..47F>
- Fleuren, S., Sutherland, W., Dunne, L., et al., 2012, *MNRAS*, 423, 2407, <http://adsabs.harvard.edu/abs/2012MNRAS.423.2407F>
- Forbes, J.C., Krumholz, M.R., Burkert, A., Dekel, A., 2014, *MNRAS*, 443, 168, <http://adsabs.harvard.edu/abs/2014MNRAS.443..168F>
- Freeman, K.C., 1970, *ApJ*, 160, 811, <http://adsabs.harvard.edu/abs/1970ApJ...160..811F>
- Genzel, R., Tacconi, L.J., Gracia-Carpio, J., et al., 2010, *MNRAS*, 407, 2091, <http://adsabs.harvard.edu/abs/2010MNRAS.407.2091G>
- Glover, S.C.O., Mac Low, M.M., 2011, *MNRAS*, 412, 337, <http://adsabs.harvard.edu/abs/2011MNRAS.412..337G>
- Gomez, H.L., Clark, C.J.R., Nozawa, T., et al., 2012a, *MNRAS*, 420, 3557, <http://adsabs.harvard.edu/abs/2012MNRAS.420.3557G>
- Gomez, H.L., Krause, O., Barlow, M.J., et al., 2012b, *ApJ*, 760, 96, <http://adsabs.harvard.edu/abs/2012ApJ...760...96G>
- González, J.E., Lacey, C.G., Baugh, C.M., Frenk, C.S., 2011, *MNRAS*, 413, 749, <http://adsabs.harvard.edu/abs/2011MNRAS.413..749G>
- González-Nuevo, J., Lapi, A., Fleuren, S., et al., 2012, *ApJ*, 749, 65, <http://adsabs.harvard.edu/abs/2012ApJ...749...65G>
- González-Nuevo, J., Lapi, A., Negrello, M., et al., 2014, *MNRAS*, 442, 2680, <http://adsabs.harvard.edu/abs/2014MNRAS.442.2680G>
- Greve, T.R., Papadopoulos, P.P., Gao, Y., Radford, S.J.E., 2009, *ApJ*, 692, 1432, <http://adsabs.harvard.edu/abs/2009ApJ...692.1432G>

- Griffin, M.J., Abergel, A., Abreu, A., et al., 2010, *A&A*, 518, L3, <http://adsabs.harvard.edu/abs/2010A%26A...518L...3G>
- Guedes, J., Mayer, L., Carollo, M., Madau, P., 2013, *ApJ*, 772, 36, <http://adsabs.harvard.edu/abs/2013ApJ...772...36G>
- Häussler, B., McIntosh, D.H., Barden, M., et al., 2007, *ApJS*, 172, 615, <http://adsabs.harvard.edu/abs/2007ApJS..172..615H>
- Hildebrand, R.H., 1983, *QJRAS*, 24, 267, <http://adsabs.harvard.edu/abs/1983QJRAS..24..267H>
- Holland, W.S., Cunningham, C.R., Gear, W.K., et al., 1998, In: Phillips, T.G. (ed.) *Advanced Technology MMW, Radio, and Terahertz Telescopes*, vol. 3357 of *Society of Photo-Optical Instrumentation Engineers (SPIE) Conference Series*, 305–318, <http://adsabs.harvard.edu/abs/1998SPIE.3357..305H>
- Hsu, L.T., Salvato, M., Nandra, K., et al., 2014, *ApJ*, 796, 60, <http://adsabs.harvard.edu/abs/2014ApJ...796...60H>
- Hubble, E.P., 1925, *Popular Astronomy*, 33, 252, <http://adsabs.harvard.edu/abs/1925PA.....33..252H>
- Hubble, E.P., 1936, *Realm of the Nebulae*
- Immeli, A., Samland, M., Gerhard, O., Westera, P., 2004, *A&A*, 413, 547, <http://adsabs.harvard.edu/abs/2004A%26A...413..547I>
- Iverson, R.J., Magnelli, B., Ibar, E., et al., 2010, *A&A*, 518, L31, <http://adsabs.harvard.edu/abs/2010A%26A...518L..31I>
- Iverson, R.J., Swinbank, A.M., Smail, I., et al., 2013, *ApJ*, 772, 137, <http://adsabs.harvard.edu/abs/2013ApJ...772..137I>
- Kashikawa, N., Shimasaku, K., Yasuda, N., et al., 2004, *PASJ*, 56, 1011, <http://adsabs.harvard.edu/abs/2004PASJ...56.1011K>
- Kennicutt, R.C., Jr., 1998, *ApJ*, 498, 541, <http://adsabs.harvard.edu/abs/1998ApJ...498..541K>

- Kessler, M.F., Steinz, J.A., Anderegg, M.E., et al., 1996, *A&A*, 315, L27, <http://adsabs.harvard.edu/abs/1996A%26A...315L..27K>
- Kormendy, J., 1977, *ApJ*, 217, 406, <http://adsabs.harvard.edu/abs/1977ApJ...217..406K>
- Kormendy, J., 1982a, *ApJ*, 257, 75, <http://adsabs.harvard.edu/abs/1982ApJ...257...75K>
- Kormendy, J., 1982b, In: Martinet, L., Mayor, M. (eds.) *Saas-Fee Advanced Course 12: Morphology and Dynamics of Galaxies*, 113–288, <http://adsabs.harvard.edu/abs/1982modg.proc..113K>
- Kormendy, J., Kennicutt, R.C., Jr., 2004, *ARA&A*, 42, 603, <http://adsabs.harvard.edu/abs/2004ARA%26A..42..603K>
- Lapi, A., González-Nuevo, J., Fan, L., et al., 2011, *ApJ*, 742, 24, <http://adsabs.harvard.edu/abs/2011ApJ...742...24L>
- Lequeux, J., Peimbert, M., Rayo, J.F., Serrano, A., Torres-Peimbert, S., 1979, *A&A*, 80, 155, <http://adsabs.harvard.edu/abs/1979A%26A....80..155L>
- Lisenfeld, U., Ferrara, A., 1998, *ApJ*, 496, 145, <http://adsabs.harvard.edu/abs/1998ApJ...496..145L>
- Longair, M.S., Lilly, S.J., 1984, *Journal of Astrophysics and Astronomy*, 5, 349, <http://adsabs.harvard.edu/abs/1984JApA....5..349L>
- Luo, W., Yang, X., Zhang, Y., 2014, *ApJ*, 789, L16, <http://adsabs.harvard.edu/abs/2014ApJ...789L..16L>
- Madau, P., Dickinson, M., 2014, *ARA&A*, 52, 415, <http://adsabs.harvard.edu/abs/2014ARA%26A..52..415M>
- Magdis, G.E., Daddi, E., Elbaz, D., et al., 2011, *ApJ*, 740, L15, <http://cdsads.u-strasbg.fr/abs/2011ApJ...740L..15M>
- Magdis, G.E., Daddi, E., Béthermin, M., et al., 2012, *ApJ*, 760, 6, <http://adsabs.harvard.edu/abs/2012ApJ...760....6M>

- Magnelli, B., Saintonge, A., Lutz, D., et al., 2012, *A&A*, 548, A22, <http://adsabs.harvard.edu/abs/2012A%26A...548A..22M>
- Magnelli, B., Popesso, P., Berta, S., et al., 2013, *A&A*, 553, A132, <http://adsabs.harvard.edu/abs/2013A%26A...553A.132M>
- Mannucci, F., Cresci, G., Maiolino, R., et al., 2009, *MNRAS*, 398, 1915, <http://adsabs.harvard.edu/abs/2009MNRAS.398.1915M>
- Mannucci, F., Cresci, G., Maiolino, R., Marconi, A., Gnerucci, A., 2010, *MNRAS*, 408, 2115, <http://adsabs.harvard.edu/abs/2010MNRAS.408.2115M>
- Miller, G.E., Scalo, J.M., 1979, *ApJS*, 41, 513, <http://adsabs.harvard.edu/abs/1979ApJS...41..513M>
- Morgan, H.L., Edmunds, M.G., 2003, *MNRAS*, 343, 427, <http://adsabs.harvard.edu/abs/2003MNRAS.343..427M>
- Morselli, L., Popesso, P., Erfanianfar, G., Concas, A., 2016, ArXiv e-prints, <http://adsabs.harvard.edu/abs/2016arXiv160707675M>
- Mushotzky, R., 2004, In: Barger, A.J. (ed.) *Supermassive Black Holes in the Distant Universe*, vol. 308 of *Astrophysics and Space Science Library*, 53, <http://adsabs.harvard.edu/abs/2004ASSL..308...53M>
- Negrello, M., Hopwood, R., De Zotti, G., et al., 2010, *Science*, 330, 800, <http://adsabs.harvard.edu/abs/2010Sci...330..800N>
- Negrello, M., Amber, S., Amvrosiadis, A., et al., 2016, ArXiv e-prints, <http://adsabs.harvard.edu/abs/2016arXiv161103922N>
- Negrello, M., Amber, S., Amvrosiadis, A., et al., 2017, *MNRAS*, 465, 3558, <http://adsabs.harvard.edu/abs/2017MNRAS.465.3558N>
- Neugebauer, G., Habing, H.J., van Duinen, R., et al., 1984, *ApJ*, 278, L1, <http://adsabs.harvard.edu/abs/1984ApJ...278L...1N>
- Noeske, K.G., Weiner, B.J., Faber, S.M., et al., 2007, *ApJ*, 660, L43, <http://adsabs.harvard.edu/abs/2007ApJ...660L..43N>

- Oesch, P.A., Brammer, G., van Dokkum, P.G., et al., 2016, *ApJ*, 819, 129, <http://adsabs.harvard.edu/abs/2016ApJ...819..129O>
- Okamoto, T., 2013, *MNRAS*, 428, 718, <http://adsabs.harvard.edu/abs/2013MNRAS.428..718O>
- Oliver, S.J., Bock, J., Altieri, B., et al., 2012, *MNRAS*, 424, 1614, <http://adsabs.harvard.edu/abs/2012MNRAS.424.1614O>
- Papadopoulos, P.P., Geach, J.E., 2012, *ApJ*, 757, 157, <http://adsabs.harvard.edu/abs/2012ApJ...757..157P>
- Pearson, E.A., Eales, S., Dunne, L., et al., 2013, *MNRAS*, 435, 2753, <http://adsabs.harvard.edu/abs/2013MNRAS.435.2753P>
- Peng, C.Y., Ho, L.C., Impey, C.D., Rix, H.W., 2010, *AJ*, 139, 2097, <http://adsabs.harvard.edu/abs/2010AJ....139.2097P>
- Pilbratt, G.L., Riedinger, J.R., Passvogel, T., et al., 2010, *A&A*, 518, L1, <http://adsabs.harvard.edu/abs/2010A%26A...518L...1P>
- Planck Collaboration, Ade, P.A.R., Aghanim, N., et al., 2015, *ArXiv e-prints*, <http://adsabs.harvard.edu/abs/2015arXiv150201589P>
- Poglitsch, A., Waelkens, C., Geis, N., et al., 2010, *A&A*, 518, L2, <http://adsabs.harvard.edu/abs/2010A%26A...518L...2P>
- Popescu, C.C., Tuffs, R.J., Dopita, M.A., et al., 2011, *A&A*, 527, A109, <http://adsabs.harvard.edu/abs/2011A%26A...527A.109P>
- Rémy-Ruyer, A., Madden, S.C., Galliano, F., et al., 2014, *A&A*, 563, A31, <http://adsabs.harvard.edu/abs/2014A%26A...563A..31R>
- Rigby, E.E., Maddox, S.J., Dunne, L., et al., 2011, *MNRAS*, 415, 2336, <http://adsabs.harvard.edu/abs/2011MNRAS.415.2336R>
- Rodighiero, G., Cimatti, A., Gruppioni, C., et al., 2010, *A&A*, 518, L25, <http://adsabs.harvard.edu/abs/2010A%26A...518L..25R>
- Rodighiero, G., Daddi, E., Baronchelli, I., et al., 2011, *ApJ*, 739, L40, <http://adsabs.harvard.edu/abs/2011ApJ...739L..40R>

- Rowlands, K., Dunne, L., Dye, S., et al., 2014, MNRAS, 441, 1017, <http://adsabs.harvard.edu/abs/2014MNRAS.441.1017R>
- Salmi, F., Daddi, E., Elbaz, D., et al., 2012, ApJ, 754, L14, <http://adsabs.harvard.edu/abs/2012ApJ...754L..14S>
- Sandstrom, K.M., Leroy, A.K., Walter, F., et al., 2013, ApJ, 777, 5, <http://adsabs.harvard.edu/abs/2013ApJ...777....5S>
- Santini, P., Fontana, A., Grazian, A., et al., 2009, A&A, 504, 751, <http://adsabs.harvard.edu/abs/2009A%26A...504..751S>
- Santini, P., Maiolino, R., Magnelli, B., et al., 2014, A&A, 562, A30, <http://adsabs.harvard.edu/abs/2014A%26A...562A..30S>
- Sargent, M.T., Daddi, E., Béthermin, M., Elbaz, D., 2013, Asociacion Argentina de Astronomia La Plata Argentina Book Series, 4, 116, <http://adsabs.harvard.edu/abs/2013AAABS...4..116S>
- Schmidt, M., 1959, ApJ, 129, 243, <http://adsabs.harvard.edu/abs/1959ApJ...129..243S>
- Schreiber, C., Pannella, M., Elbaz, D., et al., 2015, A&A, 575, A74, <http://adsabs.harvard.edu/abs/2015A%26A...575A..74S>
- Scoville, N., Sheth, K., Aussel, H., et al., 2016, ApJ, 820, 83, <http://adsabs.harvard.edu/abs/2016ApJ...820...83S>
- Scudder, J.M., Oliver, S., Hurley, P.D., et al., 2016, MNRAS, 460, 1119, <http://adsabs.harvard.edu/abs/2016MNRAS.460.1119S>
- Sérsic, J.L., 1963, Boletin de la Asociacion Argentina de Astronomia La Plata Argentina, 6, 41, <http://adsabs.harvard.edu/abs/1963BAAA....6...41S>
- Shaw, M.A., Gilmore, G., 1989, MNRAS, 237, 903, <http://adsabs.harvard.edu/abs/1989MNRAS.237..903S>
- Smith, D.J.B., Dunne, L., Maddox, S.J., et al., 2011, MNRAS, 416, 857, <http://adsabs.harvard.edu/abs/2011MNRAS.416..857S>

- Smith, M.W.L., Gomez, H.L., Eales, S.A., et al., 2012, ApJ, 748, 123, <http://adsabs.harvard.edu/abs/2012ApJ...748..123S>
- Speagle, J.S., Steinhardt, C.L., Capak, P.L., Silverman, J.D., 2014, ApJS, 214, 15, <http://adsabs.harvard.edu/abs/2014ApJS..214...15S>
- Springel, V., Wang, J., Vogelsberger, M., et al., 2008, MNRAS, 391, 1685, <http://adsabs.harvard.edu/abs/2008MNRAS.391.1685S>
- Sutherland, W., 2012, In: Science from the Next Generation Imaging and Spectroscopic Surveys, 40, <http://adsabs.harvard.edu/abs/2012sngi.confE..40S>
- Sutherland, W., Saunders, W., 1992, MNRAS, 259, 413, <http://adsabs.harvard.edu/abs/1992MNRAS.259..413S>
- Vaghmare, K., Barway, S., Mathur, S., Kembhavi, A.K., 2015, MNRAS, 450, 873, <http://adsabs.harvard.edu/abs/2015MNRAS.450..873V>
- Valiante, E., Smith, M.W.L., Eales, S., et al., 2016, MNRAS, 462, 3146, <http://adsabs.harvard.edu/abs/2016MNRAS.462.3146V>
- van der Wel, A., Bell, E.F., Häussler, B., et al., 2012, ApJS, 203, 24, <http://adsabs.harvard.edu/abs/2012ApJS..203...24V>
- Wang, L., Cooray, A., Farrah, D., et al., 2011, MNRAS, 414, 596, <http://adsabs.harvard.edu/abs/2011MNRAS.414..596W>
- Werner, M.W., Roellig, T.L., Low, F.J., et al., 2004, ApJS, 154, 1, <http://adsabs.harvard.edu/abs/2004ApJS..154....1W>
- Wright, T., 1750, *An original theory or new hypothesis of the universe : founded upon general phaenomena of the visible creation; and particularly the Via the laws of nature, and solving by mathematical principles : the Lactea ...compris'd in nine familiar letters from the author to his friendand : illustrated with upward of thirty graven and mezzotinto plates ...*
- Young, J.S., Scoville, N.Z., 1991, ARA&A, 29, 581, <http://adsabs.harvard.edu/abs/1991ARA%26A..29..581Y>